NATIONAL INSTITUTE FOR FUSION SCIENCE

Proceeding of A3 Foresight Program Seminar on Critical Physics Issues
Specific to Steady State Sustainment of High- Performance Plasmas
12 -15 December, 2017, Chongqing, China

Edited by Liqun HU, Shigeru MORITA and Yeong-Kook OH

Proceeding of A3 Foresight Program Seminar on

Critical Physics Issues Specific to Steady State Sustainment

of High-Performance Plasmas

12 - 15 December, 2017, Chongqing, China

Edited by

Liqun HU, Shigeru MORITA and Yeong-Kook OH

Abstract

A3 foresight program is a joint project on plasma physics research under the auspice of JSPS (Japan), NRF (Korea) and NSFC (China) to enhance closer collaborations among scientists in three countries. Its main purpose is to solve several key physics issues specific to steady state high performance plasmas through joint experiments on three Asian advanced fully superconducting fusion devices (EAST in China, LHD in Japan, KSTAR in Korea) and other magnetic confinement devices to carry out multi-faceted and complementary physics researches. As a major activity of this A3 program, the academic workshop is held in Korea, Japan, and China in turn. Since the first coordinator meeting at Jeju Island, Korea in 2012, eleven workshops have been held with four in Japan, four in Korea and three in China. A3 program has become an important platform for scientists of three countries to report and discuss the latest progress and achievement in steady-state sustainment of high-performance plasma. As the last workshop of this A3 program, the 12th workshop is proposed to summarize the fruitful achievements obtained within the framework of the A3 program, optimize ongoing researches, and plan on the future collaborations. This 12th A3 Foresight Program Workshop was held in Chongqing, China. The topics include current drive and profile control, transport of edge and divertor plasmas, stability of edge plasma, interaction between energetic particle and bulk plasma, and experimental and theoretical study in other relative fields.

Key words: magnetically confined devices, toroidal plasmas, high performance plasmas, steady state operation, edge plasma, divertor plasma, edge stability, high-energy particle, alpha particle and fusion plasma simulation.

Organizing Committee

Liqun HU (Institute of Plasma Physics, Chinese Academy of Sciences, China)

Shigeru MORITA (National Institute for Fusion Science, Japan)

Yeong-Kook OH (National Fusion Research Institute, Korea)

Program Committee

Liqun HU (Institute of Plasma Physics, Chinese Academy of Sciences, China)

Shigeru MORITA (National Institute for Fusion Science, Japan)

Yeong-Kook OH (National Fusion Research Institute, Korea)

Ge ZHUANG (Huazhong University of Science and Technology, China)

Hong QIN (University of Science and Technology of China, China)

Yi LIU (Southwestern Insitute of Physics, China)

Ze GAO (Tsinghua University, China)

Houyang GUO (Institute of Plasma Physics, Chinese Academy of Sciences, China)

Nong Xiang (Institute of Plasma Physics, Chinese Academy of Sciences, China)

Bingjia Xiao (Institute of Plasma Physics, Chinese Academy of Sciences, China)

Conference Secretariat

Ruijie Zhou (Institute of Plasma Physics, Chinese Academy of Sciences, China)

Shaohua Dong (Institute of Plasma Physics, Chinese Academy of Sciences, China)

Preface

Steady-state sustainment of high-performance plasmas is one of the crucial issues needed to be addressed for fusion reactor development. A3 foresight program on plasma physics newly started from August 2012 under the auspice of JSPS (Japan), NRF (Korea) and NSFC (China) to enhance closer collaborations among scientists in three countries. The main purpose of this project is to solve several key physics issues through joint experiments on three Asian advanced fully superconducting fusion devices (EAST in China, LHD in Japan and KSTAR in Korea) and other magnetic confinement devices to carry out multi-faceted and complementary physics researches.

The 1st coordinator meeting hosted by NFRI (Korea) was held in Jeju Island, Korea on 22 August in 2012. Since then, eleven seminars have been held in Japan, China, and Korea in turn. More specifically, the second meeting hosted by NIFS (Japan) was held in Kushiro, Japan during 22-25 January in 2013, followed by third meeting hosted by ASIPP (China) in Beijing, China during 20-23 May in 2013, fourth meeting hosted by NFRI (Korea) in Gyeongju, Korea during 3-4 November in 2013, fifth meeting hosted by NIFS (Japan) in Kagoshima, Japan during 23-26 June in 2014, sixth meeting hosted by ASIPP (China) in Nanning, China during 6-9 January in 2015, seventh meeting hosted by NFRI (Korea) in Chuncheon, Korea during 19-22 May in 2015, eighth meeting hosted by NIFS (Japan) in Tokyo, Japan during 1-4 December in 2015, ninth meeting hosted by ASIPP (China) in Nanning, China during 17-20 May in 2016, tenth meeting hosted by NFRI (Korea) in Jeju, Korea during 22-25 November in 2016, and eleventh meeting hosted by NIFS (Japan) in Sapporo, Japan during 11-14 July in 2017, respectively. Fruitful results from collaborative research have been summarized and discussed, and the foundations for further collaborations among scientists in China, Japan and Korea have been laid during those meetings. Also, many young scientists obtained the opportunity to get lots of valuable guidance and advices from experienced scientists.

As the last workshop of this A3 program, the twelfth meeting hosted by ASIPP (China) is held in Chongqing, China during 12-15 December in 2017, to summarize the

fruitful achievements obtained within the framework of the A3 program, optimize ongoing researches, and plan on the future collaborations. In total 57 participants attended this meeting, among which 8 from Korea, 15 from Japan, and 34 from China. In the meeting, participants gave 44 reports which focused on five categories (I: Current drive and profile control; II-a: Transport of edge and divertor plasmas; II-b: Stability of edge plasma; III: Interaction of energetic particle and bulk plasma; IV: Experimental and theoretical study in other relative fields). Those reports summarized the achievements obtained within the framework of the A3 program in the past five years, and also contained the latest results in physics research and the status of system upgrade of the main magnetic confined fusion devices in China, Japan and Korea. Participants discussed ardently on issues of interest in the reports and on future collaboration plans. Results of the collaboration based on this meeting are published as the proceeding which can ensure better communication among the A3 community. In the proceeding, 38 papers are collected in the end.

The meeting was closed with great success, summarized and clarified remarkable progress obtained through A3 collaboration in the researches concerning the above important topics. The organizing and program committees are deeply grateful to all participants and to strong and continuous support from foundation of three countries (NSFS in China, JSPS in Japan, and NRF in Korea), with whose support and corporation this A3 foresight program on plasma physics was smoothly and successfully concluded.

<div align="right">

Liqun HU, Shigeru MORITA and Yeong-KooK OH

Chairpersons of the Organizing Committee

</div>

Contents

Preface

Contents

Photo of Participants

Category II-b: Stability of edge plasma

Category III: Interaction between energetic particle and bulk plasma

Category IV: Experimental and theoretical study in other relative fields

Program

List of Participants

Progress on new LHCD antenna development

J. Kim[1], S. Wang[1], J. Han[1], H. Wi[1], T. Seong[2], M. H. Cho[2], and W. Namkung[2]

[1]National Fusion Research Institute, Daejeon, Korea

[2]POSTECH, Pohang, Korea

Abstract

New passive active multijunction (PAM) type antenna for 0.5 MW KSTAR LHCD system is under construction for a preliminary study of 4-MW PAM system and increase of power rating of current 0.5 MW system. The determination of N//, design and structure of antenna will be introduced. Prototype PAM was constructed and its low level RF characteristic such as splitting ratio and phase shift has been measured. Tools for RF measurement and the result will be shown as well.

1. Introduction

KSTAR is equipped with 0.5 MW 5 GHz LHCD system for off-axis current drive [1]. The initial antenna is a grill type antenna benchmarked Alcator C-mod. New passive active multijunction (PAM) type antenna for 0.5 MW KSTAR LHCD system is under construction. Main purpose for new PAM antenna system construction is a preliminary study before upgrade which is planned for 2021. Basic design of 4 MW antenna is mid-plane PAM as shown in Fig. 1. Before full scale construction, it is necessary to make small scale test for the accessibility check, power limitation check, design proof, and verification of the fabrication method. In addition, initial grill launcher has a power limitation. It could not apply full power of klystron. So we started new launcher development.

2. Design of PAM

The first step of antenna design is choice of N//, the parallel refractive index which consequently determine the spatial period in the direction parallel to magnetic field. N// of antenna was determined by
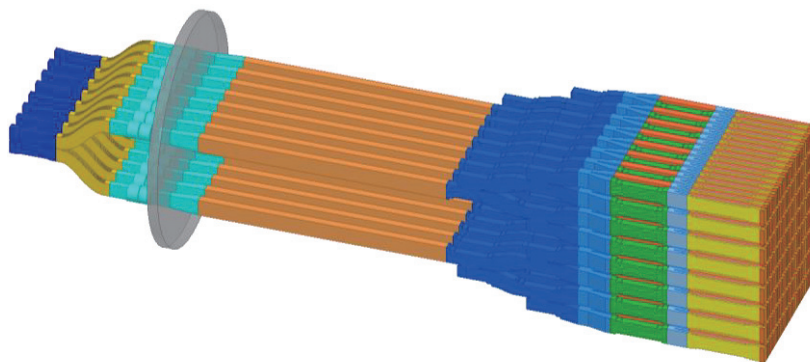
Fig.1 RF model of conceptual design for 4 MW PAM antenna of KSTAR LHCD system including RF power distribution system.

considering the accessibility of slow wave and strong electron Landau damping condition. The curves in Fig. 2 are the plots of the accessibility condition,

$$N_\parallel > N_{\parallel,acc} = \sqrt{1 - \frac{\omega_{pi}^2}{\omega^2} + \frac{\omega_{pe}^2}{\omega_{ce}^2}} + \frac{\omega_{pe}}{\omega_{ce}}$$ as a function of minor radius at various magnetic fields and plasma density. The left vertical axis is the N// of a wave and the right vertical axis is the corresponding plasma temperature for efficient electron Landau damping of the wave having the N// of left axis. The abscissa is the minor radius of the plasma. The left and right sides correspond to the high field side and low field side, respectively. Below this curve is inaccessible region and above the curve is accessible region. For example, if a wave with N// 2.5 is launched to a plasma with peak density 1 x 10^{20} m^{-3} and 2.5 T of toroidal magnetic field from high field side, the corresponding curve is this green dotted line. It can propagate freely close to 0.5 of minor radius, then reflects at inaccessible region. If the wave meets a region with plasma temperature of 4.8 keV which is resonant to N//=2.5 of LH wave before arriving here, the wave energy will be absorbed by plasma by electron Landau damping. Large N// is good for accessibility aspect but current drive efficiency is decreased as N// increases. In addition, it is difficult to make launcher with large N// since the spatial period of PAM is inversely proportional to N//. N//=2.5 was chosen for prototype PAM targeting 3 T of toroidal magnetic field with peak plasma density less than 8x10^{19} m^{-3}. Though the results are not shown here, ray tracing calculations have been performed with a scan of N// from 2.0 to 2.5 at 3 T of toroidal magnetic field with advanced tokamak profile. It showed a single pass absorption when N// is higher than 2.4 at 3 T.

The launcher has 4 rows of 17 waveguides (8 active waveguides with 9 passive waveguides alternatively). More detailed antenna information such as the detailed dimension of PAM launcher, N// spectrum and coupling properties at various plasma condition calculated using ALOHA code, and RF design of multijunction using HFSS were introduced at other references [2][3]. The peak N// was 2.5 and the coupling is quite good even at the low density around the 5 GHz cutoff.
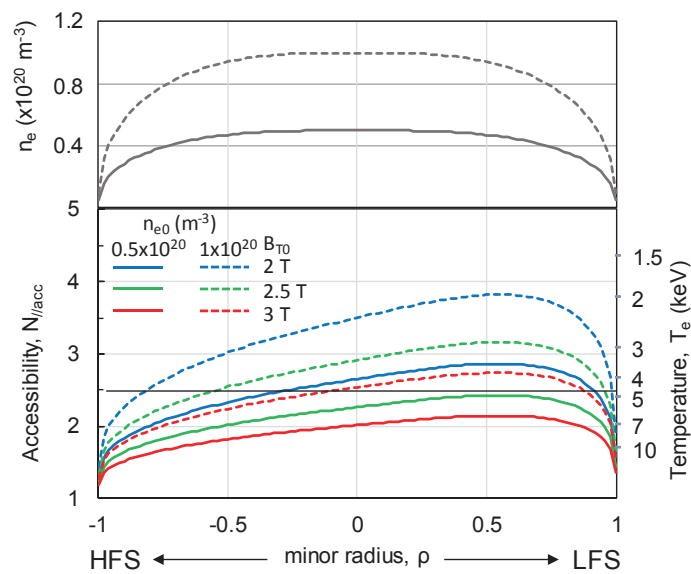
Fig.2 Density profiles (top), and the corresponding accessibility curve of lower hybrid waves (bottom) in various toroidal magnetic field.
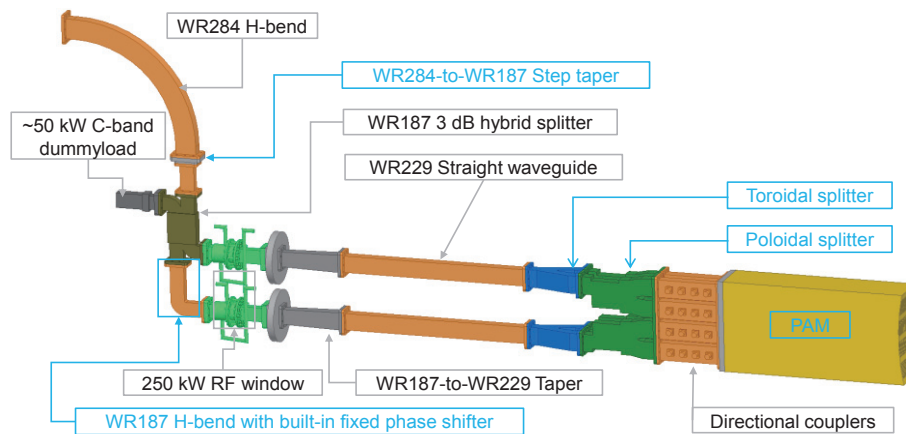
Fig. 3 Photo-like 3D CAD drawing of new 0.5 MW PAM antenna system.

Fig. 3 illustrates the three dimensional CAD drawing of prototype PAM antenna system including PAM launcher and RF feeding system. The power from the transmission line is split into two in poloidal direction by commercial WR187 3-dB hybrid splitter, then split in toroidal direction by two toroidal splitter, and again in poloidal direction by four poloidal splitter. The components with blue colored label is designed and fabricated by NFRI design and the others are commercial one.

3. Fabrication and measurement of PAM

The RF characteristics of the NFRI designed components have been measured. The role of WR187 H-bend with built-in fixed phase shifter is to give the 90 degree phase difference between two RF window inputs. Then the reflected power from plasma will be sent to the C-band dummyload connected to the rest ports of WR187 3-dB hybrid splitter instead of reflecting toward the klystron via transmission line connected to the port 1. The balance and the measured phase shift between two output ports of WR187 3-dB hybrid splitter with the H-bend is about 0.01 dB and 268 degree, respectively. The performance of toroidal splitter and poloidal splitter have been measured as well. The reflections and the balance of toroidal splitters were, respectively, lower than -30 dB and 0.1 dB. The poloidal splitter is designed based on Riblet short slot type hybrid splitter. The measured splitting ratios were -3.03 and -3.04 dB and reflection was less than -35 dB.

The PAM is composed of nine copper plates. Five of them are smooth plates and the rest four plates have waveguides machined on both sides. They stacked alternatively then brazed. Fig. 4 shows the photo of finished PAM after brazing. Launcher mouth was shaped along the plasma curvature. Inside of the antenna was inspected using endoscope after brazing.

The RF characteristics of PAM have been measured using vector network analyzer. Special tools were necessary for the RF characteristic measurement of PAM. Fig. 5 shows the cad drawing illustrating the RF measurement setup and photos of actual setup. The coaxial line is connected to a vector network analyzer. One set of multijunction is composed of one WR229 input and four outputs with 90 degree phase shift and the dimension of 58.2 mm x 7 mm. Since the input of PAM launcher is based on WR229 waveguide and the waveguide-to-coaxial adapter for C-band is WR187 size, we needed WR187-to-WR229 taper. The size

Fig. 4 The photo of finished PAM. Launcher mouth were shaped along the plasma curvature.

of active waveguide at the launcher mouth is 58.2 mm x 7 mm. Thus we designed a special tapered adapter which can be inserted into the PAM waveguides. The other ports affecting the measurement should be matched during a measurement of a port. So we made a matched load of eccosorb. The measurement was performed for each multijunction, one by one. As shown in the right bottom photos of Fig. 5, when one active waveguide is measured by the adapter, the others are matched with eccosorb.

These are a pair of adapters. Their scattering parameters were measured by inserting into a 15 cm dummy waveguides. S_{11} is less than -35 dB and the S_{21} is -0.11 dB. The performance of eccosorb matched load was also measured using a tapered adapter and a dummy waveguide. S_{11} by the eccosorb matched load was approximately less than -30 dB.

The phase and splitting ratio of each PAM multijunction were measured one by one using the tools. Measured result was shown in Fig. 6. The reflections of the multijunctions matched with eccosorb® dummyload were less than 20 dB for all multijunction, though not shown in the figure. The graph at the left shows the phase shift of four columns for eight multijunction. They are grouped two due to the length difference by the curvature shaping. MJ 2, 3, 6, and 7 are the shorter one positioned close to the poloidal center of the PAM and the other MJ 1, 4, 5, and 8 the longer one positioned far from it. Splitting ratio of each multijunction is shown in the right graph. MJ2 showed poor balance compared to others. The RF performance of the PAM is quite nice.
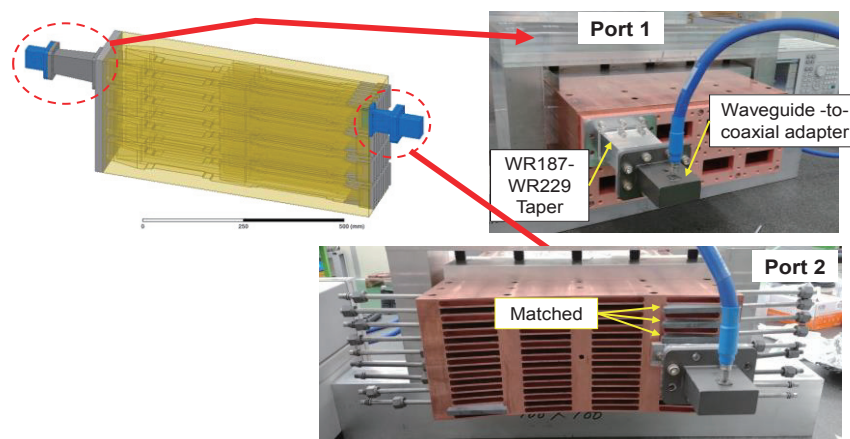
Fig. 5 The CAD illustration and the photos of RF measurement setup for PAM. Specially designed Eccosorb® matched load and the taper adapter have been used.
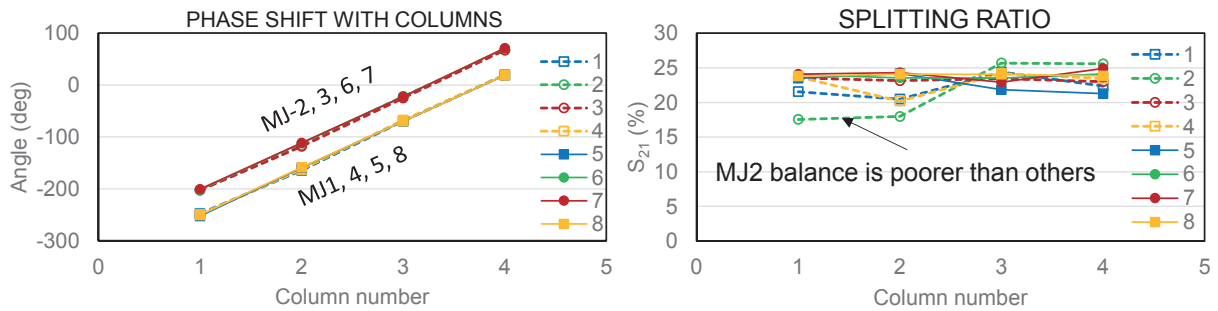
Fig. 6 Phase shift between adjacent active waveguides of each multijunction (left), Power splitting ratio preetween active waveguides of each multijunction (right)

4. Future work

High power test and conditioning for PAM and RF components should be performed in a test chamber before KSTAR installation. Conditioning process of the antenna should be set up with vacuum load. New antenna system is expected to be available in 2018 KSTAR campaign

Acknowledgements

References

[1] S. Park, et al., Fusion Sci Technol., 63 (1) (2016), pp. 49-58

[2] J. Kim, et al., Fusion Eng. Design, 123 (2017) 299

[3] J. Kim, J. Han, L. Delpech, et al., 22nd topical Conference on RF power in plasmas, Aix en Provence, May 30-June 2, 2017

Study on ECH-assisted start-up using trapped particle configuration in KSTAR and application to ITER

Jeongwon Lee[1], Jayhyun Kim[1], YoungMu Jeon[1], YoungHwa An[1], Jong-Gu Kwak[1], Min-Gu Yoo[2], Yong-Su Na[2], Y.S. Hwang[2], Yeong-Kook Oh[1] and KSTAR team

[1]National Fusion Research Institute, Daejeon, Republic of Korea
[2]Department of Nuclear Engineering, Seoul National University, Seoul, Republic of Korea

Abstract

ECH-assisted start-up using trapped particle configuration (TPC) is firstly studied in a superconducting, conventional tokamak, KSTAR. First, improved and efficient start-up using TPC than conventional field null configuration (FNC) is achieved by enhanced pre-ionization plasma quality. Reliability of TPC is investigated by 0-dimensional plasma evolution code, TECHP0D. Second, the characteristics of TPC start-up are explored with experiments. Two kind of start-up conditions of the magnetic pitch and prefill pressure are identified. Finally, reliable ITER-relevant low toroidal electric field start-up using TPC is achieved with drastically improved success rate of start-up in KSTAR.

1. Introduction

There are general issues of the ITER start-up phase: 1) the limitation of the toroidal electric field due to the superconducting solenoid coil operation, and 2) the difficulty to control the magnetic field configuration due to the large eddy current on the vacuum vessel. Therefore, ECH-assistance during the plasma start-up phase is believed to be essential for stable and robust start-up of ITER. There are many efforts to validate the ECH-assisted start-up by experiments and 0D modelling [1]–[4].

Effect of the poloidal field, especially the vertical component of poloidal field, to the open-field plasma confinement has been studied by both experimental and theoretical ways. Start-up with 40 G vertical poloidal field showed better pre-ionization and performance than field null configuration (FNC) in DIII-D [1]. In VEST device , the first spherical torus in Korea, an efficient ECH-assisted plasma start-up is achieved by changing the magnetic field structure from conventional field null configuration (FNC) to mirror-like trapped particle configuration (TPC) [5]. The TPC shows enhanced plasma confinement during the pre-ionization phase than FNC. Thanks to these improved pre-ionization plasmas, the faster plasma current initiation and the wider operation range in terms of the electromagnetic condition, prefill pressure, and ECH injection power are obtained with reduced volt-second consumptions. Comparison between the case of vertical field only as in DIII-D and the mirror-like TPC was also studied.

In this research, TPC is applied for efficient ECH-assisted plasma start-up in a conventional tokamak, KSTAR to evaluate the performance of TPC in the larger size, higher aspect ratio, and superconducting tokamak. Dedicated experiments to investigate the parametric dependency of TPC are conducted and analyzed by 0D start-up simulation code, TECHP0D. Operation window in terms of the poloidal mirror

field strength and the prefill pressure are explored [6].

2. Feasibility study of the TPC start-up in KSTAR

Plasma start-up scenario based on TPC is developed by superimposing the mirror-like magnetic configuration made by PF#5 on the conventional FNC. TPC exhibits an equilibrium-like magnetic field structure to obtain toroidal force balance during the whole start-up phase by increasing the poloidal field strength. Due to the initial charging current of other PF coils, the mirror-like TPC structure is formed only in the major radius less than 2.0 m. The 2nd harmonic, X-mode electron cyclotron (EC) heating system is used for pre-ionization of plasmas. The injection power and the frequencies are 600-750 kW and 105, 140, and 170 GHz, respectively. The resonance layer is located near the major radius of 1.65 m, to generate the ECH plasmas on TPC. To investigate the plasma characteristics during the start-up phase, diagnostic tools are carefully chosen. The basic magnetic diagnostics, fast CCD camera, interferometry, deuterium and carbon line radiation, and Electron cyclotron emission (ECE) are employed for the study.

The performance of the plasma start-up is compared between TPC and FNC in KSTAR 2015 campaign, shot #12400 and #12403, respectively. The only difference is the magnetic field configuration. The 170 GHz, X2 ECH with power up to 600 kW is injected from 60 ms before the loop voltage onset. The toroidal field strength is 2.7 T at the geometric axis and the resonance layer is 1.62 m. Toroidal injection angle of ECH is set to be co-current direction of 20°, the same configuration of ITER. The magnetic mirror ratio at the resonance layer is 1.4 and the prefill pressure is 2×10^{-5} mbar. Initial charging currents of each PF coils are identical except PF#5, which has slightly different charging current less than 10 %.

TPC shows more efficient plasma start-up property than FNC which is obtained by adding the small TPC structure with the poloidal field of 36 G to FNC. The time evolution of plasma parameters of FNC and TPC is shown in FIG.1. With identical ECH injection, pre-ionization is only observed under TPC with the density of 4×10^{18} m^{-2}. Plasma breakdown occurs with 20 ms of delay after the 2nd harmonic ECH as indicated by the peak of D_α in FIG.1. With the help of these pre-ionization plasmas, an early and fast plasma current formation is achieved by TPC. TPC requires 2 V of loop voltage for plasma current initiation, on the other hand FNC requires 3 V. Carbon impurity line intensity is sustained below the level of FNC burn-through phase under TPC.

To model the improved confinement by particle trapping effect, a factor to reduce the convective loss is adopted to the density and energy balance equations. TECHP0D [7] considers 3 convective loss mechanism, 1) loss along the magnetic field line with sound speed, 2) Bohm diffusion, and 3) grad-B and curvature drift loss. The trapping motion can reduce the parallel loss of the magnetic field which can be represented by the reducing factor. 50 % of reduction is selected in this study. The reference TPC scenario, #12400, is simulated with TECHP0D as a baseline simulation target. Basic input parameters are taken from the experiment, such as the ECH configuration, magnetic field information and applied ohmic power. The prefill pressure is determined to simulate the pre-ionization density of 4.5×10^{18} m^{-3} with full ionization.

Pure Ohmic (12393) TPC (12400) FNC (12403)
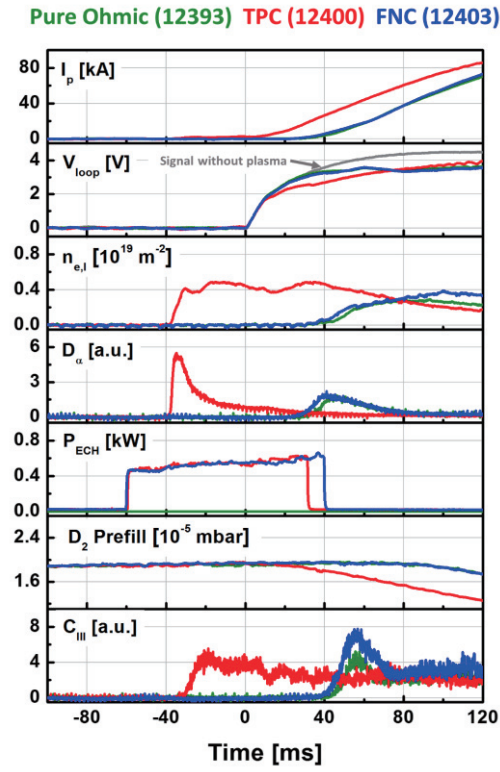
Fig. 1   Comparison of the plasma start-up performance between pure ohmic with field null, FNC and TPC with ECH. Plasma current, loop voltage, line averaged electron density, deuterium line radiation, ECH injection power, prefill pressure, and carbon line radiation. (Reuse of figure 2 in [6])
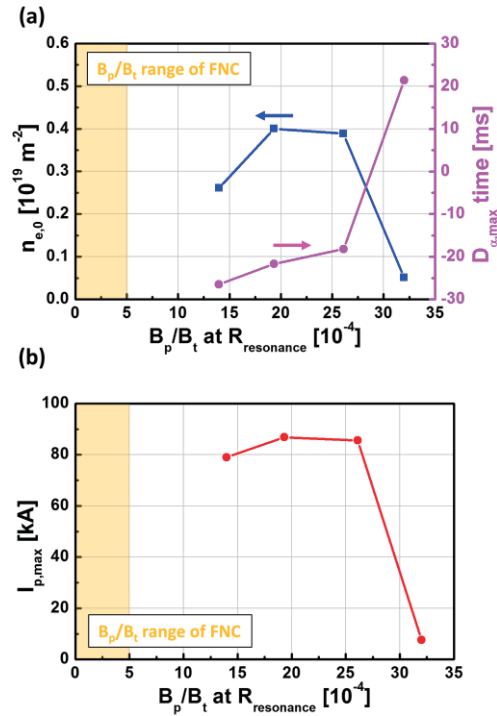
Fig. 2   (a) Pre-ionization plasma density and peak time of D_α, (b) maximum plasma current formation according to the magnetic pitch. (Reuse of figure 7 in [6])

3. Parametric dependency of TPC startup

The TPC start-up under various experimental conditions was attempted. The prefill pressure and the magnetic pitch angle were the main varied parameters in the experiments. Both parameters are closely related to the start-up issues encountered in KSTAR. ECH characteristics such as threshold power, injection angle dependency, and higher harmonic effect are not covered in this research. However, the ITER-relevant ECH configuration is tested.

First, the start-up performance according to the magnetic pitch is explored. The magnetic pitch is used to represent the magnetic field quality, defined by the ratio between poloidal and toroidal magnetic field at the ECH resonance layer. In this scanning experiment set, the toroidal field strength is fixed to be 1.7 T at the KSTAR machine axis, and the magnetic pitch is changed by variation of PF#5 coil charging current from 150 A to 600 A, which is corresponding to 25 to 55 G at the resonance layer. The 105 GHz, 600 kW of X2 ECH is injected 120 ms before the solenoid swing down for pre-ionization plasmas. The prefill pressure is fixed to be 1.9×10^{-5} mbar. The experimental results are presented in FIG.2. (a) for the pre-ionization electron density at t=0 s, and (b) for the maximum plasma current formation versus the magnetic pitch at the ECH resonance layer. The successful TPC start-up can be achieved with the magnetic pitch up to 27×10^{-4}, corresponding to the poloidal field strength of 45 G. These successful cases have the pre-ionization density order of 10^{18} m^{-2} with a peak of D_α during the pre-ionization phase and the plasma current formation up to ~90 kA at the end of the start-up phase, then the plasma control system successfully takes over the plasmas.
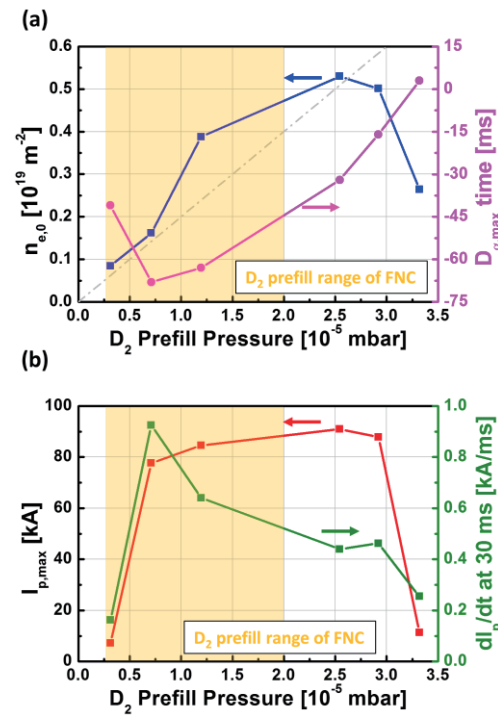
Fig.3 Parametric dependency of the deuterium prefill pressure to the TPC start-up in KSTAR. Characteristics of pre-ionization plasmas (a), and the plasma current formation (b) are depicted. (Reuse of figure 8 in [6])

Second, the prefill pressure effect is investigated to the TPC start-up scheme. The experimental results are presented in FIG.3. (a) for the pre-ionization phase, and (b) for the plasma current formation phase, respectively. The prefill deuterium pressure is varied from 0.3 to 3.5×10^{-5} mbar. The 140 GHz of ECH is applied with the maximum injection power of 750 kW and the injection angle of 15°. The magnetic pitch is fixed at 14×10^{-4}, which corresponds to the poloidal and toroidal magnetic field of 35 G and 2.5 T, respectively. Especially the toroidal field of 2.3 T at the machine axis allows the ECE measurement at the ECH plasma region so that the tendency of electron temperature against the prefill condition can be identified. The prefill pressure range of 0.7 to 3.0×10^{-5} mbar show successful plasma current formation up to 90 kA at the end of the start-up phase with the pre-ionization density of 0.15 to 0.5×10^{19} m^{-2}. The D_α peak shows that the ionization occurs during the pre-ionization phase indicated with the negative D_α peak time. The pre-ionization density linearly increases with the prefill pressure up to 0.5×10^{19} m^{-2} as shown in FIG.3 (a). It is notable that TPC could be helpful to resolve the prefill control issue by increasing the prefill operation range above the expected pressure range due to the influence of NBI. Finally, the plasma current rising speed is inversely proportional to the prefill pressure within the start-up successful cases. It is shown in FIG.3 (b), depicted by green line. It is observed that the prefill pressure as low as possible within appropriate operation range is desired to efficient plasma current formation.

Low electric field start-up using TPC is conducted in KSTAR for demonstrating the ITER-relevant start-up. In ITER, it has been noticed that the toroidal electric field is restricted by the superconducting solenoid coils and it makes difficulties for reliable plasma start-up. The low toroidal electric field start-up experiments of TPC and FNC are performed and compared in FIG.4. The applied toroidal electric field is less than 0.3 V/m during the whole start-up phase, which is lower than the ITER target value. For pre-ionization, the 140 GHz, X2 ECH power up to 750 kW is injected for 90 ms with co-current toroidal angle of 15 degree. With FNC, no pre-ionization plasmas is detected and the plasma current formation is failed. On the other hand, the pre-ionization plasma with density of 1×10^{18} m^{-2} is formed with a D_α peak before the solenoid swing down and the plasma current of 60 kA is achieved at the end of the pre-programmed start-up phase with TPC. The prefill pressure is reduced to half value of the normal toroidal electric field operation for reliable deuterium burn-through at the reduced ohmic power. The carbon line radiation shows no severe impurity influx. This result shows not only the reliability of the TPC scheme in the ITER-relevant condition, but also the expansion of the operation condition for various physics experiments in KSTAR including the reversed plasma current operations for the QH-mode study where the start-up was very unstable with FNC.

4. Conclusion

The plasma start-up using TPC is successfully demonstrated in KSTAR. Owing to improved confinement of ECH pre-ionization plasmas, the earlier and the faster plasma current formation can be obtained with the wider operation range in terms of the deuterium prefill pressure and the magnetic pitch at the identical loop voltage compared with FNC. Such efficient plasma start-up with ECH plasmas is also confirmed by the start-up modeling code, TECHP0D where the open-field confinement model is newly improved in this work. It is shown that the confinement can be enhanced by the particle trapping motion.

TPC is helpful to overcome the limitation of FNC such as the poloidal magnetic field and prefill pressure control issues in KSTAR, and also expected in ITER. The physics background of the operation limits in terms of the deuterium prefill pressure and the magnetic pitch is investigated with TECHP0D. It is revealed that the lower and the upper prefill limit result from the convective loss of plasmas before the closed flux formation and the loss of electron energy by ionization during the plasma current formation phase, respectively. A feasibility study of ITER start-up scenario is conducted by using TPC under the ITER-relevant conditions established in KSTAR. The applied toroidal electric field is less than 0.3 V/m during the whole start-up phase, which is lower than the ITER target. In these experiments, the TPC scenario shows a stable plasma start-up with advantages of early current initiation without delicate magnetic field control. Using TPC, not only severe volt-second savings but also stable superconducting operations with a reduced required toroidal electric field are achieved which is promising for a reliable and stable plasma start-up in ITER.
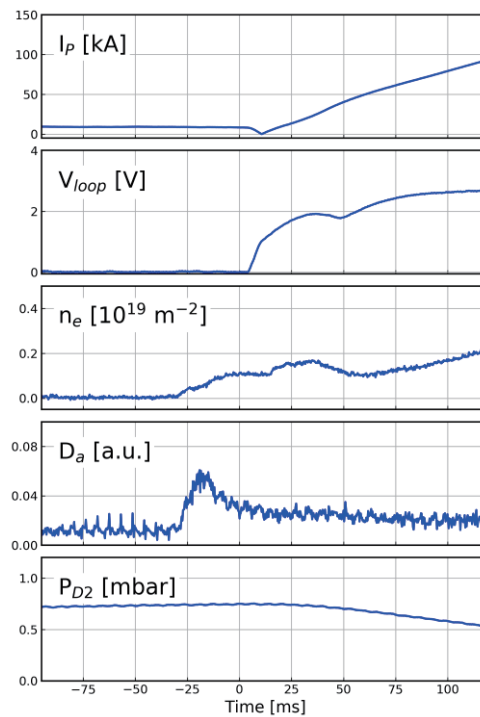
Fig.4 Experimental result of low toroidal electric field start-up using TPC in KSTAR. Successful plasma start-up is achieved with pre-ionization plasma and mild impurity radiation loss.

References

[1]   G. L. Jackson *et al.*, "Plasma Initiation and Start-Up Studies in the DIII-D Tokamak with Second-Harmonic EC Assist," *Fusion Sci. Technol.*, vol. 57, no. 1, pp. 27–40, Jan. 2010.

[2]   K. Hada, K. Nagasaki, K. Masuda, R. Kinjo, S. Ide, and A. Isayama, "Analysis of ECRH Pre-Ionization for Plasma Start-Up in JT-60SA," *Plasma Fusion Res.*, vol. 7, no. 0, pp. 2403104–2403104, 2012.

[3]   Y. S. Bae *et al.*, "ECH pre-ionization and assisted startup in the fully superconducting KSTAR tokamak using second harmonic," *Nucl. Fusion*, vol. 49, no. 2, p. 022001, Feb. 2009.

[4]   H.-T. Kim, A. C. C. Sips, P. C. de Vries, and JET-EFDA Contributors, "Plasma burn-through simulations using the DYON code and predictions for ITER," *Plasma Phys. Control. Fusion*, vol. 55, no. 12, p. 124032, Dec. 2013.

[5]   Y. An *et al.*, "Efficient ECH-assisted plasma start-up using trapped particle configuration in the versatile experiment spherical torus," *Nucl. Fusion*, vol. 57, no. 1, p. 016001, Jan. 2017.

[6]   J. Lee, J. Kim, Y. An, M.-G. Yoo, Y. S. Hwang, and Y.-S. Na, "Study on ECH-assisted start-up using trapped particle configuration in KSTAR and application to ITER," *Nucl. Fusion*, vol. 57, no. 12, p. 126033, Dec. 2017.

[7]   Y. S. Bae and A. C. Engl, "Study on Pre-Ionization Using Second-Harmonic Electron Cyclotron Waves for the KSTAR First Plasma," *J. Korean Phys. Soc.*, vol. 51, no. 4, p. 1313, Oct. 2007.

Recent Research Status of NIFS NBI

K. Tsumori[1,2], K. Ikeda1, H. Nakano[1,2,] M. Kisaki[1], Y. Haba[3], K. Nagaoka[1,3], I. Mario[4], S. Kamio[1], Y. Fujiwara[1] and M. Osakabe[1,2]

[1]National Institute for Fusion Science, Toki 509-5292, Gifu, Japan

[2]Graduate University for Advanced Studies, Toki 509-5292, Gifu, Japan

[3]Nagoya University, Furo-cho 1, Chikusa-ku, Nagoya 464-8603, Japan

[4]Max-Planck-Institut für Plasmaphysik, Bereich ITER-Technologie & -Diagnostik / N-NBI,

Boltzmannstr. 2 85748 Garching, Germany.

Abstract

Neutral Beam Injection (NBI) with deuterium beams has been started in the Large Helical Device (LHD) at the National Institute for Fusion Science (NIFS) since 2017.   While the positive-ion based NBI systems injected the deuterium beams successfully, the deuterium negative ion (D^-) current decreased and co-extracted electron current increased in the negative-ion based NBI systems.   This is considered that so-called caesium (Cs) effect is reduced by changing the filling gas to the negative ion sources from hydrogen (H_2) to deuterium (D_2).   In order to resolve the issues related to the D^- operation, beamlet diagnostics have started at NIFS-NBI test stand.   We could obtain the beamlet data using those diagnostics successfully and the data analyzed will be possible to lead to the improvement of LHD negative-NBI system.

1. Introduction

Deuterium plasma experiment provides important data related to isotope effects necessary to understand fusion plasmas such as plasma transport [1-5], generation of fast neutrons due to D-D reaction [6-8], enhancement of the sputtering yield at the divertor [9-11] and hydrogen isotope inventories [12,13]. Those data are important to design the fusion machines in future and the fusion-plasma reactors.   Since the last week of January 2017, the deuterium experimental campaign has been conducted in the National Institute for Fusion Science (NIFS) [14].   Both of the positive- and negative-NBI systems are utilized to inject hydrogen and deuterium beams.   Since the beam energies of the positive-NBI systems have been increased in deuterium beam injections and the beams were successfully injected.   On the other hand, the beam power injected with negative-NBI systems were lower than the expected power, 70 % of the injection power of H- case.   That is because decrease of D- ion current and increase of co-extracted electron current. Those are observed in the other negative ion accelerations at QST [15-18] and IPP Garching [19-22] and are the common issue to be solved for future negative-NBI systems.

In order to solve the problem related to the difference of H- and D- beams, diagnostics of the ion-source plasmas have been continued.   The beam characteristics, however, is necessary to be investigated together with the measurement of the source plasmas.   Especially, the formation of meniscus,

which is the boundary of source plasma and beam region, is the most important to resolve the mechanism of the extraction of negative-ion beams.

In the following sections, the difference of H₋ and D₋ beams are introduced firstly, beamlet diagnostic systems newly installed in NIFS-NBI test stand will be discussed, and summarized all at the last section.

2. INJECTION OF H₋ AND D₋ BEAMS

In the LHD experimental campaign in 2017, two positive-NBI systems, beamline #4 and #5, were upgraded their beam energies from 40 keV for hydrogen beams up to 60 and 75 keV for deuterium beams, and the electrode gaps are expanded from 6 mm to 8 and 9 mm, respectively.   As the results, the injection powers of 9.4 MW and 10.6 MW at the maximums have been obtained in the beamline #4 and #5, respectively.   No significant difference of the beam characteristics was observed in the hydrogen and deuterium beams in the positive-NBI.

On the other hand, the beam energies of the negative-NBI systems have been kept at 190 keV to suppress the energy transfer from injected ions to electrons in the LHD plasma.   Due to the limitation of the D₋ acceleration except for the LHD experimental room, no investigation has been done for the beams, and, therefore, magnetic and accelerator configurations optimized for H₋ beams have been applied for the beam injection in the deuterium experimental campaign in 2017.   Initially, injection with H₋ beam has continued for four months and the beam switched to D₋ beam.   The changes of negative-ion current, I_{neg}, and the ratio of electron to negative-ion current, I_e / I_{neg}, are shown in Fig. 1(a) and (b), respectively.
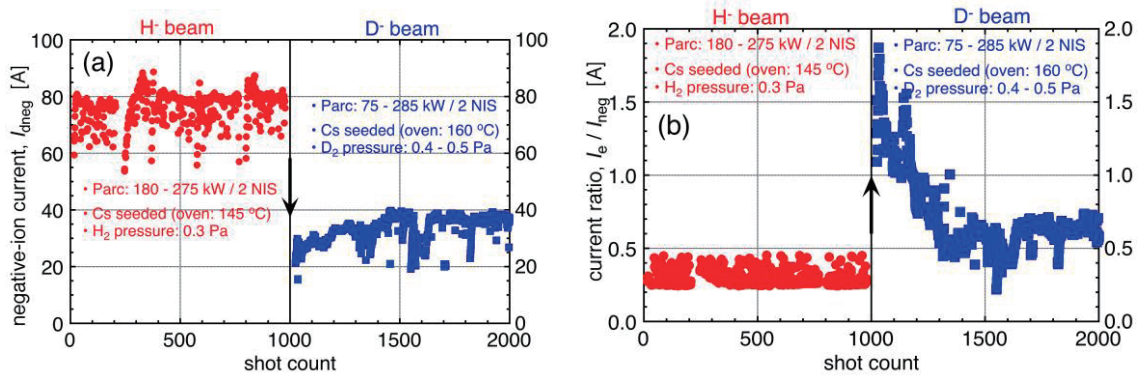
Fig. 1(a) Changes of negative ion current, I_{neg}, at the replacement of H₋ and D₋ beam operations, and (b) changes of the current ratio of co-extracted electrons to negative ions, I_e/ I_{neg}, at the replacement of H⁻ and D₋ beam operations.

The data were obtained for one week in both of H₋ and D₋ beam operation.   As indicated in Fig. 1(a), the current of H₋ ions reaches more than 80 A and decreases abruptly down to 25 A just after switching from H₋ to D₋ beams.   Notice that the beam condition is the same in both H₋ and D₋ beam, initially.   The decrease of the negative ion current was larger than what we expected; the expected ratio of D₋ to H₋ beam current was ~70 %.   That is because the degradation of the negative ion current and increase of the ratio of co-extracted electron current to D₋ current, which is shown in Fig. 1(b).   The current ratio increased form ~35 % to 180 % just after switching the beam species from H₋ to D₋ ions.   The ratio decreased

exponentially by being adjusted the ion-source parameters, such as D_2 gas pressure fed to the ion source and Cs seeded rate as well as the bias voltage, which is available to control the electron current.   The bias voltage needed to increase from 3 to 7 V and it is considered that the plasma potential of D_2 plasma goes up to ~7 V.

Another difference between H₋ and D₋ operations was consumption of seeded Cs.   To maintain the sufficient D₋ current, it was necessary to introduce more Cs in the D₋ operation.   This is considered correlative to the observation of twice higher intensity of the optical emission from Cs atoms (Cs I) at D₋ operation; i.e. Cs condensed on the inner walls of ion-source plasma chamber evaporates more in the D_2 discharge [23].

Although cause of the difference of H₋ and D₋ accelerations is not clear, it could be assumed following three mechanism taking place in the D_2 discharge;

The magnetic field is not optimized and is week to D_2 discharge and higher flux of plasma particles hit on the plasma grid, which is the convertor surface of negative ion production.

Survival probability, which is a ratio that negative ion can escaped from the convertor surface without back-tunneling of electron in the affinity level of the ion, becomes lower at D₋ formation because of the slower velocity of D₋ ions normal to the surface.   Where the survival is represented with Eq. (1) below [24];

$$P_s(t) = 1 - \exp(-4\pi\Delta_0\, e^{-\gamma v t}/h\gamma v) \tag{1}$$

where, Δ_0 is the broaden width of the electronic state induced by the interaction between the metal and affinity level of the D₋ ion, v is escaping velocity and γ is a constant.

Since the energy transfer from deuterium positive ions and/or atoms is higher than those particles in hydrogen plasma, evaporation rate of Cs atom on the plasma grid is higher at D_2 discharge [25].

More or less, it is obvious that so-called Cs effect, which enhances negative ion density and reduces the electron density inside plasma chamber of the ion source, decreased in the D₋ operation.   Further investigation is necessary to extract the dominant mechanism to cause the difference of H₋ and D₋ accelerations.

3. BEAMLET DIAGNOSTICS

As is described elsewhere, we have investigated the plasma characteristics in the beam extraction region of negative ion source by applying an integrated system with several diagnostic modules such as Langmuir probe, cavity ringdown measurement, photodetachment directional Langmuir probe [26-31]. Although this diagnostic system is possible to provide the data about the difference of H₋ and D₋ formations and flows at the beam extraction region, most effective method is to compare the meniscus formation and of flows of negative ions and electrons through the meniscus.   It is, however, very difficult and dangerous to install the diagnostics near the boundary of the source plasma and high voltage beam region.   We have, therefore, started to measure the beamlet characteristic, which could give the information of the meniscus formation.

Beam extracted from NBI ion source is formed with several hundred of beamlet accelerated through

each apertures of accelerator grids.   The most effective method to investigate the beam characteristics is to understand the individual beamlet trajectories and beamlet distributions in both of real and velocity spaces. For these purposes, three new diagnostic modules have been installed.

The first module is a beamlet monitoring module made of CFC (Carbone Fiber Composite) tile, whose fiber is set in the parallel direction of beam axis.   The tile is installed in a vacuum at beam drift tube and the multi beamlets are exposed perpendicular to the beam axis.   The diffused thermal image of the beamlets are observed on the opposite side of the CFC tile as an Infra-red (IR) images.   The heat carried with individual beamlets transfer in the pallarel direction of CFC fiber is 10 times higher than in the perpendicular direction and IR beamlet images can be separately obtained on the opposite side of the beam exposed tile surface.   The error due to the perpendicular thermal diffusion is possible to be corrected with numerical calculation.   A schematic view of the beam let monitor is shown in Fig. 2 and the IR image is observed through a IR window in the Figure.   A typical beamlet IR images observed with this beamlet monitor is shown in Fig. 3.   By fitting 2D-Gaussian function to the pixel map of the IR images, beamlet widths in the real space and beamlet shifts are accurately obtained within the sub-millimeter order.
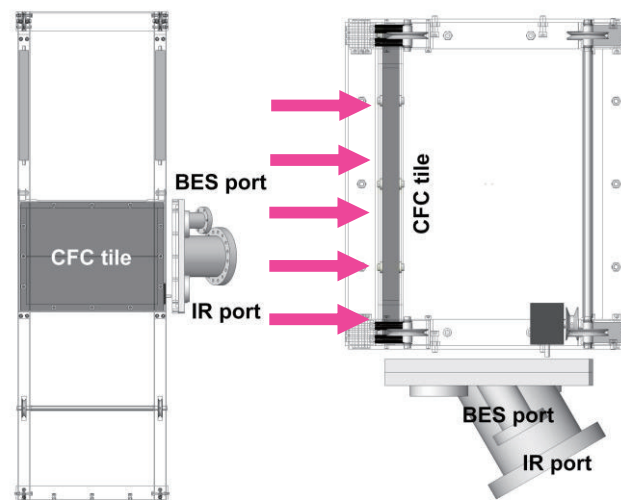
Fig. 2 Schematic views of the NIFS beamlet monitor.   View from the upstream of the beamlets (left) and top view of the monitor (right figure).   Magenta arrows indicate the direction of H- beamlets.

The second is Beam Emission Spectroscopy (BES) module, whose window is set just above the tile of beamlet monitor (see Fig. 2).   The BES measures the Doppler shift of the beamlets and is available to observe the beamlet divergence and beamlet deflection in the velocity space.   In addition, the module is possible to measure the beam components stripped at extraction and acceleration gaps.   As described in the previous section, the filling gas pressure might be increased at D- acceleration and it is expected the stripped beam components becomes larger in that case.   This measurement is useful to evaluate what percentages of the beam is lost at the accelerator.   Typical BES spectra is indicated in Fig. 4(a).   The sharp peak on the right-hand side indicate the Balmer α emission from beam plasma generated with the

collision between the beam particle and residual gas in the drift tube.   A peak on the left-hand side shows the beam composition and the shift from the static composition corresponds to the beam velocity.   By changing the vertical position, different BES spectra is obtained as shown in Fig. 4(b).   At this position, the beam compositions of two vertical beamlet rows mixes and the deflections from the two beamlet rows shown as a superposition of the two Doppler peaks.   in this experiment, the intensity of stripped beam spectra were very low intensities, because the pressure of the residual H_2 gas was too low.

The last module is an emmitance meter applied a pepper pod installed at 10 mm downstream of the beamlet monitor.   The pepper pod equips a multi pinholes with each diameter of 1 mm and 3 mm intervals between nearest neighbor pinholes in the horizontal and vertical directions.   The beamlet component through each pinhole is exposed on the Kapton foil set at the distance of 100 mm from the multi-pinhole plate and recorded as a photo image.   By analyzing the widths of the exposed images and the positions, beamlet characteristics in the velocity space is obtained as well as the BES.

Although those three diagnostic modules have been installed in 2017, it was possible to obtain successful experimental data.   The data are considered useful for the understanding the mechanisms of meniscus formation and of extraction of negative-ion beam.   Beamlet diagnostics in D- beam acceleration is impossible at NIFS-NBI test stand due to the limitation of neutron generation outside the LHD experimental room.   Nevertheless, the analyses of the diagnostics of H- acceleration are expected to be useful for the LHD NBI improvement.
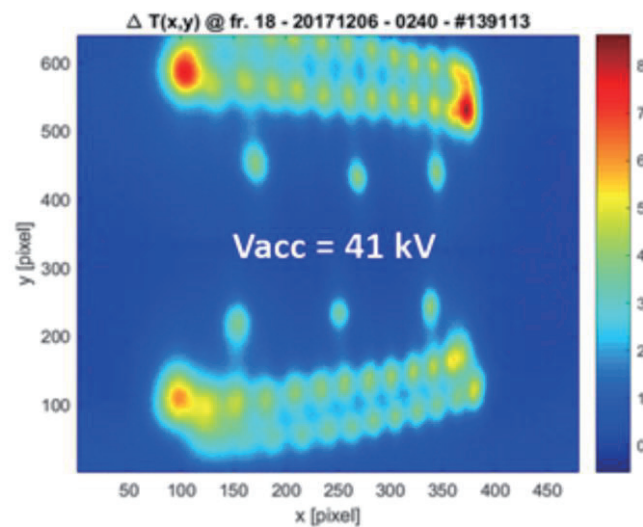
Fig. 3 IR image of multi-beamlets with pseudocolour.   Region of the beamlet apertures are masked at plasma grid.
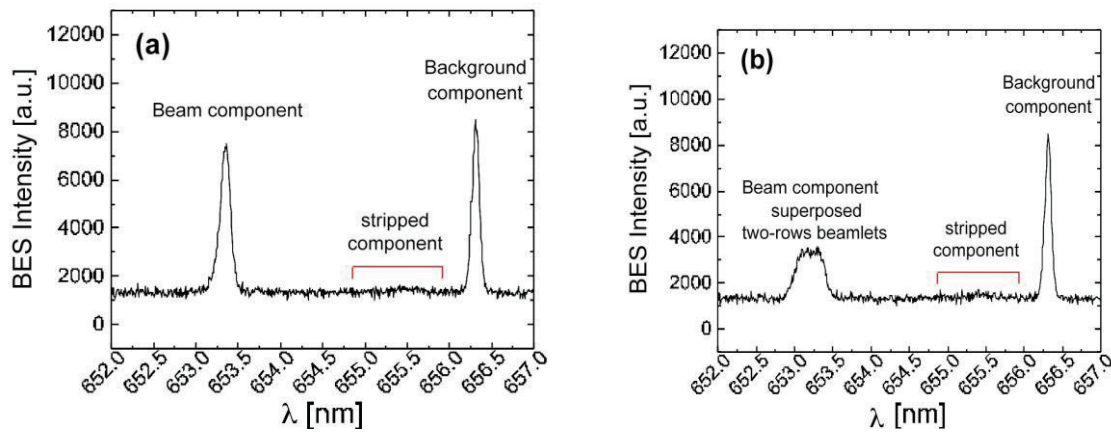
Fig. 4 (a) Beam emission spectra observed at a single beamlet row.   Two clear peaks on the right- and left- hand sides correspond to "background" and "beam" Balmer a emissions, respectively.   Between those peaks "stripped beam" component appears.   (b) The spectra observed at the intermediate position of two beamlet rows.

4. Conclusion

In the LHD deuterium experiment started from 2017, deuterium beam has been injected using three negative-ion based NBI beamlines.   Comparing to the H₋ beam acceleration, D₋ ions current decreased about 1/3 and co-extracted electron current increased.   The consumption of Cs was higher and more Cs vapor was necessary to seed in the negative ion sources for LHD NBI.   Those phonological results is possible to be interpreted as a degradation of Cs effect and it is considered that the Cs atoms on the inner walls of the ion source chamber at the D_2 discharge evaporates more than the case of H_2 discharge.

For the purpose to investigations the difference between H₋ and D₋ accelerations, three beamlet diagnostic modules, beamlet monitor with CFC tile, beam emission spectroscopy and emittance meter have been installed at NIFS-NBI test stand.   Despite of the starting phase of the experiments, successful data were obtained using those modules.   The analyzed results will be useful to understand the mechanism causing the differences in H₋ and D₋ accelerations and to optimize the negative-NBI for D₋ acceleration.

References

[1] M. Bessenrodt-Weberpals et al., Nucl. Fusion **33** (1993) 1205

[2] J. Roth and C. Garcia-Rosales, Nucl. Fusion **36** (1997) 897.

[3] J.G. Cordey et al., Nucl. Fusion **39** (1999) 301.

[4] G. Saibene et al., Nucl. Fusion **39** (1999) 1133.

[5] H. Urano et al., Nucl. Fusion **52** (2012) 114021.

[6] R.E. Chrien et al., Nucl. Fusion **23** (1983) 1399.

[7] O. N. Jarvis et al., Fusion Eng. Design **34-35** (1997) 59.

[8] M.-L. Mayoral et al., Phys. Plasmas. **11** (2004) 2607.

[9] Fan C. Sze et al., J. Nucl. Mat. **266-269** (1999) 1212.

[10]Y. Oya et al., J. Nucl. Mat. **313-316** (2003) 209.

[11]C. Hopf and W. Jacob, J. Nucl. Mat. **342** (2005) 141.

[12]P. Franzen et al., Nucl. Fusion **37** (1997) 1375

[13]H.Bergsåker et al., J. Nucl. Mat. **145-147** (1987) 727.

[14]Y. Takeiri et al., Nucl. Fusion **57** (2017) 102023

[15]T. Inoue et al., Rev. Sci. Instrum. **61** (1990) 496.

[16]M. Kuriyama et al., Rev. Sci. Instrum. **71** (2000) 751.

[17]M. Kuriyama et al., Fusion Sci. and Technol. **42** (2002) 410.

[18]S. Mori and O. Fukumasa Rev. Sci. Instrum. **79** (2008) 02A507.

[19]U. Fantz et al., Nucl. Fusion **46** (2006) S297.

[20]P. Franzen et al., Nucl. Fusion **55** (2015) 053005.

[21]U. Fantz et al., Rev. Sci. Instrum. 8**7** (2016) 02B307.

[22]C. WImmer et al., J. Appl. Phys. **120** (2016) 073301.

[23]K. Ikeda et al., Rev. Sci. Instrum. (to be published).

[24]J. K. Nerskov and B. I. Lundqvist Phys. Rev. **B19** (1979) 5661.

[25]M. Wada Rev. Sci. Instrum. (to be published).

[26]K. Tsumori et al., AIP conference proceedings **1515** (2013) 149.

[27]K. Ikeda et al., New J. Phys. **15** (2013) 103026.

[28]H. Nakano et al., AIP conference proceedings **1515** (2013) 237.

[29]S. Geng et al., Rev. Sci. Instrum. **87** (2016) 02B103.

[30]K. Tsumori et al., AIP Conference Proceedings **1869** (2017) 030001.

[31]K. Tsumori and M. Wada New J. Phys. **19** (2017) 045002.

Effect of LHCD on plasma current profile in EAST

B J Ding for LHCD group, EAST team and collaborators

Institute of Plasma Physics, Chinese Academy of Sciences, Hefei 230031, China

Abstract

Lower hybrid current drive (LHCD) is an important heating system for long pulse plasma with high performance in EAST. The effect of LHCD on current profile was summarized, including edge parameters, LH frequency, LH spectrum and plasma density. The role of parasitic effects of edge plasma on LHCD is studied and it can be mitigated by increasing source frequency or lowering recycling. Lower recycling and higher LH frequency are preferred for LHCD at higher density. Effect of LH spectrum and plasma density on LHCD suggests that the optimization is possible methods to control current profile. Results are encouraging that LHCD is essential for current profile control in reactor grade plasmas.

1. Introduction

Lower hybrid current drive (LHCD) has the attractive property of high off-axis (r/a ≈ 0.7) [1] current drive efficiency making this a useful technique for broadening the current density profile in order to create non-monotonic (shear reversed) profiles of the safety factor – q(r) with $q_{min} > 2$ and large shear reversal radius (r/a ≈ 0.7). The resulting profiles of safety factor allow access to improved energy confinement regimes with high fractions of the non-inductive bootstrap current (≈ 60-70%) [2], thus enabling achievement of the steady state Scenario-4 in the ITER device [3]. However, how to improve LHCD capability and control current profile at high density is an important issue to be solved before this application, which is mainly affected by collisional damping (CA) losses [4], parametric instability (PI) [5,6], scattering by density fluctuations (SDF) [7,8], and LH wave accessibility. In this paper, Effect of LHCD on plasma current profile in EAST will be summarized.

2. Parasitic Effect in edge region on LHCD

2.1 Effect of edge parameters (2.45GHz) [9]

In order to explore the experimental condition for high CD efficiency at high density in EAST, experiments with 2.45GHz LHW were studied [9] with different wall conditions, i.e., poor and strong lithiumization. The effect of driven current is estimated by the count of hard X-ray rate (60keV~200keV) normalized by the injected LHW power, which is proportional to current driven efficiency. Results shown in Fig. 1 (a) suggest that the strong wall lithiumization promotes the occurrence of the LHCD effect at high density. The frequency spectrum collected by a RF probe located outside the machine consists a broadening at around the LH wave operating frequency, and a sideband shifted of an amount in the range of the ion-cyclotron frequency (IC-sideband). The observed trend of increase the IC sideband level with density (see Fig. 1(b)) is consistent with the sharp decay of HXR, supporting that the PI plays a key role in

affecting LHCD. Lower electron density in the edge region in the case of strong lithiation (see Fig. 2) reduce PI [6] as well CA [4], thus providing condition favorable for the occurrence of the LHCD effect into the plasma core.
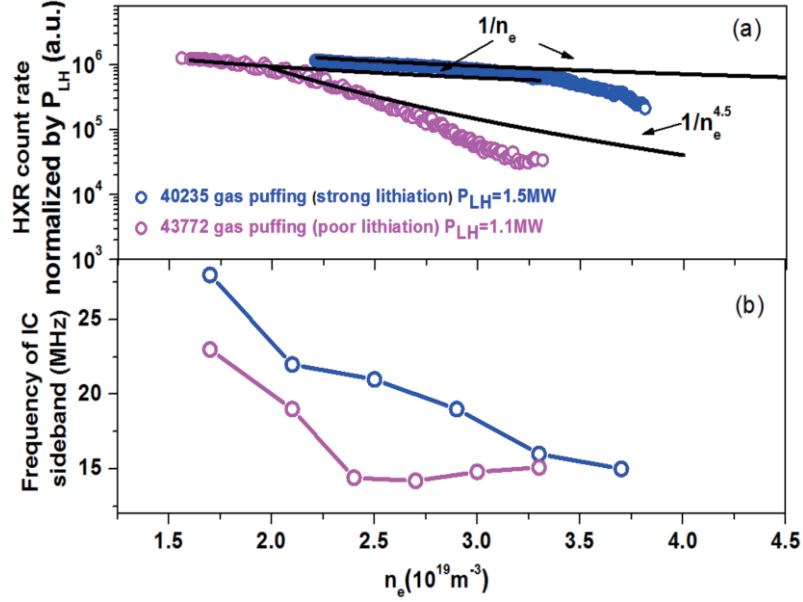
Fig. 1 (a) Relationship between HXR counts and density (b) Frequency of IC sidebands
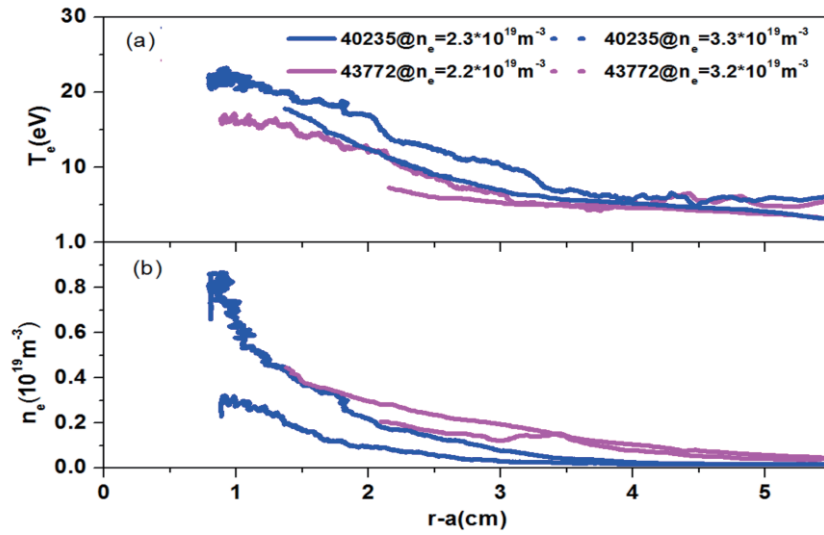
Fig. 2 Edge temperature (a) and (b) density profile measured by Langmuir probe

2.2 Effect of LH frequency (4.6GHz *vs* 2.45GHz) [10]

In order to study the effect of frequency on LHCD characteristics, two different frequency waves (2.45GHz and 4.6GHz) with the same power (P_{LH} = 1.05MW) were injected successively in one discharge with almost constant density (n_e = 2.0 × 10^{19}m^{-3}) and the typical waveform are shown in Fig.3. It is seen that the residual voltages (V_{loop}) are 0.27V and 0.18V respectively for current drive with 2.45GHz and 4.6GHz, indicating better CD efficiency for 4.6GHz waves. Also, the internal inductance is higher with the 4.6GHz LH wave injection, indicating the difference in the current profile. Though power spectrum is an important parameter affecting wave propagation and power deposition, simulations suggest that the discrepancy in the initial spectrum could not dominate the difference in current drive. A comparison of frequency spectra between two waves is illustrated in Fig. 4, from which it is seen that larger spectral broadening occurs for 2.45GHz case, indicating stronger PI behaviour. This result would explain the better CD effect with 4.6GHz LH wave in terms of reduced parasitic PI effect, as previously reported [6,11].

The related results indicate that the 4.6 GHz frequency is more useful for producing stronger LHCD on EAST, and that the 2.45 GHz operation would require an optimization in terms of PI effect mitigation, hence, optimizing current profile.
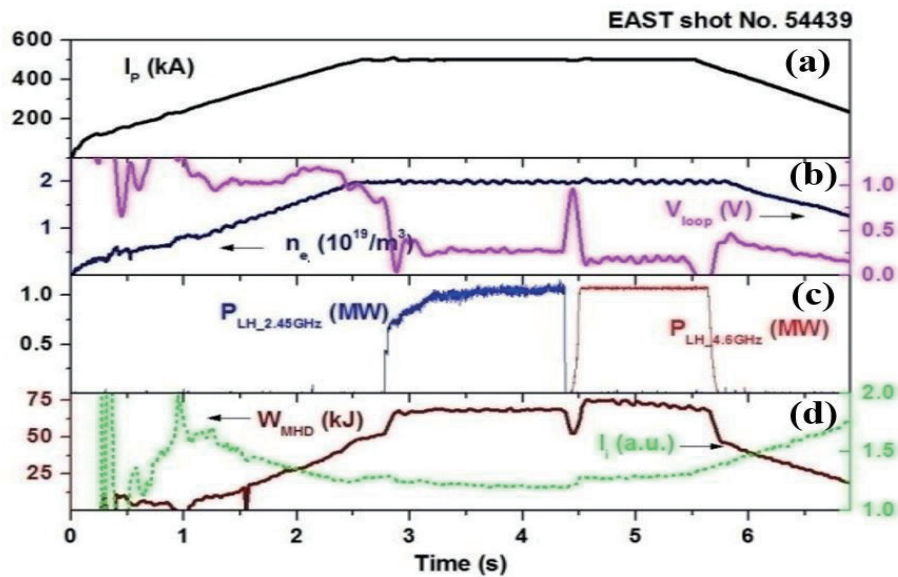
Fig. 3 Effect of LH frequency on LHCD
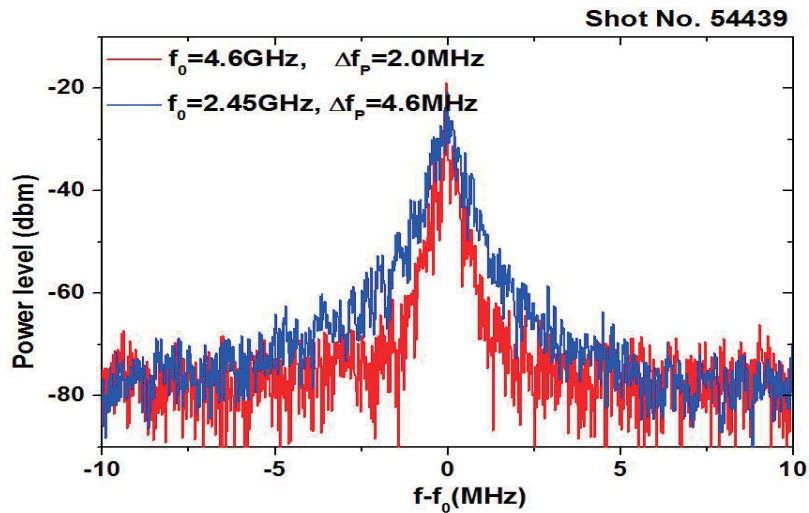
Fig. 4 Frequency Spectrum by a RF

3. Effect of LH spectrum on LHCD (4.6GHz and 2.45GHz) [12]

To explore long pulse and high performance with LHCD, the effect of LH spectrum with 4.6GHz system on LHCD characteristics was investigated [12] in EAST. The experiments were carried out with different toroidal phase differences ($\Delta\varphi=0^\circ$, 90°, 180°, -90°) between the main waveguides. Experimental results are shown in Fig.5. It is seen that the smallest consumptions of magnetic flux in Fig. 5(d) occurs with $\Delta\varphi=900$, suggesting the highest CD efficiency. The internal inductance (l_i), shown in Fig. 5 (e), is the largest with $\Delta\varphi=90^\circ$, whereas it is the lowest with $\Delta\varphi=-90^\circ$, implying the most peaked current density profile with $\Delta\varphi=90^\circ$. Possible reason for the discrepancy in the CD characteristic between the four cases could be that the spectrum in the main lobe with $\Delta\varphi=90^\circ$ has a single main peak, whereas the others are compound, especially in the case of $\Delta\varphi=-90^\circ$. Such preliminary results indicate the possibility of profile control by changing the wave spectrum.
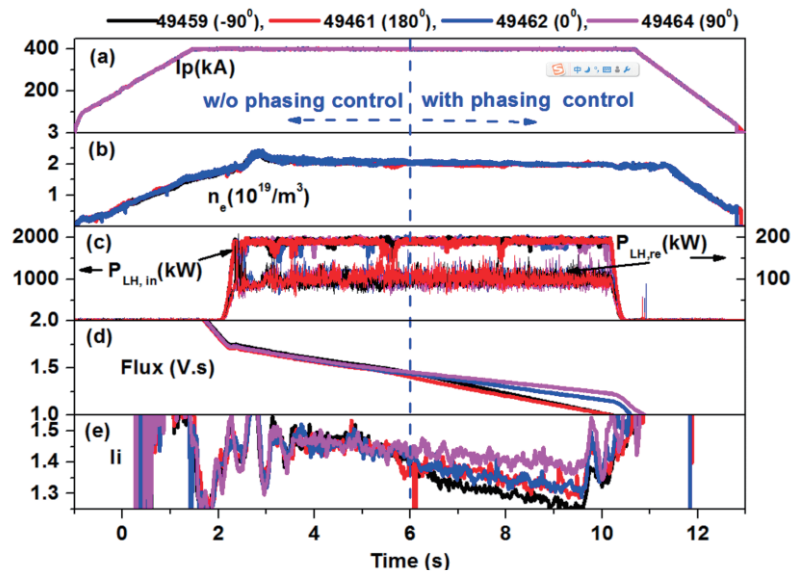
Fig. 5 Effect of spectrum on CD efficiency and current profile

4. Effect of density on LHCD (4.6GHz) [13]

On EAST, effect of density on current profile was investigated. The electron density was systematically varied in order to modify the deposition profile of the external LHCD, while keeping the plasma in fully-noninductive conditions to avoid Ohmic current that would tend to peak the current profile. The LHCD profile is expected to become more off-axis with higher density and the total current profile should become broader at higher density. The EAST experiments achieved a series of L-mode edge, noninductive discharges with I_p = 400 kA and line averaged density in the range 1.8–3×10^{19} m^{-3}. As expected, the current profile broadened with increasing density, as shown in figure 6 by the lower value of the internal inductance, l_i. Results of the reconstructions are shown in figure 7, confirming that broader current profiles are obtained at higher density.
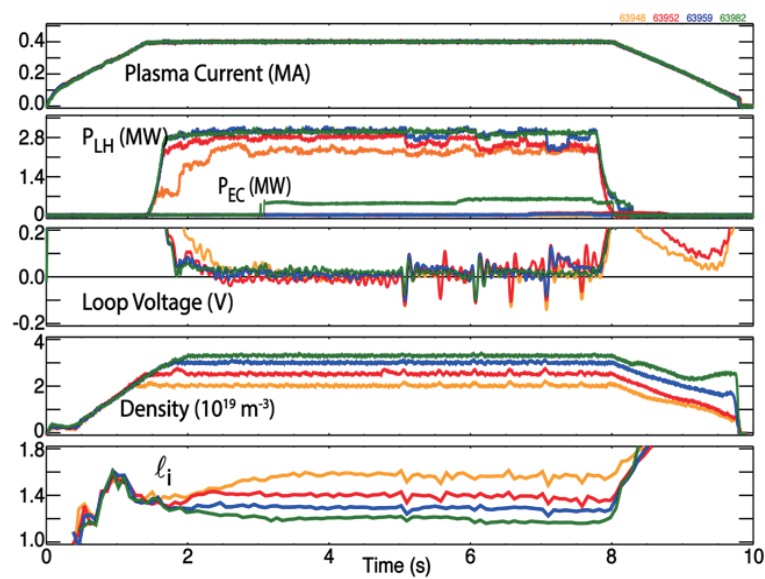
Fig. 6 Effect of density on LHCD
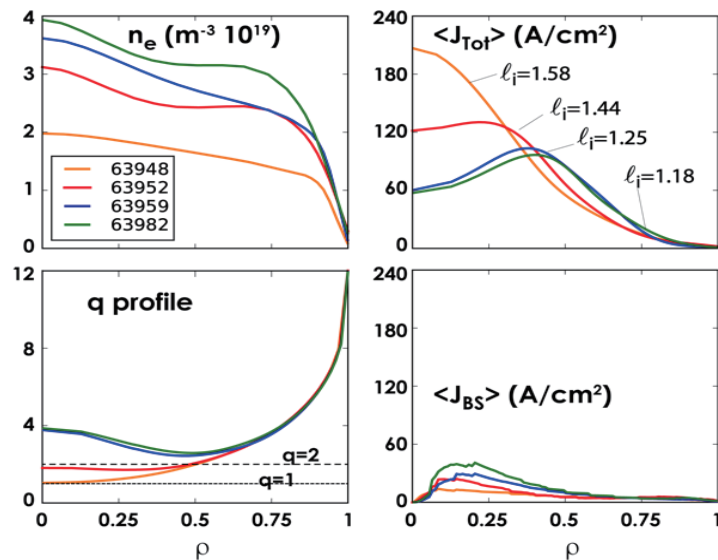
Fig. 7 Radial profiles for 4 didischarges

5. Conclusion

The effect of LHCD on current profile was summarized, including edge parameters, LH frequency, LH spectrum and plasma density. The role of parasitic effects of edge plasma on LHCD is studied and it can be mitigated by increasing source frequency or lowering recycling. Lower recycling and higher LH frequency are preferred for LHCD at higher density. Effect of LH spectrum and plasma density on LHCD suggests that the optimization is possible methods to control current profile.

References:

[1]   J. Decker *et al*, *Nucl. Fusion* **51** (2013) 073025.

[2]   C. Gormezano *et al*, *Nucl. Fusion* **47** (2007) S285.

[3]   X. Litaudon *et al*, *Plasma Phys. Contr. Fusion* **44** (2002) 1057.

[4]   P. T. Bonoli and R. C. Englade *Phys. Fluids* **29** (1986) 2937.

[5]   C. S. Liu and V. K. Tripathi *Phys. Rep.* **130** (1986) 143.

[6]   R. Cesario *et al Phys. Rev. Lett.* **92** (2004) 175002.

[7]   Y. Peysson *et al Plasma Phys. Control. Fusion* **53** (2011) 124028

[8]   P. T. Bonoli and E. Ott *Phys. Fluids* **25** (1982) 359

[9]   B. J. Ding et al., *Nucl. Fusion* **55** (2013) 113027.

[10] M H. Li *et al.*, *Phys. Plasmas* **23** (2016) 102512.

[11] G. M. Wallace *et al Phys. Plasmas* **17** (2010) 082508.

[12] F. K. Liu *et al.*, *Nucl. Fusion* **55** (2015) 123022.

[13] A. M. Garafalo *et al.*, Nucl. Fusion **57** (2017) 076037.

Recent Progress of long pulse H-mode operation on EAST

J. P. Qian[1], X. Z. Gong[1], B. N. Wan[1], J. G. Li[1] E. Li[1], F. K. Liu[1], Y. P. Zhao[1], M. Wang[1], H. D. Xu[1], A. Garofalo[2], A. Ekedah[3], S. Y. Ding[1], H. Juan[1], L. Zhang[1], Q. Zang[1], H. Q. Liu[1], L. Zeng[1], S. Y. Lin[1], B. Shen[1], B. Zhang[1], L. M. Shao[1], B. J. Xiao[1], J. S. Hu[1], C. D. Hu[1], L. Q. Hu[1], L. Wang[1], Y. W. Sun[1], G. S. Xu[1], Y. F. Liang[1], N. Xiang[1] and the EAST team

[1]Institute of Plasma Physics, Chinese Academy of Sciences, Hefei 230031, China

[2]General Atomics, San Diego, California, 92186-5608, USA

[3]CEA, IRFM, F-13108 Saint Paul-lez-Durance, France

Abstract

Recent progress of long pulse H-mode operation on EAST is reported. A steady state long pulse H-mode discharge duration over 100s with ITER like tungsten divertor has been obtained using only RF heating and current drive. 0D modeling suggests high power injection and high confinement quality are prerequisites for the next goal of high bootstrap current ($f_{bs} \sim 50\%$). Techniques of broadening current density profile for improving confinement is demonstrated.

1. Introduction

Long-pulse steady-state operation is one of the most challenges to a fusion reactor, which requires the resolution of several issues, such as external non-inductive current drive (CD) and self-generated bootstrap current, robust plasma heat flux and particle exhaust control and so on. High β_P scenario is attractive since it stays away from current limit to maximize self-driven bootstrap current towards the high pressure for high performance with smaller requirement of external CD.

Experimental Advanced Superconducting Tokamak (EAST), as a first fully superconducting tokamak, aims to develop steady state long pulse scenario and relevant physics research in support to steady state of ITER and CFETR [1]. In order to investigate long-pulse steady-state tokamak physics, EAST has also equipped with capabilities of dominant electron heating, low input torque and ITER-like tungsten divertor.

2. Progress of long pulse H-mode operation on EAST

EAST (major radius R=1.8 m, minor radius a=0.45 m, plasma current $I_P < 1.0$ MA toroidal field $B_T < 3.5$T) has a flexible Poloidal Field (PF) control system with a set of 12 independently power supplies and a pair of internal water-cooled coils, accommodating both single null and double null divertor configurations. EAST is equipped with an actively water-cooled ITER-like tungsten divertor with power handling capability of ~ 10 MW/m^2, upper and lower divertor cryo-pumps for particle exhaust, and high power continuous wave (CW) injection for plasma current drive and heating by Lower Hybrid Current Drive (LHCD), Electron Cyclotron Heating (ECH) and Ion Cyclotron Resonant Frequency (ICRF).

On EAST, the fully non-inductive high β_P scenario has been developed towards more ITER-relevant conditions. Building on the previous long pulse H-mode experiments, a recent discharge of duration over

100 seconds [2-3] has been obtained through the multi-RF power combination, shown in Fig.1. The plasma configuration is the upper single null. Loop voltage was well controlled to be zero which indicates fully non-inductive current drive condition. Small ELMs were obtained in this long pulse H-mode discharge, which facilitate the RF power coupling in the H-mode phase. A confinement enhancement factor relative to standard H-mode, H_{98y2} of 1.1-1.2 was achieved and maintained constant during the discharge. The electron temperature profile and transport analysis suggest that eITB exists inside the rho<0.4 regime. A good impurity and particle fluxes control was achieved by applying on-axis ECRH, possibly due to the control of core density and temperature profiles. The total radiation power was kept almost constant in the whole discharge.
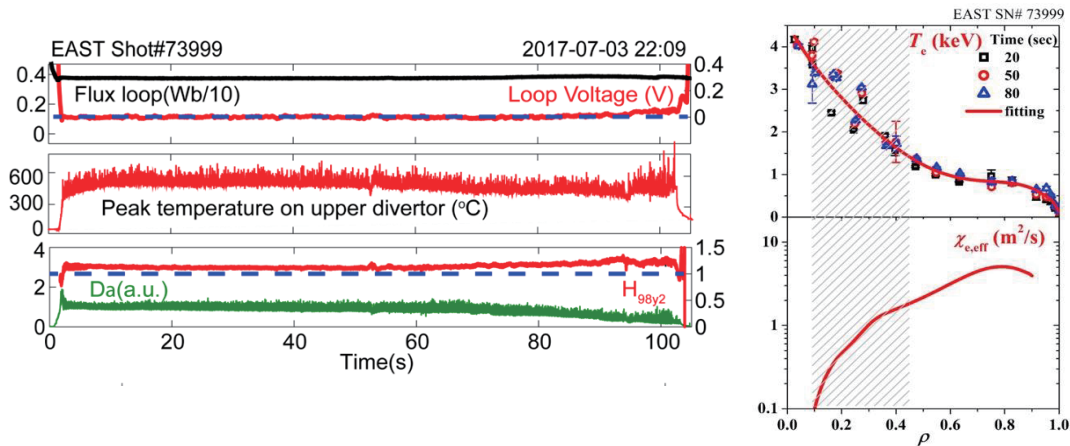
Fig.1 On the left are time histories of flux loop, loop voltage, peaked temperature on the upper divertor, confinement enhancement factor H_{98y2}, and the D_α. On the right is measurements of the radial profile of the electron temperature at several times and experimental thermal diffusivity of electron.

More high β_P experimental results on EAST were performed and are summarized in figure 2, where the grey boundary shows the operational space. It shows that the regime of nearly zero loop voltage is typically obtained at the moderate density, ($<n_e> \sim 2.5 \sim 3.5 \times 10^{19}$ m^{-3}), while relatively high β_P are accessed with the combined heating of NBI and RF. On EAST, increasing $<ne>$ will require more external CD power or more self-driven bootstrap current to compensate the reduced LHCD efficiency. In addition, the confinement versus β_P shows that the confinement increases with the increase of β_P, which suggest that higher β_P allows higher confinement. This result is consistent with the high β_P joint experiment on DIII-D, where Shafranov shift was believed as the dominant stabilizing effect for the suppression of the turbulence at low toroidal rotation [4].

As one of the key elements for long pulse operation, the efficiency of LHCD was systematically investigated and compared between two LHW systems, i.e., 2.45GHz and 4.6GHz [5]. In the experiments, we found that 4.6GHz has the higher current drive efficiency and better confinement than 2.45GHz because of weaker non-linear effect. And also, strong lithium coating which changes edge parameters, like reducing edge recycling and increasing electron temperature, suppresses non-linear effect, enabling a higher LHCD

efficiency. For long pulse operations, the off-axis LHCD, one side, was used to save flux consumption, the other side was to optimize the current density profile to avoid MHD activities like sawtooth.
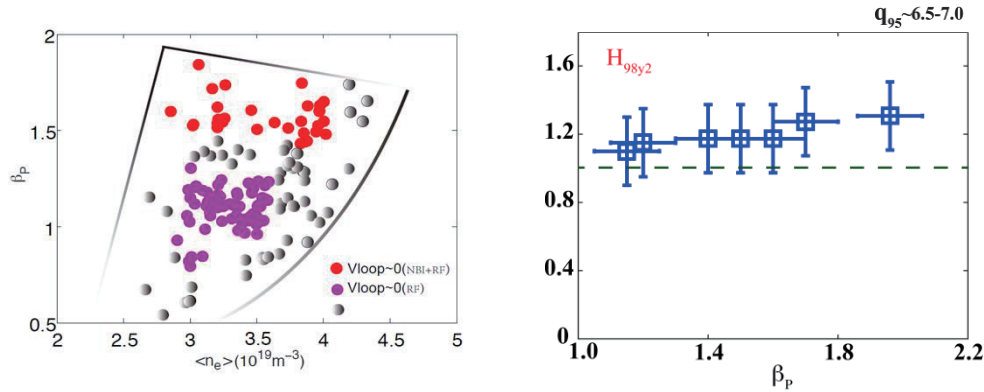
Fig.2 On the left is the EAST high β_P operational space; the right is confinement versus the value of β_P

3. Future plan for developing high β_P, high bootstrap current fraction scenario

To meet the next goal of EAST long pulse operation (50% f_{bs}), a 0D model has been used to calculate steady state solutions at I_P= 450 kA with varying levels of total injected power (shown in figure 3). The calculation suggests that steady-state at high performance requires not only increased injected power, but also significantly improved energy confinement quality. The calculations show that at present level of confinement (H_{98y2}=1.1), quadrupling (from ~4 MW to ~16 MW) the injected power can only barely double the β_P (from ~0.9 to 1.8). If higher confinement can be accessed, steady-state high performance with $\beta_P \geq 2.5$ is possible to obtain 50% bootstrap current fraction.

Current density profile control or optimization, as a key issue for improving the confinement quality, was performed on EAST. A promising technique of using a large fraction of LHCD to replace the Ohmic current was demonstrated when plasma reaches the flat top (see in figure 4). In a set of recent EAST experiments, the line averaged electron density was systematically varied in order to modify the deposition profile of the external LHCD, while keeping the plasma in fully non-inductive conditions to avoid Ohmic current penetration. The LHCD profile is expected to become more off-axis with higher density, because radial penetration of the wave is reduced at higher density. More detail can be found in Ref. [6]

Simultaneous magnetic and kinetic plasma control based on extremely simple data-driven models and a two-time-scale approximation has been developed [7] and will be used to active control the current density profile in EAST through the collaboration with CEA, which will further contribute to the high bootstrap current, high β_P scenario development.
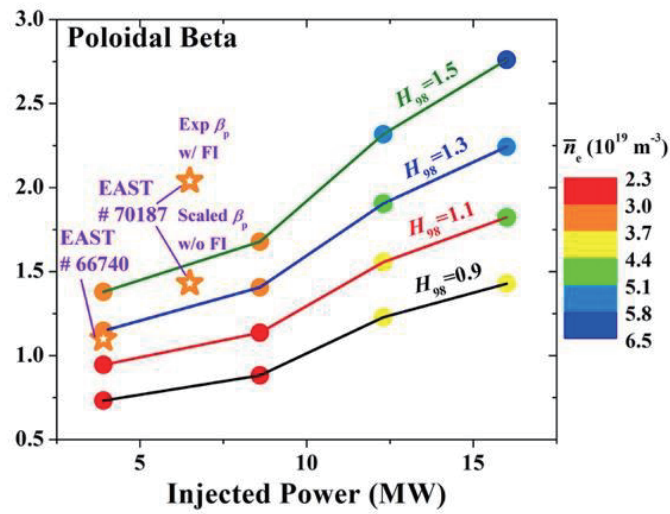
Fig.3 0D modeling predictions of poloidal beta versus injected power assuming plasma current I_P=450 kA and different levels of energy confinement quality.
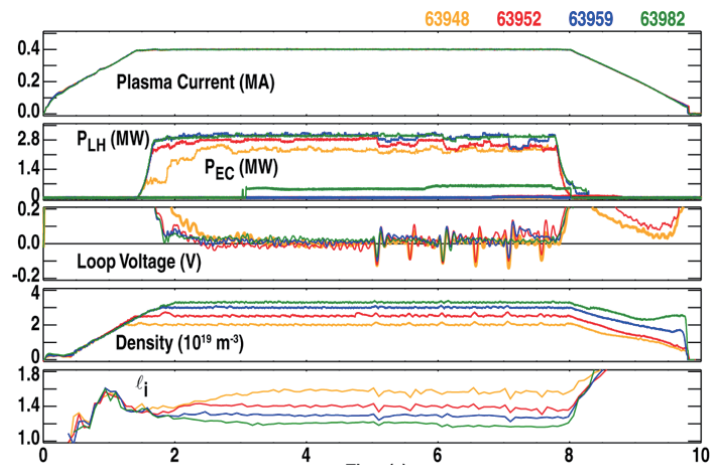
Fig.4 Density scan in fully non-inductive discharges operating on tungsten divertor shows broader current profiles with higher density.

4. Summary

In all, 100s long-pulse fully non-inductive steady-state scenario with a good plasma performance ($H_{98y2}\sim 1.1$) and a good control of impurity and heat exhaust with the tungsten divertor has been demonstrated on EAST. The broader current profile control by varying the deposition profile of the external LHCD, which will further strengthen the high β_P scenario development for achieving high-performance, steady-state on EAST in the near future. Next, EAST will aim to provide a suitable platform to address physics and technology issues relevant for steady-state advanced high-performance H-mode plasmas with high power injection. For this goal, a new lower divertor suitable for water-cooled tungsten PFCs will be installed in 2019.

Acknowledgements

References

[1] B. Wan et al 2017 *Nucl. Fusion* 57 102019

[2] X. Gong et al., *59th Annual Meeting of the APS Division of Plasma Physics*, October 23–27, 2017, Milwaukee, Wisconsin, USA

[3] Y. Liang et al., *1st Asia-Pacific Conference on Plasma Physics* 2017, Chengdu, China

[4] J. Qian et al 2017 *Nucl. Fusion* 57 056008

[5] A. Ekedahl *1st Asia-Pacific Conference on Plasma Physics* 2017, Chengdu, China

[6] A. M. Garofalo et al 2017 *Nucl. Fusion* 57 076037

[7] D. Moreau et al 2018 submitted IAEA FEC, India

Summary of theory and simulation activities of ASIPP in A3 program

T.Y. Xia[1], N. Xiang[1], Y.J. Hu[1,2], Y.B. Pei[1,3], J. Ma[1] and G.Z. Jia[1]

[1]Institute of Plasma Physics, Chinese Academy of Sciences, Hefei, 230031, Anhui, China
[2]Center for Integrated Plasma Studies, University of Colorado at Boulder, Boulder, Colorado 80309, USA
[3]University of Science and Technology of China, Hefei, 230026, Anhui, China

Abstract

Under the support of A3 project, ASIPP has collaborated with NIFS to import MEGA code to fill in the blank of the energetic particles physics in the simulation platform. The Alfven eigenmodes and the fishbone modes driven by fast ions on EAST are simulated by this code. The physics research on LHW are studied within the support of A3 due to the characteristic LHW heating on EAST. The SOL current driven by LHW has been implemented in the BOUT++ simulations and is found to be able to broaden the SOL width, which makes the simulated scaling closer to the EAST measurements. For the understanding of the two LHWs injections on EAST, the nonlinear process between LHW and tokamak physics are simulated by GeFi. The generations of the high harmonic modes and sidebands through nonlinear mode-mode coupling are found to provide new power channels, and reduce the reflection significantly as the wave amplitude increases. The effects of perturbed orbits on the interactions of electrons with two LHWs resonant with electrons at different phase velocities shows that when the resonances of these two LHWs are overlapped sufficiently, the damping of the off-resonant wave and the oscillatory behavior of the wave amplitude are observed. A Flux Difference Splitting simulation capability for MHD systems based on a finite volume spatial discretization has been developed under A3 project. This code has been used to study the long time nonlinear dynamics of the coalescence instability.

1. Introduction of the simulation progress of A3

Before the A3 project, ASIPP has started to construct the tokamak simulation platform within the plasma codes of series of different physics models. The target of this platform is to build the integratable simulation codes which cover different spatial and temporal scales, from the core to the edge, from the radial frequency to energy confinement time, from low to high collisionality region. Almost all the physics models for plasma physics are included, such as fluid, continuum, gyro-kinetic and hybrid models. This platform can contribute the physics understanding and prediction to the present tokamak experiments, and even be able to design the physics of the future magnetic confinement fusion facilities, especially for CFETR. Therefore, during the implementation phase of the A3 project, the simulations on the edge plasmas, radio frequency waves and MHD code developments get forwards. Especially for the simulations on the energetic particles (EPs), the collaborations between ASIPP and NIFS are built in order to fill in the blank of this platform.

The paper is outlined as follows. The second section is about the progress of the collaboration between

ASIPP and NIFS on the hybrid simulation codes MEGA for the understanding of EP driven modes. Sec. 3 talks about the progress of the edge plasma physics. In Sec. 4, the simulation proceeding on the radio frequency waves are introduced. The developments of the MHD codes within the support of A3 project is shown in Sec. 5. The last section is summary.

2. Progress on the simulations of energetic particles

Kinetic-MHD hybrid simulations using MEGA code [1], which is imported from NIFS, are carried out to investigate fast-ion-driven modes on EAST [2]. Three typical kinds of fast-ion-driven modes, namely, toroidicity-induced Alfven eigenmodes, reversed shear Alfven eigenmodes, and energetic-particle continuum modes, are observed simultaneously in the simulations. The simulation results are compared with the results of an ideal MHD eigenvalue code, which shows agreement with respect to the mode frequency, dominant poloidal mode numbers, and radial location. The modes in the hybrid simulations take a twisted structure on the poloidal plane, which is different from the results of the ideal MHD eigenvalue code. The twist is due to the radial phase variation of the eigenfunction, which is attributed to the non-perturbative kinetic effects of the fast ions. By varying the stored energy of fast ions to change the fast ion drive in the MEGA simulations, it is demonstrated that the twist (i.e., the radial phase variation) is positively correlated with the fast ion drive.
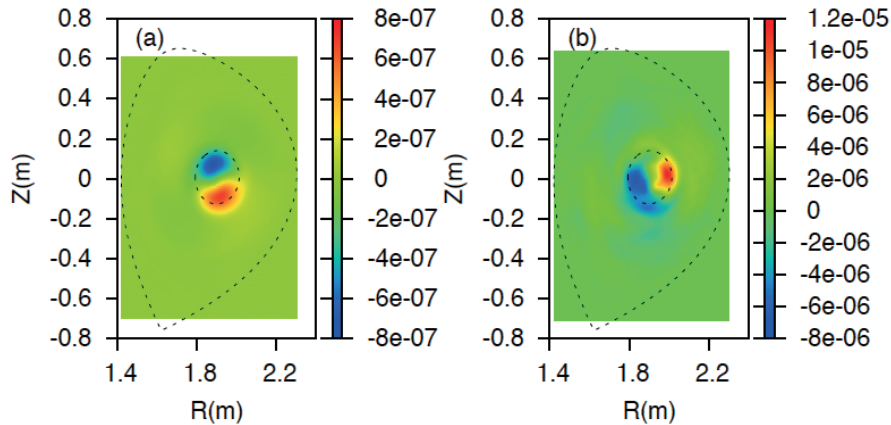
Fig.1 The Spatial profile of the toroidal electric field on a poloidal plane for the linear stage (a) and nonlinear stage (b) of the fishbone modes [3].

The fishbone modes excited by fast ions on EAST are also investigated by MEGA code (see Fig. 1)[3]. The simulations use realistic equilibrium reconstructed from experiment data with the constraint of the q=1 surface location. Anisotropic slowing down distribution is used to model the distributions of the fast ions from neutral beam injection. The resonance condition is used to identify the interaction between the fishbone mode and the fast ions, which shows that the fishbone mode is simultaneously in resonance with the bounce motion of the trapped particles and the transit motion of the passing particles. Both the passing and trapped particles are important in destabilizing the fishbone mode. The simulations show that the mode frequency chirps down as the mode reaches the nonlinear stage, during which there is a substantial

flattening of the perpendicular pressure of fast ions, compared with that of the parallel pressure. For passing particles, the resonance remains within the q=1 surface, while, for trapped particles, the resonant location moves out radially during the nonlinear evolution. In addition, parameter scanning is performed to examine the dependence of the linear frequency and growth rate of fishbones on the pressure and injection velocity of fast ions.

3. Progress on the simulations of edge physics

In order to understand the role of turbulence on the divertor heat flux width and predict the heat flux distributions for the future tokamaks, such as ITER and CFETR, the six-field two-fluid module based on Braginskii equations has been used to simulate the transient heat fluxes distributions of EAST ELMing H-mode [4] and C-Mod EDA H-mode discharges [5]. Based on the simulations, the Eich's scaling from the multi-machine scaling can be reproduced [6], as shown in Fig. 2. The anomalous electron transport in this model is the dominant mechanism to transport the particle and heat from the pedestal region into SOL. The magnetic fluctuations of the mode are smaller than the electric field fluctuations. Statistical analysis of the type of turbulence shows that the turbulence transport type (blobby or turbulent) does not influence the heat flux width scaling. The two-point model differs from the simulation results but the drift-based model shows good agreement with simulations.

However, for the EAST cases, the simulated width is only half of that measured from the EAST divertor probes [7], but agrees well with the international multi-machine scaling law Eich's Scaling. The reason is believed to be caused by the special heating method on EAST: the radio frequency (RF) waves, especially the low hybrid wave (LHW). The LHW can drive the helical filamentary current (HFC) in the SOL region which can changes the boundary topology by the radial magnetic field, and then increase the flux expansion [8]. In order to find the physics mechanism for the LHW effects on heat flux, the six-field two-fluid module is extended to add the HFC in SOL region. The HFC is modeled as the force-free form and with the same amplitude and position as the EAST experiments. The simulations show that, although the radial magnetic field induced by this HFC could be much smaller than the perturbed field, it is still able to force the perturbations with the same toroidal mode number to grow up at the start of the linear phase. This forced mode is effective to compete with the spontaneous fluctuations and change the spectrum of the eigenmodes even in the linear phase. This leads to the obvious suppression of the edge turbulence. The preliminary results shows that the HFC with the toroidal mode number n=5 is able to increase the SOL width by ~25%, and the peak parallel heat flux towards divertor target is decreased by 32%. The broadening of the particle flux by HFC clearly shows the secondary striate filaments on divertor target, which is similar to the splitting of the strike point found by the divertor probes.
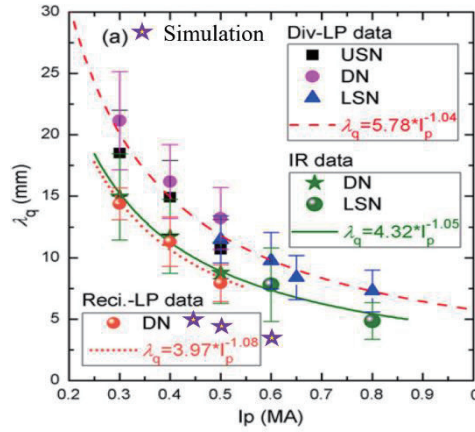
Fig.2 The simulated SOL width [1] reproduces the Eich's Scaling, but is only half of the measurements on EAST [4.7].

4. Progress on the theory and simulations of RF waves on tokamak

Since the RF heating and current driving is the characteristic of EAST long pulse discharges, the physics of the wave-plasma interactions are very important to be studied, especially for the nonlinear effects of coupling and absorption of the waves. The A3 project supports the research of the interactions between RF wave and tokamak plasmas in ASIPP, such LHWs. Steady-state operations of EAST tokamak requires efficient non-inductive plasma current drive. Lower hybrid current drive (LHCD) is currently the most efficient method to drive the plasma current and is able to provide a continuous off-axis toroidal current for plasma control [9].

The propagation and mode conversion of LHWs in an inhomogeneous plasma are investigated [10] by using the nonlinear δf algorithm in a two-dimensional particle-in-cell simulation code based on the gyrokinetic electron and fully kinetic ion (GeFi) scheme [11]. The nonlinear effects are emphasized. The dependences of the reflection coefficient on the scale length of the density variation are compared with the results based on the linear full wave model for cold plasmas [12]. It is indicated that the mode conversion for the waves with a frequency of 2.45GHz ($\omega \sim 3\omega_{LH}$, where ω_{LH} represents the lower hybrid resonance frequency) and within Tokamak relevant amplitudes can be well described in the linear scheme. As the frequency decreases, the modifications due to the nonlinear terms become important. For the low-frequency waves ($\omega \sim 1.3\omega_{LH}$), the PIC simulation is consistent with linear full wave analysis when the wave amplitude is small. As the wave amplitude increases, the generations of the high harmonic modes and sidebands through nonlinear mode-mode coupling provide new power channels, and thus could reduce the reflection significantly.

In present-day LHCD experiments, the input power of the LHW is typically up to a few mega-watts. The nonlinear processes, for example, the spectrum sidebands [13] and broadening [14] due to the parametric instabilities have been observed in LHCD experiments. The motion of a charged particle in the fields of two plane waves can be described by a two-degree-freedom Hamiltonian system. Large scale stochasticity [15, 16], which is large scale chaos actually, emerges when the resonances overlap. This

stochasticity may lead to particle diffusion and heating. Karney [17] studied the stochastic ion heating by a LHW. It was found that, for ions with velocities perpendicular to the background magnetic field in the field of an LHW and a constant background magnetic field, where is the frequency of the wave and is the wave number perpendicular to the background magnetic field, the motion is stochastic when resonances overlap in surface of section plots.
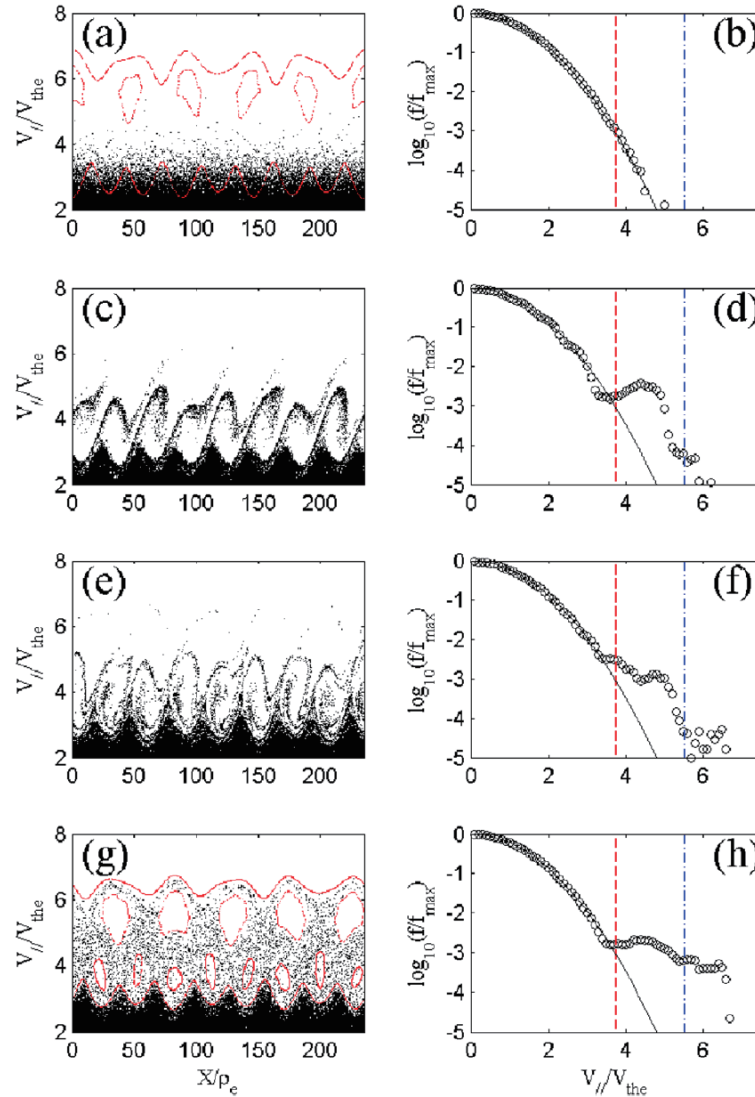
Fig.3 the positions of the electron in the phase space (left column) and the corresponding distribution functions (right column) at different simulation time [18]. These red lines (formed by points) in (a) and (g) are the boundaries of the chaotic sea and the islands in Poincare sections.

However, concerning two longitudinal waves in plasma, most of the published works focused only on the dynamics of the particles. The wave amplitudes were assumed to be unchanged during solving the motion equation. However, due to the energy transfer between the electrons and waves, the wave amplitudes can vary during the interaction. How the energy exchange between waves and plasmas is affected by the electron perturbed orbits is not well understood. To gain insights into this problem, the interaction of electrons with two LHWs is studied via self-consistent simulations.

The effects of perturbed orbits on the interactions of electrons with two LHWs simultaneously, one of which is resonant with electrons at a low phase velocity (v_{p1}=3.8V_{the}, where v_{p1} is the wave phase velocity and Vthe is the electron thermal speed) while the other is off-resonant at a high phase velocity (v_{p2}=5.5V_{the}), have been studied by using the particle simulation code based on the gyro-kinetic electron and fully-kinetic ion (GeFi) model. When the amplitude of the off-resonant wave is sufficiently small so that the resonances of these two waves do not overlap, the variation of the resonant wave amplitude is similar to that predicted by O'Neil theory. With the amplitude increasing, the two resonances overlap and large scale chaos emerges. As a result, the damping of the resonant wave can be enhanced, which is due to that the trapped electron orbits are significantly perturbed by the off-resonant wave. The diffusion process gives rise to the enhanced damping. When the overlap is sufficiently large, the damping of the off-resonant wave and the oscillatory behavior of the wave amplitude are observed, as shown in Fig. 3. In addition, the resonant plateau in the distribution function can be broadened due to the change of the chaotic region boundaries as the electron perturbed orbits are taken into account [18].

(a) t=0.0   (b) t=2.8

(c) t=11.5   (d) t=30.0
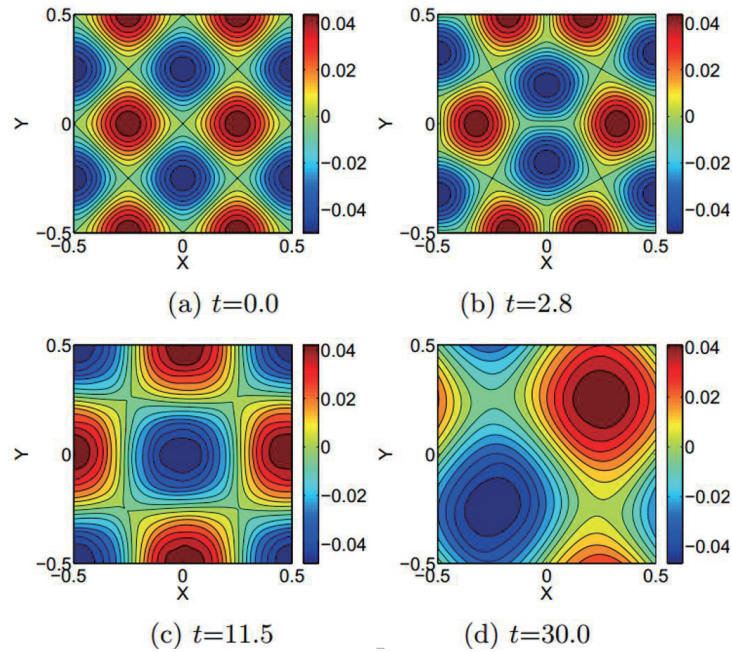
Fig.4 Evolution of magnetic fields of coalescence instability at different time. [19]

5. MHD code development under the support of A3

A Flux Difference Splitting (FDS) simulation capability for MHD systems based on a finite volume spatial discretization has been developed by ASIPP [19]. This numerical approach solves for the weak solution of the integrated form of ideal/resistive MHD equations in the forms of conservation laws for mass, momentum, energy, and magnetic flux. The nonlinear discontinuity-like structures as the current sheet are able to be solved accurately and the physical relevant solutions can be obtained. The numerical code has been applied to study the long time nonlinear dynamics of the coalescence instability in which the

capabilities of maintaining conservation laws, capturing discontinuities are required (see Fig. 4). It is verified that small structures in the instability oscillate with time and then merge into medium structures in a coherent manner. The medium structures then evolve and merge into larger structures, and this trend continues through all scale-lengths. The energy curves simulated show the time evolution of magnetic, kinetic and internal energy while keeping the total energy conservative.

6. Summary

Under the support of A3 project, the collaborations between ASIPP and NIFS are executed to import the kinetic-MHD hybrid code MEGA, which fills in the blank of the energetic particles physics in the simulation platform of ASIPP. The Alfven eigenmodes and the fishbone modes driven by fast ions are simulated by this code. The mode frequency chirps down as the mode reaches the nonlinear stage, while a substantial flattening of the perpendicular pressure of fast ions happens, compared with that of the parallel pressure. The analysis on the mode structures suggests the dependency of the linear frequency and growth rate of fishbones on the pressure and injection velocity of fast ions.

According to the characteristic LHW heating on EAST, the physics research on LHW are studied within the support of A3. The scaling of the H-mode heat flux width on divertor target of EAST are reproduced by BOUT++. The simulations without the LHW effects are consistent with the multi-machine scaling, but the amplitudes are only half of the measurements of EAST. The SOL current driven by LHW has been implemented in the simulations and is found to be able to broaden the SOL width, and decrease the peak amplitude of heat flux.

For the understanding of the two LHWs injections on EAST, the nonlinear process between LHW and tokamak physics are simulated. GeFi code are used to simulate the propagation and mode conversion of LHWs in an inhomogeneous plasma. The generations of the high harmonic modes and sidebands through nonlinear mode-mode coupling are found to provide new power channels, and thus could reduce the reflection significantly as the wave amplitude increases. The effects of perturbed orbits on the interactions of electrons with two LHWs resonant with electrons at different phase velocities are also studied by GeFi. When the resonances of these two LHWs are overlapped sufficiently, the damping of the off-resonant wave and the oscillatory behavior of the wave amplitude are observed.

References

[1] Y. Todo and T. Sato, Phys. Plasmas 5, 1321 (1998).

[2] Youjun Hu, Y. Todo,Youbin Pei, Guoqiang Li, Jinping Qian, Nong Xiang, Deng Zhou, Qilong Qilong, Juan Huang, and Liqing Xu, Phys. Plasmas 23, 022505 (2016).

[3] Youbin Pei, et al., Phys. Plasmas 24, 032507(2017).

[4] T.Y. Xia et al., Nucl. Fusion 57, 116016 (2017).

[5] B. Chen et al., Nucl. Fusion 57, 116025 (2017).

[6] Eich T. et al., Phys. Rev. Lett. 107 215001 (2011).

[7] L. Wang et al., Nucl. Fusion 54, 114002 (2014).

[8] Y.F. Liang et al., PRL 110, 235002 (2013).

[9] N.J. Fisch, Reviews of Modern Physics, 59(1):175-234 (1987).

[10] Guozhang Jia, Nong Xiang, Xueyi Wang, Yueheng Huang, and Yu Lin, Physics of Plasmas , 23, 012504 (2016).

[11] Yu Lin, Xueyi Wang, Zhihong Lin, and Liu Chen, Plasma Phys. Controlled Fusion 47, 657 (2005).

[12] Guozhang Jia, and Zhe Gao, Physics of Plasmas, 21, 122121 (2014).

[13] S.G. Baek, R.R. Parker, S. Shiraiwa, G.M. Wallace et al., Plasma Physics and Controlled Fusion, 55(5):052001 (2013).

[14] R. Cesario, V. Pericoliridolfini. Nuclear Fusion, 27(3):435-445 (1987).

[15] G. Zaslavsk, N. Filonenk, Soviet Physics Jetp-Ussr, 27(5):851-&. (1968).

[16] D.F. Escande, Physica Scripta, T2:126-141 (1982).

[17] C.F.F. Karney, Physics of Fluids, 21(9):1584-1599 (1978).

[18] Y.H. Huang et al., Phys. Plasmas 23, 092114 (2016)

[19] J. Ma et al., Plasma Science and Technology, 18, (7) 714 (2016).

The development of the multi-pulse laser blow-off system in the HL-2A tokamak and its preliminary application

K. Zhang[1], P. Sun[1], D. L. Zheng[1], Y. Xu[2], Z. Y. Cui[1], Z. T. Liu[1], C. F. Dong[1], P. Lu[1] and Q. W. Yang[1]

[1]Southwestern Institute of Physics, P. O. Box 432, Chengdu 610041, China

[2]Institute of Fusion Science, School of Physical Science and Technology, Southwest Jiaotong University, Chengdu 610031, China

Abstract

The laser blow-off (LBO) technique is an important approach for impurity injection and related transport studies in the magnetically confined fusion research due to its significant advantages in the quantity control, reproducibility and transient features. Recently, a multi-pulse LBO system has been developed in the HL-2A tokamak, which was updated from the single pulse preceding system by the introduction of novel designs of a two dimensional (2D) optical steering assembly. In this article, the design and setting up details of the new system is illustrated. Preliminary experimental results employing this system is presente.

1. Introduction

Impurities are kinds of inherent sources in all magnetic confinement fusion devices. In addition to plasma facing materials and fusion-generated helium ash, the means of "impurity seeding" for actively mitigating the divertor heat load introduces considerable amount of impurities in fusion plasmas[1]. With accumulation of impurities in the core, the plasma quality is severely deteriorated through radiative cooling and fuel dilution, which may result in a halt of the discharge or even a major disruption. Considering the design of a whole tungsten first wall in ITER, it is imperative to understand impurity behaviors and the underlying physics of impurity transport. For the impurity study of both intrinsic and extrinsic species, techniques for impurity injection are routinely required to produce a pulsed impurity source. The most prominent feature of employing LBO in impurity injections lies in the excellent control of the injection amount to obtain adaptive perturbations to the plasmas of almost any conditions. However, the benefits of multiple injection operations[2] into a single plasma is too much appealing for the impurity transport studies, as is revealed in the scenarios employing supersonic molecular beam injection (SMBI) technique for gaseous impurity injections in the HL-2A[3]. Recently, a novel design two dimensional (2D) optical steering assembly is successfully developed in the HL-2A tokamak, upgrading the system with the capacity of performing multiple ablations by preset timing in a single discharge.

2. The laser blow-off (LBO) system

The schematic layout of the LBO system in HL-2A is shown in figure 1. The system employs a pulsed

Nd: YAG laser for film ablation, the 1064nm output laser beams are 6mm in diameter and 10ns in pulse width, the output energy and frequency are tunable with 2J and 30Hz maximum values respectively. A 635nm diode laser is colinearly aligned to indicate the infrared ablating beam to facilitate the system setup. The pulsed laser beams are directed along the Z direction into the window of the 2D optical steering assembly by a series of mirrors which are omitted in the schematic for simplicity. The 2D optical steering assembly, mounted on a linear stage, steers and focuses the laser beam onto desired positions on the target slide installed inside the vacuum tube behind the fused silica window, located 710mm from the plasma edge slightly below the midplane. All the optical components are optimized for the infrared to be highly transmissive, with damage thresholds of $4J/mm^2$ for the 10ns pulse width to adequately ensure the safety of these components. This configuration is tested to allow for up to 30Hz reproducible operations in a tabletop experiment. Even though higher operating rate can be achieved by replacing the laser with a higher performance one, the present configuration is sufficient considering the conditions of typical HL-2A plasmas.
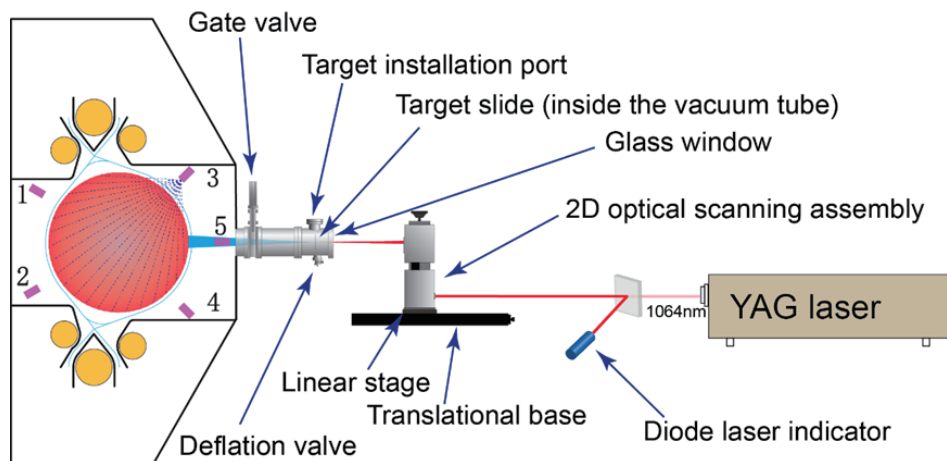
Fig. 1 Schematic layout of the multi-pulse LBO system in HL-2A.

The two-dimensional (2D) optical steering assembly is an integrated optical system to deflect (and focus) the laser beam onto different locations of the target plane (X-Y plane) with a very high temporal response. This is achieved by employing two galvanometer scanners, deflecting the laser beam in X and Y directions respectively. Because of the geometric design, the rotation range of the scanners are very small, less than 1 degree for the entire target scanning, the temporal response can be very high. The optical components of the assembly are embedded in two vertically arranged and bellow connected metal housings to prevent unintentional damage of the alignment or contamination of the components. The upper box of the assembly is vertically adjustable to align the optical path to be in the horizontal plane. The whole assembly is mounted on an electric linear stage along the Z direction in order that the ablation size on the target side can be adjusted.

The linear stage and the scanners are respectively controlled by a mutual industrial computer, connected through RS232 ports driven by respective controllers. The trigger signal of the ablation

operations is provided by a waveform generator that is synchronized with the HL-2A discharge control signal and the output feedback signal of the laser is ported to the scanning control program to steer the beam to the next scanning location on the target slide. The steering of the beam is controlled in the program in the form of coordinates, which is calibrated with the target locations in the setting up phase of the system. With proper calibration, the misalignment of the linear stage with the optical axis of the converging lens can be compensated by the beam steering, and the requirement for alignment in the setting up phase of the system is not so strict.

3. Experimental results

The system is routinely employed in HL-2A experimental scenarios, can becomes a powerful tool in studying the interactions of impurity with the bulk plasmas as well as impurity transport, in this section, some preliminary examples are presented.

(1) Impurity modulation[4]

The impurity source modulation experiments implement repeated LBO injections with a specific period to modulate the harmonics of the impurity source in the edge. Figure 2 is the evolutions of the plasma parameters in a discharge with 7-pulse aluminium injections beginning at t=600ms. The LBO injections are performed on the flattop of the discharge at 100ms intervals, denoted in vertical yellow dashed lines in the figure. It is seen from the figure that the edge and central electron temperature, the plasma current and loop voltage of the plasma was hardly perturbed by the injections. The line averaged density increases by approximately 3% at the instant of the injections and continue to grow due to the transport and ionization of the impurity particles, the overall increase is within 10% compared with the pre-injection values. In this sense, the perturbations introduced by the LBO injections are negligible. By contrast, there are remarkable responses in the radiation signals due to the enhancement of radiation enhancement effects of the aluminium impurity, which is favorable to obtaining good signal to noise ratio. In this scenario, with typical impurity confinement times of approximately 70 ms, the reproducibility of the injections is justified by the good similarity of the pulses considering the time span.

(2) Iron transport in different heating regimes[5]

Trace amounts of iron particles are injected into the combined ECRH and NBI heating phase and ohmic phase in the same discharge. Figure 3 shows a comparison of the time traces of bolometer signals and Fe spectral lines measured with a EUV spectrometer with a data acquisition time of 6 ms/frame. It is quite evident that in the ECRH plus NBI heating phase iron transport in the core plasma is significantly enhance whereas no obvious change is observed in the edge.

(3) Impurity ELM mitigation[6]

As is shown in figure 4, iron particles are injected into an ELMy H-mode phase of an HL-2A discharge at t=750ms and t=850ms respectively. As indicated in red shadows, immediately after the impurity injections, the ELM bursts are mitigated with smaller amplitude. The second injection provide a good confirmation of the reproducibility of this phenomenon. The difference in duration and frequency in the mitigation phase of the Dα signal provide good data for parametric dependence analysis that may shed light on the underlying physics.
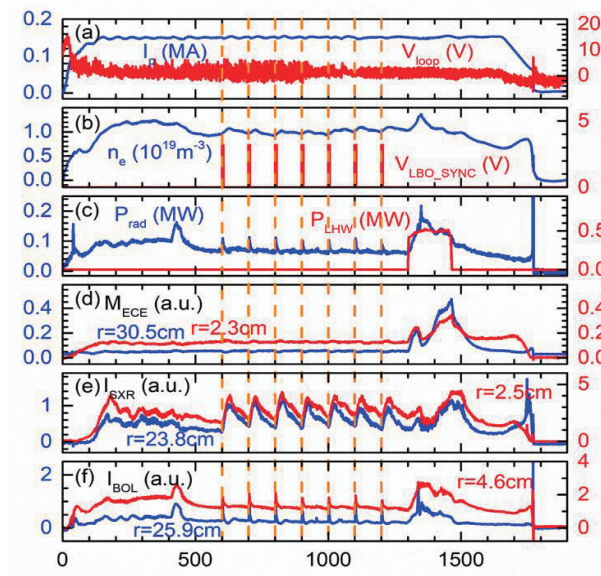
Fig. 2 The evolutions of (a) plasma current I_p and loop voltage V_{loop}, (b) line averaged electron density $\bar{n}_e$ and LBO synchronization V_{LBO_SYNC}, (c) total radiation power P_{rad} and lower hybrid wave heating power P_{LHW}, (d) edge and central electron temperatures measured by ECE, (e) soft x-ray signals of lines of sight from the edge and center, (f) bolometer signals of lines of sight from the edge and center of an HL-2A discharge #30263 with 7-pulse LBO aluminium injections, the vertical yellow dashed lines
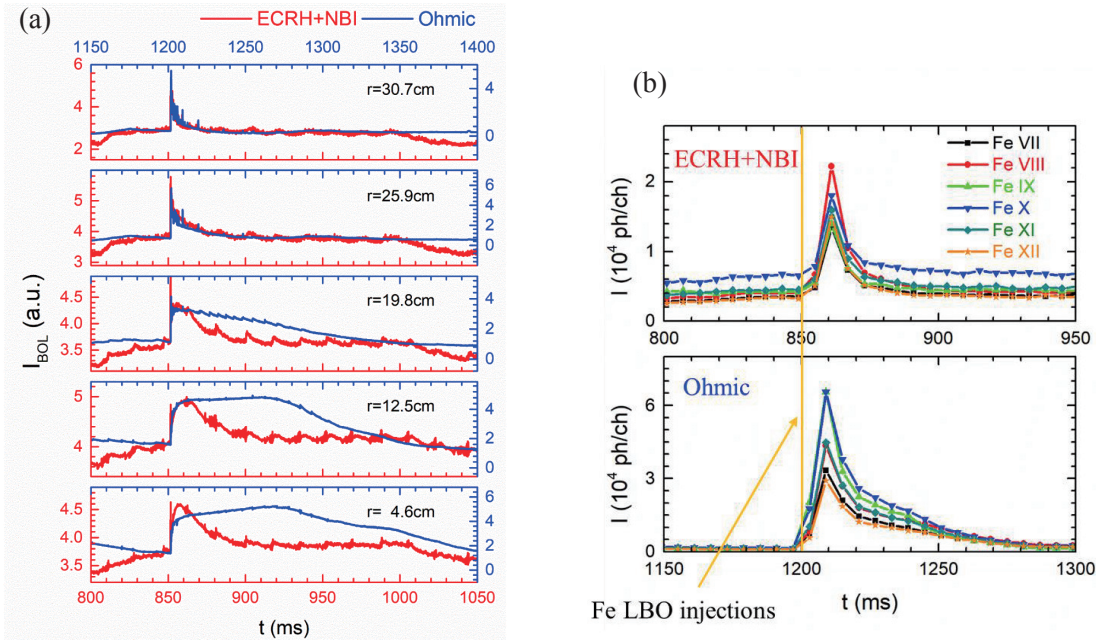
Fig. 3 Time evolutions of (a) bolometer signals of different line of sight during the ECRH and NBI heating phase (red) and ohmic (blue) phase of the discharge, (b) spectral lines from Fe VII through Fe XII during the ECRH and NBI heating phase (top) and ohmic (bottom) phase.
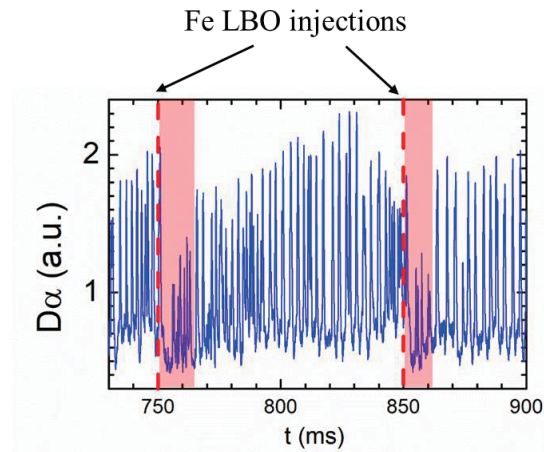
Fig. 4 Dα signal during the ELMy H-mode phase of an HL-2A discharge with LBO iron injection indicated in red vertical lines.

4. Summary

A multi-pulse laser blow-off system was successfully developed and implemented in experimental scenarios. The merit of the system in amount control and outstanding reproducibility was clearly evidenced in experimental measurements. The upgrade to the multi-pulse operations has essentially enhanced the flexibility of experimental schemes. More importantly, repeated injections into an identical plasma substantially increases the credibility of parameter scan. Based on this powerful diagnostic tool, the possibility and flexibility of experimental scenarios are extremely expanded.

Acknowledgements

References

[1]   Kallenbach a et al. 2013, Plasma Phys. Control. Fusion, 55, 124041

[2]   Howard NT et al. 2011, *Rev. Sci. Instrum.*, 82, 33512

[3]   Cui XW et al. 2013, Chin. Phys. B, 22, 125201

[4]   Gentle K. et al. 1992, Nucl. fusion, 32, 217

[5]   Cui, ZY, et al. "Study of impurity transport in HL-2A ECRH L-mode plasmas with radially different ECRH power depositions" Nucl. Fusion, 2018, to be published

[6]   Zhang YP, et al. "Control of edge localized modes by pedestal deposited impurity in the HL-2A tokamak", Nucl. Fusion, 2018, to be published

Study of Erosion/Deposition in KSTAR Ohmic plasma Discharge on Mid-plane Region

S.H.Son[1, 2], E.N.Bang[1], S.H.Hong[1]

[1]National Fusion Institute Research Institute, Daejeon 34133, Korea

[2]Department of Physics, Chungnam National University, Daejeon 34134, Korea

Abstract

The erosion/deposition experiments were conducted in 2017 KSTAR campaign on mid-plane region to study deposition/erosion and H/D retention on the wall surface. For this experiments, the cavity technique was utilized. The H (D) content of a-CH layer inside the cavity sample were about 40 %. In 2017 campaign, the particle source of deposited layer on the wall surface have abundant contained CH_4 radical, because a large amount of hydrogen isotopes were released by hot-wall condition operation. In Ohmic plasma case, the retention rate. The observed surface loss probability depends on the direction for alignment to magnetic field line. Total retention rate was in a range from 4.7 x 10^{-4} to 5.3 x 10^{-3} D g/s.

1. Introduction

There is no complete confinement in magnetic fusion devices. And always interaction of plasma particles with wall material might be in tokamak. Erosion of plasma facing component and redeposition of eroded material causes retention of fuel. So tritium or fuel retention in tokamak would be one of most critical issues over ITER and DEMO devices. During the plasma operation, ion and charge exchange neutrals bombard the carbon plasma facing components (PFCs), and carbon and hydrocarbon species was released depending on the energy of impinging particles and the temperature of the PFC. Released particles made by erosion can be transported, and can make deposited hydrocarbon layer in tokamak remote anywhere. After that, it is also used as resource for re-erosion. For that reason, erosion/deposition experiment using cavity technique was conducted in KSTAR Ohmic plasma discharge. In this paper, the method of the cavity technique will introduce for erosion/deposition experiments, an analysis of hydrocarbon layer and surface loss probability in low field side mid-plane region of KSTAR during 2017 hot-wall condition operation will be reported.

2. Cavity technique and experimental setup

Tokamak are large devices and there are different boundary conditions including toroidal magnetic field, deposition and erosion characteristics are not easy to trace and quantify. To overcome such difficulties, cavity technique was used. This figure is shown particle collision to be happened in the cavity structure. After incoming particle collision in cavity structure, the thickness will be changed. The eroded or deposited profile of thin film layer in the cavity can provide several information, for example the particle incident pattern, the color change on surface after exposure to the plasma. Especially, the thickness profile provides information about time averaged particle flux. For this technique, pre-requisites are needed, but these two

pre-requisites are easily fulfilled at low pressure region.
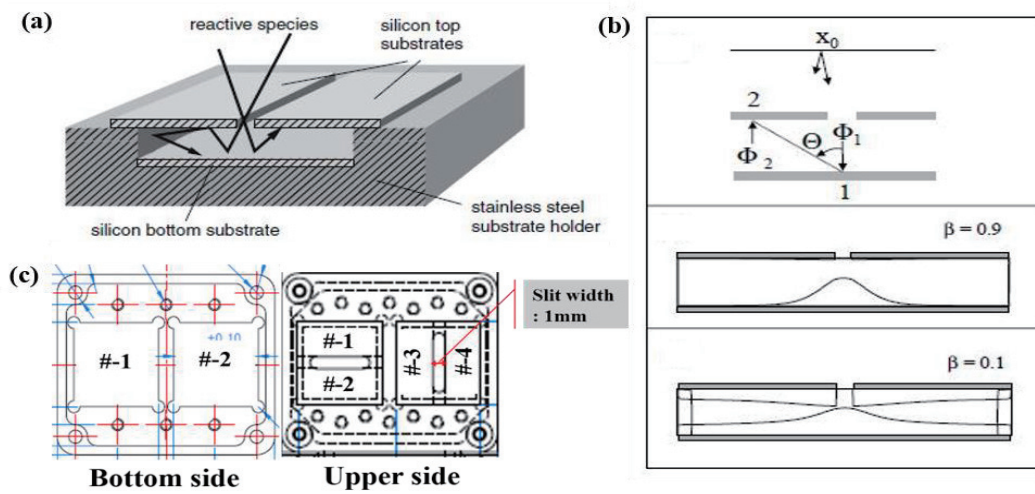
Fig. 1 (a) principle of a cavity probe: reactive particles enter the cavity through the slit an deposited films on the inner surface [1], (b) schematic of the cavity made of silicon wafer and thickness profile according to surface loss probability (β) [2], (c) the cavity structure for KSTAR experiments.

The reason is that mean free path at a low pressure of less than $\sim 10^{-3}$ torr is larger than several cm, while the slit size of cavity is 1~2 mm. The thickness profile depends only on surface loss probability (beta). The beta is consist of sticking coefficient and reflected probability with surface (gamma). But the hydrocarbon case, the gamma can set almost to zero. So the beta can understand as a sticking coefficient on the surface. Beta can calculate by comparing the amount of deposition inside the cavity with that on the side walls over an area of slit. Figure 1 shows a different thickness profile shape according to beta and this is used cavity structure with 1 mm slit width in my experiments. For erosion and deposition experiments, a-CH film was prepared. And thickness and optical property such as refraction index (n) of thin film of cavity sample was measured by ellipsometry. The cavity sample are exposed using manipulator system in KSTAR [3].
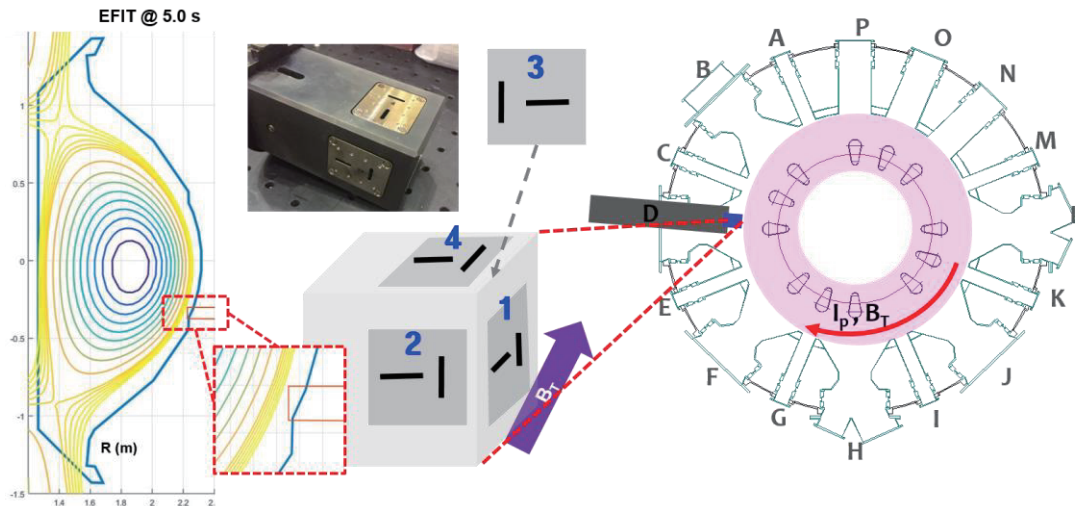
Fig 2 Cavity sample location in Ohmic discharge and a direction of cavity slit opening of alignment to I_p and B_T.

After exposing a cavity sample, the a-CH film is measured again by ellipstometry. This procedure leads to estimation of incident particle flux and experimental retention rate. After exposing a cavity sample, the a-CH film is measured again by ellipsometry. This procedure leads to estimation of incident particle flux and experimental retention rate. For exposing a-CH film using the cavity technique, we define the cavity sample position as shown in fig.2. The cavity structure has two slit opening. Contribution of ion and charge exchange neutrals could be separated, since one is aligned parallel to the magnetic field line and other is perpendicularly aligned. Each cavity sample was installed on a different four direction (front/I_p/reversed I_p/top) with respect to the toroidal magnetic flied line (B_T).

3. Results

Measured refraction index (n) of ellipsometry was in a range from 1.70 ~ 1.78. Carbon density and hydrogen content of deposited film is derived from n. The H (D) content of a-CH layer inside the cavity sample were about 40 %. Carbon density maximum 4.43 $\times$ 10^{15} in I_p direction cavity sample. Fig 3 shows change of thickness profile and calculated surface loss probability (β) according to cavity position and direction of slit opening. In this case, bottom side sample was only calculated. The averaged value of β was drew ≤ 0.3, and the maximum value of β is 0.65 in I_p direction cavity sample. The carbon flux in all direction of cavity sample is higher in toroidal gap than that poloidal gap.

Compared with average gas balance, value of post mortem analysis retention increased in 2017 hot-wall condition operation. (Magenta symbols are hot-wall condition operation). Hot-wall condition means averaged PFC temperature was kept in 150°. Normal wall condition was measured in 2009-2010 campaign [4]. Hot-wall condition operation let be released hydrogen isotopes from wall hydrocarbon, and the particle source of deposited layer on the wall surface might have abundant contained CH_4 radical. Another major difference with precedent study is a distance from plasma. In this case, cavity sample was installed outer wall. The distance gap between hot-wall and normal wall is almost ~ 30 cm. A difference value of β indicates change of incoming particle on surface from ion to neutral due to far distance from

plasma.
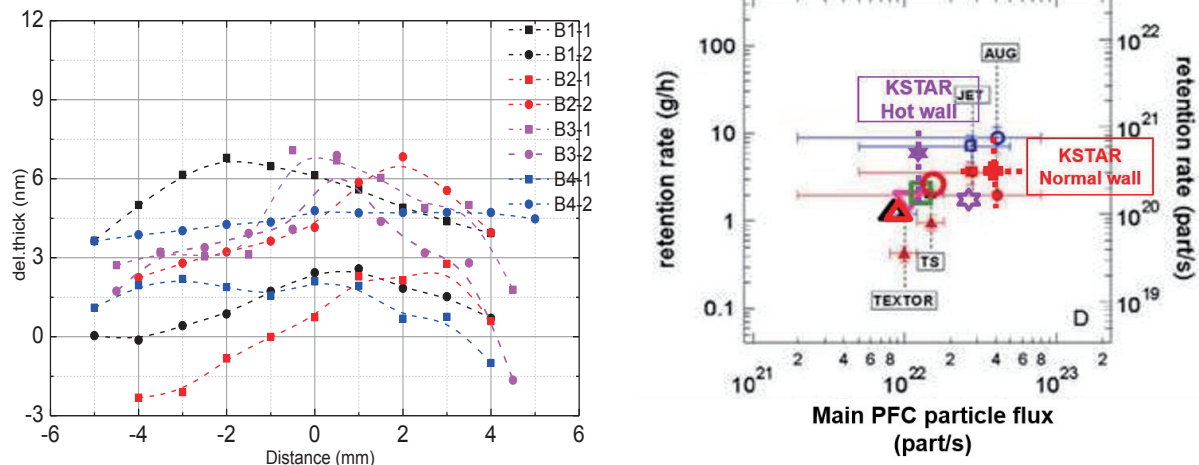
Fig 3. Thickness profile with surface loss probability (β) and total retention multi-machine scaling.

4. Summary and discuss

The erosion/deposition experiments were conducted in 2017 KSTAR campaign on mid-plane region to study deposition/erosion and H/D retention on the wall surface. For this experiments, the cavity technique was utilized. The cavity sample was exposed in Ohmic plasmas. The H (D) content of a-CH layer inside the cavity sample were about 40 %. The observed surface loss probability (β) depends on the direction for aligned to magnetic field line. Carbon density in deposited layer has a maximum value of 4.43 $\times$ 10^{15} in I_p direction cavity sample. Total retention rate was in a range from 4.7×10^{-4} to 5.3×10^{-3} D g/s. Compared with average gas balance, value of post mortem analysis retention increased in 2017 hot-wall condition operation. It means the particle source of deposited layer on the wall surface have abundant contained CH_4 radical, because a large amount of hydrogen isotopes were released by hot-wall condition operation. Futrher investigation must be done conducted experiment in the other plasma condition such as L- and H-mode.

Acknowledgements

References

[1] A. von Keudell et al., Nucl.Fusion 39 (1999) 1451

[2] C. Hopf et al, J. Appl. Phys., 87 (2000) 6

[3] S. H. Son et al., Fus. Eng and Des 109-111 (2016) 406-410

[4] S. H. Hong et al., J. Nucl. Mater. 403 (203) S698-S709

W atomic model validation by CoBIT and W ion measurements in LHD core plasmas

D. Kato[1,2,3], H.A. Sakaue[1], I. Murakami[1,2], M. Goto[1,2], T. Oishi[1,2], S. Morita[1,2],

N. Nakamura[4], X.-B. Ding[5] and C.-Z. Dong[5]

[1]National Institute for Fusion Science, Toki 509-5292, Gifu, Japan

[2]Dept. of Fusion Science, SOKENDAI, Toki 509-5292, Gifu, Japan

[3]Dept. of Advanced Energy Engineering, Kyushu University, Kasuga 816-8580, Fukuoka, Japan

[4]Inst. for Laser Science, Univ. of Electro-Communications, Chofu 182-8585, Tokyo, Japan

[5]Key Lab. of Atomic and Molecular Physics and Functional Materials of Gansu Province, College of

Physics and Electronic Engineering, Northwest Normal University, Lanzhou, China

Abstract

A collisional-radiative model for tungsten highly charged ions is developed with atomic data calculated by HULLAC code. The present model is validated by comparing Extreme-Ultra-Violet spectra measured by a compact electron-beam-ion-trap (CoBIT). Tungsten spectra in Large Helical Device (LHD) core plasmas are analyzed with the present model and it is applied to tungsten ion measurements at LHD.

1. Introduction

Tungsten (W) will be used as divertor materials in ITER. Impact of tungsten contamination in the core plasmas is a big concern because a large radiation power loss by the tungsten ions is predicted. Thus, W behaviors in magnetic confinement plasmas have intensively been studied with large devices. Emission line spectra of up to 48 times ionized W ions have been reported with large devices, e.g. ASDEX-U, JET, JT-60U, LHD, EAST. These charge states would be dominant in edge plasmas of ITER. Strong emission lines from these charge states are observed in soft X-ray and Extreme-Ultra-Violet (EUV) regions. The largest radiation power is emitted by Unresolved-Transition-Array (UTA) due to n = 4 – 4 transitions at 5 – 6 nm (Fig. 1). The UTA is quasi-continuum emission which consists of many emission lines of different charge states in a limited wavelength range.

We developed collisional-radiative (CR) models for line emission of W highly charged ions based on a fully relativistic ab-initio calculations of atomic data using HULLAC code [1]. The model is validated by comparing with EUV spectra of W ions in a compact electron beam ion trap (CoBIT). With the CR model, W spectra are analyzed and used to W ion measurements in Large Helical Device (LHD).
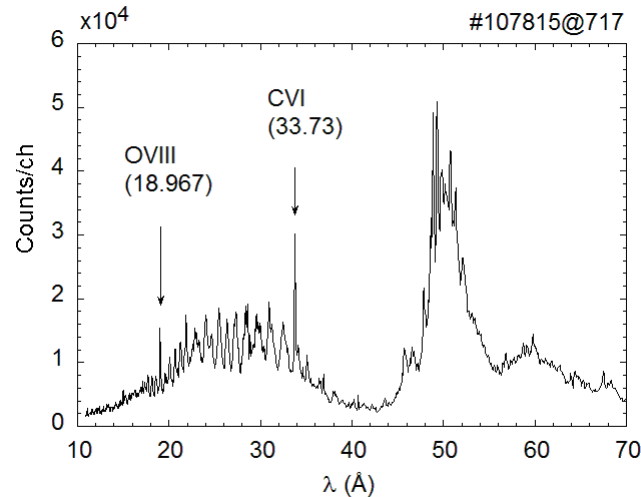
Fig. 1 EUV spectra of W highly charged ions in Large Helical Device (LHD) plasmas.

2. W atomic model validation by CoBIT measurements

Emission line intensity due to a transition between two levels is expressed by a product of the Einstein's A coefficient and a population density of the upper level. The population densities are calculated by the collisional-radiative model. This model is obtained as a quasi steady-state approximation of kinetic equations for excited state population densities at a given electron temperature (energy) and density. We obtained atomic data for a few tens of thousands energy levels included in the collisional-radiative model using HULLAC code which implements fully relativistic ab-initio calculations of energy, radiative transition, electron collision and photoionization of highly charged ions. The present transport-free atomic model is validated by comparing EUV spectra of W highly charged ions in the CoBIT.

The CoBIT [2,3] is designed to be operated at electron beam energies of a few hundreds eV up to a few keV, which enables us measurements for the charge states observed in the existing large plasma devices (see Fig. 2). W is introduced in the CoBIT as vaporized W hexa-carbonyl, $W(CO)_6$. Ions trapped by an axially applied electrostatic potential well at the central drift tube and a radial space charge potential are successively ionized to higher charge states by the mono-energetic electron beam compressed by a magnetic field of 0.2 T. The electron density interacting with the ions are typically 10^{16} m^3, about three orders of magnitude smaller than that in fusion plasmas. Maximum charge states and charge state distribution can be controlled by the electron beam energy and gas pressures. CoBIT is operated with the gas pressure of 10^{-7} Pa, which gives a narrow charge state distribution of the trapped ions. The CoBIT is equipped with measuring instruments including the grazing incidence flat-crystal EUV spectrometer and the Czerny-Turner type UV-Visible spectrometer.
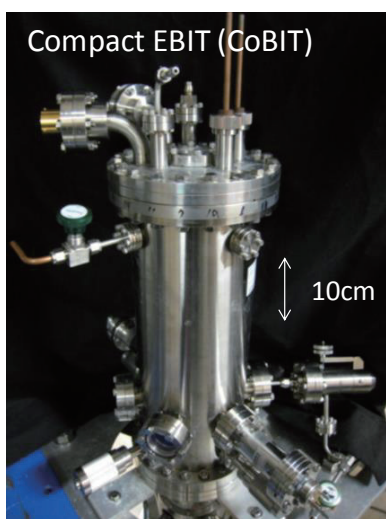
Fig. 2 Picture of CoBIT.
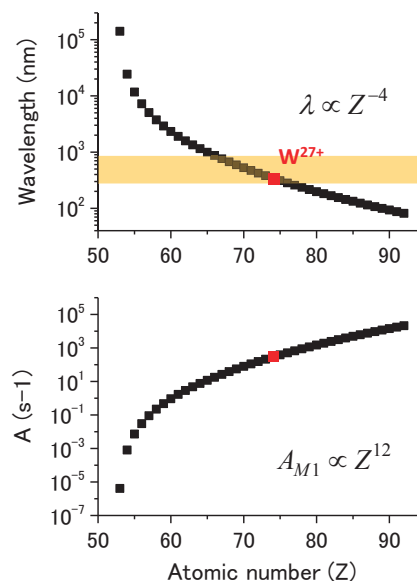
Fig. 3 Wavelengths (upper) and probabilities (lower) of M1 transition in the 4f doublet.

3. Analysis of W spectra and W ion measurements in LHD

Since divertor in the LHD is made of graphite, the primary impurity in LHD plasmas is carbon and a small amount of metal elements, such as iron from in-vessel stainless steel plates. Tungsten is injected as a solid pellet by pneumatic systems with pressurized He gas. LHD plasmas are sustainable with a significant amount of heavy elements by NBI heating.

The present atomic model, which is validated by CoBIT measurements, is used to analyze EUV spectra observed in LHD plasmas. The synthesized spectra of the present atomic model are reconciled well with the LHD spectra. Charge state distributions of W highly charged ions with which the synthesized spectra are obtained are compared with theoretical models. The present results have better agreements with the models of Asmussen and ADAS, although a large uncertainty remains in the present results. Radiation power rates are calculated with the charge state distribution at two temperatures of 0.7 keV and 1.5 keV, which agree with model calculations within factor of 2 [4]. However, experimental measurements by Sudo et al. [5] give significantly smaller values. Large uncertainties still remain in the radiation power rates of W highly charged ions.

Visible spectroscopy will facilitate more precise measurements. Emission lines are isolated in spectra and opacities are negligible, which facilitate ion density measurements. Fusion neutron shielding of detectors is not necessary by using optical fibers. However, application of such visible lines to W measurements is exclusively limited to neutral or low charge states. Wavelengths of magnetic-dipole (M1) transitions in the 4f doublet (fine-structure) decrease rapidly as atomic number increases (see Fig. 3). M1 lines of highly charged W ions in the 4f ground states fall into UV-Visible range. The transition probability becomes very large for heavy elements dominating over two photon transitions. Such M1 lines have been

observed and applied for W ion measurements at LHD.

W lines, which are apparent only in the spectra measured after W pellet injection, indicated by red arrows have vertical profiles localized in core plasmas (Fig. 4). 11 lines of W highly charged ions are identified in 330 – 390 nm in the present measurement [6,7]. In this spectrum, one W line at 337.7 nm is assigned due to an M1 transition of W^{27+} ions in the 4f ground state and two lines at 333.7 and 335.7 nm are due to M1 transitions of W^{26+} ions in the $4f^2$ ground state. The central wavelengths of these M1 lines coincide with EBIT measurements. State-of-the-art ab-initio atomic structure calculations by Multi-Configurational Dirac-Fock (MCDF) method and Relativistic Many-Body Perturbation Theory (RMBPT) are reported for these lines. The theoretical values agree with the present measurements within a few %. However, the experimental uncertainty is much smaller, 4 significant figures.

Radial distributions of ion densities for W^{27+} and W^{26+} are deduced from the vertical profiles of the M1 lines at four instants of time after W pellet injection. Ion density ratios W^{27+}/W^{26+} obey ionization equilibrium values calculated with CADW ionization [8] and modified ADPAK recombination [9] rate coefficients in a temperature range of 0.5 – 1.5 keV. Only at the instance when a steep gradient of temperature profile at the edge is observed, a significant deviation from the ionization equilibrium is seen.
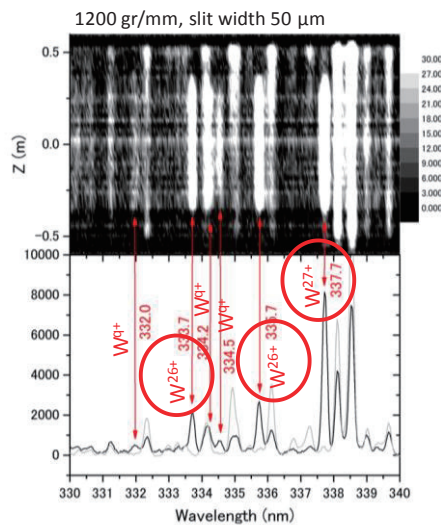
Fig. 4 UV-Visible spectra of W highly charged ions in LHD core plasmas (lower) and its vertical profiles (upper).

4. Summary

Spectral data of W^{q+} ions are measured systematically with a compact EBIT (CoBIT). Present CR model and atomic data in the model are benchmarked by comparing with the CoBIT measurements. EUV and UV-Visible line emissions of W^{q+} ions in LHD are identified based on the CR model. Synthesized spectra elucidate charge state distribution and W ion density in LHD core plasmas. Ionization equilibrium using CADW ionization and modified ADPAK recombination rate coefficients is benchmarked by comparison with present measurements of W^{27+}/W^{26+} density ratios for $T_e = 0.5 \sim 1.5$ keV. Significant discrepancy from the ionization equilibrium is observed at the instance when a steep gradient of temperature profile at the edge is observed.

Acknowledgements

References

[1] A. Bar-Shalom, M. Klapisch and J. Oreg, J. Quant. Spectr. Radiant. Trans. 71 (2001) 169.

[2] N. Nakamura et al., Revi. Sci. Instrum. 79 (2008) 063104.

[3] H.A. Sakaue et al., JINST 5 (2010) C08010.

[4] I. Murakami et al., Nucl. Fusion 55 (2015) 093016.

[5] S. Sudo et al., Plasma Fusion Res. 9 (2014) 1202147.

[6] D. Kato et al., Phys. Scr. T156 (2013) 014081.

[7] K. Fujii et al., J. Phys. B: At. Mol. Opt. Phys. 50 (2017) 055004.

[8] S.D. Loch et al., Phys. Rev. A 72 (2005) 052716.

[9] T. Putterich et al., Plasma Phys. Control. Fusion 50 (2008) 085016.

Deuterium depth profiles on coated lithium layer in EAST

N. Ashikawa[1,2], Y.W. Yu[3], Z.H.Hu[3], K. Katayama[4], M.Z. Zhao[3], F. Ding[3], J.S. Hu[3] and G.N. Luo[3]

[1]National Institute for Fusion Science, Toki, 509-5292 Japan

[2]SOKENDAI, Toki, 509-5292 Japan

[3]Institute of Plasma Physics Chinese Academy of Science, Hefei, China

[4]Kyushu University, Kasuga, 816-8580 Japan

Abstract

Trapped deuterium (D) in coated lithium layers was investigated in EAST. Depth profiles of deuterium retention in lithium layers were analyzed using glow discharge optical emission spectroscopy. Thick lithium layer of 7.2 micron was coated on tungsten specimen at the high field side during one experimental campaign of EAST, and deuterium was trapped in the lithium layer until interface. Higher oxygen intensities were counted in the lithium layers and it suggested that lithium forms oxide. From one day sample exposure, D was observed on the surface layer only and D intensities were about one order of magnitude lower than that of long term exposure. Hence, higher D trapping in lithium layer was performed by long term plasma-lithium interactions.

1. Introduction

In EAST, lithium wall conditionings was operated as general operational methods [1]. Lithium has easily to make chemical bindings, such as hydride, oxide, so on. Lithium wall conditions have been operated at the beginning of experimental campaign, and every morning before plasma operations in general. Reductions of deuterium after lithium conditioning were observed by spectroscopy diagnostics and H-mode operations with long pulse discharges about 100 seconds were operated. But trapped deuterium in lithium layers using surface analyzer was not observed yet. In this report, trapped deuterium was analyzed at the first time and their depth profiles are shown.

2. Experimental setup

In this work, deuterium retention in long term sample exposures and short term sample exposures was compared. For long term exposure, tungsten (W), molybdenum, carbon specimens were installed at the high field side of tokamak in plasma vacuum vessel and the size of these specimens is 10 mm x 10 mm x 2 mm. Specimens were adjoining each other. Coated lithium layer on tungsten specimen is clearly shown and a smooth interface of coated lithium layer is shown in Fig.1. These specimens were designed for target materials of the laser induced breakdown spectroscopy measurement and were exposed to plasmas during one experimental campaign in 2016.

For short term exposure, W and stainless steel 316 specimens were set on the MAPES [2]. Before the

morning Li wall conditioning, specimens were installed to plasma vacuum vessel by MAPES and these specimens were taken out from the plasma vacuum vessel after the end of plasma discharged on the day. Hence, specimens exposed to all wall conditionings and main plasma discharges during one day in EAST.

Surface morphologies were measured by the scanning electron microscope (SEM) and cross-section of coated layers and base materials were treated by focus ion beam (FIB) with Gallium gasses. Deuterium depth profiles were measured by glow discharge optical emission spectroscopy (GD-OES). Surface analysis was done in Japan.

3. Results and discussions

Figure 1 shows a cross-section image by the SEM secondary electron image after focus ion beam (FIB) treatment on a tungsten specimen. Coated lithium layer on tungsten specimen and a smooth interface layer of coated lithium are clearly shown. The upper side of the cross-section (dark gray) shows coated lithium layer of 7.2 microns and the lower side of the cross-section (light gray) shows tungsten specimen. Cross-section image of coated lithium layer on carbon specimen were shown in Fig.2. From SEM secondary electron image, an interface of lithium layer was not clear as shown in Fig.2 (a). Fig.2 (b) shows a cross-section image by SEM backscattered electron image of sub-surface layer on carbon specimen. From a difference of mass number between lithium and carbon, different colors such as dark color by carbon and light gray by lithium were shown in Fig. 2(b). A thickness of coated lithium is about 1.5 micron. Similar thicknesses of coated lithium layer between tungsten and carbon specimens were estimated. But differences of coated layers were observed. Chemical bindings between carbon and lithium were considered as a reason of these different lithium thickness on carbon and tungsten.

Figure 3 shows depth profiles of deuterium (D), tungsten (W), carbon(C), oxygen (O), lithium (Li) on tungsten specimens measured by GD-OES. In coated lithium after one experimental campaign, deuterium was trapped in lithium layer and it was reach until interface. Carbon and Oxygen were trapped in lithium as a similar depth region as shown in Fig.3 (a). In coated lithium after one day plasma experiments, deuterium trapped near surface region only. Oxide and carbide to lithium were negligible into the lithium layer.

Hence, higher deuterium, oxygen, carbon were performed during long term plasma-lithium interactions. In the case of coated boron on the plasma facing walls, retained boron film can trap oxygen and influence of boron film was kept long term [4]. Efficiencies of deuterium reduction by lithium are kept during long term, and then higher deuterium trapping in lithium layer during one experimental campaign was observed.
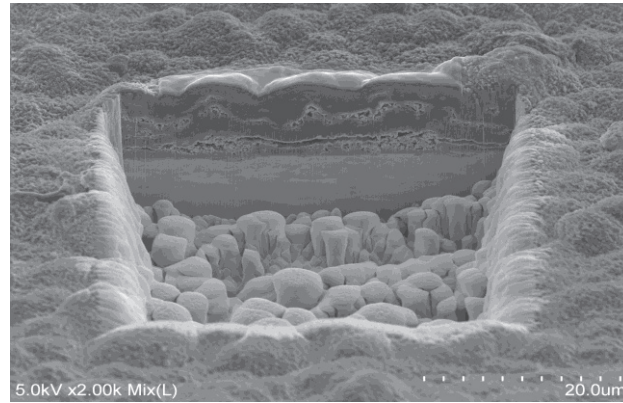
Fig.1 Cross-section image by SEM secondary electron image after focus ion beam (FIB) treatment on a tungsten specimen. The upper side of the cross-section (dark gray) shows coated lithium layer of 7.2 microns and the lower side of the cross-section (light gray) shows tungsten specimen.
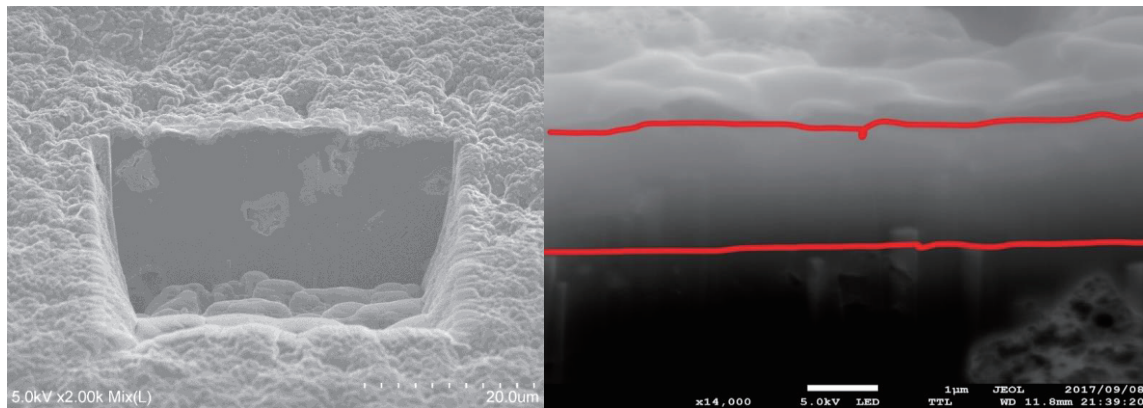
Fig.2 (a) Cross-section image by SEM secondary electron image after focus ion beam (FIB) treatment on a carbon specimen. (b) Cross-section image by SEM backscattered electron image of sub-surface layer. A region between red lines is coated lithium layer on carbon specimen.
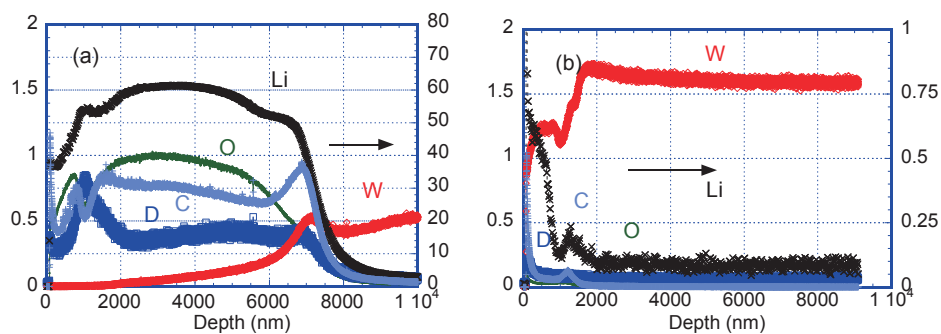
Fig.3 Deuterium depth profiles measured by glow discharge optical emission spectroscopy. (a) Tungsten specimen during long term plasma exposure at the high field side in 2016 experimental campaign in EAST. (b) Tungsten specimen during one day plasma exposure using MAPES in EAST [3].

4. Summary and future works [3]

Depth profiles of deuterium retention in lithium layers were analyzed in EAST. Thick lithium layer of 7.2 micron was coated at the high field side during one experimental campaign in EAST. Deuterium was trapped in the lithium layer until interface. Higher oxygen intensities were counted and it was related to lithium oxide. D did not observed in W bulk.

From one day sample exposure, deuterium was observed on the surface layer only and D intensities were about one order of magnitude lower than that of long term exposure. Hence, higher D trapping in lithium layer was performed by long term plasma-lithium interactions.

5. Acknowledgements

References

[1] G.Z. Zuo, J.S.Hu, et al., J. Nucl. Mater. 438 (2013) S90.

[2] F. Ding, et al., J. Nucl. Mater. 455 (2014) 710.

[3] N. Ashikawa, Y.W.Yu, J. Wu, E. Bang, S. Son, K. Katayama, et al., ITC-26/APFA-11 conference, Oral-1, December 2017, Toki, Japan.

[4] N. Ashikawa, K. Kizu, et al., J. Nucl. Mater. 363-365 (2007) 1352.

Spectroscopic study of carbon impurity flow in the edge stochastic magnetic field layer of Large Helical Device

T. Oishi[1,2], S. Morita[1,2], S. Y. Dai[3], M. Kobayashi[1,2], G. Kawamura[1], Y. Liu[2], M. Goto[1,2], and the LHD Experiment Group[1]

[1]National Institute for Fusion Science, Toki 509-5292, Gifu, Japan

[2]Department of Fusion Science, SOKENDAI, 322-6 Oroshi-cho, Toki 509-5292, Japan

[3]Key Laboratory of Materials Modification by Laser, Ion and Electron Beams (Ministry of Education), School of Physics, Dalian University of Technology, Dalian 116024, PR China

Abstract

The parallel flow of carbon impurity in a thick stochastic magnetic field layer called "ergodic layer" located at the edge plasma of Large Helical Device (LHD) is studied by space-resolved vacuum ultraviolet (VUV) spectroscopy. The carbon flows have directions same as the friction force calculated with a three-dimensional simulation code, EMC3-EIRENE. The flow velocity is smaller in the deuterium discharge compared to that in the hydrogen discharge, which indicates existence of some isotope effect in the impurity transport.

1. Introduction

Stochastization of edge magnetic fields is extensively studied not only for the ELM mitigation but also for the plasma detachment and the impurity transport. A thick stochastic magnetic field layer called "ergodic layer" of the large helical device (LHD) consists of stochastic magnetic fields with three-dimensional structure intrinsically formed by helical coils, while well-defined magnetic surfaces exist inside the last closed flux surface [1]. It is therefore extremely important to study the impurity behavior and transport in the ergodic layer and to compare with those in the scrape-off layer of tokamaks. In LHD, it is found that carbon impurities are screened by the presence of the ergodic layer [2] and iron impurities are more effectively screened. As a result, the iron density in core plasmas of LHD is found to be extremely low despite the stainless steel vacuum vessel [3]. A transport model for the impurity behavior in the ergodic layer has been proposed considering the parallel momentum balance on impurity ions along a magnetic field line connecting the core plasma and the divertor plate based on the following equation;

$$m_Z \frac{\partial V_{Z//}}{\partial t} = -\frac{1}{n_Z}\frac{\partial T_Z n_Z}{\partial s} + ZeE_{//} + m_Z \frac{V_{i//} - V_{Z//}^{imp}}{\tau_s} + 0.71Z^2 \frac{\partial T_e}{\partial s} + 2.6Z^2 \frac{\partial T_i}{\partial s},$$

where five terms in the right-hand side are contributions of impurity ion pressure gradient, parallel electric field, friction force between bulk ions and impurity ions, electron thermal force, and ion thermal force, in the order [4]. Among these terms, the friction force term and the ion thermal force term are the dominant terms. When the ion density gradient increases, the friction force increase resulting the impurity flow is directed toward divertor plates, which means the impurity screening. On the other hand, when the ion

temperature gradient increases, the ion thermal force increases resulting that the impurity flow is directed toward the core plasmas, which means the impurity accumulation.   Based on the model, the parallel flow of the impurity ions is considered to be a key mechanism to determine impurity distributions in the ergodic layer.   Therefore, in this study, measurement of carbon impurity flow is attempted by using a space-resolved VUV spectroscopy and relation between the flow and the impurity screening effect is discussed.

2. Measurements of flow velocity of the carbon impurity

Figure 1 shows a typical waveform of a discharge with a magnetic configuration with R_{ax} = 3.6 m and the toroidal magnetic field, B_t, of 2.75 T.   Power of the electron cyclotron heating (ECH) and the neutral beam injection based on the negative ion sources (n-NBI) central electron temperature and central electron density, and the plasma stored energy are shown together.   The discharge initiated by ECH is grown by three n-NBI beams with total port-through power of 10 MW and maintained with a flat-top phase for 1 s as shown in Fig. 1.   The working gas was H_2 and the beam particle of the neutral beam was hydrogen in this shot (denoted as "H-discharge").   We also performed a similar operation for a discharge in which the working gas was D_2 and the beam particle of the neutral beam was hydrogen (denoted as "D-discharge"). A space-resolved VUV spectroscopy was attempted in the flat-top phase of the discharges by using a 3m normal incidence VUV spectrometer [5].   The edge flow profile is investigated with high spatial resolution by using the viewing angle of the edge profile measurement of the VUV spectroscopy from Doppler shift of the second order of CIV line emission (2 × 1548.20 Å) at a horizontally-elongated plasma position of LHD.

Figure 2 shows vertical profiles at the bottom edge of the ergodic layer of (a) CIV line intensity, (b) ion temperature, and (c) flow velocity derived from the CIV line emission measured by VUV spectroscopy for an H-discharge and a D-discharge with a magnetic configuration with R_{ax} = 3.6 m and B_t = 2.75 T.   The observation range of the edge profile measurement of the VUV spectroscopy is also shown in Fig. 2(d). The flow velocity along the sightline, v_R, is given by $v_R = c (\Delta\lambda / \lambda)$, where c is the light speed, $\Delta\lambda$ the Doppler-shift and λ the wavelength of line emission.   The measured flow velocity is projection of the flow along the observation chord which can be approximately considered to be the direction of the plasma major radius.   Therefore, a variable of v_R is used to indicate the measured flow value.   Positive and negative sign in the horizontal axis of Fig. 2(c) corresponds to the outboard an inboard direction along the plasma major radius, respectively.   As shown in the figure, the emission intensity is larger in the D-discharge than that in the H-discharge because the sputtering rate of carbon atoms from the divertor plates is larger in the D-discharge.   The ion temperature has no clear change between the H-discharge and the D-discharge. The flow velocity toward the outboard direction develops clearly with the maximum value at Z = -480 mm, which is a location close to the outermost region of the ergodic layer in the H-discharge.   This direction is same as the friction force in the parallel momentum balance for R_{ax} = 3.6 m calculated with EMC3-EIRENE code [6].   On the other hand, the maximum value of the flow velocity in the D-discharge is clearly smaller than that in the H-discharge.

The electron density dependence of the maximum value of the observed flow is summarized in Fig. 3.

All plots in the figure have directions same as the friction force.   In the case of the H-discharge, the flow increases with the electron density.   The result supports a prediction by the simulation that the friction force becomes more dominant in the force balance in higher density regime, which results in the increase of impurity flow causing the impurity screening.   In the case of the D-discharge, the flow has a smaller value. In the friction force term in the equation of the momentum balance, $m_Z \dfrac{V_{i\parallel} - V_{Z\parallel}^{imp}}{\tau_s}$, the thermal velocity of the bulk ion, $V_{i\parallel}$, and the collision time between the bulk ion and the impurity ion, τ_s, might be changed between the H-discharge and the D-discharge.   Further experiments and simulations for the H-D comparison are needed to clarify the difference.
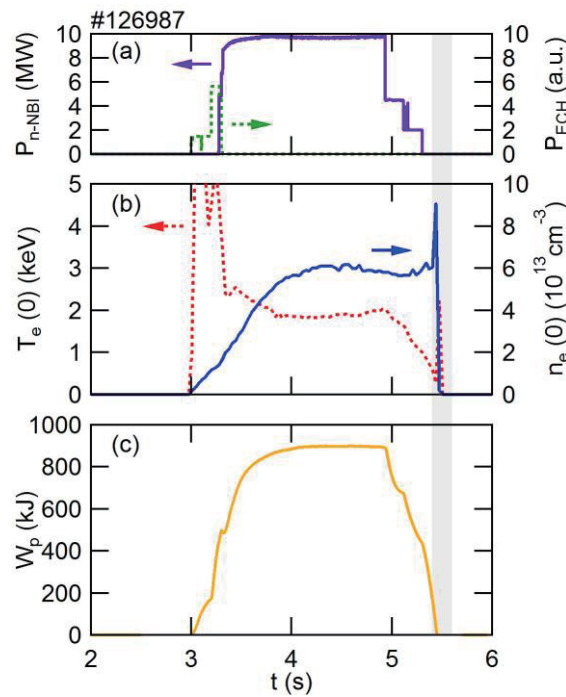
Fig. 1 Typical waveform of an H-discharge in which the space-resolved VUV spectroscopy is attempted. (a) ECH and n-NBI power, (b) central electron temperature and central electron density, and (c) plasma stored energy.
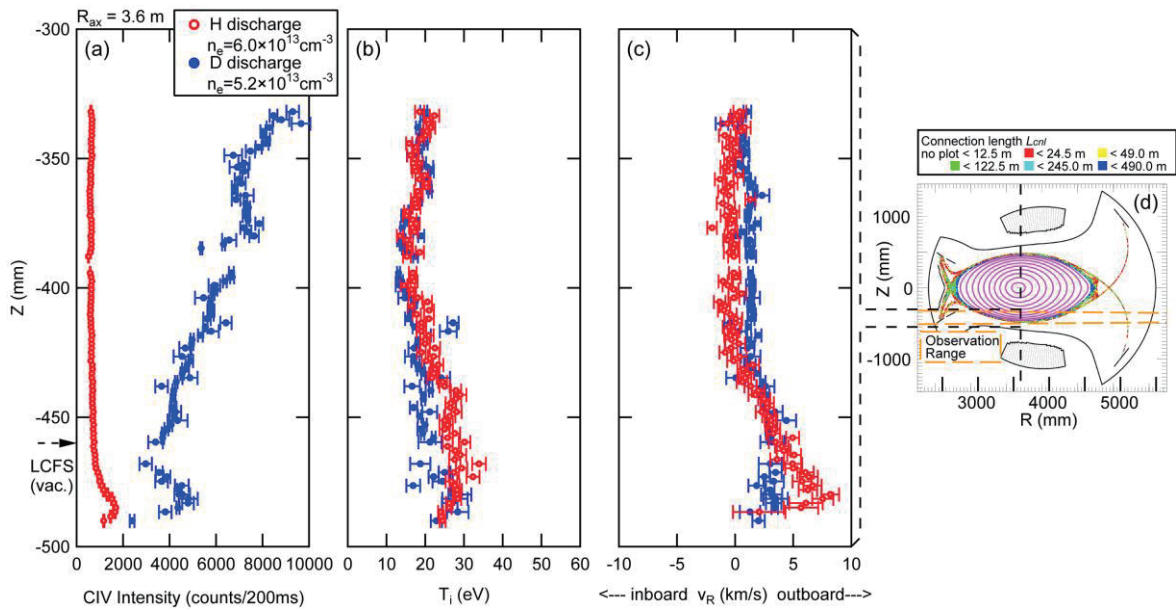
Fig. 2 Vertical profiles at the bottom edge of the ergodic layer of (a) CIV line intensity, (b) ion temperature, and (c) flow velocity derived from the Doppler profile of the second order of CIV line emission (2 × 1548.20 Å) measured by VUV spectroscopy for inward-shifted magnetic configuration with R_{ax} = 3.6 m in a hydrogen discharge (red open circle) and a deuterium discharge (blue closed
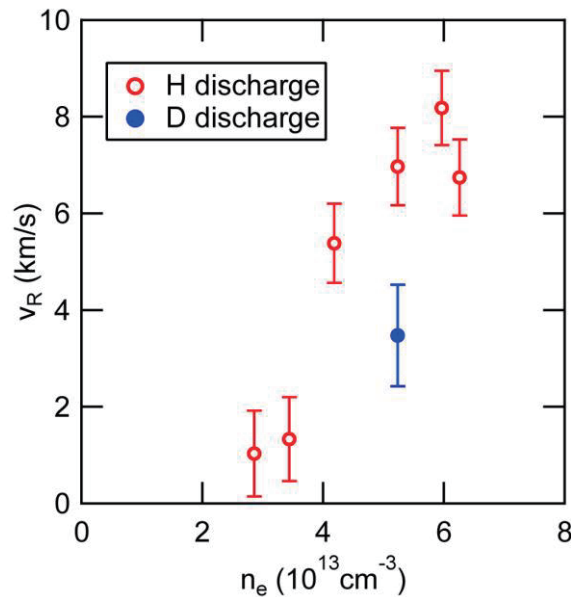
Fig. 3   Observed C^{3+} flow at the bottom edge of the ergodic layer in the H and D discharges as a function of density for inward-shifted magnetic configuration with R_{ax} = 3.6 m.

3. Summary

The parallel flow of carbon impurity in a thick stochastic magnetic field layer called "ergodic layer" located at the edge plasma of Large Helical Device (LHD) is studied by space-resolved vacuum ultraviolet (VUV) spectroscopy in a hydrogen discharge and a deuterium discharge.   The carbon flows have directions same as the friction force calculated with a three-dimensional simulation code, EMC3-EIRENE. The flow velocity is smaller in the deuterium discharge compared to that in the hydrogen discharge, which indicates existence of some isotope effect in the impurity transport.

Acknowledgements

References

[1] T. Morisaki, K. Narihara, S. Masuzaki *et al.*, J. Nucl. Mater. **313-316** (2003) 548.

[2] M. B. Chowdhuri, S. Morita, M. Kobayashi *et al.*, Phys. Plasmas **16** (2009) 062502.

[3] S. Morita, C. F. Dong, M. Kobayashi *et al.*, Nucl. Fusion **53** (2013) 093017.

[4] M. Kobayashi, S. Morita, C. F. Dong *et al.*, Nucl. Fusion **53** (2013) 033011.

[5] T. Oishi, S. Morita, C. F. Dong *et al.*, Appl. Opt. **53** (2014) 6900.

[6] T. Oishi, S. Morita, S. Y. Dai *et al.*, Nucl. Fusion **58** (2018) 016040.

Molecular simulation for the investigation of helium bubble effects on plasma irradiation to tungsten material

S. Saito[1], H. Nakamura[2,3], M. Tokitani[2], N. Ashikawa[2,4], and K. Katayama[5]

[1]National Institute of Technology, Kushiro College, Kushiro 084-0916, Hokkaido, Japan

[2]National Institute for Fusion Science, Toki 509-5292, Gifu, Japan

[3]Nagoya University, Toki 509-5292, Gifu, Japan

[4]Graduate University for Advanced Studies, Toki 509-5292, Gifu, Japan

[5]Kyushu University, Kasuga 816-8580, Fukuoka, Japan

1. Introduction

As a result of the nuclear fusion between hydrogen (H) and deuterium (D), helium (He) ashes are generated. The He ashes are transported from plasma to the diverter plates along with magnetic field lines. Therefore, the investigation of He retention in divertor plates are one of the key topics for the achievement of the steady state operation of nuclear fusion devices. Tungsten (W) materials are employed for diverter plates in many devices such as ITER. Many experiments reported that He bubbles are generated in the surface of the W materials by He plasma irradiation. Because of the morphological change of He bubble generation, the He absorption process may change dynamically. Therefore, it is important to investigate the effect of the bubble generation on the plasma-surface interaction (PSI) on the W materials.

Conventional binary collision approximation (BCA) simulation codes, for example, EDDY (erosion and deposition based on a dynamic model) [1], TRIM.SP (transport of ions in matter) [2], and ACAT (atomic collisions in an amorphous target) [3], have been applied to PSI-related studies without taking into account structural changes of target materials. When the crystalline structure destroyed by plasma irradiation, the plasma-material interaction changes. In our previous research [4-7], we extended the BCA simulation code ACAT to AC∀T (atomic collision in any structured target). The AC∀T code treats any structure of target materials, including single crystals, polycrystals, crystals with defects, and amorphous crystals, although the original ACAT code only treats amorphous structures. The AC∀T code is also extended to handle cumulative structural changes of target materials. In this study, therefore, AC∀T code is performed to investigate the dynamical change of He absorption rate by morphological change by helium bubble generation.

2. Simulation method

Figure 1 shows the schematic diagram of binary collision approximation. A projectile is injected into a target material. The projectile collides with the nearest-neighbor atom. The other interaction between the surrounding atoms and the projectile is neglected in BCA simulation. The momentum of the projectile changes upon collision; subsequently, the projectile collides with the next target atom. In the collision process of BCA, the motion of carbon atoms that collide with the projectile depends on their received

kinetic.
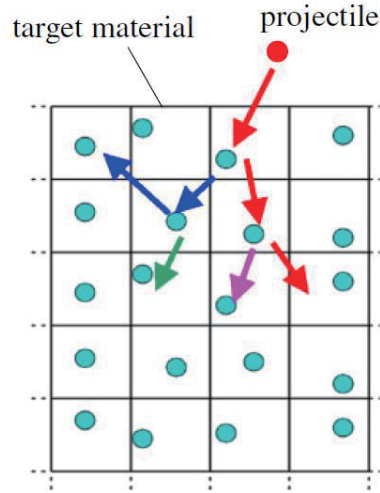
Fig. 1 Schematic diagram of binary collision approximation. [4]

energy E_t. When E_t is lower than the binding energy of the target atom E_B, the target atom does not move. On the other hand, when E_t is larger than E_B, the target atom recoils. The motions of recoil atoms are solved in the same way as that of the projectile. The scattering angles of the projectile and the target atom at each collision are obtained analytically in a two-body interatomic potential $V(r)$, where r is the distance between the projectile and the target atom. In our BCA code named ACⱯT, the Moliere approximation to the Thomas–Fermi potential is employed:

$$V(r) = \frac{Z_1 Z_2 e^2}{r} \Phi\left(\frac{r}{a}\right)$$

$$\Phi\left(\frac{r}{a}\right) = 0.35 \exp(-0.3x) + 0.55 \exp(-1.2x) + 0.10 \exp(-6.0x)$$

Where Z_1 and Z_2 are the atomic numbers of the projectile and the target atom, e is the electronic charge, and a is the screening length, which depends on Z_1 and Z_2.

Projectile and recoil atoms which stop in target material move toward their stable positions because of the interatomic force. The surrounding atoms of the projectile and the recoil atoms are also move toward their stable positions. Moreover, the surrounding atoms of lattice defect, also move toward their stable positions. To take into account this structural relaxation process of target materials, an interatomic potential $U(\{r\})$ is introduced for our simulation. Here, $\{r\}$ denotes a set of positions of all atoms in a system. The relaxed structure of target material is obtained by minimizing the potential energy $U(\{r\})$. For our simulation, the following tungsten-helium potential is employed for $U(\{r\})$:

$$U(\{r\}) = \frac{1}{2} \sum_{i,j \neq i} V_{z_1 z_2}(r_{ij}) - \sum_{i}^{w} F(\rho_i(\{r\}))$$

where $r_{ij} = |r_i - r_j|$ is the distance between the i-th and j-th atoms. The two-body potential function $V_{z_1 z_2}(r_{ij})$ is a polynomial functions based on AFS potential. The atomic number Z_i is 74 and 2 for tungsten

and helium atoms, respectively. The function $F(\rho_i(\{r\}))$ is an embedded energy. The symbol Σ^W_i indicates summation over only the tungsten atoms. For more detail of the tungsten-helium potential, please see ref. 8.

3. Simulation model

As shown in Fig. 2, a polycrystalline W material is prepared as the target material. 40,000 He atoms are injected into the target material one by one. Each grain has perfect single crystalline structure with randomly set crystalline angel. The incident energy is set to 1000 eV. The incident angle is set to parallel to the *z* axis. Incident position in *x*- and *y*-coordinates are set randomly. Periodic boundary condition is used in *x*- and *y*-directions. Relaxation procedure explained before is performed every 1000 He injection.
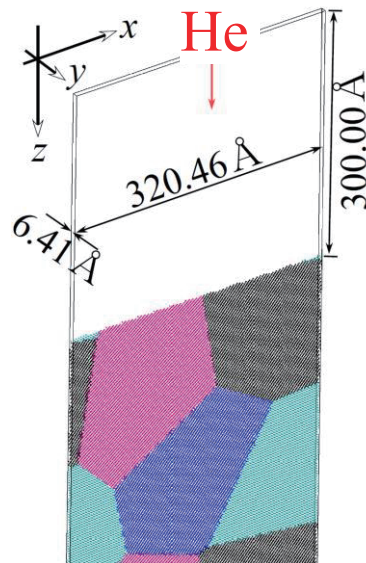
Fig. 2 Simulation model for He injection into polycrystalline W material. [9]

4. Simulation results

Figure 3 shows the time evolution of the target material. The red and black dots denote W and He atoms respectively. As injection number increases, He bubble grows near the surface of the target materials. Figure 4 shows the time evolution of the He absorption rate. The absorption rate decreases first, then, it turns to increase. The first decrease is caused by the morphological change from crystalline to amorphous structure by He irradiation. Because the channeling pass disappears as randomness of the surface structure increases, the probability of the reflection of incident He atoms increases. Therefore, the absorption rate approaches to the value of amorphous case. However, the absorption rate turns increase. This increase is caused by the helium bubble generation in the target material. Incident helium atoms lose their maximum kinetic energy when they collide with a He atom which has the same mass. Therefore, absorption rate increases as bubble grows because the incident helium atoms easily stop in He bubbles.
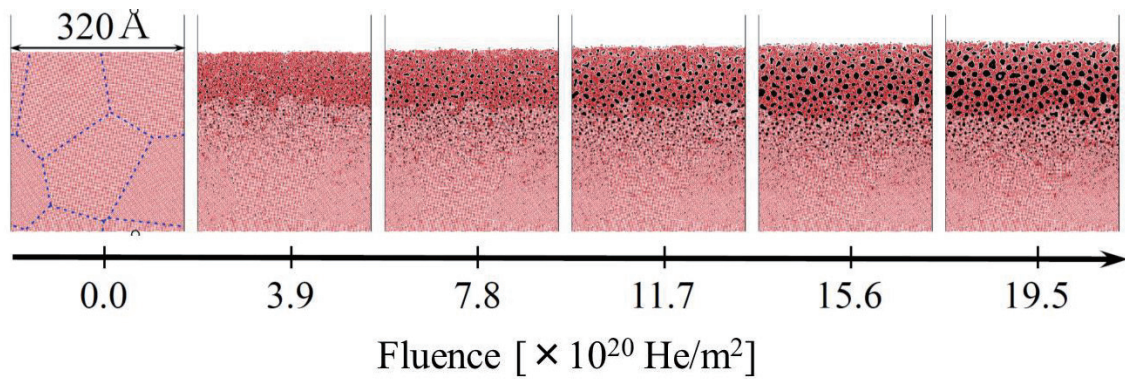
Fig. 3 Time evolution of the target material. [9]
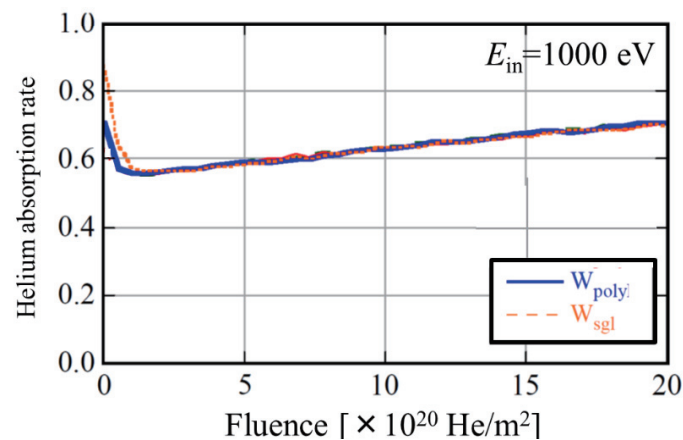
Fig. 4 Time evolution of the He absorption rate. W_{poly} and Wsgl are the results for the case where the target material has polycrystalline and single crystalline structure, respectively. [9]

5. Summary

BCA calculation of He injection into W is performed for the investigation of the dynamical change of the absorption rate. The absorption rate decreases first because of the morphological change from crystalline to amorphous structure. However, the rate turns to increase because of the growth of helium bubbles.

References

[1] K. Ohya and R. Kawakami, Jpn. J. Appl. Phys. 40 (2001) 5424.

[2] J. P. Biersack and W. Eckstein, Appl. Phys. A 34 (1984) 73.

[3] Y. Yamamura and Y. Mizuno, IPPJ-AM-40, Institute of Plasma Physics, Nagoya University (1985).

[4] S. Saito, A. Takayama, A. M. Ito, and H. Nakamura: Proc. Int. Conf. Modeling and Simulation Technology, 2011, p. 197.

[5] S. Saito, *et al.*, Jpn. J. Appl. Phys. 52 (2013) 01AL02.

[6] S. Saito, *et al.*, J. Nucl. Mater. 438 (2013) S895-S898.

[7] S. Saito, *et. al.*, Jpn. J. Appl. Phys. 55 (2015) 01AH07.

[8] A. M. Ito, *et. al.*, Phys. Scr. T159 (2014) 014062.

[9] S. Saito, *et al.*, Jpn. J. Appl. Phys. 57, (2017) 01AB06.

Simulation Analysis of Impurity Transport Induced by Dust Emission in the Ergodic Magnetic Field Line Structures in the Large Helical Device

M.Shoji[1], G.Kawamura[1], R.Smirnov[2], A.Pigarov[2], Y.Tanaka[3], S.Masuzaki[1], Y.Uesugi[3] and the LHD Experiment Group[1]

[1]National Institute for Fusion Science, Toki 509-5292, Gifu, Japan

[2]University of California at San Diego, La Jolla 92093, CA, USA

[3]Kanazawa University, Kakuma 920-1192, Kanazawa, Japan

Abstract

The dust shielding effect by intrinsic ergodic magnetic field line structures (ergodic layer) formed around the main plasma confinement region is investigated using a three-dimensional peripheral plasma fluid code (EMC3-EIRENE) coupled with a dust transport simulation code (DUSTT). Simulations performed in three different magnetic configurations having narrow, medium, and wide ergodic layers show that the wide ergodic layer is not always effective for shielding the main plasma from the dust emission. Optimum operational regimes for controlling the influence of the dust emission on the sustainment of plasma discharges are found by investigating the impurity ion content in the peripheral plasma in various plasma heating powers and plasma densities in the three magnetic configurations.

1. Introduction

While some recent long pulse discharges in LHD were terminated by carbon dust emission from the divertor region, which were caused by the exfoliation of carbon-rich mixed material deposition layers accumulated near the divertor plates (isotropic graphite) [1-3], some long pulse discharges were interrupted by the iron dust emission from the surface on helical coil cans (stainless steel) just after the appearance of sparks (arcing). An observation with a stereoscopic fast framing camera revealed that iron dust released from the arcing point penetrated into the main plasma confinement region to cause the radiation collapse [4]. An impurity transport simulation by a fully three-dimensional peripheral plasma fluid code (EMC3-EIRENE) [5] coupled with a dust transport simulation code (DUSTT) [6-8] shows that the plasma discharges are interrupted by much lower amounts of iron dust emission from the helical coil can compared to that of carbon dust emission from the divertor region [9]. The simulation proves that the effect of the strong plasma flow in the divertor legs prevents the carbon dust from penetrating into the main plasma. On the other hand, the iron dust launched from the helical coil can directly reaches the peripheral plasma (the ergodic layer) without the intersection of the divertor legs. It is likely that the iron dust emission will be a serious obstacle for sustaining long pulse discharges in LHD.

The peripheral plasma formed around the Last Closed Flux Surface (LCFS) in the ergodic layer can effectively prevent the iron dust from penetrating into the main plasma by evaporating the dust due to the plasma heat load on the dust. The configuration of the ergodic layer is controlled by changing the helical

and poloidal coil currents, accompanying the shift of the radial position of the magnetic axis R_{ax}. The inward, medium, and outward magnetic axis shift configurations (R_{ax}=3.60, 3.75, and 3.90 m) have narrow, medium, and wide ergodic layers, respectively. The wide ergodic layer appears to be effective for controlling the influence of the iron dust on the main plasma. In order to investigate the dust shielding effects, impurity transport simulation was performed using the EMC3-EIRENE and DUSTT.

2. Setup of impurity transport simulation in the LHD peripheral plasma

A three-dimensional model for the impurity transport simulation is shown in Figure 1. The model includes the peripheral plasma (ergodic layer), the divertor legs, the vacuum vessel, the helical coil cans, and the divertor components for one-half of the helical coil pitch angle (18° in toroidal direction) [10]. The surface temperature of the vacuum vessel and the divertor components are set to 300 K and 500 K, respectively. The iron dust source locates on the surface of a helical coil can in the inboard side of the torus which was identified by the observation with the stereoscopic fast framing camera [4]. The poloidal cross-section of a typical plasma density profile in the peripheral plasma at the toroidal angle where the iron dust source exists (a toroidal angle ϕ=10.625°) is also presented. A number of test particles (two million at the maximum), which are representatives of iron dust, are launched from the iron dust source. An enlarged image of the iron dust trajectories is presented in the right figure, showing that most of the iron dust directly reaches the peripheral plasma. The initial dust velocity released from the dust source is set to be 5 m/s which is estimated by the observations with stereoscopic fast framing cameras. The angle of an initial direction of dust emission is randomly chosen from a cosine distribution biased to the direction to the plasma center. The size of a dust (radius) is selected from a Junge distribution in the range from 1 μm to 0.1 mm. The trajectories of the iron dust released from the dust source are traced by the DUSTT. In this code, it is assumed that the shape of the dust is spherical and that the dust consists of a single element. Thus, iron was adopted as the representative element for stainless steel in which the dominant constituent element is
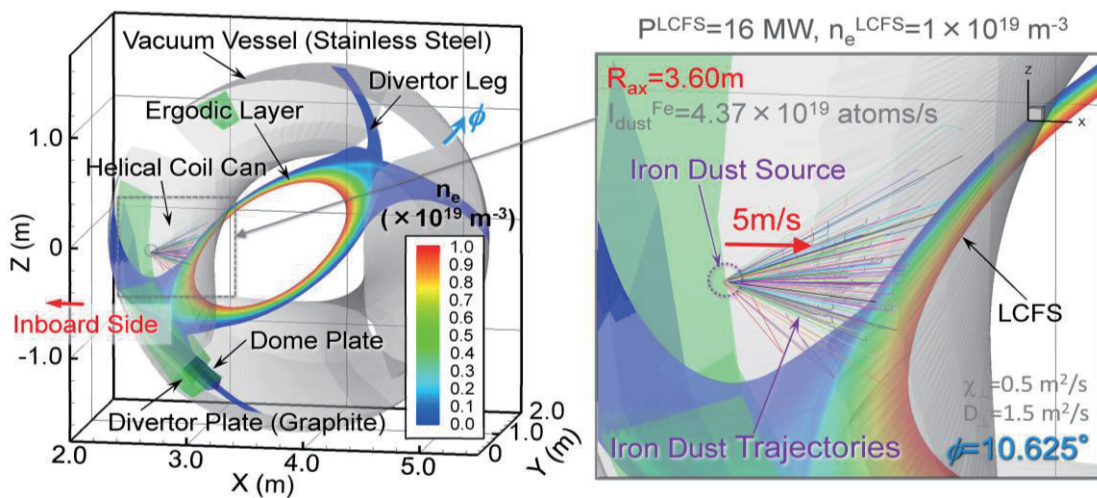

Fig.1 A three-dimensional model for impurity transport simulation using the EMC3-EIRENE coupled with the DUSTT. The plasma density profile at the toroidal angle where the iron dust source exists is also shown.

production, and impurity production by sputtering on the surface of the vacuum vessel and the divertor plates is not included for the simple calculation. Steady state background plasma parameter profiles for the DUSTT code are provided by the EMC3-EIRENE in which the perpendicular particle and the thermal diffusion coefficients are assumed to be 0.5 and 1.5 m^2/s, respectively. These are typical values in the LHD peripheral plasma obtained by fitting simulations to measurements of the electron density and the temperature profile. The EMC3-EIRENE calculates the density profile of the impurity (iron) ions by solving the continuity and the momentum balance equations of the impurity ions for each ionization stage along magnetic field lines. A converged solution of plasma parameter profiles such as the plasma density and temperature, the plasma flow velocity, the radiation power, and the impurity ion density are obtained by an iterative calculation scheme between the two simulation codes [9]. The input parameters for the simulation are the plasma heating power and the plasma density at the LCFS (P^{LCFS} and n_e^{LCFS}).

3. Investigation of optimum operational regimes for controlling the impurity ion content

Finding the optimum operational regimes for controlling the influence of the iron dust emission on the peripheral plasma is essential for sustaining long pulse discharges in LHD. The total iron ion content $Q^{Fe\ ion}$ in the peripheral plasma (including the ergodic layer and the divertor legs) is adopted as an indicator of the iron dust shielding effect. The total iron ion content in the three magnetic configurations was investigated in various plasma heating powers and the plasma densities at the LCFS (P^{LCFS} and n_e^{LCFS}). The total iron ion content is scanned in the ranges of the plasma heating power and the plasma density ($1\ MW \leq P^{LCFS} \leq 16$ MW and $1\times10^{19}\ m^{-3} \leq n_e^{LCFS} \leq 8\times10^{19}\ m^{-3}$). The parameter $Q^{Fe\ ion}$ is calculated by summing the value $n_{i,j,k}^{Fe\ ion} \times V_{i,j,k}$ in the model for the simulation. Here, $n_{i,j,k}^{Fe\ ion}$ and $V_{i,j,k}$ are the sum of iron ion densities with all ionization stages and the grid cell volume at the position assigned by the radial, poloidal, and toroidal index numbers i, j, and k in the model, respectively. Figure 2(a), (b), and (c) depict the two-dimensional contour plots of the total iron ion content in the peripheral plasma in the three magnetic configurations. Areas painted over in white indicate the parameter ranges where a converged solution is not obtained. In this case, the electron temperature significantly drops and the radiation power induced by iron ions drastically increases. This situation indicates that the plasma is not stably sustained because of the insufficient plasma heating power induced by radiation cooling due to the iron dust.

The figure indicates that the parameter condition for the optimum operational regimes is quite different in between R_{ax}=3.60 and 3.90 m. In the inward magnetic axis shift configuration (R_{ax}=3.60 m), there are two choices for favorable plasma discharges with reduced iron ion content. Plasma discharge operation with high plasma heating powers ($P^{LCFS} \geq 12$ MW) and a quite low plasma density (n_e^{LCFS}=1×10^{19} m^{-3}) (indicated as "A" in figure 2(a)) gives a low iron ion content, and operation with the high plasma heating powers and high plasma densities (n_e^{LCFS}>6×10^{19} m^{-3}) (as "B") is also desirable. On the other hand, in the outward magnetic axis shift configuration (R_{ax}=3.90 m), operation with the high plasma heating powers and the low plasma density (shown as "C" in figure 2(c)) brings catastrophic increase in the iron ion content, which is not appropriate for stable steady-state plasma discharges. Operation with the high plasma heating powers and relatively higher plasma densities (n_e^{LCFS}>6×10^{19} m^{-3}) (as "D") is effective for diminishing the impurity ion content. The simulation for R_{ax}=3.75 m presents an intermediate trend

between those for R_{ax}=3.60 and 3.90 m. In this magnetic configuration (R_{ax}=3.75 m), favorable operational conditions for shielding the dust are those with the high plasma heating powers and higher plasma densities (as "E" in figure 2(b)).
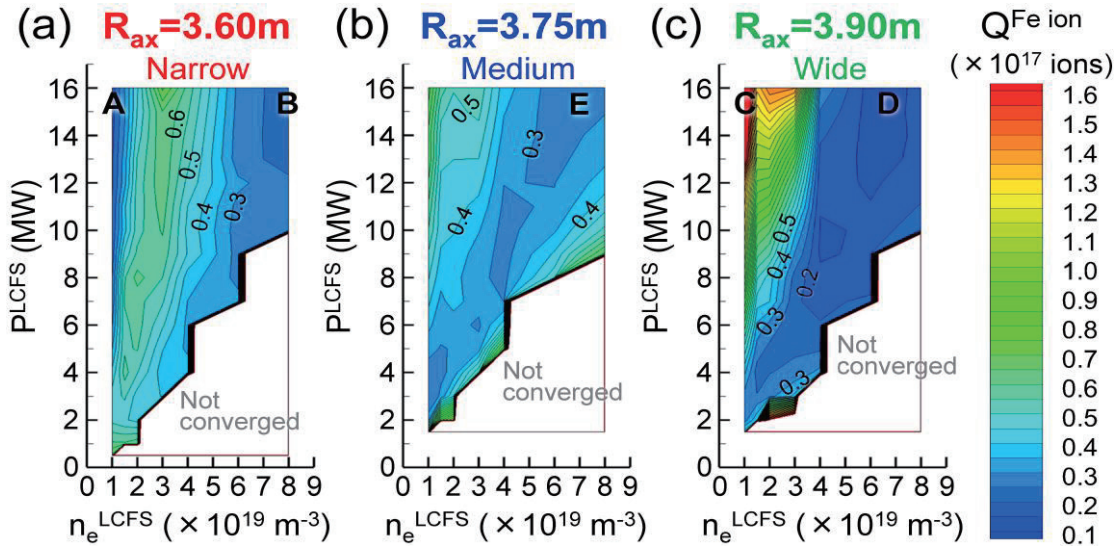
Fig.2 Contour plots of the total iron ion content in the three magnetic configurations (R_{ax}=3.60, 3.75, and 3.90 m) in the two-dimensional ranges of the plasma density (n_e^{LCFS}) and the plasma heating powers

References

[1]   M. Shoji et al., Nucl. Fusion **55**, 053014 (2015).

[2]   Y. Yoshimura et al., Nucl. Fusion **56**, 046005 (2016).

[3]   M. Tokitani et al., J. Nucl. Mater. **463**, 91 (2015).

[4]   M. Shoji et al., Plasma and Fusion Res. **11**, 2402056 (2016).

[5]   Y. Feng et al., Plasma Phys. Control. Fusion **44**, 611 (2001).

[6]   A. Yu Pigarov et al., J. Nucl. Mater. **363-365**, 216 (2007).

[7]   R. D. Smirnov et al., Plasma Phys. Control Fusion **49**, 347 (2007).

[8]   Y. Tanaka et al., J. Nucl. Mater. **415**, S1106 (2011).

[9]   M. Shoji et al., Nuclear Materials and Energy **12**, 779-785 (2017).

[10] G. Kawamura et al., Contrib. Plasma Phys. **54**, 437 (2014).

Development of wall conditioning, plasma fueling and ELM control in EAST in the last few years

J.S. Hu[1,2,*], J.L. Hou[1,3], X.L. Yuan[1,3], Y.W. Yu[1], Z. Sun[1], J.H. Wu[1], W. Xu[1,3] and EAST vacuum group

[1]Institue of Plasma Physics, Chinese Academy of Sciences, Hefei, 230031, China

[2]CAS key Laboratory of Photovoltaic and energy conservation materials, Hefei, 230031, China

[3]University of Science and Technology of China, Hefei, 230026, China

Abstract

Corresponding of upgrading of plasma facing components of EAST, especially installation of an ITER-like W divertor, wall conditioning, plasma fueling and ELM control are need to be improved for the achievement of high-power, long-pulse H-modes. Recently, besides of baking, glow discharge cleaning and ion cyclotron radio frequency cleaning, lithium coating is routinely used for the recycling and impurities control instead of boronization and siliconization. At the same time, supersonic molecular beam injection has replaced gas puffing for plasma density feedback control. And a new steady-state operated 10Hz pellet injector system has been developed for core plasma fueling. Moreover, a few new edge local mode control systems, including 50Hz pellet injection, SMBI, Li granules dropper and Li pellet injection, have been successfully developed. This paper gives a brief introduction of the development of those systems and its application in EAST for high performance plasmas.

1. Introduction

The Experimental Advanced Superconducting Tokamak (EAST) is a non-circular, fully superconducting, steady-state experimental device with ITER-like configuration. The mission of EAST is to establish a scientific and technological foundation for next generation tokamak devices. The goals of EAST include conducting of long pulse, high performance H-mode discharges heated mainly by radio frequency (RF) heating and deploying high-Z plasma-facing components (PFCs) prototypical of reactors, e.g. the use of ITER W mono-block technology. The machine has major radius R=1.85m, minor radius r < 0.45m, with an eventual goal of 1000 sec long pulse length. The move toward high-Z PFCs is occurring in a staged implementation; the device used all graphite PFCs until 2012; then the central column tiles were changed to Mo, and recently the upper divertor tiles were replaced with W mono-block. To achieve long pulse recycling and impurity control, besides of baking, glow discharge cleaning and ICRF cleaning, Li wall conditioning instead of boronization and siliconization is deployed, via a combination of overnight evaporation and periodic use of real time Li aerosol or granule injection. At the same time, supersonic molecular beam injection(SMBI) has replaced gas puffing for plasma density feedback control. And a new steady-state operated 10Hz pellet injector system has been developed for core plasma fueling. Moreover, edge local mode control systems, including 50Hz pellet injection, SMBI, Li aerosol dropper and Li

granules injection, have been successfully developed. This paper gives a brief introduction of the development of those systems and its application in EAST for high performance plasmas.

2. Wall conditioning

2.1 Wall cleaning (Baking, GDC, ICRF)

Wall cleaning, such as baking, plasmas discharge cleaning using GDC or ICRF, has been employed since the beginning of EAST operation in 2006, and served as basic methods for impurities removal and recycling control [1-3]. Baking by using hot N2 flowing in heating tubes inside heat sinks could supply 400 ℃ hot N2 with a pressure of 6 kg/cm^2. Longer baking using a temperature of first wall at ~ 200 ℃ is normally used before plasma operation. Glow Discharge Cleaning (GDC) normally using in EAST without toroidal magnetic field whereas Ion Cyclotron Radio Frequency (ICRF) discharge cleaning used in the present of magnetic field. Four anodes with independent power supply are employed for GDC. Recently, by upgrading power supply and anode structure, we increase the plasma current up to 6 A of each GDC anode (3A in EAST is enough in most cases) to increase its removal efficiency, as the fig.1 (left) shown. To develop the ICRF discharge cleaning is quite important to enhance its utilization in superconducting tokamak, such as ITER. Two dedicated antennas, which was installed since 2006, are used during ICRF discharge cleaning with a working power of 10-20kW. In the last two years, to increase the flexibility, a new ICRF power generator was employed to replace the old generator which was used for auxiliary plasma heating in HT-7, as the fig.1 (right) shown. The new ICRF power generator could work in frequency of 27.12 or 41.68 MHz, and the maximum output power is 50 kW, both the output power and duty cycle of ICRF waves could be flexibly controlled for discharge cleaning. A remote-control system also has been developed, which reduced man power to carry out the ICRF cleaning. Before plasma operation, well organized long pre-wall conditioning using baking and GDC cleaning by turn of He and D2, the base vacuum of EAST plasma vessel could reach 2-3×10^{-6} Pa, which make it easy to build the first plasma in each running campaign. During plasma operation, ICRF discharge cleaning could be easily used at the interval of plasma discharges to remove hydrogen isotopies retained on walls to reduced edge recycling.
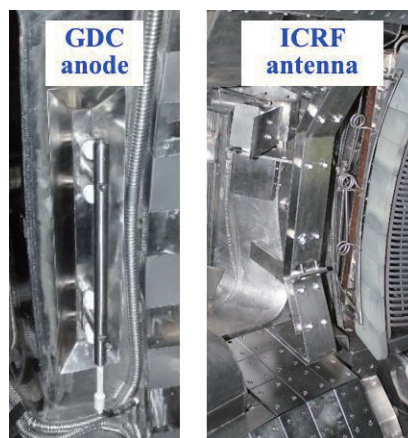
Fig. 1 GDC anode (left) and ICRF belt antenna (right) in EAST tokamak

2.2 Wall coating (Li coating)

The first Li coating had been carried out since 2009 [4]. Recently, Li evaporation coating systems were developed to improve the coating coverage and uniformity, especially increased the coverage on the divertor region [5]. A dedicated bidirectional Li oven, which can simultaneously both upward and downward evaporation to the top tungsten divertor and bottom carbon divertor, as shown in Fig.2. In addition, to increase the Li coating distribution and total coverage, we increase the coating system using three ovens well positioned in toroidally-symmetric manner. Meanwhile, the movable systems were designed to insert ovens to near center of the plasma vessel to increase the line-of-sight coating area on the vacuum chamber walls. With the development of Li coating system, the Li coverage was gradually increased to ~90% of full inertial area coverage in 2014 campaign, compared to ~35% in 2010 and ~85 in 2012, as shown in Fig. 3. The top tungsten divertor and bottom carbon divertor were both effectively covered. In most cases, Li coating was carried out by coupling Li evaporation into ICRF wave-assisted plasma discharges, which improved Li coat uniformity and lifetime. Those upgrading made Li coating became as a most effective method to reduce impurities, recycling and also the ratio of H/(H+D), compared to cleaning, boronization and siliconization. With accumulation of Li coating with 10-45g Li in each morning, impurities, recycling and also the ratio of H/(H+D) in plasma are continually reduced, typically the suppression of tungsten impurity (as shown in Fig. 3.), which make a great contribution on the new achievement of 101.2s record long H-mode plasma in 2017.
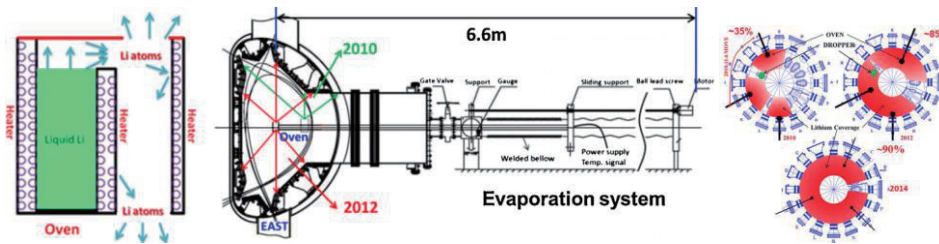
Fig. 2. Schematic diagram and coating coverage of the upgraded Li evaporation system on EAST
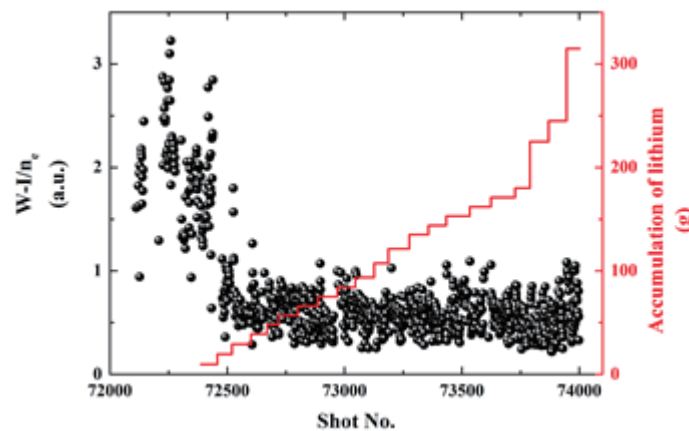
Fig. 3 Tungsten impurity in plasmas with accumulation of Li coating in each morning during EAST operation (New achievement of 101.2s long pulse H mode at shot No. 73999)

To facilitate long-pule operation on EAST, beside of Li coating, a real-time injection of fine Li aerosol ("Li dropper") was successfully developed [6]. Using a Li dropper, real-time Li aerosol injection during plasma operation on walls pre-coated with Li between discharges is expected to repair and replenish the initial Li coating. Using a resonating piezoelectric disk with a central aperture, the dropper injects an evaporating Li aerosol (droplet diameter ~ 45 μm) into the plasma scrape-off layer (SOL) by simply dropping spherical Li granules in a controlled manner. Li aerosol can be reproducibly injected in EAST through the upper divertor gap in H-mode discharges with an adjustable flow rate of 30~60 mg/s. The location of the aerosol injector with the downward trajectory of injected Li particles and the sequence of true color images of Li evaporating, ionizing and being transported are shown in the Fig. 4. The velocity of the aerosol was about 9m/s, driven by gravity when contacting the SOL plasma. During the active Li wall conditioning, Li aerosol quickly ionized in the plasma edge and formed a layer of Li^{+1} ions which seemed to provide radiative heat exhaust. Real-time Li aerosol injection effectively reduced the tungsten impurity both at edge and core plasma in L-mode discharges. In long pulse H-mode discharges, the tungsten and molybdenum impurity content in plasma core decreased by half with real-time Li aerosol injection, as shown in Fig. 4. And the core radiation reduced obviously due to lower high Z impurity content. This reduction of impurity after Li injection mainly was due to the reduced plasma-wall interaction.
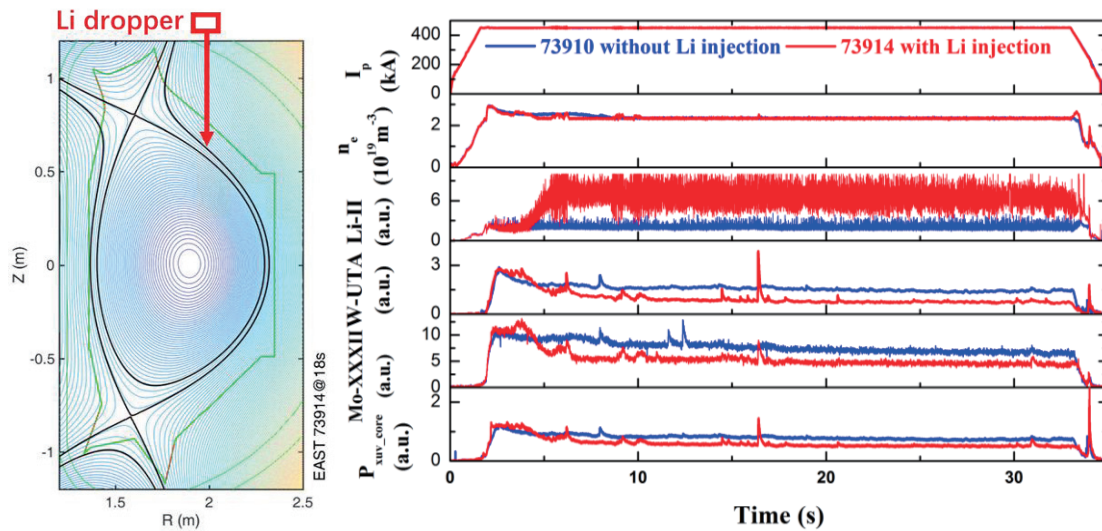
Fig. 4. Comparison of two long pulse H-mode discharges with (red trace) and without (blue trace) real-time Li aerosol injection (upper signal configuration, Paux=3MW)

3. Plasma fueling

3.1 Gas puffing system

The gas puffing system on EAST is used for not only plasma fueling, but also to provide gas for wall condition and impurity gases, such as Ar, Ne, for physics research, such as diagnostic, heat load control and disruption mitigation [7]. With the increase of requirement, the system was expanded to increase its functions, i.e. gas injections near low hybrid wave (LHW) antennas and Ion Cyclotron Resonance

Frequency (ICRF) antennas to improve the power coupling, as shown in Fig. 5. Recently, a feedback control system was developed to automatically fill the gas supply tanks to a stable pressure in the range for precise measurement (1.4–1.7 ATM), which was achieved by feedback controlled electropneumatic valve. Now, the system includes 8 ports at top and bottom divertors (at outer target, inner target and dome) for radiation/detachment divertor experiments. It also includes 11 ports are located at mid-plane at low field side (2 for plasma fueling, 3 for wall conditioning, 1 used to inject argon for diagnostic, 2 located near LHW antennas, 3 located near ICRF antennas) and 1 ports located at high field side. Electromagnetism valves with a maximum flow rate of 125 Pa·m^3/s are used for wall conditioning and piezoelectric valves with a maximum flow rate of 0.83 Pa·m^3/s are used for plasma filling and other applications. To reduce the response time of gas injection, the valves of the gas injection ports was moved into the window ports near divertor. This upgrading is quite successful to reduce the response time from ~80ms to 20ms.
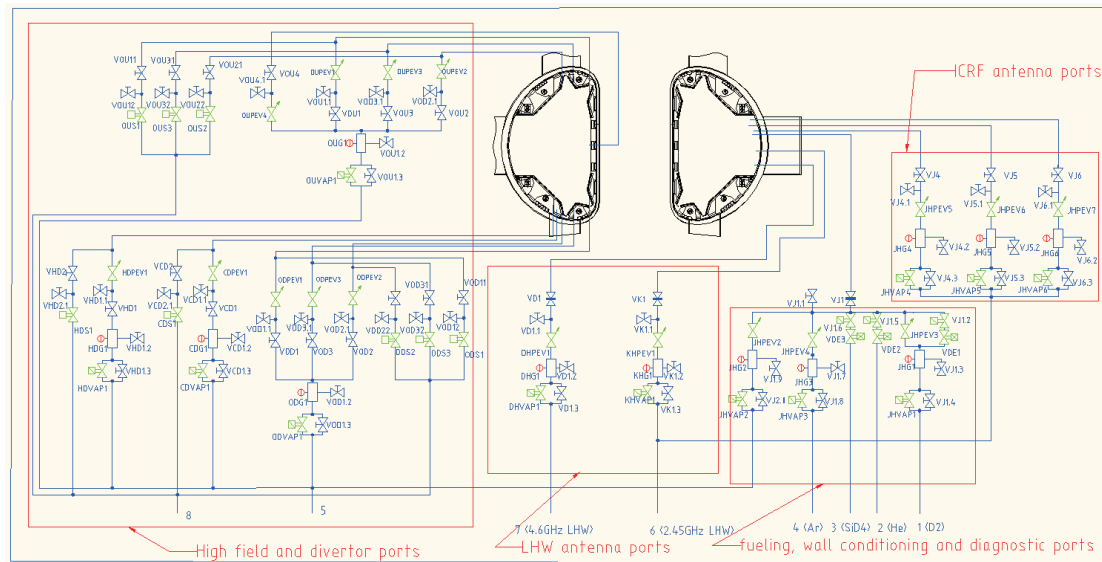
Fig. 5 Gas puffing system of EAST

3.2 Supersonic molecule beam injection

To provide an advanced fueling system with a high fueling efficiency, deep particle deposition and fast response-time, three sets of SMBIs has been developed in the past few years, respectively for good plasma density control, ELM mitigation, and also impurity gas injection for radiation divertor research. The SMBI is designed to produce 400-1200 m/s molecular beam of hydrogen/deuterium, which is derived by a high-pressure source and though a dedicated Laval nozzle. The pulse of the beam injection is adjustable with a maximum frequency of 250 Hz. Its plasma response time is less than 5ms. To reduce the electromagnetic interference from the EAST during the discharge process, a shield is installed outside the nozzle. With a cryogenic cooling system is embedded in the shield, The SMBI could inject gas both in room temperature and low temperature at -80 ℃. Experimental results show that it has a fueling efficiency, higher than that of gas puffing by a factor of about 2. Compared gas puffing, SMBI have been testified as a better control system to feedback control plasma density [8]. Recently, a scalable structure was implemented in the design of the SMBI to adjust the distance between the nozzle and the EAST device, as

shown in Fig. 6. The aforementioned scalable structure uses screws with bellows to regulate the distance between the nozzle and the EAST. Specifically, the nozzle can be adjusted towards the EAST by 0.5 m and 0.25 m via the scalable structures, respectively. This could reduce the long path, about 2m, of gas beam after injected from the Laval nozzle. New experiments show that the nearer the nozzle to plasma, the higher fueling efficiency could be obtained, as shown in Fig. 7 [9].
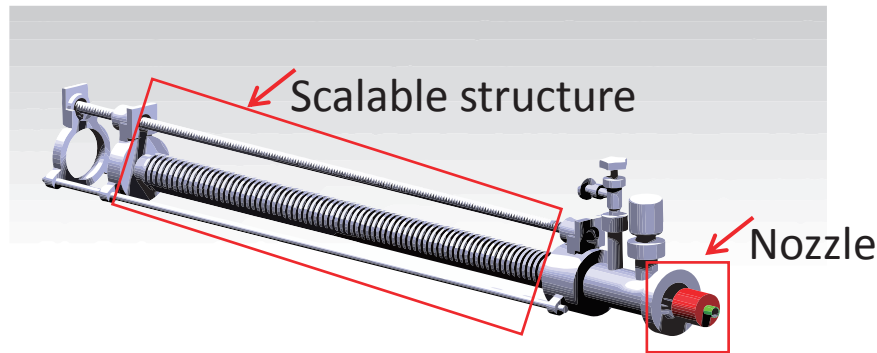
Fig. 6 Scalable structure of SMBI
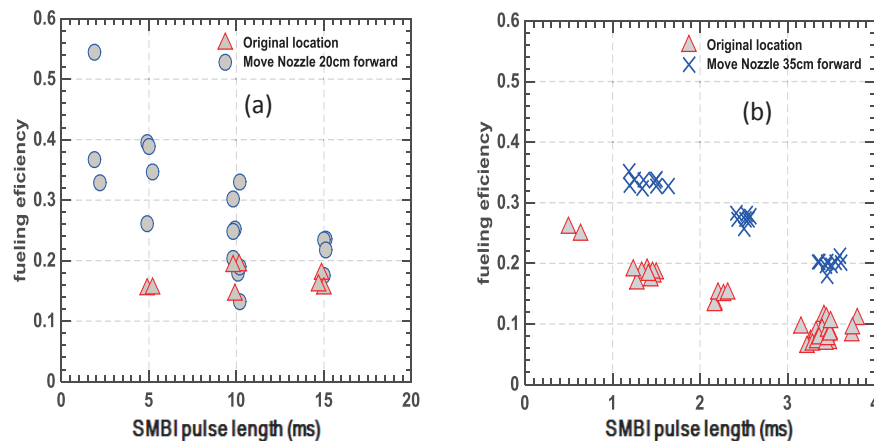
Fig. 7 Comparison of fueling efficiency between original location and moved position of the Laval nozzle to plasma (a) 20cm; (b) 35cm

3.3 10Hz pellet injection

Fuel pellet injection is developed for core plasma fueling to achieve high density plasma due to it has a highest fueling efficiency compared to other present fueling techniques. To meet the scientific goals of the EAST is to achieve high performance plasmas with discharge duration up to 1000 s. A new steady-state operated 10Hz pellet injector system has been developed for mainly plasma fueling, as shown in Fig. 8 [10]. The pellet injector based on a screw extruder is able to fire pellets in steady state mode with reliability

greater than 95%. With both the length and diameter of 2 mm and nominal atoms of 3.78×10^{20}, a cylinder-shaped deuterium pellet could be fabricated at a frequency of 10Hz by this injector for more than 1000 s. The pellets can be injected from the low field side (LFS) or high field side (HFS) of EAST with the velocity of $150 - 300$ m s^{-1}. After successful engineering commissioning, the injection system served at EAST 2012 campaign and some new experimental results were obtained. Results show that pellet could injected to the center of plasma with a highest fueling efficiency that gas puffing and SMBI. And it is found that pellet injected from HFS leads to a double density increment than that from LFS injection [11]. Recently, using this system, snake perturbation [12] and various L-H transition [13] have been successfully induced on EAST, as shown in Fig. 9. Those experiments are beneficially for the understand of MHD behavior in plasmas, and the physics behind of L-H transition.
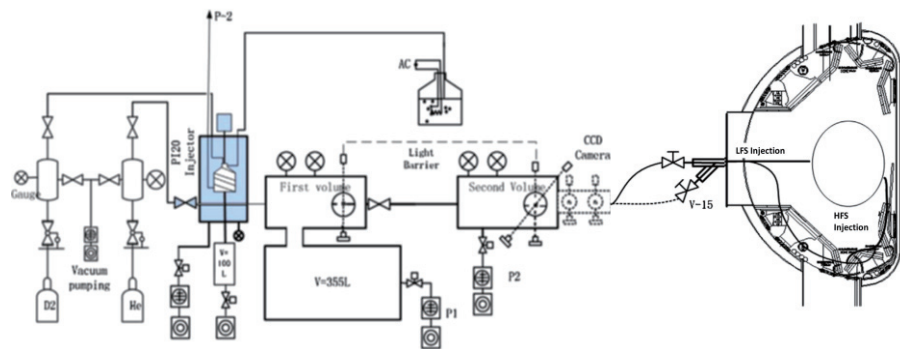
Fig. 8 The schematic drawing of 10 Hz pellet injector on EAST
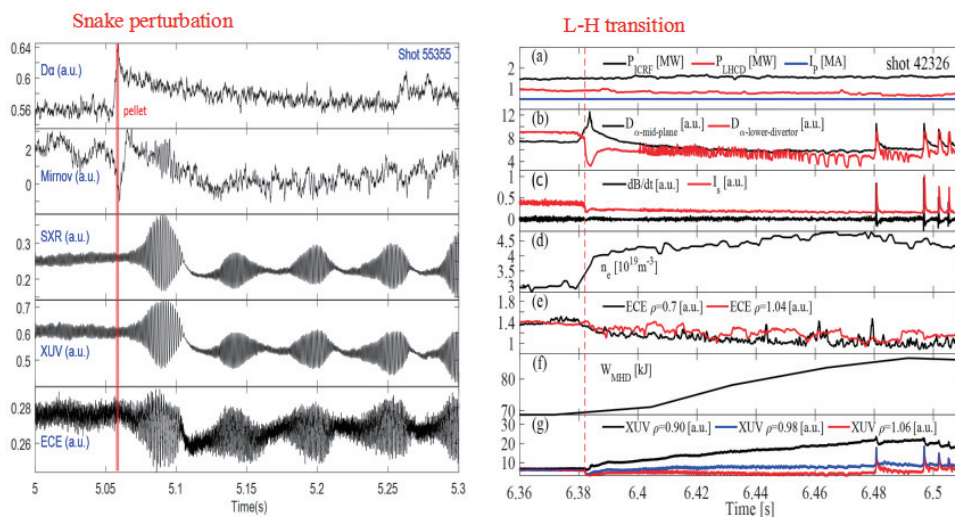
Fig. 9 Temporal evolution of characteristic signals recorded of snake perturbation and L-H transition after pellet injection

4. ELM control

4.1 Li aerosol injection for ELM suppression

In the past few years, Li aerosol injection is not only used for real-time wall conditioning but also confirmed as an effective method for ELM elimination or suppression in EAST in the first time. ELM suppression by real-time Li aerosol injection was firstly demonstrated in EAST with lower and upper graphite divertors in 2012, observing that an edge coherent magnetohydrodynamic (MHD) mode was observed to contribute for the continuous heat and particle flux exhaust [6]. The injection facilitates H-mode maintenance and enables the plasma to rapidly enter the ELM-free H-mode regime with the ELM-free period greatly exceeding the energy confinement time. Repeatable long-pulse H-mode with a record ELM-free period lasting ~18 s, about 450 times the energy confinement time, as well as impurity accumulation was prevented, were obtained. New founding shows that Li aerosol injection promotes the growth of an Edge Coherent Mode (ECM), which provides continuously heat and particle exhaust, thus preventing impurity accumulation and facilitating steady-state H-mode operation with a long ELM-free period.

Recently, a similar experiment was carried out in EAST in single null configuration using upper tungsten divertor. It was found the injection of Li aerosol could be using for ELM suppression to get long ELM-free discharges via reduced tungsten impurity accumulation using tungsten divertor, as shown in Fig. 10. Hence there is substantial interest in extending the early EAST results, both to discharges that use W PFCs, to see if a conditioning effect becomes more obvious, and also to higher confinement discharges. Moreover, these discharges exhibited good energy confinement, with confinement H_{98} factor>1, and there is clear evidence of a cumulative wall conditioning effect. The overall confinement factor H_{98} remained at ~ 1.2, which was about 50% higher than the $H_{98} \sim 0.75$ obtained during ELM elimination with Li aerosol injection into the carbon divertor in the previous ELM elimination experiments. A cumulative wall conditioning effect of the Li aerosol injection was observed by comparing the baseline of Dα of sequence discharges, as documented with the previous Li aerosol injection and Li coating experiments in EAST.
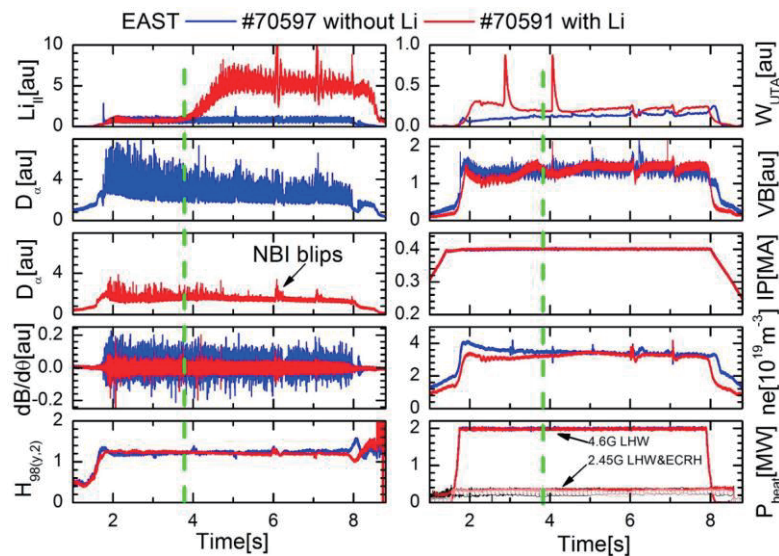
Fig. 10 Time traces comparing reference (#70597-blue) ELMy H-mode and one with Li aerosol

4.2 Li granules injection for ELM trigger

A new method using a multi-chamber Li granule injector (LGI) for ELM triggering experiments has been developed in EAST. First experimental results of ELM control by LGI were confirmed in EAST with a carbon divertor [14, 15], as shown in the Fig. 11. The improved apparatus employed in recent experiments is capable of injecting four different sizes of spherical granules which cover the range of ~0.2–1 mm. Available velocities range from ~30 to 110 m/s and granule injection frequencies can range from single granule injection to frequencies approaching 800 Hz for the smallest size granules (0.2–0.4 mm). It is found that the LGI has good capacities, i.e., allowing good flexibilities in granule size selection, injection rate, and injection velocity. In the recent experiments, LGI was used for ELM triggering and pacing in EAST with Tungsten divetor [16]. ELM trigger efficiency is nearly 100% with an upper single-null configuration if granules size larger than 0.6mm (an average velocity of Vg ≈ 75 m/s with an average injection rate of 99 Hz), as shown in Fig. 12 and Fig. 13.
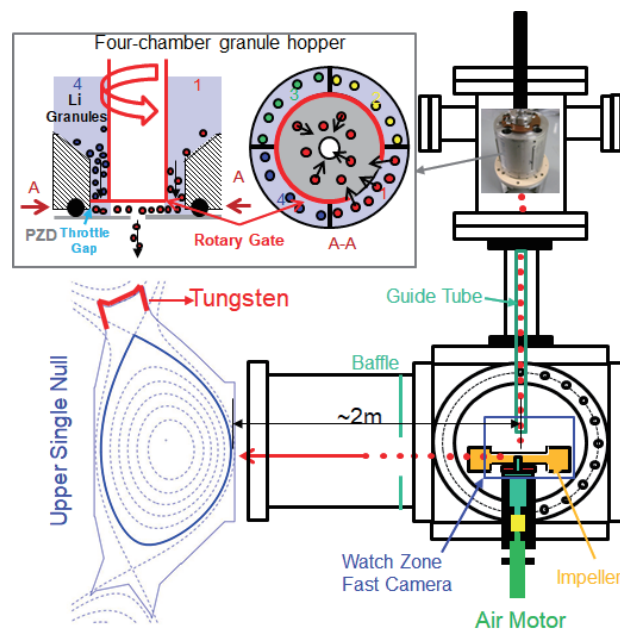
Fig. 11 The schematic representation of Li Granule Injector
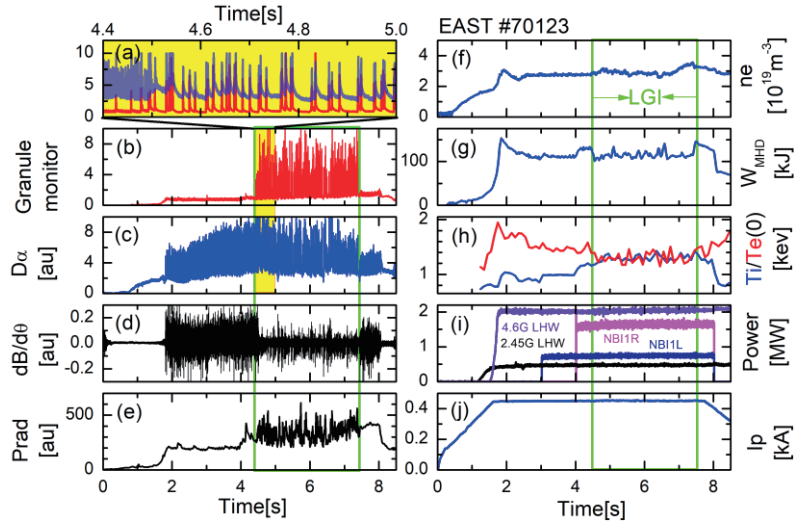
Fig. 12 Typical shot of ELM-pacing by Li granule injection during 4.4-7.4s.
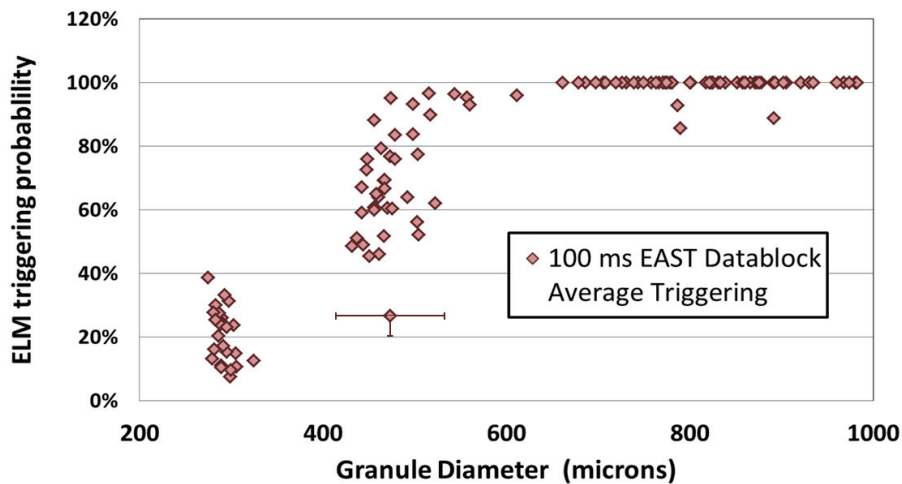
Fig. 13 ELM triggering probability for different granule sizes

4.3 Supersonic molecule beam injection for ELM control

Beside of plasma fueling, SMBI also used for ELM trigger and suppression. Using the Laval nozzle, ELM mitigation with single and multi-pulses of SMBI has been demonstrated earlier in EAST [17]. The experiments show that the ELM mitigation effect was observed to be increased with SMBI pulse length of individual SMBI injections. It was observed that a single 16 ms pulse of SMBI could affect ELMs for a time (130 ms) much longer than the injection pulse length, as shown in Fig. 14. After the SMBI injection, the energy and the density kept rising, which indicted plasma stays in H-mode and the confinement time both for energy and particles increased. Further, using multi-pulse injection with pulse lengths of 8ms, the influence time for ELMs mitigation reached as high as 500 ms. Compared to plasmas without SMBI

injection, ELMs were suppressed and its frequency increased by a factor of 2. Further, a quasi-steady scenario with ELM mitigation exceeding 3s was achieved with continuous periodic SMBI. The degradation of energy confinement with SMBI injection is less than 10%, which is similar as ELM induced degradation. At the same time, a distinctly striated heat flux (SHF) measured by IR camera, induced by SMBI with multi-pulses, appeared at ~13cm poloidally outboard of the outer strike point (OSP), as shown in Fig. 15. Raising the individual SMBI pulse lengths clearly tended to increase the peak heat flux at the SHF region while simultaneously lowering the peak heat flux at the OSP region.
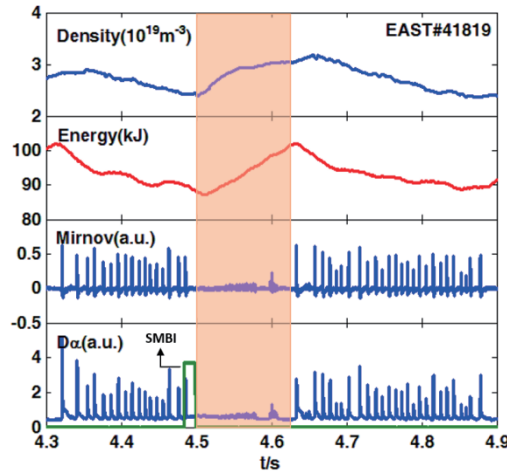
Fig. 14 ELMs mitigation using SMBI with a single pulse of SMBI with the pulse width of 16 ms
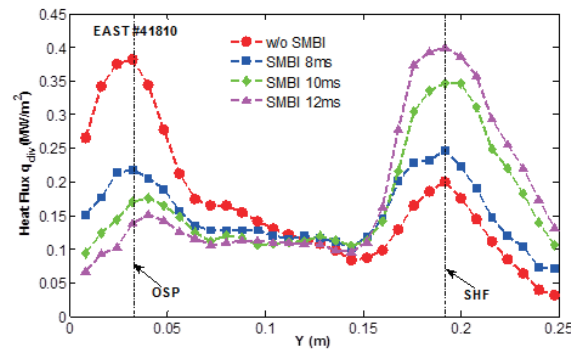
Fig. 15 Heat flux could be transferred between the OSP and SHF regions by adjusting the durations of the individual SMBI pulses

4.4 Development of 50Hz pellet injection

Meanwhile, injection of small deuterium pellets with high frequency is a traditional and widely used methods to control ELM. It has been chosen for ITER to trigger ELMs.　To testified ELM control in long H-mode plasmas, a 50 Hz pellet injector, which could be operated in a steady-state mode, has been developed in the last two years [18]. It has two same modules of pellet injection system with a pellet injection frequency of 25Hz. Each module consists of a screw extruder for solid hydrogen isotope ice

production surrounded with a thermal screen to protect the extruder from heat radiation. Two independence helium flow regulators for temperature regulation and stabilization for pellet fabrication.   And two acceleration system, including cutter for solid hydrogen isotope pellet formation and a fast valve for pellet acceleration. Helium is used as propellant gas for pellet acceleration. The system has been past engineering commission and is ready for the plasma experiment in EAST [19]. During engineering commission, it testified that the that the average pellet injection velocity and propellant gas pressure had a power-function relationship. And, the reliability of the injected pellets is higher than ~70%, as shown in Fig. 16.
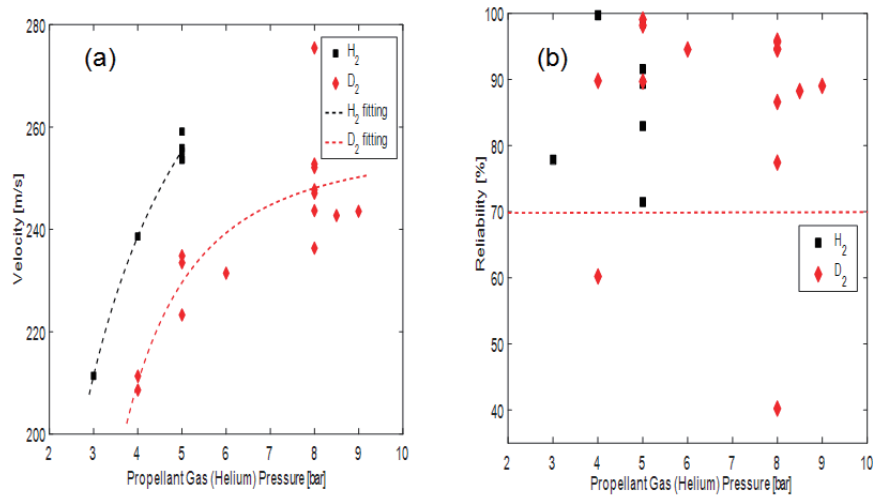
Fig. 16 Results of engineering commission of 50 Hz pellet injector (a) the relationship of average pellet injection velocities and pressure of propellant gas, (b) the reliability at various pressure of the propellant gas

Summary

In the past few years, as well as the upgrading of plasma facing components and auxiliary heating power of EAST, wall conditioning, plasma fueling and ELM control have been successfully developed for the achievement of high-power, long-pulse H-modes. Based well cleaning using baking, GDC and ICRF associated plasma, Li wall conditioning have been developed, via a combination of overnight evaporation and periodic use of real time Li aerosol or granule injection. This method has the most effectiveness on impurities suppression, recycling control and the ratio of H/(H+D) reduction and become as some routine wall conditioning methods in EAST. It makes a great contribution on the improvement of plasma performance, i.e. new achievement of record long, 101.2s, H-mode plasma in EAST.   At the same time, significant improvement of plasma fueling system has been made. Gas puffing system and SMBI system has been upgraded to meet various mission, i.e. plasma fueling, ELM control, experiments of radiation and detachment divertor. Good plasma density feedback control has been achieved using SMBI with a high fueling efficiency.   And a steady-state operated 10Hz pellet injector system has been developed for core plasma fueling. In plasmas with proper parameters, this pellet could induce snake perturbation and various L-H transition, which is useful for the investigation of MHD behavior in plasmas, and the physics behind of

L-H transition. Moreover, various traditional and novel systems for edge local mode control has been developed. Li granules injection could trigger ELMs with an efficiency of 100% if its diameter bigger than 0.6mm. Li aerosol injection would suppress ELMs both on carbon walls and tungsten walls. Long ELM free H-mode could be achieved, indicating Li aerosol injection is an effective method to suppress ELMs for future fusion devices. SMBI is also testified as an effective method to suppress ELMs. A 50Hz pellet injection system has been past engineering commission and is ready for ELM control experiments. Upgrading and application of those system will be continued to meet plasmas with high parameters, i.e. with 10-30MW heating, full tungsten walls, and long pulse about several hundred second.

References

[1] J.S. Hu, et al., Fusion Engineering and Design 84 (2009): 2167–2173.

[2] J.S. Hu, et al., J. Nucl. Mater. 376 (2008): 207–210.

[3] Y.W. Yu, et al., Plasma Phys. Control. Fusion 53 (2011): 015013.

[4] G.Z. Zuo, et al., Plasma Science & Technology, 2010. 12(6): 646-650.

[5] Z. Sun, et al., Fusion Engineering and Design, 2014. 89(12): 2886-2893.

[6] J.S. Hu, et al., Physical Review Letters, 2015. 114(5).

[7] J.S. Hu, et al., Fusion Engineering and Design 84 (2009): 2167–2173.

[8] X.W. Zhen, et al., Plasma Physics and Controlled Fusion 55(2013): 115010.

[9] X.L. Yuan, et al, Development and implementation of Supersonic Molecular Beam Injection for EAST tokamak, submitted to Fusion Engineering and Design.

[10] C.Z. Li, et al., Fusion Engineering and Design89(2014): 99-103.

[11] C.Z. Li, et al., Plasma science and technology 16(2014): 913-918.

[12] X.J. Yao, et al., Plasma Phys. Control. Fusion 58 (2016): 105006.

[13] X.J. Yao, et al., Nucl. Fusion 57 (2017): 066002.

[14] Mansfield D K, et al. Nuclear Fusion 53 (2013): 113023.

[15] J.S. Hu, et al. Fusion Engineering and Design 89 (2014): 2875-2885.

[16] Sun Z, Lunsford R, Maingi R, et al. Nuclear Fusion 2018 58.

[17] J.S. Hu, et al., Journal of Nuclear Materials 463 (2015): 718–722.

[18] X.J. Yao, et al., Fusion Engineering and Design 114 (2017): 40-46.

[19] Jilei Hou, Yue Chen, Igor Vinyar, et al., Measurement of velocity and reliability of 50 Hz pellet injector for EAST, submitted to Fusion Engineering and Design.

Tungsten control in long-pulse H-mode discharges in EAST tokamak

L. Zhang[1], S. Morita[2,3], Z. Xu[1], X. D. Yang[1], X. Z. Gong[1], Y. M. Duan[1], Y. Yuan[1], Z. Sun[1], F. Ding[1],J. Huang[1], Y. W. Sun[1], T. Ohishi[2,3], Z. W. Wu[1], L. Q. Hu[1], G. S. Xu[1], X. D. Zhang[1] and EAST team

[1] Institute of Plasma Physics Chinese Academy of Sciences, Hefei 230026, China

[2] National Institute for Fusion Science, Toki 509-5292, Gifu, Japan

[3] Graduate University for Advanced Studies, Toki 509-5292, Gifu, Japan

Abstract

Tungsten impurity is well controlled in EAST H-mode discharges applying on-axis RF heating and Li wall conditioning, which provide great benefit to achieve the reproductive long pulse H-mode discharges (pulse length >60s) with low level of tungsten concentration (Cw), e.g. 3.0×10^{-6}-1.5×10^{-5}. Cw in core plasma decreases by about 40% due to the injection of on-axis ECRH with power of 0.35MW. In order to enhance the particle recycling control, the real-time Li aerosol injection has also applied in addition to routine lithium coating wall conditioning on EAST. It is found that with Li aerosol injection, stable profiles of tungsten are sustained both in the plasma core and at more peripheral region, while the concentrations are halved compared to the normal H-mode discharge, suggesting a reduced tungsten source with Li injection. This report presents the experimental results.

1. Introduction

Tungsten will be used in ITER divertor and is the top candidate plasma facing material for DEMO and future fusion reactor. In order to examine the heat and particle exhaust capability of tungsten divertor, several tokamak devices have installed tungsten plasma facing components (PFCs), e.g. ASDEX-U [1] and WEST [2] with full tungsten environment, JET with ITER-like wall [3], EAST with tungsten monoblock upper divertor [4]. Unfortunately, it has been observed that the steady state H-mode in EAST is limited by largely increased radiated power in plasma core due to tungsten accumulation or large tungsten content. Tungsten control is therefore a crucial issue for EAST long-pulse H-mode operation. Basically tungsten control requires the control of tungsten source and its transport into plasma core through SOL and plasma edge. It is found in ASDEX-U and JET tokamaks that higher edge localized mode (ELM) frequency fELM by enhanced divertor gas puffing [5-7], high heating power injection [1] and ELM pellet pacing [1] is effective to control tungsten accumulation. In EAST H-mode discharge, it was also observed that fELM plays an important role in tungsten content in main plasma, e.g. the relative tungsten concentration decreases by about one order of magnitude when fELM increase from tens to hundreds Hz in NBI-heated H-mode discharges [8]. The suppression of tungsten in plasma core with higher fELM may originate in the enhancement of impurity flushing out on the pedestal top. It is found that sufficient on-axis heating power provided by electron cyclotron resonance heating (ECRH) in ASDEX-U [1, 6] and ion cyclotron resonance

heating (ICRH) in JET [9] is also effective to avoid the tungsten accumulation. The increased turbulent impurity transport in plasma core is found during the phase with on-axis heating [10]. Wall conditioning is found to be effective to suppress the impurity source. In order to enhance the edge recycling control, the real-time Li aerosol injection has also applied in addition to routine lithium coating wall conditioning on EAST. An effective suppression of tungsten source was observed after lithium aerosol is injected [11]. This report presents the recent experimental results of tungsten control in plasma core with application of on-axis ECRH and lithium aerosol injection.

2. Experimental setup

EAST is a full superconducting tokamak device with advanced divertor configuration and utilizes several heating schemes similar to ITER. In order to improve the machine capability toward high-performance steady-state discharge operation, the EAST heating system has been developed multiple heating and current driving systems. i.e., two LHW (f_{LHW1}/f_{LHW2}=2.45/4.6GHz, P_{LHW1}/P_{LHW2}=4/6MW) systems, co-current and counter-current NBI [11] (P_{NBI}=4MW, E_{NBI}=50-80keV) systems, ICRH (f_{ICRH}=25-70MHz, P_{ICRH}=12MW) system and ECRH (f_{ECRH}=140GHz, P_{ECRH}=0.5MW) system. The long-pulse H-mode operation is attempted with pure RF heating scheme due to their continuous operation capability. The upper graphite divertor has been also replaced by the ITER-like W/Cu monoblock [4] with the heat exhaust capability up to 10MW/m^2. The EAST operation has been thus restarted in 2014 with lower graphite divertor, molybdenum first wall and upper tungsten divertor.

Two flat-field EUV spectrometers working in 20-500Å wavelength range have been installed on the EAST tokamak to measure line emissions from highly ionized tungsten ions with fast time response of 5ms/frame [12] and its radial profiles with high spatial resolution of 0.8cm [13] respectively. The unresolved transition array (UTA) composed of several ionization stages, e.g. W^{27+}-W^{45+}, emitted in a wavelength range of 45-70Å is used for analyzing the uniform tungsten concentration Cw for typical ELMy H-mode discharges in EAST, while the approaches is good for limited discharges. For most discharges, the UTA spectral intensity divided by line-averaged density, IW-UTA/ne, is used for estimating the relative tungsten content. Tungsten source is evaluated from W I line (400.9nm) measurement with S/XB method.

3. Tungsten control with on-axis ECRH

In typical EAST RF H-mode discharge (shot #73886) as shown in Fig. 1, the total injected power of 2.55MW comes from 1.8MW LHW, 0.4MW ICRH and 0.35MW ECRH, in which the power of ECRH is deposited at ρ<0.1. After the ECRH is switched off at t=6.7s, fELM decreases from ~180Hz to ~120Hz, high-Z impurity of Fe, Mo and W build up quickly and Cw increases by 40% at most. As shown in Fig. 2 that a hollow soft X-ray profile change to a peaked one after ECRH switched off, which indicates an effective control of high-Z impurity by on-axis ECRH. In EAST long-pulse H-mode operation, on-axis ECRH was superimposed on the LHW and ICRH heating phase during the whole H-mode to avoid the high-Z impurity accumulation and control high-Z impurity content.
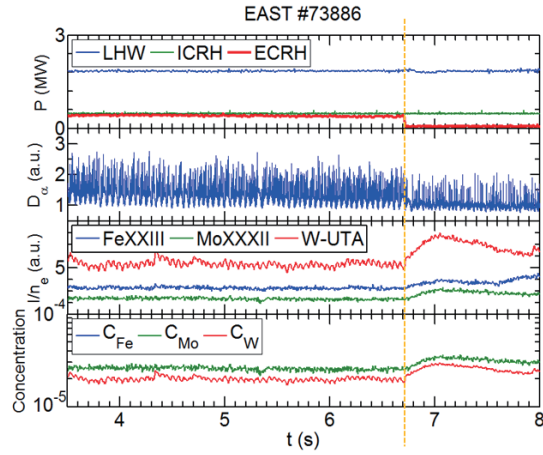
Fig.1 Time evolution of (a) injected power of LHW, ICRH and ECRH (b) divertor D_α, (c) n_e normalized line intensity of FeXXIII at 132.91Å MoXXXII at 127.87 Å and W-UTA in the range of 45-70 Å (composed of W^{27+}-W^{45+} ions), and (d) Impurity concentration of Fe, Mo and W
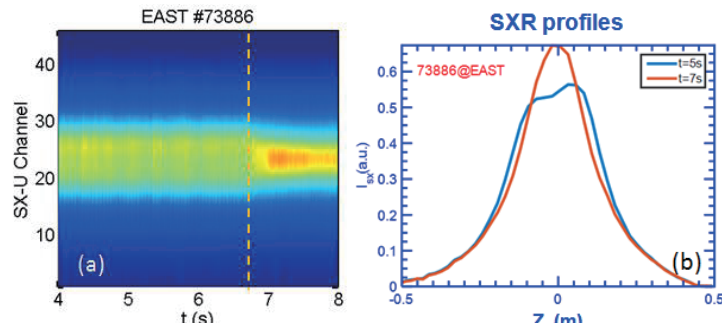
Fig.2 (a) Time evolution of soft X-ray profile, (b) radial profile of soft X-ray before and after ECRH switched off. The time when the ECRH is switched off is indicated by a vertical dashed line in (a).

4. Tungsten control with lithium aerosol injection

In EAST long-pulse H-mode operation, tungsten concentration is halved during the steady H-mode phase with real-time lithium aerosol injection comparing the normal discharges without lithium injection as shown in Fig. 3, which demonstrates the effective tungsten suppression with strong lithium coating conditioning. Tungsten source, tungsten contents at peripheral region and in plasma core are observed to be reduced by half with lithium injection. Impurity ion profiles are compared between discharges with and without Li aerosol injection as illustrated in Fig. 4. Radial profiles clearly indicate the reduction of tungsten ions not only in plasma core but also at more peripheral region. Li aerosol injection can also effectively reduce the Fe and Mo content in addition to tungsten. The reduction of tungsten source after Li injection may originate in reduced edge recycling and particle removal via surface pumping.
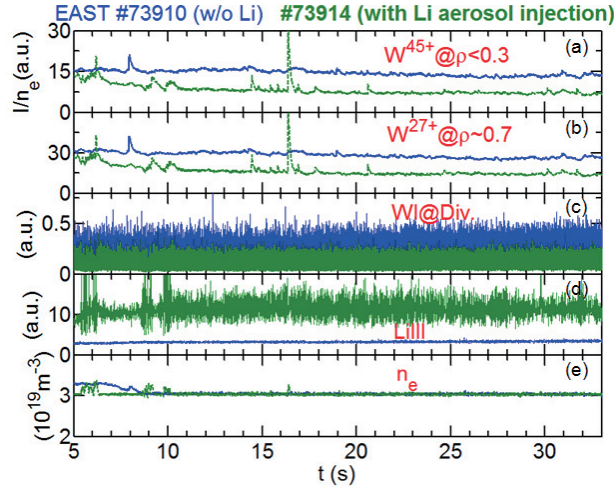
Fig.3 Time evolutions of (a) W^{45+} (at 127.0 Å) intensity at plasma core, (b) W^{27+} (at 49.4 Å) intensity at plasma outer region, (c) WI (at 400.9nm) intensity at upper divertor target, (d) LiIII (135.0 Å) and (e) chord-averaged electron density n_e
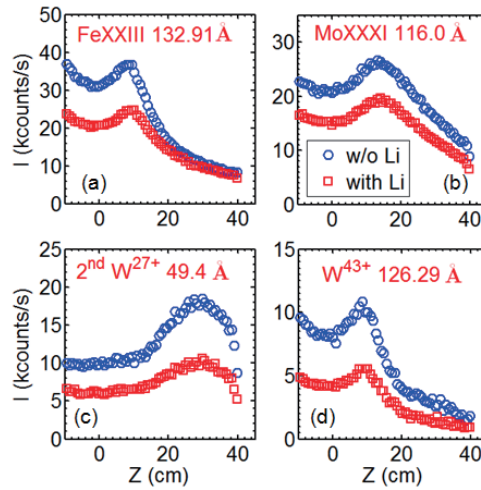
Fig.4 Radial profiles of line intensities of (a) FeXXIII at 132.91 Å, (b) MoXXXI at 116.0 Å, (c) 2nd order W^{27+} at 49.4 Å and (d) W^{43+} at 126.29 Å

5. Conclusion

Various experimental approaches are attempted for the tungsten suppression. Especially, the application of on-axis ECRH and lithium aerosol injection is proved to be effective to control tungsten concentration in plasma core in RF heating H-mode discharges. In addition, small ELM amplitude during all H-mode phase and high power ratio of LHW also play an important role in tungsten control in this H-mode scenario, which is not included in this work. As a result, reproducible long pulse H-mode discharges with low tungsten concentration (CW close to 10-6) have been successfully obtained in EAST by applying multiple experimental approaches. The investigation of tungsten control scenario explored during long pulse H-mode phase in EAST is significant for steady-state operation of ITER and design of first wall in future fusion

reactor. Quantitative study on edge and core tungsten transports is being carried on by impurity transport simulation based on experimental data.

Acknowledgments

Reference

[1] R. Neu, *et al.*, Plasma Phys. Control. Fusion 49 (2007) B59

[2] J. Bucalossi, *et al.,* Fus. Eng. Des. 89 (2014) 907

[3] G. F. Matthews, *et al.*, Phys. Scr. T145 (2011) 014001

[4] D. M. Yao, *et al.,* Fusion Eng. Des. 98-99 (2015) 1692

[5] A. Kallenbach, *et al.,* Nucl. Fusion 49 (2009) 045007

[6] N. Fedorczak, *et al.,* J. Nucl. Mater. 463 (2015) 85

[7] R. Neu, *et al.,* Nucl. Fusion 45 (2005) 209

[8] L. Zhang, *et al.,* Nucl. Mater. Energy 12 (2017) 774-778

[9] E. Lerche, *et al.,* Nucl. Fusion 56 (2016) 036022

[10] C. Angioni, et al., Nucl. Fusion 57(2017) 056015

[11] W. Xu, *et al.*, Active suppression of tungsten impurity influx using lithium aerosol injection in EAST, IAEA 2nd Technical Meeting on Divertor Concepts, Suzhou, China November 13-16, 2017

[12] L. Zhang, *et al.,* Rev. Sci. Instrum. 86, 123509 (2015)

[13] L. Zhang, *et al.,* Extreme Ultraviolet Spectrometers for Measurement of Tungsten Spectra on EAST (oral), 30th ITPA Topical Group on Diagnostics, June 21-24, 2016, Novosibirsk, Russia

Recent Progress on W-related PWI Studies on EAST

R.Ding, L. Wang, F. Ding, Y. W. Yu, L. Zhang, K. F. Gan, J. P. Qian, Y. Liang, G. S. Xu, B. J. Xiao, Y. W. Sun, H. Xie, G-N. Luo, J. L. Chen, X. Z. Gong, J. S. Hu, J. G. Li, B. N. Wan, H. Y. Guo and EAST team

Institute of Plasma Physics, Chinese Academy of Sciences, Hefei 230031, Anhui, P.R. China

Abstract

Plasma wall interaction (PWI) in tokamaks will have a serious impact on the lifetime of plasma facing components, the performance of fusion plasmas and the tritium retention in devices. Tungsten (W) is the most promising candidate material for the divertor region of next step fusion reactors, such as ITER. The Experimental Advanced Superconducting Tokamak (EAST), which can operate with long pulse, high performance plasma and W divertor, provides a good platform for the W related PWI studies under steady state plasma. In this paper, recent progress on W-related PWI studies on EAST are summarized. According to the edge spectroscopic observations, W erosion rates and impurities content in the plasma are characterized and analyzed. Correspondingly, W erosion and re-deposition at the divertor region was simulated by the Monte Carlo code ERO. Furthermore, control of W erosion via different means was studied.

1. Introduction

Plasma wall interactions (PWI) in a tokamak may lead to a wide range of plasma and plasma facing components (PFCs) degrading effects, such as surface erosion, consequent re- or co-deposition with fuel and plasma contamination [1]. Tungsten is foreseen as the most promising candidate as divertor materials for the next fusion devices (such as ITER), due to its good thermal-mechnical properties [2]. In order to test the tungsten divertor operation, the tungsten PFCs have been used in several current tokamaks. In 2014, the upper graphite divertor in EAST was replaced by the ITER-like actively water cooled tungsten divertor [3]. After that, several campaigns have been performed with the tungsten divertor for long-pulse discharges. In the following, recent progress on tungsten-related PWI studies on EAST is presented.

2. Characterization of tungsten source in EAST

As a high Z material, the sputtered W impurity would result in strong radiation losses and degradation on the plasma performance. Wall conditioning in EAST is an essential way to suppress impurity level in plasma and to reduce tungsten sputtering. As shown in Fig. 1, both Si and Li were used as the wall coating materials for more than one month each in 2016 EAST spring campaign [4]. The impurity information can be measured by a passive spectroscopic system which can measure various visible emission lines across outboard mid-plane scrape off layer (SOL) and upper W divertor. The spectroscopic observation reveals that both Si and Li coating can suppress the intrinsic impurity levels. Compared to Si coating, Li coating

can more effectively suppress the in-vessel impurities, thus mitigating the W source in upper divertor. After opening vacuum vessel, impurity level increases significantly. It is also shown that W source presents a clear correlation with C and O levels.
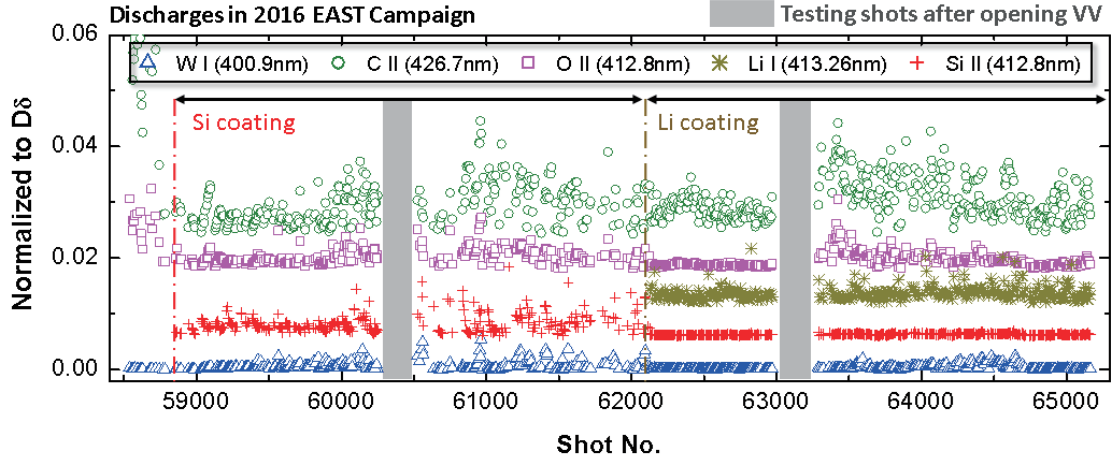
Fig.1 Intensity evolution of WI, CII, Si II, Li I and O II emissions normalized to D_δ in UO divertor region as function of shot number in 2016 EAST campaign. [4]

According to the spectroscopic observation, it is found that impurity production is significantly increased with higher heating power. Higher heating power will lead to higher electron temperature and ion saturation current level along the divertor target. Since the lower divertor material in EAST is carbon, higher plasma parameters at the divertor will result in higher erosion and thus higher low-Z impurities concentration in the SOL. As tungsten sputtering is mainly caused by low-Z impurities, higher low-Z impurities in the background plasma can enhance W sputtering. According to the analysis of W sputtering with different heating regimes, it is shows that there is more W sputtering by (Neutral Beam Injection) NBI and Ion cyclotron Resonance Heating (ICRH) than Electron cyclotron Resonance Heating (ECRH).

In H-mode discharges, it is shows that W erosion is mainly dominated by Edge localized modes (ELMs). During an ELM cycle, ELM-induced W erosion is about 70% of the total W erosion. The W peak erosion position at the divertor target is different for the two phases, intra-ELM and inter-ELM. The W peak erosion is close to the strike point (SP) during intra-ELM while the W peak erosion moves away from the SP during inter-ELM.

3. ERO simulation of W erosion and redeposition for EAST upper divertor

Based on the plasma operations with tungsten divertor, the 3D Monte Carlo code ERO has been used to simulate W erosion and re-deposition for the upper outer divertor region of EAST tokamak [5], as shown in Fig. 2. The simulations are performed in comparison with the measurements in attached L-mode plasma conditions. Background plasma parameters are reconstructed according to the electron density and temperature profiles measured by LPs and magnetic field configuration from EFIT calculations.
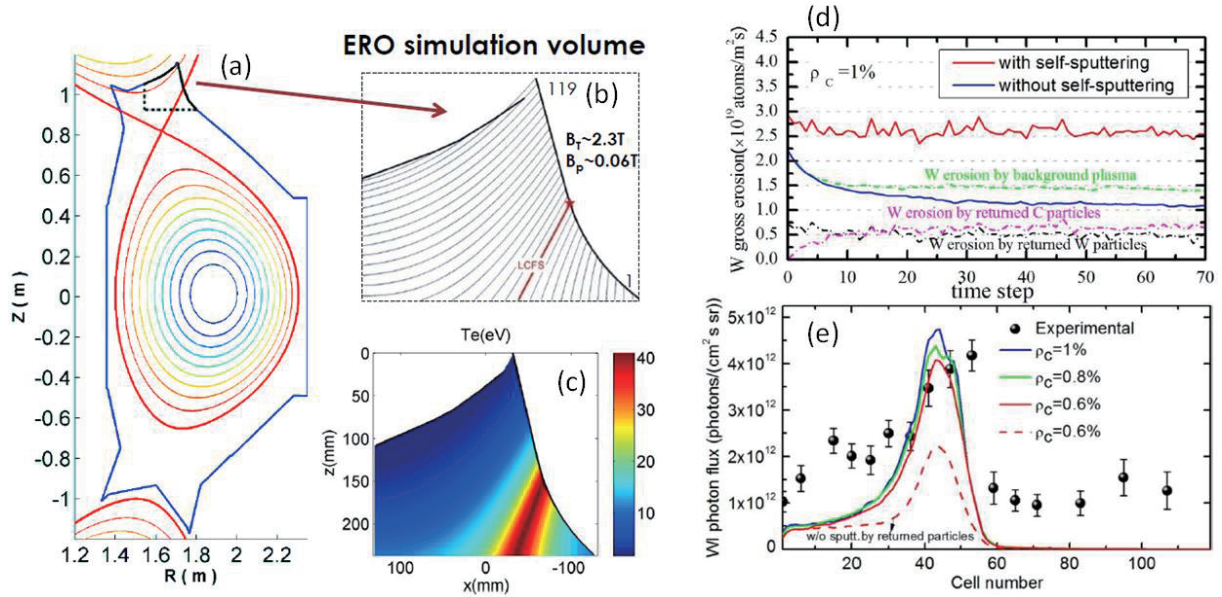
Fig.2 W erosion and re-deposition modelled by the ERO code. (a) and (b) show the magnetic configuration reconstructed by EFIT; (c) indicates the 2D distribution of electron temperature at the divertor region; (d) shows the time evolution of W erosion for the cases with and without self-sputtering; (e) illustrates the ERO modelled WI emission in comparison with the experimental measurements [5].

The simulations indicate that the influence of sputtering by returned eroded particles can significantly enhance the W gross erosion rate especially near the strike points where most eroded particles return. On the one hand, sputtering of C by the returned eroded particles can reduce the C ratio in surface interaction layer. On the other hand, the W erosion rate is enhanced due to the sputtering by both returned C and W particles. Although the W sputtering yield by C is lower than that by W, more returned C particles leads to similar erosion rates caused by returned C and W particles. There are two effects on W erosion rates by C concentration in the background plasma: C ratio in surface interaction layer and W erosion caused by C incidence. When the C concentration is low, W erosion rate increases with higher C concentration. A further increase in C concentration leads to more C in the surface interaction layer and thus lower W erosion rate. The modelling indicates that net carbon deposition occurs on the dome plate and part of the vertical plate close to the dome plate, whereas tungsten net erosion occurs on most of the vertical plate. With the C concentration of about 0.6%–1%, the modelled WI photon fluxes along the target are in a reasonable agreement with experimental measurements.

4. Control of W sputtering

W impurity in plasma will lead to a large radiation enhancement. With impurities accumulations in the core, the radiation losses can lead to a significant degradation of the plasma confinement. Reducing W sputtering is very important to reduce the W source and W concentration in the plasma core. In EAST tokamak, various methods have been developed and tested to control the W sputtering. Firstly, resonant magnetic perturbation (RMP) can effectively suppress the ELM. The ion incident flux to the divertor plate can be reduced, and thus result in lower intra-ELM erosion. The neon Supersonic Molecular Beam

Injection (SMBI) is another useful method. The SMBI in EAST is injected from Lower field side at mid-plane. It is found that during the SMBI, the electron temperature at the divertor target is lower and W sputtering flux is reduced, as shown in Fig. 3. Furthermore, real-time Li aerosol injection is shown to be a good method for reducing W sputtering. Long-pulse H modes with 18 s ELM-free phase were achieved on EAST with the help of Li aerosol injection. Li aerosol injection can enhance the radiation in the divertor region and thus lead to a lower electron temperature at the divertor target. Therefore the carbon impurity concentration in the SOL region is reduced which in the following lead to a lower W sputtering. Li wall coating effect could also be enhanced by Li aerosol injection.
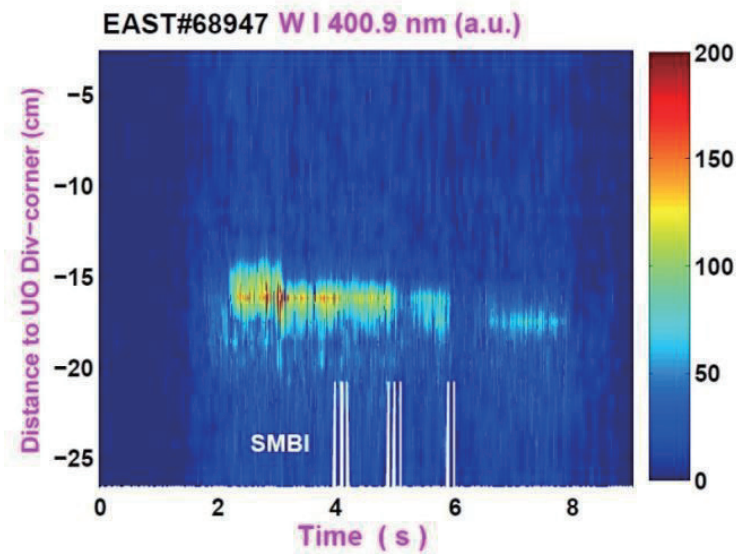
Fig.3 Time evolution of WI line emission along the EAST upper outer

5. Summary

In summary, various W-related PWI studies have been performed on EAST to understand W erosion and its mitigation. With the edge spectroscopic observation, the impurities in plasma and W erosion were characterized. The ERO code was successfully applied to simulate the W erosion at divertor region. W erosion has been controlled via different means. In the near future, the lower divertor of EAST will be upgraded to W/Cu PFCs, which allow us to better study the W-related PWI issues.

Acknowledgements

References

[1] G. Federici, C. H. Skinner, J.N. Brooks, et al. Nucl. Fusion **41** (2001) 1967.

[2] R. A. Pitts, S. Carpentier, F. Escourbiac, et al. J. Nucl. Mater. **438** (2013) S48-S56.

[3] D. M. Yao, G. –N. Luo, S. J. Du, et al, Fus. Eng. and Design, **98-99** (2015) 1692-1695.

[4] H. M. Mao, F. Ding, G. –N. Luo, et al. Nucl. Mater. and Energy, **12** (2017) 447-452.

[5] H. Xie, R. Ding, A. Kirschner, et al. Phys. Of Plasmas, **24** (2017) 092512.

SOLPS modelling of edge plasma and impurity transport in EAST

Fuqiong Wang [1], Y. M. Duan [2], X. J. Zha [1], F. C. Zhong [1], L. Q. Hu [2], H. W. Lu [1], L. Li [1]

[1] Department of Applied Physics, College of Sciences, Donghua University, Shanghai 201620, China

[2] Institute of Plasma Physics, Chinese Academy of Sciences, Hefei 230031, Anhui, China

Abstract

The newly developed SOLPS-ITER code package has been used to investigate the effects of drifts on the in-out/up-down asymmetry of divertor heat/particle fluxes in EAST. Characteristics of the divertor heat/particle fluxes in a double null (DN) discharge with $B \times \triangle B$ points to the upper and lower directions have been investigated by SOLPS-ITER calculations. It is found that the classical drifts will directly affect the parallel plasma flow velocity, and thus affect the divertor asymmetry of particle fluxes. The divertor heat fluxes can also be affected, but not so evidently as that for the divertor particle fluxes. Besides, the influences of classical drifts on the transport properties of W impurity have been investigated by performing the coupled SOLPS-DIVIMP modeling, finding that the leakage of the W impurity from the divertor region to the core will be greatly affected, due to the fact that friction force exerted on the impurity ions has been greatly affected.

1. Introduction

Divertor particle and heat controllability is one of the most critical issues to be solved for the long-pulse and/or high power operation of the future fusion devices, such as ITER and DEMO. EAST, the first fully superconducting tokamak in the world, is designed to study key issues of plasma physics and fusion technology in steady-state operation in support of ITER. As the advance of the EAST experimental campaigns, the heating power has been increased step by step. Thus, divertor asymmetry, a ubiquitous feature in tokamaks, becomes more and more important for the operation and design of EAST divertors, especially for the H-mode discharges [1].

Divertor asymmetry can be driven by the classical drifts [2-9] and the different distributions of the particle and heat sources in the inboard and outboard sides, e.g. enhanced ballooning-like transport near the outboard midplane [10-12]. However, the change of the divertor asymmetry is usually associated with the classical drifts, including the $E \times B$ drift and the grad-B drift . To predict and/or interpret the effects the classical drifts on the divertor asymmetry, modeling on the main characteristics of the divertor heat and particle fluxes in EAST discharges with grad-B drift points towards the upper and lower 'X' point directions has been performed and will be presented in this paper. Besides, the effects of $E \times B$ drift and grad-B drift on the divertor asymmetry have been differentiated. Due to the fact that the plasma flows can been greatly affected by the classical drifts, and thus the friction force, defined as $m \frac{(v_i - v)}{\tau_s}$, exerted on the impurity ions will definitely be affected. We have also studied the influences of classical drifts on the W

impurity transport to get hints on how to control the leakage of W impurity from the divertor region to the core.

SOLPS [13-16], the coupling of 2D multi-fluid plasma code B2/B2.5 [16]and the Monte Carlo neutral transport code Eirene [14], has been widely used for the edge plasma and impurity transport modeling. In SOLPS, lots of complicated physics processes, e.g. drifts, ballooning like transport, etc., can be considered. At present, various versions of SOLPS code packages have been developed, including SOLPS4.x, SOLPS5.x, SOLPS6.x and SOLPS-ITER. Here, in this paper the plasma conditions have been constructed by SOLPS-ITER code [17], which is the latest version of SOLPS. As for the W impurity transport modeling, the Monte Carlo code DIVIMP [18] has been selected to use, since it is more effective than the SOLPS code to be used for the high-Z impurity transport modeling.

This paper has been organized as follows: section 2 will introduce SOLPS-ITER modeling of divertor asymmetry, including the effects of E×B drift and the grad-B drift on the divertor heat and particle asymmetry. Section 3 will show the SOLPS-DIVIMP modeling of the influence of drifts on the W impurity transport. The summary and conclusions will be presented in section 4.

2.   SOLPS-ITER modeling of drifts on the divertor asymmetry

2.1 models used in the simulation
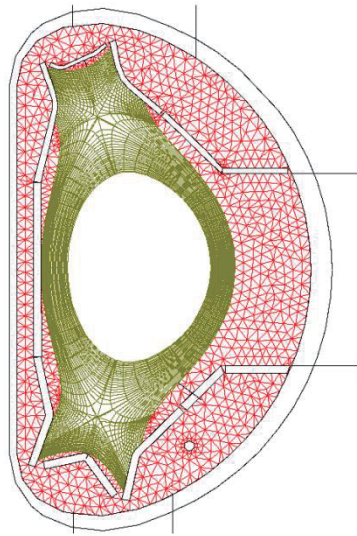
Fig. 1 grids used for the SOLPS-ITER calculation

To investigate the effects of classical drifts on the in-out and up-down asymmetry, a double null (DN) discharge with toroidal field $B_T \sim 2.0T$ has been selected to model. Fig. 1 shows the grids for the SOLPS-ITER calculation, including the quasi-orthogonal grids for the B2.5 calculation and the triangular grids for the EIRENE calculation. The B2.5 calculation grids are generated based on the MHD equilibrium from EFIT code and the EAST geometry. From fig. 1, the B2.5 calculation region extends from the scraped-off layer (SOL) to the region which is often referred to as the outer core by ~5cm. Since the neutral transport cannot be restricted by the magnetic field, so that the calculation region of the neutral transport code EIRENE not only includes the B2.5 calculation region but the gaps between the B2.5 calculation

region and the plasma facing components (PFCs), see fig. 1.

Main inputs for the SOLPS-ITER calculation are as follows:

(1) At the inner core boundary, the density of the deuterium ion D^+ $n_s = 1.2e19 m^{-3}$. The neutral deuterium D^0 density is very low due to the high temperature and strong ionization there. Thus, n_0 at the core-edge interface is set to be 0. Also, an assumption that $T_e = T_i = 350$ eV is made.

(2) At the divertor target plates, the standard sheath boundary condition is applied. According to the Bohm criterion, the flow needs to be at least sonic speed at the entrance of the sheath $nV_{\parallel} = nb_x C_s$. With the inclusion of the drifts, the target sheath boundary condition would become : $nV_{\parallel} + nV_{E \times B} = nb_x C_s$.

(3) At the wall and the dome-side boundaries of PFRs, the radially decay length of the electron and ion temperature λ_T is set to 0.01 m. The ion leakage is given by $\Gamma_{leak} = \alpha c_s n_a$, where c_s is the sonic speed and n_a is the density of the species a, $\alpha = 0.001$ for ions. The ions leak off and recycle to neutrals. The recycling coefficient at the targets and wall is set to be 1.0. The recycling coefficient is set to be 0.95 at the entrances of the pumping holes, giving a pumping speed up to $\sim$70 $m^3.s^{-1}$.

Transport parallel to the magnetic field is assumed to be classical but flux limited: for neutral diffusion, flux is limited to the thermal flux; electron and ion parallel heat fluxes are limited to 30% and 60%, respectively, of the thermal fluxes. Sensitivity of solutions to these flux limits is not considered here, but should not qualitatively affect the results. Due to the lack of the reliable physical models, the cross-field heat and particle diffusivities are usually assumed to be constant, which is considered to be the simplest and appropriate approximation introducing the least variables. Typically, similar to that for ITER, assumes that the anomalous particle diffusivity, $D_{\perp} = 0.5 m^2/s$, and the thermal heat diffusivities, $\chi_{\perp i} = \chi_{\perp e} = \chi_{\perp} = 1.0 \ m^2/s$. For simplicity, the inward pinch velocity, V_{pinch}, is set to 0.

Table 1. Reactions considered in the EIRENE calculation

Index	Reactions	Type
1	$e + D \rightarrow 2e + D^+$	Ionization
2	$D^+ + D \rightarrow D + D^+$	Charge exchange
3	$e + D_2 \rightarrow 2e + D_2^+$	Ionization
4	$e + D_2 \rightarrow e + D + D$	Dissociation
5	$e + D_2 \rightarrow 2e + D + D^+$	Dissociative ionization
6	$D^+ + D_2 \rightarrow D^+ + D_2$	Elastic collision
7	$D^+ + D_2 \rightarrow D + D_2^+$	Charge exchange
8	$e + D_2^+ \rightarrow e + D + D^+$	Dissociation
9	$e + D_2^+ \rightarrow 2e + D^+ + D^+$	Dissociative ionization
10	$e + D^+ \rightarrow D$	Recombination

In the modelling, the atomic and molecular processes involving D^0 neutrals, D_2 molecules, and D_2^+ molecular ions, including charge exchange, ionization, and recombination are controlled self-consistently via

an iterative coupling of plasma transport computations with the kinetic Monte-Carlo neutral particle transport simulation code EIRENE. The atomic data for the SOLPS-ITER calculation has been provided by ADAS [19]. Those detailed reactions are shown in table 1.

2.2 Effects of classical drifts on the divertor asymmetry

By performing SOLPS-ITER calculation with the models presented above, the divertor heat and particle fluxes of the no drift case, normal B_T case and the reversal B_T case have been generated and are shown in fig. 2, where normal B_T means that the grad-B drift ($\mathbf{B} \times \nabla\mathbf{B}$) points to the lower 'X' point, while the reversal B_T means that the grad-B drift points to the upper 'X' point. From fig. 2, for the no drift case, no evident in-out and up-down asymmetry have been found. However, both the peak values and the decay lengths of the divertor D^+ fluxes changes as the change of the direction of toroidal field B_T, i.e. the direction of drift velocity, so that the in-out and up-down divertor particle asymmetry has been evidently changed. Detailed investigation about the relationship between the classical drifts and the decay lengths of the divertor heat and particle fluxes in EAST will be focused and presented on in the future work.
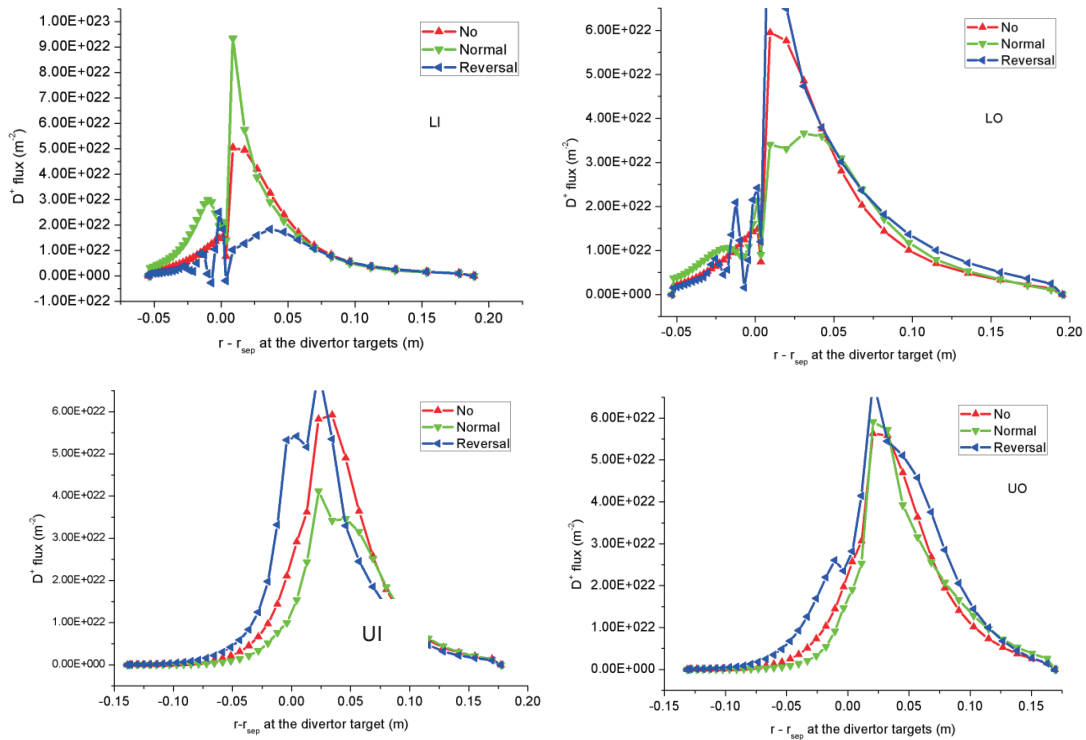
Fig. 2 D^+ fluxes onto the lower inner (LI), lower outer (LO), upper inner (UI) and the upper outer (UO) targets for the no drift case, normal B_T case and the reversal B_T case.
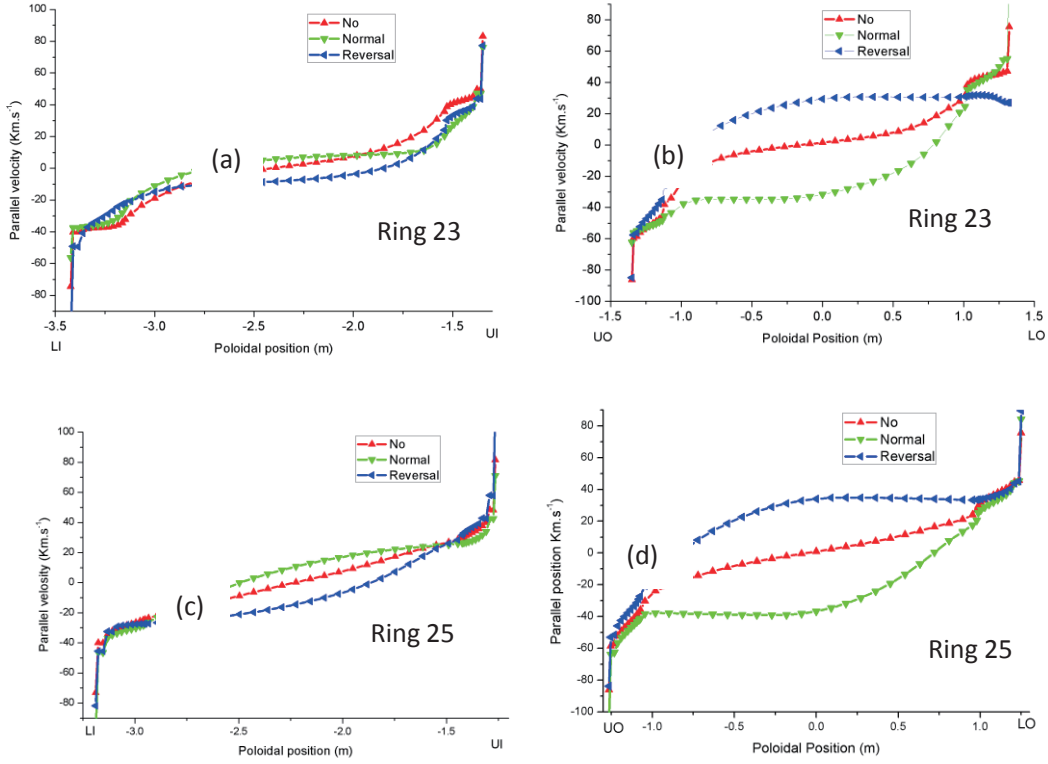
Fig. 3 Parallel plasma flow velocity along the inboard ((a), (c))and outboard ((b), (d))SOL flux tubes

Some recent research [21] finds that the poloidal drift $E_r \times B$ could play a dominant role in the up-down asymmetry, The main physical mechanism can be attributed to the target sheath boundary condition, which must be modified on the account of drifts as follows:

$$nV_\parallel + nV_{E \times B} = nb_x C_s$$

To hold this equation, the parallel velocity ($V_\parallel$) is adjusted according to poloidal drift velocity $V_{E \times B}$. According to fig. 3, the parallel velocity $V_\parallel$ is ~10-100 $Km.s^{-1}$, and $V_\parallel$ has evidently been changed by the classical drifts, so that the plasma conditions, including the plasma density and particle flux will be adjusted by drifts. Also, we have tried to differentiated the effects of grad-B drift and $E \times B$ drift on the divertor particle fluxes. From the calculation, the grad-B drift and $E \times B$ drift velocity have the same orders of magnitude (~$10^3 m.s^{-1}$). Also, the grad-B drift and $E \times B$ drift have almost the same effects on the divertor particle fluxes.

Fig. 4 shows the heat fluxes onto the lower inner (LI), lower outer (LO), upper inner (UI) and the upper outer (UO) divertor target for the no drift case, normal B_T case and the reversal B_T case. From fig. 4, the classical drifts can also have effects on the divertor heat fluxes, including the peak values and the decay lengths of the divertor heat fluxes, but not so evident as the effects on the divertor particle fluxes, the reason for which will be described in the following part.
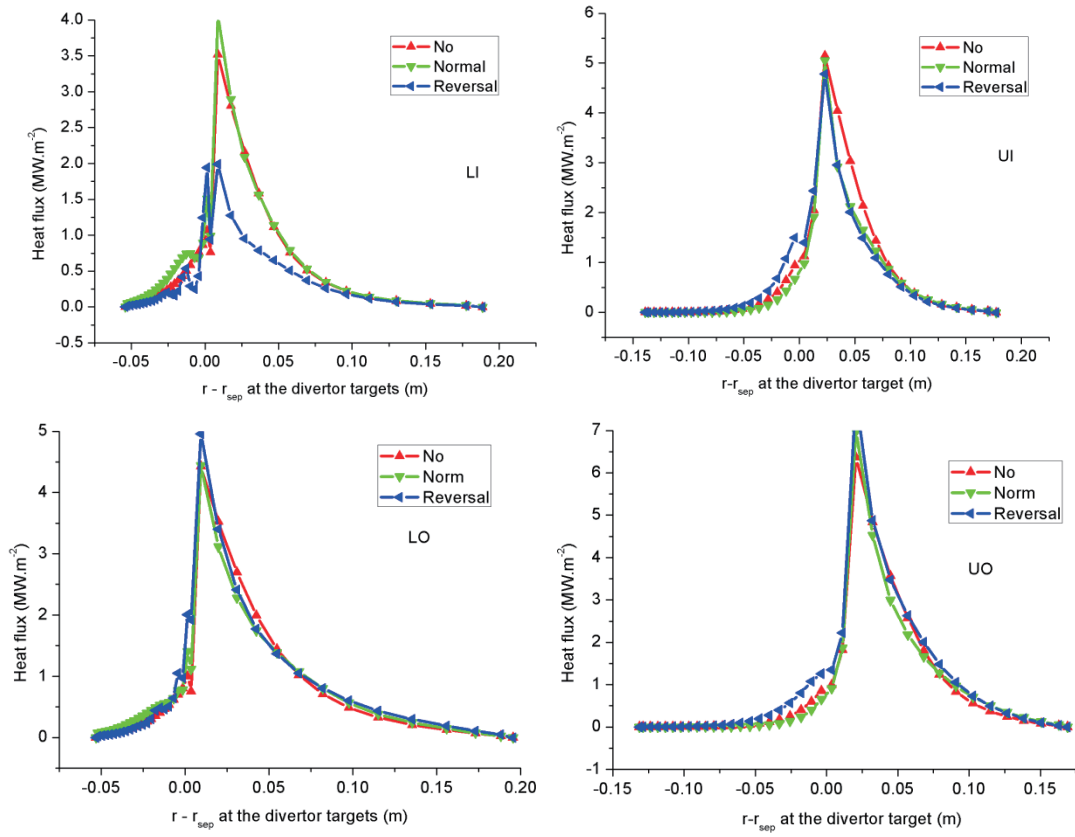
Fig. 4 Total heat flux onto the lower inner (LI), lower outer (LO), upper inner (UI) and the upper outer (UO) targets for the no drift case, normal B_T case and the reversal B_T case.

In the calculation, total heat flux onto the divertor target fht is given by: *fht=fhpe+fhme+fhe+fhmi+fhi+fhj* from which, the total target heat flux consists of the target flux of the potential energy released from the electrons (fhpe), the kinetic energy of the electrons (fhme) and ions (fhmi), the electric heat energy *fhj*, as well as the heat flux of electrons (*fhe*) and ions (*fhi*) due to the conductive and convective processes. More detailed description of these components of the target heat flux can be seen in reference [20]. Fig. 5 shows the ion heat flux onto the different divertor targets. By comparing fig. 5 and fig. 2, we can see that the divertor D^+ flux and the ion heat flux (*fhi*) have very similar profiles for the same divertor target, so that the divertor ion heat fluxes could also be affected significantly. However, the divertor ion heat flux only take a small part of the total divertor heat flux, as can be seen from the comparison between fig. 4 and fig. 5, so that the total divertor heat flux have not been evidently affected by the classical drift. That is to say, from SOLPS-ITER calculation the classical drifts will mainly affect the divertor ion heat fluxes, while the other components of the total divertor heat fluxes cannot be evidently affected by the usual drifts.
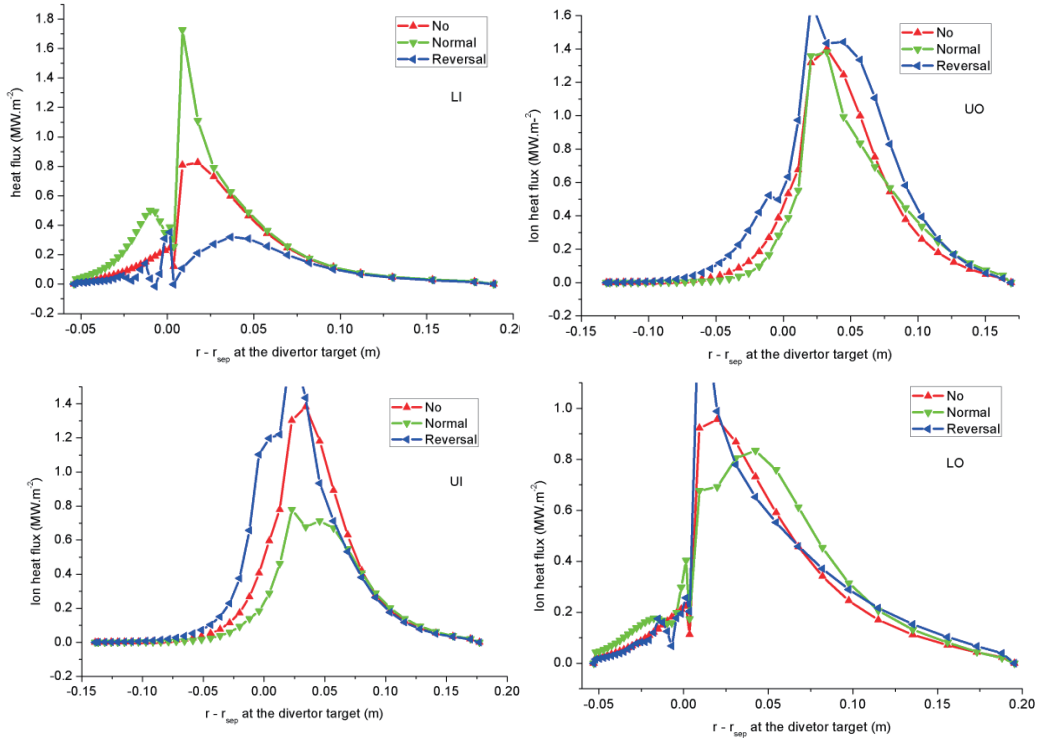
Fig. 5 Ion heat flux onto the lower inner (LI), lower outer (LO), upper inner (UI) and the upper outer (UO)

3. Effects of the classical drifts on the W impurity transport

3.1 models for the impurity transport modeling
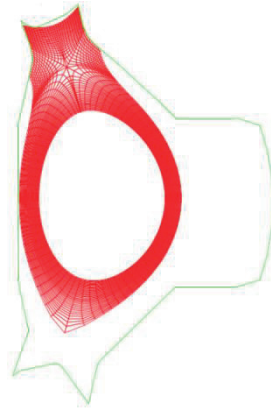
Fig. 6 grids used for the W impurity transport

DIVIMP is a widely used Monte Carlo impurity transport code, which traces the motion and ionization state of the impurities. Although the DIVIMP code has previously been developed for modeling of C impurity transport for the single null discharges, this code is very effective at high-Z (e.g. W) impurity transport modeling. Since in 2014, the upper divertor of EAST has been changed to be made of tungsten, this section will focus on DIVIMP modeling of W impurity transport for an EAST upper single null (USN) discharge. Grids for the calculation are shown in fig. 6. The background plasma conditions (n_e, T_e, T_i, $v_∥$, E, …) for DIVIMP calculation has been provided by SOLPS with the models described in section 2.1. Based

on the SOLPS provided plasma conditions, the sputtering fluxes of W impurity from the upper divertor of EAST have been calculated. After that, the W atoms W^0 will be launched from the divertor target plates. The launching probability from a specific element of the divertor target plates is proportional to the sputtering flux there. For the W impurity atoms, they are assumed to travel in straight line until they hits at some other surfaces or they are ionized to be impurity ions. When the impurity neutrals strike at the surface of the plasma facing components, they are assumed to be reflected from the surface based on the reflection model coupled in TRIM. Once the W atoms are ionized to be W ions, their parallel-to-B motion and cross-field motion will be treated separately [22].
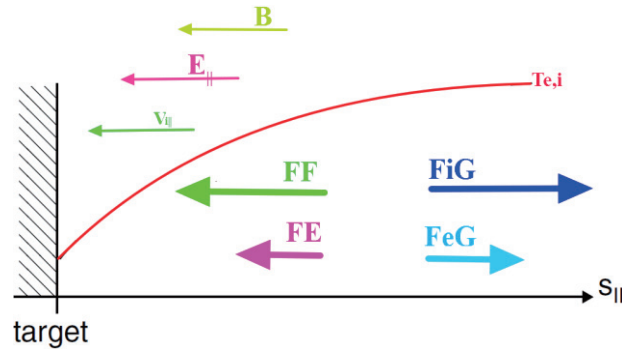
Fig. 7 Forces assumed to be exerted on the impurity ions in the direction parallel to B

The cross-field motion is assumed to be anomalous with the diffusivity $D_\perp = 1.0\,\mathrm{m/s^2}$ In the direction parallel to B, total force exerted on the impurity ion can be described as [22] follows (see fig. 7):

$$m\frac{dv}{dt} = F_{total} = -\frac{1}{n}\frac{dp}{ds} + m\frac{(v_\parallel - v)}{\tau_s} + ZeE + \alpha_e\frac{dT_e}{ds} + \beta_i\frac{dT_i}{ds}$$

Where $-\frac{1}{n}\frac{dp}{ds}$ is the pressure gradient force, s is the distance along the magnetic field line, $m\frac{(v_\parallel-v)}{\tau_s}$ is the friction force, ZeE is the electric force, $\alpha_e\frac{dT_e}{ds}$ and $\beta_i\frac{dT_i}{ds}$ are the electron and ion temperature gradient force respectively. Among all the components of the total force, the thermal force and friction force are usually much larger than others. Usually, the temperature gradient force tends to drive the impurity ions from the divertor region to the upstream, while the friction force tends to drag the impurity ions to the divertor region. Therefore, the leakage of the impurity ions from the divertor region to the core is the competition between the friction force and the thermal force. As is mentioned above, the classical drifts will directly affect the parallel plasma flow velocityV_1, and thus the friction force F_{fric} could be definitely affected. Accordingly, we have performed DIVIMP modeling of W impurity transport in EAST for the no drift case, normal B_T case and the reversal B_T case.

3.2 Effects of drifts on the W production and transport of W impurity
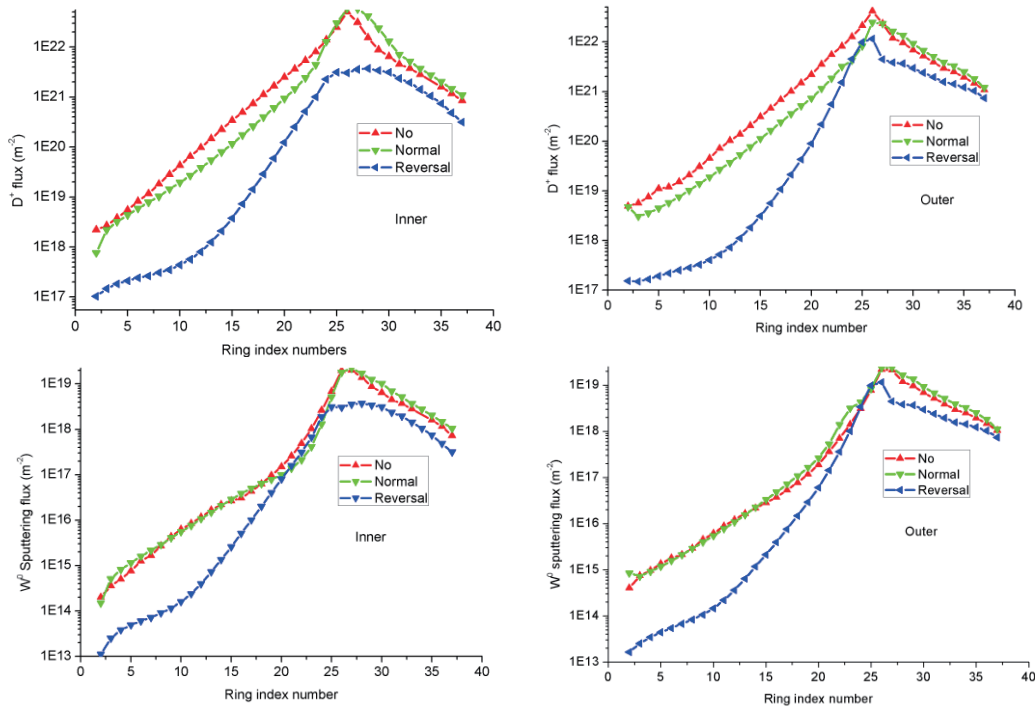
Fig. 8 Calculated D^+ flux and the W^0 sputtering flux from the upper inner and outer divertor respectively.

As is mentioned above, the deuterium ion D^+ flux, as well as the plasma temperature at the divertor region, can be greatly affected by the classical drifts. Therefore, the sputtering flux of the W impurity form the divertor targets due to the bombardment of the D^+ could definitely be affected, just as fig. 8 shows. The calculated W^0 sputtering yield, defined as the ratio of the integrated W sputtering flux (f_w in table 2) to integrated target D^+ flux, is of 10^{-4} orders of magnitude for all the three cases. Also, from fig. 8 the sputtering yield, determined by the D^+ flux, the electron and ion temperature (T_e, T_i) at the divertor targets, has been changed as the change of the direction of the drift velocity.

Table 2 shows some important information about the production and transport of W impurity, including the integrated W sputtering flux from the divertor targets f_w, the content of W impurity, i.e. the ratio of the W impurity density to the electron density, in core c_{w_core}, the maximum values of the friction force exerted on the W^{+1} ions F_{fric_max}, and the leakage of the W impurity from the divertor region from which they are sputtered to the core, which is defined to be the ratio of the W impurity density in core to the W impurity density in the divertor region. From table 2, we can see that these different cases have quite different core leakage of W impurity. For this USN discharge, P_{SOL}=1.0 MW, n_u=2.0e19 m^{-3}, the normal B_T case has the lowest core leakage of W impurity and thus the lowest content of W impurity in core, while the reversal B_T case has the highest core leakage and W content in core. The reason for this is that friction force exerted on the impurity ions in the normal B_T case is much larger than that in the reversal B_T case in most of the divertor region. This result is in consistent with the theory presented in section 3.1. Also, from the calculation results we may draw a conclusion that the transport processes of W impurity could be controlled

by introducing some artificial flows into the plasma.

Table 2 Information about the production and transport property of W impurity for the three cases.

case	f_w	Leakage	c_{w_core}	F_{fric_max}
No drift	2.306E+18	3.882E-03	7.577E-05	4.9E-17
Normal	2.769E+18	2.556E-03	4.939E-05	6.5E-17
Reversal	9.034E+17	1.011E-02	1.645E-04	1.8E-18

4. Summary and conclusions

In this paper, we have performed some preliminary modeling work to investigate the effects of the classical drifts on the divertor particle and heat fluxes. It is found that The usual drifts can evidently affect plasma flow velocity, and thus affect the plasma density and the divertor particle fluxes. The divertor heat fluxes can be affected by the usual drifts not so evidently as that for divertor particle fluxes, the reason for which is that the classical drifts could mainly affect the convective and conductive ion heat flux, taking only a small part of the total divertor heat flux.

Besides, we have investigate the effects of classical drifts on the W impurity transport by performing the coupled SOLPS-DIVIMP modeling, finding that both the production and the transport processes of the W impurity con be affected by the classical drifts. For the case in which the friction force is larger, it has lower W impurity core leakage and lower W content in core. Based on this result, it seems that the transport process of W impurity could be controlled by artificially introducing some flows into the plasma.

In conclusion, the usual drifts, including the grad-B drift and the $E \times B$ play a significant role in the edge plasma and impurity transport. Much future work is still needed to get the quantitative relationship between the classical drifts and the decay length of the divertor heat/particle fluxes and the relationship between drifts and impurity transport.

Acknowledgements

References

[1] J.B. Liu, H.Y. Guo, L. Wang, et al., Nucl. Fusion **56** (2016) 066006

[2] Eich T. et al 2009 J. Nucl. Mater. 390–1 760–3

[3] Asakura N. et al 2004 Nucl. Fusion **44** 503–12

[4] Faitsch M. et al 2015 Plasma Phys. Control. Fusion **57** 075005

[5] Chankin A.V. et al 2015 Plasma Phys. Control. Fusion **57** 095002

[6] Churchill R.M. et al 2013 Nucl. Fusion **53** 122002

[7] Rozhansky V. et al 2012 Nucl. Fusion **52** 103017

[8] Rognlien T.D. et al 1999 J. Nucl. Mater. 266–9 654–9

[9] Goldston R.J. 2012 Nucl. Fusion **52** 013009

[10] Eich T. et al 2011 Phys. Rev. Lett. **107** 215001

[11] LaBombard B. et al 2004 Nucl. Fusion **44** 1047–66

[12] Boedo J.A. 2009 J. Nucl. Mater. 390–1 29–37

[13] Schneider R. et al 1992 J. Nucl. Mater. 196–198 810

[14] Reiter D. 1992 J. Nucl. Mater. 196–198 80

[15] Coster D.P. et al 1997 J. Nucl. Mater. 241–243 690

[16] Braams B.J. 1986 PhD Thesis Computational Studies in Tokamak Equilibrium and Transport, Rijksuniversiteit, Utrecht, Netherlands

[17] Wiesen S., et al., Journal of Nuclear Materials **463** (2015) 480–484

[18] Stangeby P.C. et al 1988 Nucl. Fusion **28** 1945

[19] Porter G D, et al., Nucl. Mater. 266-269, 917 (1999)

[20] Y. Chen. Phys. Plasma **18**, 062506 (2011)

[21] Rozhansky V, et al., Nucl. Fusion **52** 103017

[22] Stangeby P.C. 2000 The Plasma Boundary of Magnetic Fusion Devices (Bristol: Institute of Physics Publishing)

Investigation of density limit and MARFE by Polaris on J-TEXT tokamak

P. Shi[1], G. Zhuang[2], Z.P. Chen[1], the J-TEXT team

[1]Huazhong University of Science and Technology, Wuhan Hubei, 430074, China

[2]2University of Science and Technology of China, Hefei, 230026, China

Abstract

Multifaceted asymmetric radiation as well as strong poloidal asymmetry of the electron density from the edge, dubbed as "MARFE", has been observed in high electron density Ohmically heated plasmas on J-TEXT tokamak. Equilibrium reconstruction based on the measured data from the 17-channel FIR polarimeter-interferometer indicates that an asymmetric plasma current density distribution forms at the edge region and the plasma current shrinkage locates at the MARFE affected region. Furthermore, associated with the localized plasma current shrinkage, a locked mode MHD activity is excited, which then terminate the discharge with a major disruption. Localized plasma current shrinkage at the MARFE region is considered to be the direct cause for the density limit disruptions, and the proposed interpretation is consistent with the experimental observations.

1. Introduction

The thermonuclear power in a tokamak reactor is proportional to the square of electron density ($\sim n_e^2$) demands that the future tokamak reactors must operate at high density safely. However, the existence of density limit disruption [1,2] can be an important obstacle to that goal. Recently, the experiment for investigation of density limit disruption has been carried out on J-TEXT tokamak. The phenomenon of multifaceted asymmetric radiation from the edge (dubbed a "MARFE") during density limit discharge has been identified firstly on J-TEXT by several diagnostics. During the MARFE evolution, strong poloidal asymmetry of electron density and line radiation at edge has been observed. Besides, it is found that the plasma current distribution also shows asymmetric behavior at edge, by analyzing the data from FIR polarimeter-interferometer(POLARIS). Based on the experimental observations, a new mechanism is proposed to explain the density limit disruptions associated with MARFEs.

2. Experiment

The experimental observations of high-density discharges on J-TEXT confirm that these discharges are frequently disrupted as the plasma density approaches an upper limit and they have almost identical performance. A typical high-density disruption discharge (shot #1038116) is shown in Fig. 1. The discharge is terminated at $t = 0.41\ s$ and the maximum central line-averaged density is $5.6\times10^{19} \text{m}^{-3} = 0.67\ n_G$ where n_G is the Greenwald density [3]. During the interval of $0.2\ s < t < 0.4\ s$, the central (at $r = 0\ cm$) line-averaged electron density $n_e(0)$ keeps increasing (Fig. 1(d)) and n_e at $r = -24\ cm$ (very edge of HFS) suddenly surges upward at about $t = 0.33\ s$ while it changes little or even drops at $r = 24\ cm$ (very edge of

LFS) as shown in (Fig. 1(e)). At the same time of HFS edge density surging upward, the C_{III} line emission at HFS edge also soars upward, as Fig. 1(f) shows. Fig. 1 indicates that an asymmetry of density and C_{III} line emission profiles occurs between the very edge of LFS and HFS. The plasma horizontal displacement is stable after 0.3 s, as shown in Fig. 1(d). So the effect of plasma displacement on the edge density variation can be excluded. Additionally, the plasma horizontal position can be manifested by the Faraday rotation angle (α) near the magnetic axis. As showed in Fig. 1(j), the α at $r=3cm$ almost remains constant near zero during the edge density asymmetry increasing, indicates that the global position of plasma column changes little. Therefore, it can be concluded that the electron density asymmetry on the same magnetic surface occurs at edge. In addition, the visible CCD camera records a bright blob at the edge of HFS after that asymmetric plasma behaviors occur, as shown in Fig. 1(k). It is observed that a bright blob appears and locates outside of the plasma at $t = 0.30$ s, however, there is no asymmetry (between the LFS and HFS edge region) in the radial profiles of the electron density and C_{III} emission, as shown in Fig. 1(e) and 1(f). As time evolves, the blob gets brighter and moves into the edge region of the plasma for $t = 0.34$ s, and the asymmetry in the profiles of n_e, I_{CIII} and B_θ are enhanced. Afterwards, the bright blob stays inside the plasma edge region for a few tens milliseconds, then it gradually rotates poloidally at $t = 0.39$ s and the discharge is terminated by a disruption at $t = 0.41$ s. The diagnostic signals above indicate that a poloidally local region with high density and strong line emission forms at HFS edge after plasma density exceeds a threshold before density limit disruption. All the characteristics of this phenomenon are referenced to the MARFE, which always occurs in high density tokamak plasma.

In Fig. 1, the Faraday rotation angle measured by POLARIS is proportional to the product of electron density and parallel magnetic field, $\alpha \sim \int n_e B_\parallel dZ$. Therefore, the ratio ($\alpha/n_e$) between Faraday rotation angle and electron density is strongly dependent on $B_\parallel$. To some degree, the evolution of α/n_e reflects the variation of $B_\parallel$. The radial distribution of α/n_e for discharge in Fig. 1 is plotted in Fig. 2(d). Additionally, Fig. 2 also plots the radial distributions of line-averaged electron density (Fig. 2(a)) measured by the POLARIS, radiation power (Fig. 2(b)) by the AXUV measurement, intensity of C_{III} line emission (Fig. 2(c)). After MARFE onsets (0.34 s and 0.39 s), the radial distributions of line-averaged electron density and C_{III} line emission appear significantly asymmetry at the edge, being consistent with the data in Fig. 1. Besides, the asymmetric distribution is also observed on α/n_e, which decreases greatly at HFS edge after MARFE onset, meanwhile, α/n_e at other positions almost remains constant during the plasma density increasing. The value of α/n_e at $r = -24$ cm decreases by more than 60% from the time of MARFE onset to disruption. According to the occurring time and location, the decrease of α/n_e at HFS edge is inferred to be result of MARFE, just similar to the increase of density and line radiation.
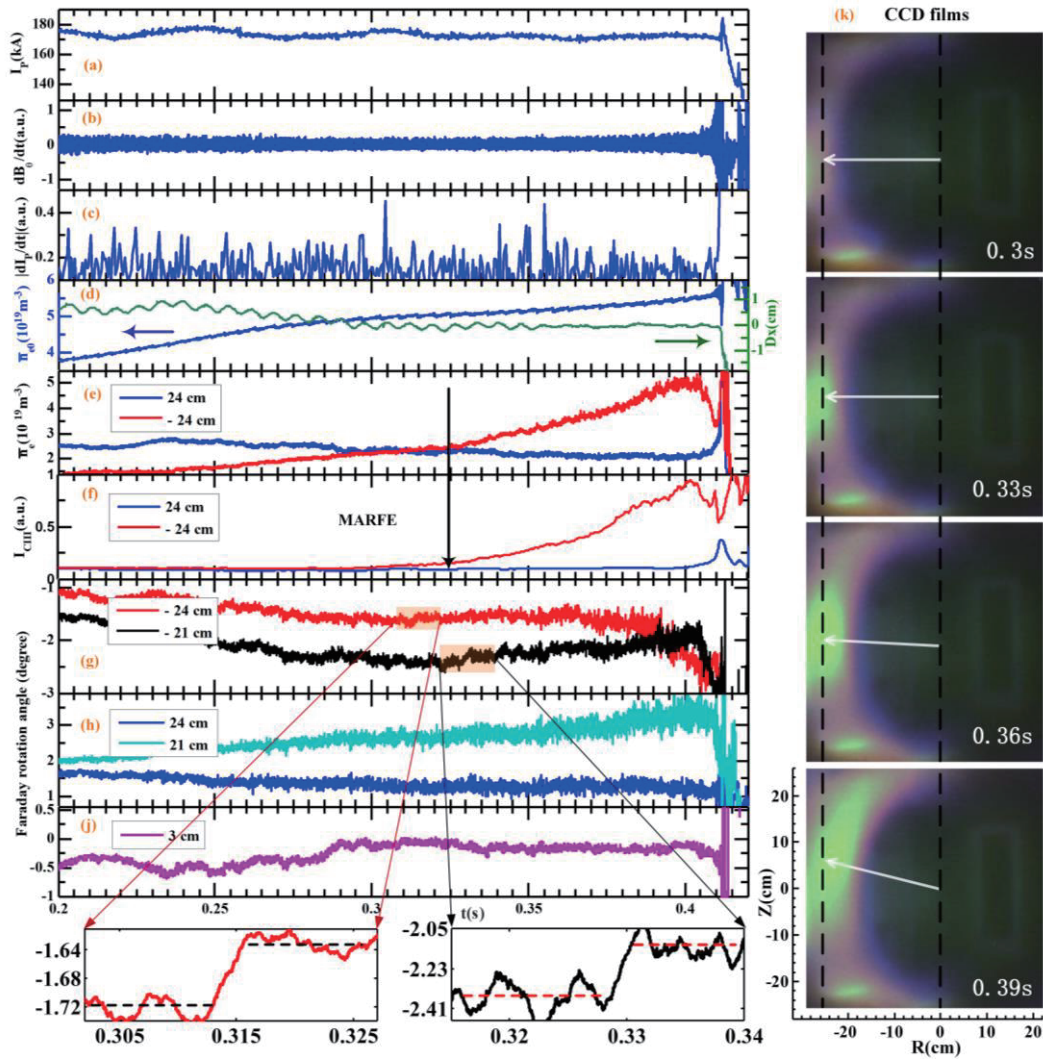
Fig.1 A typical density limit disruption discharge. (a)The total plasma current, (b) the edge magnetic coil signal, (c) dIp/dt from a magnetic probe, (d) central line-averaged density measured by FIR polarimeter-interferometer and the plasma horizontal displacement, (e) line-averaged density at r=±24cm, (f) CIII line emission at r=±24cm, the 2-channel line-integral Faraday angle at the edge of (g) HFS and (h) LFS, (j) the line-integral Faraday angle at r=3cm, (k) CCD camera records.
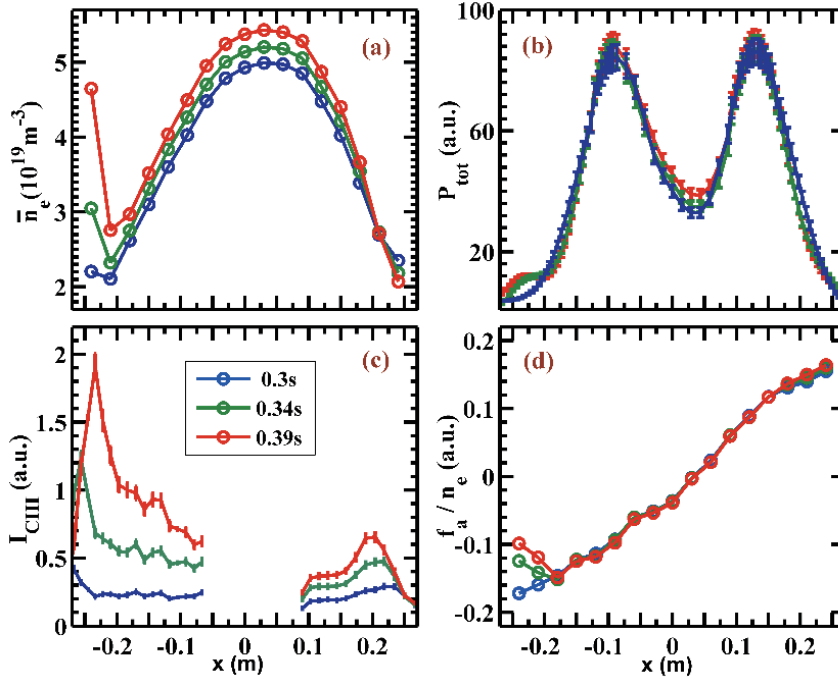
Fig.2 Time evolution of radial distributions of (a) line-averaged electron density measured by POLARIS, and (b) radiation power profiles measured by AXUV, and (c) CIII line radiation intensity obtained by PDA array, and (d) ratio of line-integral Faraday rotation angle to electron density from the POLARIS.

3. Discussion

In order to understand the POLARIS data, the whole plasma region is divided into three regions, as shown in Fig. 3(a), where Region A is the innermost region with symmetric distribution of plasma current, Region B marks the region where the magnetic field lines distort at the edge of MARFE area (similar to a 'limiter'), and Region C is the MARFE area where the plasma current is approximated by zero. Corresponding to the 2-D distribution of plasma current density and electron density, the radial profiles of current density and electron density at midplane (Z=0) are shown in Fig. 3(c) and 3(d), together with the symmetric results from ERP, which removed the four channels at HFS edge. Furthermore, the line-integral Faraday rotation angle and electron density are obtained and shown together with the measured results and ERP results in Fig. 3(e) and 3(f), respectively. It is observed from Fig. 3(e) and 3(f) that the calculated Faraday rotation angle and electron density from the reconstructed current and density distributions are in agreement with the POLARIS measurements, indicating that localized plasma current shrinkage at the MARFE region is pronounced and reasonable.
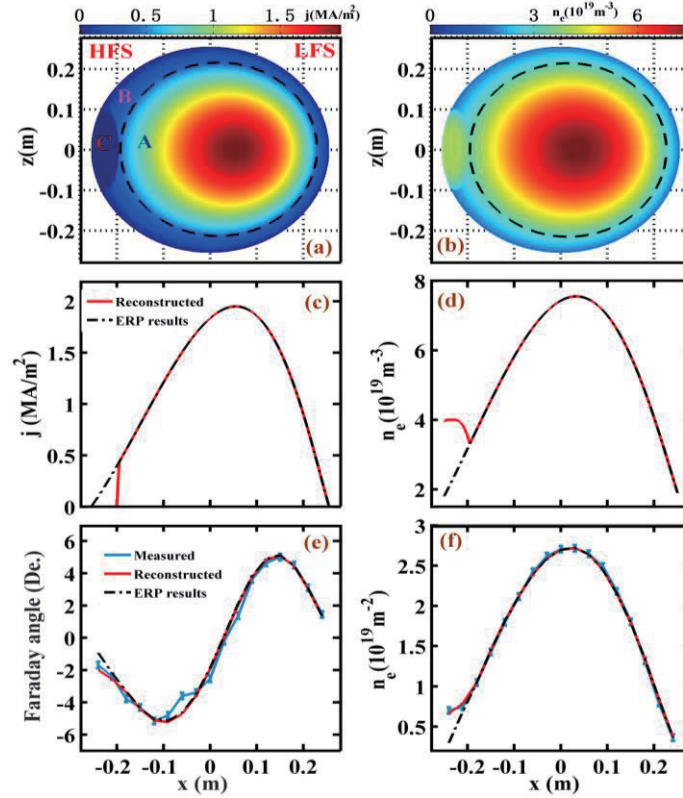
Fig.3   (a) The constructed plasma current distribution, (b) the constructed electron density distribution, (c) the plasma current profile at the midplane from that plasma current distribution and ERP results, (d) the electron density profile at the midplane from that electron density distribution and ERP results, (e) the line-integral Faraday rotation angle, and (f) line-integral electron density from the reconstructed plasma current and electron density distributions, ERP results and POLARIS measurements.

Since the localized plasma current shrinks in the MARFE region, the symmetry of confined magnetic field structure is broken, the radial magnetic field is no longer zero. The distribution of radial magnetic field is obtained by taking the non-zero current density in Region B into account as shown in figure 4(a), and the radial magnetic field along $q = 2$ surface is also shown in Fig. 4(b). It is found that the radial magnetic field reach $\sim 100G$ at the $q = 2$ surface, and it would have the similar effect as error magnetic field. When the asymmetry expands into the inner region of plasma, the influence of the MARFE on the edge region of HFS gets larger, and the magnitude of the radial magnetic field becomes considerably larger and much closer to the $q = 2$ rational surface. At last the strong enough radial magnetic field may trigger locked mode and a major disruption happens. The Fig. 4 (c) plots the 2-D distribution of poloidal magnetic field difference (ΔB_θ) between with and without current shrinkage. It shows that the current shrinkage caused by MARFE has strong influence on the B_θ nearby the HFS edge, while it has little effect on the B_θ at LFS. The Fig. 4 (d) plots the ΔB_θ distribution at $|r|=0.312\ m$. It shows that the B_θ at 180° decreases $\sim 50\ G$ after the current shrinkage occurring. It is reasonable comparing to the experimental result. The results indicate that the localized plasma current shrinkage may be the cause for density limit disruption.
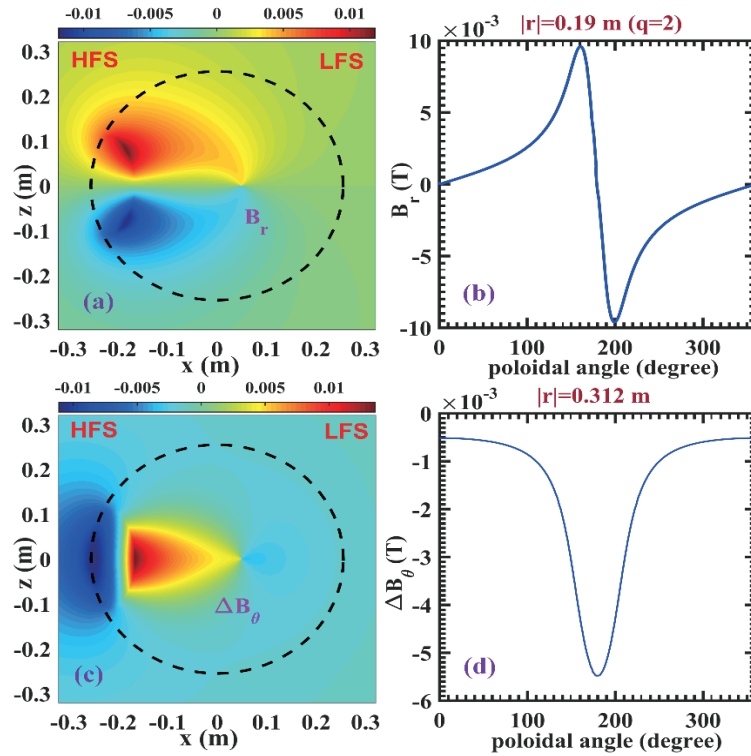
Fig.4   (a) the radial magnetic profile for entire section; (b) the radial magnetic profile at $q=2$ surface; (c) the profile of poloidal magnetic difference (ΔB_θ) between with and without current shrinkage; (d) profile of ΔB_θ at $|r|=0.312$ m (the Mirnov coils position). The black dash lines indicate the LCFS surface ($|r|=25.5$ cm).

4. Summary

The high density Ohmically heated plasma characterized by MARFEs has been observed on the J-TEXT tokamak, and those discharges always end by a major disruption. The MARFEs on J-TEXT are mainly characterized by a poloidally localized region with high density and strong line emission occurring at HFS edge, and a 'bright blob' at HFS edge getting into the plasma. At the time of MARFE onset, a sudden drop on Faraday rotation angle at HFS edge is observed, infers a sudden change of plasma current density at HFS edge. By further analyzing the data from 17-channel POLARIS, the poloidal asymmetry on poloidal magnetic field during MARFEs has been found for the first time. Based on the measured electron density and Faraday rotation angle data, asymmetric density profiles and plasma current density distributions are reconstructed. The constructed plasma current density distribution indicates that the plasma current shrinks in the MARFE region. Such localized plasma current drop would produce a radial magnetic field of ~100 G around the q = 2 surface, which may be sufficient to trigger the 2/1 locked mode and cause the major disruption. The results presented in this letter offer a possible interpretation for the mechanism of MARFE and density limit disruptions.

Reference:

[1] Murakami M. Callen J. D. and Berry L. A. 1976 Nucl. Fusion 16 347

[2] Greenwald M. et al 1988 Nucl. Fusion 28 2199

[3] Greenwald M. 2002 Plasma Phys. Control. Fusion 44 R27

Progress in relation to VUV diagnostics in the HL-2A tokamak

Z.Y. Cui, D.L. Zheng, K. Zhang, P. Sun, C.F. Dong, P. Lu, B.Z. Fu, Z.T. Liu, Z.B. Shi and Q.W. Yang

Southwestern Insititute of Physics, P.O.Box 432, Chengdu 610041, China

Abstract

A 20 cm normal incidence vacuum ultraviolet (VUV) monochromator with fast time response has been developed for measuring edge impurity line emission in the wavelength range of 300-2000 Å on HL-2A tokamak.   The wavelength dispersion of 4nm/mm is achieved with a 1200 g/mm concave holographic grating.   The effective aperture of the monochromator is f/4.5.   The time resolution is 17 μs by using a channel electron multiplier (CEM) as a detector.   The wavelength calibration by using a hollow cathode light source with the helium and argon gases in the laboratory and the preliminary results of the edge impurity line emissions from the HL-2A plasmas are presented in this paper.

1. Introduction

Since spectroscopy is very important for impurity monitor and studies, a vacuum ultraviolet (VUV) spectrometer working in the wavelength range of 300~3200 Å and two extreme ultraviolet (EUV) spectrometers working in the wavelength range of 30~500 Å have been developed in HL-2A [1-3].   The VUV spectrometer and a EUV spectrometer can even measure the vertical profiles of impurity line emissions by adopting space-resolved slits, which are located between the entrance slit and grating for the former and at the entrance slit for the latter.   The time resolution of the spectrometers are 6 ms for the spectra measurement and ≥ 100 ms for the vertical profile measurement.   The spectral resolution is 0.15 Å for the VUV system and 0.22 Å at λ = 200 Å for the EUV systems.   Based on those measurements, impurity behaviors have been studies in HL-2A [4-6].

On the other hand, the diagnostics with fast time response are indeed needed for impurity study in relation to some fast events, such as impurity injections with the laser bow-off and ELMs in the H-mode discharges.   Therefore, a monochromator equipped with a CEM detector is developed in HL-2A to measure the time behavior of impurity ions with low ionization energy.

2. High-speed VUV system

The HL-2A tokamak is a double-null divertor tokamak with a major radius of R=165 cm and a minor radius of a=40 cm.   The discharge operation is generally performed at a toroidal magnetic field of $B_t =$ 1.2-2.4 T and a plasma current of I_p = 150–480 kA.   A schematic view of the HL-2A device combined with the 20 cm normal incidence VUV (VUV-20) system is illustrated in Fig. 1(a).   The monochromator (McPherson Model 234/302) is installed at the mid-plane diagnostic port with ϕ 63 cm in HL-2A and evacuated by a turbo molecular pump with pumping speed of 400 l/s.   A 1200 g/mm concave holographic

grating with Al-MgF2 coating is used and the size of the grating is 40×45 mm.   The effective aperture of the monochromator is f/4.5.   The grating can be manually rotated through a knob and the corresponding wavelength at the exist slit is indicated by a counter, which is connected to the drive system of the grating.
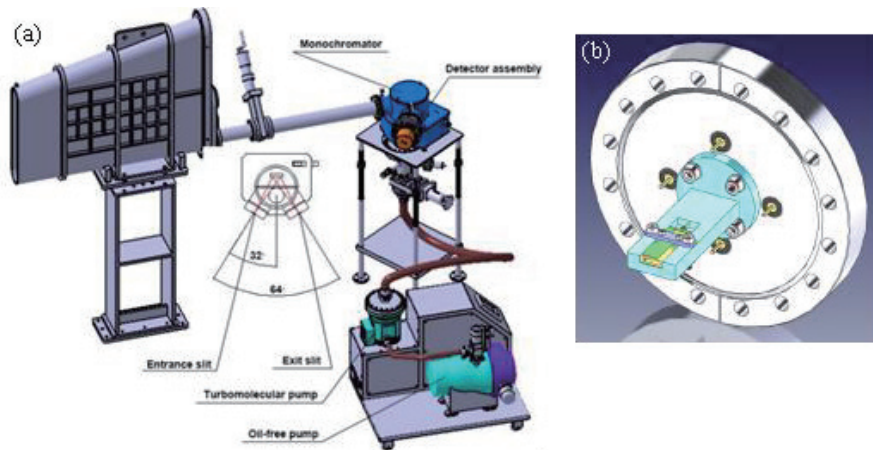
Fig.1 Schematic view of (a) 20 cm normal incidence VUV monochromator system and (b) CEM

A channel electron multiplier (SJUTS, Model KBL210) is installed at the exit slit of the monochromator, as shown in Fig. 1(b).   A plastic support is designed to fix the CEM to the exit slit part. A rubber O-ring seal is used for the vacuum condition.   Three metal electrodes are used for the electric power connection.   Since the voltage provided to the CEM   by a power supply (Stanford Research Systems, Inc. Model: PS350) can reach to 3.2 kV, a shield cover is made to protect the electrodes from the attachment.   The method to avoid electromagnetic interferences during the plasma discharges is also adopted when the shield cover is designed.   A threshold value of the current is set at the power supply to avoid a damage caused by the instantaneous high current to the CEM.

The detection efficiency of the CEM with Al-MgF2 coating is illustrated as a function of wavelength in Fig. 2.   It shows that the high efficient can be obtained in the wavelength range of 300-1200 Å, at which the typical impurity line emissions from the edge plasma are located.   Considering different line emissions having different intensities, an amplifier/attenuator is adopted in the circuit of the data acquisition.   In the first use of the VUV-20 system, the sampling frequency is 60kHz.   The data is then transferred to HL-2A data analysis system by RJ45 cable.
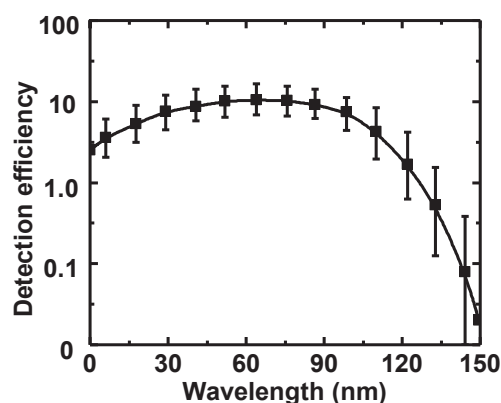
Fig.2 Detection efficiency of the CEM.

3. Calibration with hollow cathode light source

Since the CEM is used instead of the CCD as the detector in the present VUV system, the wavelength calibration is necessary before the system is used in the experiments.   The calibration is carried out by using a hollow cathode light source with Helium and Argon gases in the laboratory.   The light source is working with a continuous gas discharge under the gas pressure of $4\sim4.5\times10^{-1}$ Torr for Helium and $2\sim3\times10^{-1}$ Torr for Argon.   A water cooling system is adopted to the light source.   The output signals of the CEM is recorded by a oscilloscope during the wavelength calibration.   The value displayed on the screen of the oscilloscope is changed when the grating is rotated.   Then the relation between the wavelength and the counter can be exactly obtained.   In general, a line emission with strong intensity can be covered by at least 5 counts.   That means the spectral resolution of the VUV-20 system is enough for identifying the impurity line emissions from the plasma edge.
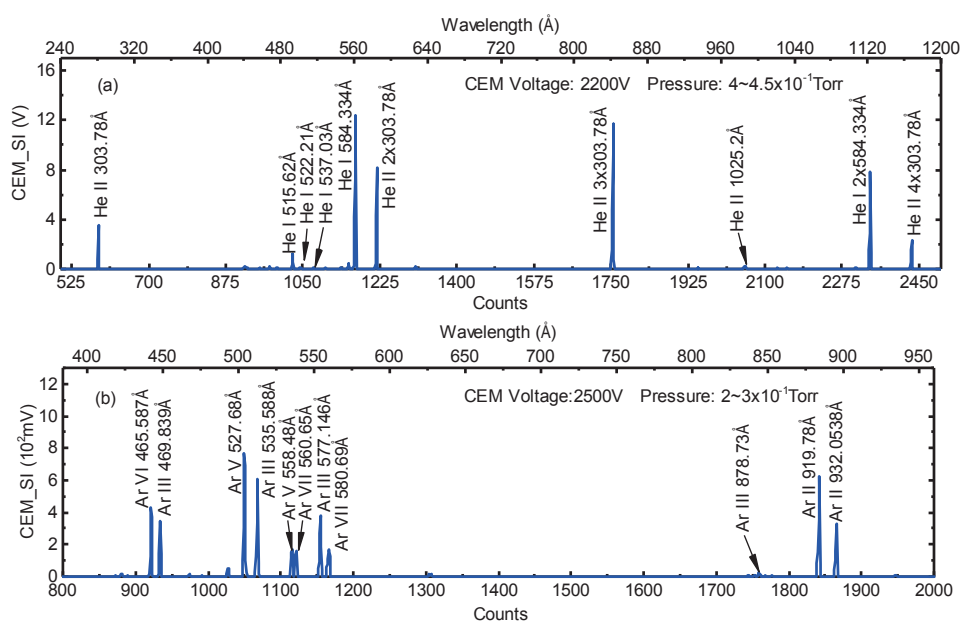
Fig.3 Line emissions from (a) Helium and (b) argon discharges with a hollow cathode light source.

By plotting all the signals together, the calibration results are shown in Fig.3(a) and (b) for the Helium and Argon spectra, respectively.   The typical line emissions of Helium in this wavelength range are HeII $(1s^2S_{1/2}-2p^2P^0_{3/2}$, 303.78Å), HeI $(1s^21S_0-1s5p^1P^0_1$, 515.62Å) and HeII $(1s^21S_0-1s2p^1P^0_1$, 584.33Å).   Their higher order lines, especially for HeII (303.78Å) and HeII (584.33Å), can be also recorded with strong intensity.   The main line emissions of Argon are ArVI $(3s3p^24P_{5/2}-3s3p3d^4P^0_{3/2}$, 465.59Å), ArIII $(3s^23p^43P_1-3s^23p^33d^3P^0_2$, 469.84Å), ArV $(3s^23p^23P_2-3s^23p^33S^0_1$, 527.68Å), ArIII $(3s^23p^43P_1-3s^23p^33d^3D^0_2$, 535.59Å),   ArV $(3s^23p^21D_2-3s3p^31P^0_1$,   558.48Å),   ArVIII $(3p3d^3P^0_3-3D^23F_4$,   560.65Å),   ArIII $(3s^23p^43P_1-3s^23p^34s^5S^0_2$, 577.15Å),   ArVII $(3p^23P_2-3p3d^3F^0_3$,   580.69Å),   ArII $(3s^23p^52P^0_{3/2}-3s3p^62S_{1/2}$, 919.78Å) and ArII $(3s^23p^52P^0_{1/2}-3s3p^62S_{1/2}$, 932.05Å) as plotted in FIG. 3(b).   The intensity of most line emissions of Helium and Argon are strong enough and some are even saturated.   A adjustable attenuator is used in the data acquisition circuit.   Note that the spectral lines are sharp and clear while the stray light is week.   Those are mainly due to the inner surface of the monochromator being blackened.

4. Experimental result from HL-2A plasmas

The performance of VUV-20 monochromator has been carried out after the system is installed at a mid-plane port of the HL-2A tokamak.   For its first operation, the frequency of the data acquisition is 60 kHz.   Time traces of typical impurity line emissions from the HL-2A plasmas are plotted in Fig.4.   Each line emission (CIII, CIV, Lα, SiIV, OVI and NV) is measured from different discharge.   There are NBI around ~0.6<t<~1.2s in Fig.4(a)-(c) and around ~0.3<t<~0.8s in Fig.4(f).   Two line pairs of OVI ($1s^22s^2S_{1/2}$-$1s^22p^2P^0_{3/2}$, 1031.93Å and $1s^22s^2S_{1/2}$-$1s^22p^2P^0_{1/2}$, 1037.6Å) and NV ($1s^2s^2S_{1/2}$-$1s^2p^2P^0_{3/2}$, 1238.82Å and $1s^2s^2S_{1/2}$-$1s^2p^2P^0_{1/2}$, 1241.80Å) are measured from discharges with the same plasma conditions, as shown in Fig.4(e) and (f).   The intensities of OVI (1038Å) and NV (1243Å) are just a half of intensities of OVI (1032Å) and NV (1239Å), respectively.   As shown in Fig.4(c), the H-mode is formed during the time period of 0.75-1.1 s.   The ELMs can be clearly seen in the Lα signals when the data is expanded.   The results show that the VUV-20 system works very well.
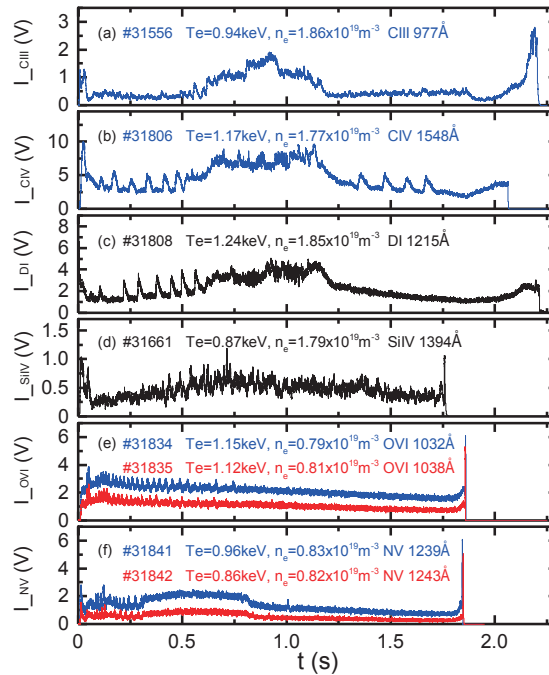
Fig.4 Time evolution of typical impurity line emissions in wavelength range of 500-2000 Å

5. Summary

A fast time response VUV system has been successfully developed by using a CEM as a detector in HL-2A.   The time resolution is ~17 μs for the first use.   By blackening the inner surface of the monochromator, high S/N signals have been obtained.   The wavelength calibration has been carefully done with the helium and argon gases.   The dependence of the wavelength on the counts is obtained in the wavelength range of 300-1900Å.   The time behavior of typical impurity line emissions in the wavelength range is observed in the HL-2A plasmas.   The intensities of most line emissions are strong enough and the ELMs in the H-mode can be clearly seen.   Impurity behaviors in the edge region of H-mode plasmas will be further investigated in the future.

References

[1] Z. Y. Cui et al., Rev. Sci. Instrum. 81 (2010) 043503.

[2] H.Y. Zhou et al., Rev. Sci Instrum. 83 (2012) 10D507.

[3] Z. Y. Cui et al., Rev. Sci. Instrum. 85 (2014) 11E426.

[4] Z. Y. Cui et al., Nucl. Fusion, 53 (2013) 093001.

[5] Z. Y. Cui et al., Nucl. Fusion, 55 (2015) 093034.

[6] Z. Y. Cui et al., Nucl. Fusion, 58 (2018).

Progress in impurity study based on EVU spectrometers in HL-2A

Chunfeng Dong[1], Zhengying Cui[1], Shigeru Morita[2], Ping Sun[1], Kai Zhang[1], Lei Feng[1] and Dianlin Zheng[1]

[1]Southwestern Institute of Physics, P. O. Box 432, Chengdu 610041, China
[2]National Institute for Fusion Science, Toki 509-5292, Japan

Abstract

Two extreme ultraviolet (EUV) spectrometers have been developed on HL-2A with different purposes related to impurity study.　One of them (EUVL-I) is used to measure the spectral wavelength with high time response for impurity monitoring, and the other one (EUVL-II) with space-resolved capability is used to measure the vertical distribution of impurity line emissions in HL-2A plasma.　The absolute intensity calibration of EUVL-II spectrometer is done by comparing the bremsstrahlung continuum intensity between EUV and visible wavelength ranges.　The line of sight of EUVL-II is inclined to a downward direction to measure an entire profile of the impurity line emission at lower half ($0 \leq Z \leq -40$cm) of HL-2A tokamak plasmas.　The vertical position of impurity profile is absolutely calibrated by a metal bar with different widths installed at the diagnostic port, and the calibration is done with changing wavelengths. The spectra of tungsten introduced by laser blow-off (LBO) system is recorded by the EUVL-I spectrometer, and quasi-continuum spectra of tungsten is observed in three wavelength ranges of 25-42Å, 47-70Å and 140-280Å.　In addition, isolated line emissions of tungsten emitted from W^{6+} ion are measured for the first time in tokamak plasma, and are identified as 216.219Å (5p-5d) and 261.387Å (5p-5d), respectively.

1. Introduction

Spectroscopy provides a powerful tool to investigate impurity behavior in high temperature plasma. Impurity in plasma is mainly originated from the interaction of the plasma and plasma facing components. Tungsten is designated as the only material for ITER divertor plates.　The previous result shows impurity accumulation of high-Z elements at plasma core due to the neoclassical effect [1].　Therefore, it is essentially important to monitor the behavior of tungsten ions in ITER plasma, especially in divertor region. Since the electron temperature ranges in 25-100eV with a peak temperature of 150eV around X-point, the ionization states of W^{3+} to W^{10+} will be expected to appear in divertor plasmas and the wavelength range of 150-450Å is demonstrated to offer the best spectral region due to the existence of strong resonance lines of several tungsten ions [2].　As a result, it is highly desired to develop the spectroscopy in the extreme ultraviolet (EUV) range.

2. EUVL-I and EUVL-II spectrometer system

In order to monitor the impurity behavior and study impurity transport, two EUV spectrometers called EUVL-I and EUVL-II are developed in HL-2A.　The EUVL-I spectrometer is used for spectra wavelength measurement with high response and the EUVL-II spectrometer is used for impurity vertical profile measurement.　The arrangements of EUVL-I and EUVL-II spectrometers in HL-2A tokamak are shown in Fig. 1.　As shown in Fig. 1, the EUVL-I spectrometer is installed at position near the equatorial plane and the distance between the entrance slit and plasma center is 4.1m.　The line of sight of EUVL-II is inclined to a downward direction to measure an entire profile of the impurity line emission at lower half ($0 \leq Z \leq -40$cm) of HL-2A tokamak plasmas.　The distance between entrance slit and plasma center is 7.37m along the horizontal direction.　Both of EUVL-I and EUVL-II spectrometer have the similar structure, i.e., consisting of an entrance slit, a varied-line-spacing holographic grating and a CCD detector.　In the case of EUVL-II spectrometer, a spaced-resolved slit is additionally installed to realize the vertical profile measurement.　The entrance silt with width of 30μm is utilized in EUVL-I spectrometer and a spectral resolution of 0.22Å at 200Å is obtained.　The width of entrance slit and space-resolved slit of EUVL-II spectrometer are 100μm and 0.5mm, respectively.　The detective area of CCD camera is 26.6×6.6mm^2 corresponding to 124×255 pixels.　An electric motor is externally controlled for the wavelength scan through LAN network, and it enables the wavelength measurement of EUVL-I spectrometer in wavelength range of 20-500Å.　Since the CCD detector is rotated 90° in EUVL-II spectrometer system for vertical profile measurement, the size used to record spectra wavelength is reduced by a factor of 4, indicating a narrower wavelength range of EUVL-II spectrometer.　In order to realize measurement in the similar wavelength range to EUVL-I, a two-stage wavelength scanning system for moving CCD position along the focal plane is designed for EUVL-II and it enables the vertical profile measurement in wavelength range of 30-650Å.
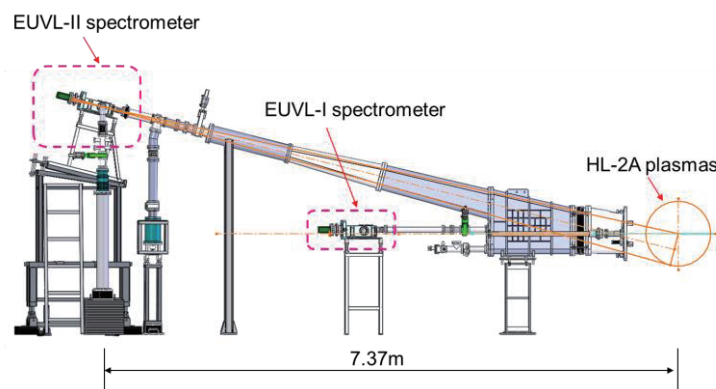
Fig. 1 The arrangement of EUVL-I and EUVL-II spectrometers in HL-2A.

3. Absolute intensity calibration of EUVL-II spectrometer

In order to quantitatively study impurity behavior, the absolute intensity calibration of EUV spectrometer is needed.　The branching ratio technique is one of the conventional method for the absolute intensity calibration of vacuum ultraviolet (VUV) spectrometer, and another method is to used standard

light source.   Both methods have their limits and are not suitable for the absolute intensity calibration of EUV spectrometer.   Here, the absolute intensity calibration is done by comparing the bremsstrahlung continuum intensity between EUV and visible wavelength ranges [3].

The bremsstrahlung radiation power in unit of W cm^{-3} Å^{-1} is expressed by

$$p_{brem} = \frac{1.89 \times 10^{-28} n_e^2 Z_{eff} g_{ff}}{T_e^{1/2} \lambda^2} \exp(-\frac{12400}{T_e \lambda}) \tag{1}$$

where Z_{eff} is the effective ion charge, g_{ff} is the free-free gaunt factor, and λ is the corresponding wavelength in unit of Å.

When both the EUV and visible bremsstrahlung radiation are measured simultaneously, the radiation power ratio of EUV bremsstrahlung to visible bremsstrahlung can be derived from Eq. (1) as

$$\frac{p_{brem\_EUV}}{p_{brem\_Vis}} = (\frac{\lambda_{Vis}}{\lambda_{EUV}})^2 \frac{g_{ff\_EUV}}{g_{ff\_Vis}} \exp\left[-\frac{12400}{T_e}(\frac{1}{\lambda_{EUV}} - \frac{1}{\lambda_{Vis}})\right] \tag{2}$$

where P_{brem_EUV} and P_{brem_Vis} are the bremsstrahlung radiation power in EUV and visible ranges, and g_{ff_EUV} and g_{ff_Vis} are the gaunt factors in EUV and visible ranges, respectively.   The bremsstrahlung radiation in EUV range could be obtained based on the Eq. (2) by taking account of the wavelength and electron temperature, since it is easy to get bremsstrahlung radiation in visible range with absolute value. Then, the absolute intensity calibration factor for EUV spectrometer could be obtained by comparing the calculated bremsstrahlung radiation with the one measured experimentally. The bremsstrahlung radiation from calculation and experiment at different wavelength positions are shown in Fig. 2(a).   It can be seen that both have the similar tendency, decreasing with increasing wavelength.   The calibration factors at the selected wavelength positions are shown in Fig. 2(b), in which the hollow circle indicates the factor from experiment and solid line indicates the fitting curve.   Finally, the calibration factor at 20-300Å is obtained as shown in Fig. 3.   Here, the calibration factor increases with wavelength, indicating higher sensitivity at shorter wavelength range.   However, the calibration factor below 50Å is also increased due to grating efficiency.
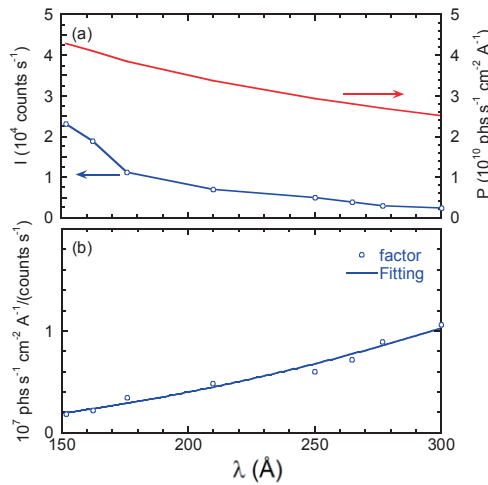
Fig. 2 (a) Bremsstrahlung radiation from calculation and experiment at different wavelength positions, and (b) the absolute intensity calibration factor.
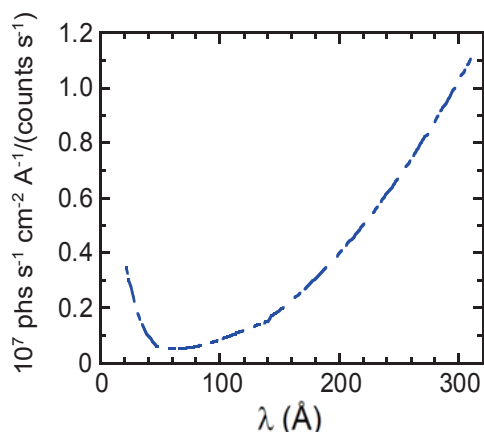
Fig. 3 Absolute intensity calibration factor of EUVL-II spectrometer as a function of wavelength.

4. Vertical position calibration of EUVL-II spectrometer

EUVL-II spectrometer is developed for the impurity vertical profile measurement and detecting the emission from the lower half of plasma, i.e., $-5 \leq Z \leq -45cm$, as shown in Fig. 1. The vertical profile recorded by CCD detector is in unit of channel combined by several pixels as the upper horizontal axis shown in Fig. 4 in which vertical profile of CVI (1s-2p: 33.73Å) is presented. For the quantitatively analysis, the absolute vertical position of impurity profile is required. In other word, we have to find the spatial position corresponding to the channel. A metal bar with width of 1cm is installed at the diagnostic port for the purpose. And an intensity gap could be observed in the impurity profile as shown in Fig. 4, since the intensity there is hided by the metal bar. Based on the metal bar, the spatial position of channel could be obtained as the lower horizontal axis shown in Fig. 4. Here, a simple geometrical relation is used for the calibration, i.e., the detectable range is proportional to the distance from CCD detector to entrance slit of EUVL-II spectrometer. From the principle of this EUV spectrometer, we know that the distance from CCD detector to entrance slit is a function of wavelength and is increasing with wavelength. Therefore, the vertical position calibration has to be done in working wavelength range of EUVL-II spectrometer.

The vertical profiles of CVI (33.73Å×2) and HeII (303.78Å) measured with a metal bar in ch230-290 are shown in Fig. 5, in which the arrow indicates the center of the hided area. It is seen that the center is shifted from ch259 in CVI to ch263 in HeII, indicating that it is necessary to do the vertical position calibration at different wavelength. Finally, the position of metal bar projected onto CCD detector as a function of wavelength is obtained as shown in Fig. 6 in which the blue solid circle is from the experiment and solid line is fitting curve. It can be seen that position of metal bar projected onto CCD detector is shifted to reduced channel with increased wavelength.
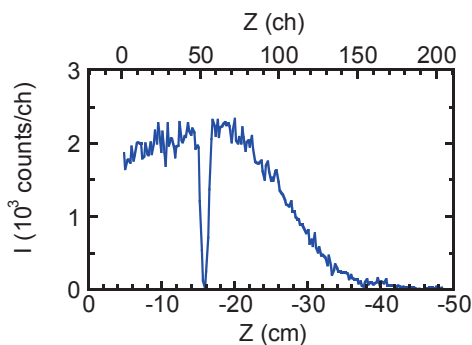
Fig. 4 Vertical profile of CVI (1s-2p: 33.73Å) in unit of channel (upper horizontal axis) and cm (lower horizontal axis).
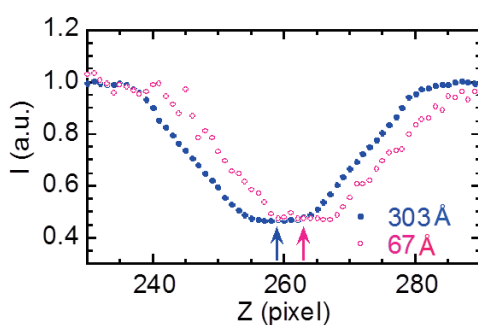
Fig. 5 Vertical profiles of CVI (33.73Å×2) and HeII (303.78Å) measured with a metal bar.
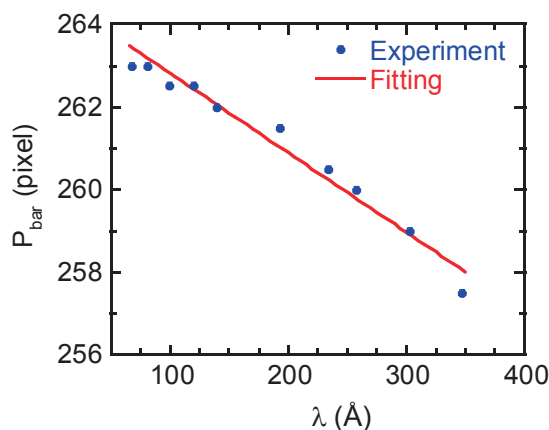
Fig. 6 Position of metal bar projected onto CCD detector as a function of wavelength.

5. Tungsten spectra observed by EUV spectrometer

In order to study tungsten spectra in HL-2A, the laser blow-off (LBO) system is utilized for the tungsten introduction. The tungsten spectra are observed by EUV spectrometer in the wavelength range of 25-290Å as shown in Fig. 7(a) and (b) with spectra before the tungsten injection. It should be noted that the spectra showed here are combined from several discharges since the wavelength interval from EUV spectrometer for one discharge can not cover the wavelength from 25-300Å. As seen in Fig. 7, tungsten quasicontinuum at different wavelength ranges are observed, i.e., in 25-42Å, 47-70Å and 140-280Å. As observed in other machines, the spectra around 50Å are attributed to the superposition of emissions from

different ionization states, and are mainly contributed by line emissions from W^{14+} to W^{23+} ions in the present HL-2A experiment.   Additional emissions appeared from 100Å to 120Å which have the similar structure to spectra around 50Å are identified to be the second order of spectra around 50Å.   The quasicontinuum from 140 to 280Å with lower intensity are also observed and found be emitted from the lower charge states, and the charge states of WXXII-XXX are considered to contribute to the spectra band around 30Å.

In addition, two isolated spectral lines with strong intensity at wavelength of 216Å and 261Å are also observed after the tungsten injection, as shown in Fig. 7(b).   In order to identify the lines, the temporal behaviors of the lines are compared with the spectral lines emitted from the intrinsic impurities.   The main intrinsic impurities in HL-2A tokamak are carbon, oxygen and helium, accompanying with iron, nitrogen and molybdenum in some discharges.   The time traces of HeII (303.78Å), OVI (150.09Å), FeXV (284.15Å), CVI (33.73×4Å, fourth order) are used for the comparison together with quasicontinuum of tungsten at 212Å and the two newly appeared lines.   Finally, it concludes that the newly appeared lines should emitted from a new element.   These two lines always come in pairs with the same temporal evolution, indicating these lines should be produced by the same elements.   Compared with the line lists from NIST Database [4], these two lines are finally identified to be the transitions of 5p-5d at 216.219Å and 5p-5d at 261.387Å from W^{6+} ion.   Although it is the first result from tokamak plasmas, it shows the same result as the result from SSPX [3].
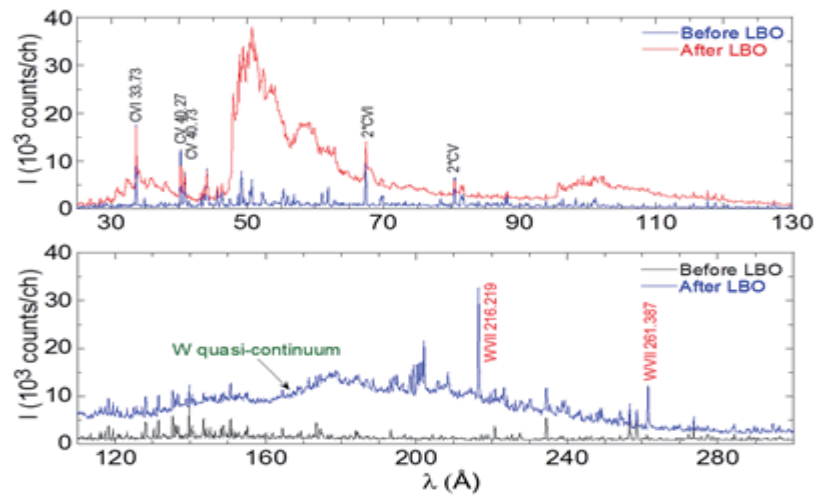
Fig. 7 EUV spectra in wavelength ranges of (a) 25-130Å and (b) 110-290Å before and after tungsten injection.

6. Summary

Two EUV spectrometers (EUVL-I and EUVL-II) are successfully developed in HL-2A for impurity profile measurement and impurity transport study.   The absolute intensity calibration of EUV spectrometer is done based on the bremsstrahlung measurement in both EUV and visible ranges.   A metal bar is utilized for the absolute vertical position of impurity profile.   The vertical calibration is done as a function of wavelength.   Tungsten is introduced into HL-2A plasma by means of LBO system and the tungsten

spectra is measured by EUV spectrometer in wavelength range of 25-300Å. The result shows that quasicontinuum are observed at three different wavelength ranges, i.e., in 25-42Å, 47-70Å and 140-280Å. Line emissions from W^{6+} ion are measured for the first time in tokamak plasmas and identified to be 216.219Å (5p-5d) and 261.387Å (5p-5d).

Acknowledgement

Reference

[1] Hirshman S.P, et al., 1981 Nucl. Fusion **21 1079**

[2] Clementson J. et al., 2010 J. Phys. B: At. Mol. Opt. Phys. **43** 144009

[3] Dong. C.F. et al 2011 Rev. Sci. Instrum. **82** 113102

[4] Ralchenko Y, Kramida A E, Reader J and NIST ASD Team (2008) NIST ASD Atomic Spectra Database (ver sion 3.1.5) [online at http://physics.nist.gov/asd3, august 25 2008]

An n=1 explosive instability and its role in disruptions

A. Y. Aydemir, B. H. Park and Y. K. In

National Fusion Research Institute, Daejeon 34133, S. Korea

Abstract

Low-n kink-ballooning modes not far from marginal stability may exhibit a bifurcation between two very distinct nonlinear paths that depends sensitively on the background transport levels and linear perturbation amplitudes. Here an $n = 1$ infernal mode is investigated in reversed shear equilibria where the region around the safety-factor minimum provides the low-shear conditions necessary for instability. For a certain range of parameters, a relatively benign path results in a saturated "long-lived mode" (LLM) that causes little confinement degradation. At the other extreme, the quadrupole geometry of the 2/1 perturbed pressure field evolves into a ballooning finger that subsequently transitions from exponential to explosive growth. The finger eventually leads to a fast disruption with precursors too short for any mitigation effort. Interestingly, the saturated LLM state is found to be metastable; it also can be driven explosively unstable by finite- amplitude perturbations. Similarities to some high-β disruptions in reversed-shear discharges are discussed.

1. Introduction

Since both NTM's and RWM's grow on a slow, resistive time scale, disruptions caused by these modes are easily identified by their long precursors on various diagnostics. In fact, because of their relatively slow time scale, these are precisely the type of disruptions that are targeted by various disruption mitigation schemes, which require at least a few 10's of milliseconds of warning time[1, 2]. However, tokamaks disrupt for a wide variety of reasons (see for example [3]), and not all disruptions follow this slow path where their arrival is well-advertised in advance; some in fact occur with little warning. Unfortunately, their very fast time scale apparently makes detailed studies difficult, and their appearance in the experimental literature has been rare, especially in the last decade where the emphasis seems to have shifted to mitigation of slow, NTM or RWM-mediated disruptions.

There do exist some documented high-β disruptions with precursors of the order of a millisecond or less. For example: β-limit disruptions in TFTR due to toroidally localized ballooning modes in the presence of $n = 1$ magnetohydrodynamic (MHD) activity [4,5], localized resistive interchange modes that couple to a global $n = 1$ mode and lead to a disruption in negative central shear (NCS) discharges in DIII-D[6,7], and disruptions following an internal transport barrier (ITB) collapse in JET[8]. In these discharges, some of the important details were clearly different: in TFTR, at least initially, the $q = 1$ surface was involved, whereas DIII-D and JET presumably both had $q_{min} \simeq 2$. But generally, a large pressure gradient in regions of weak magnetic shear is believed to have played an essential role in all of them.

Linear stability analysis alone cannot explain the fast timescale of these disruptions. The mode has to

be growing near Alfvenic rates to account for the time scale, but it is not clear how a discharge evolving on the slow transport time scale can generate an unstable mode with a near-Alfvenic growth rate without producing a long series of precursor oscillations during its sub-Alfvenic period. Thus we have to consider processes that can make changes in the growth rate $\gamma(t)$ much faster than expected from transport alone.

There are nonlinear processes in plasmas that can generate explosive (faster-than-exponential) growth while the underlying mode is still not far from marginal stability. In a numerical study of the semi-collisional/collisionless $m = 1$ mode using a reduced two-fluid model, nonlinearities involving the parallel pressure gradient were shown to give a near-exponential increase in the growth rate of the mode[9], providing a possible explanation for precursor-less, fast sawtooth crashes. Similarly, Cowley and colleagues[10,11] have shown that the nonlinear evolution of pressure-driven modes can generate finite-time singularities, again demonstrating how a long period of precursors can be avoided during a fast disruptive event.

2. The explosive instability and disruptions

An ideally unstable $n = 1$ mode with its large growth rate will naturally lead to a fast disruption. As discussed at some length in the Introduction, however, MHD modes are not "born" in this robustly unstable state. They tend to come into existence as weak resistive instabilities as the equilibrium slowly (on transport time scale) passes through some marginal stability point due to the evolving discharge conditions. Hence our goal in this section is to demonstrate how a weak resistive instability can evolve into a robust mode that will result in a fast disruption with only a brief period of precursors. Thus we start with a weakly unstable equilibrium where some of the relevant parameters are: $q_0 = 2.145$, $q_{min} = 2.023$, $q_l = 9.424$, $\beta_N = 1.67$. With weak shear and $q_{min} > 2$, an important feature of the linear eigenfunction is the dominance of the $m = 2$ poloidal component. This is clearly seen in Fig. 1(a), which shows the quadrupole geometry of the pressure. This perturbation leads to an elliptical deformation of the flux surfaces in the core plasma that eventually forms a ballooning finger, as seen in Figs. 1(b-c). The finger pushes through the flux surfaces on near-Alvenic time scales and brings the core plasma in contact with the boundary (Fig. 1(d)). Using typical parameters for modern tokamaks ($B = 3$ T, $n_e = 10^{19}$ cm^{-3}, $R_0 = 1.5$ m), the state with no visible deformation in Fig. 1(b) and the final state in Fig. 1(d) are separated by less than 1 ms. Thus an actual disruption following this path would have a very short warning time.

There have been observations of ballooning fingers during high-β disruptions in TFTR[4,5]. JET also has reported similar results. During disruptions following an ITB collapse, localized disturbances in the ECE data that propagate from the ITB to the edge at velocities approaching 3km/s are seen. These experimental observations can be associated with the radial propagation of a ballooning finger as shown here. In fact, a comparison of synthetic ECE diagnostics from our calculations with the JET data from Ref. [12] (their Fig. 4) shows good agreement, as seen in Fig. 2.
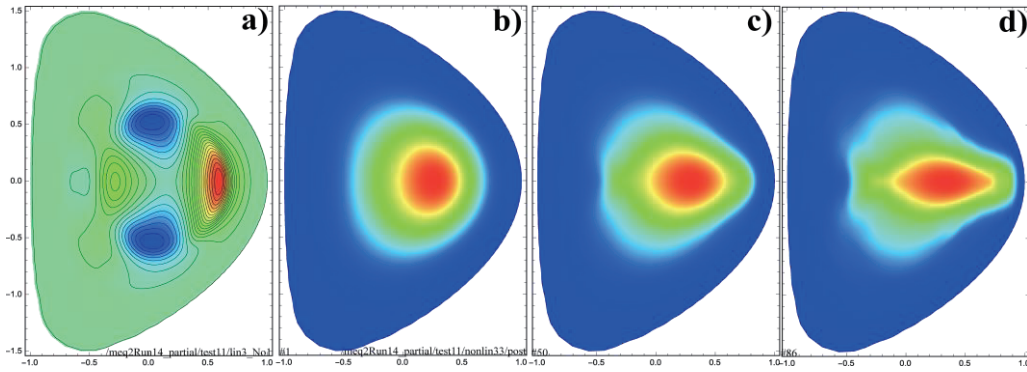
Fig.1 The pressure field. (a) n = 1 eigenfunction showing the dominance of the m = 2 harmonic. The ballooning nature of the mode, with its in-out asymmetry, is easily visible. (b-d) Nonlinear development of the explosive finger. In units of the poloidal Alfven time, $t_b = 2.242 \times 10^3$, $t_c = 4.008 \times 10^3$, $t_d = 4.271 \times 10^3$.
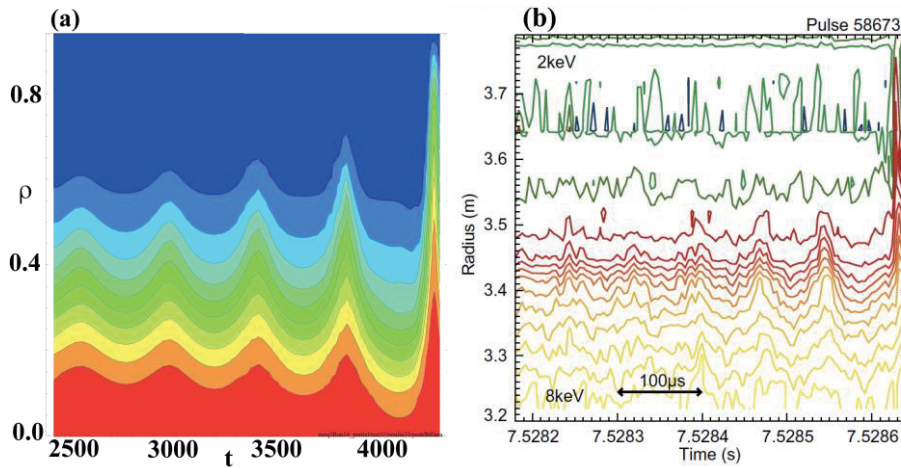
Fig.2 Comparison of synthetic ECE diagnostics with the JET data from Ref. [12]. (a) Computational data with an assumed rigid toroidal rotation of period $425\tau_A$. Note the narrowing of the finger in the time domain as it propagates radially outward, which of course corresponds to toroidal localization. (b) Experimental ECE contours from JET (Fig. 4 from Ref. [12], used with permission).

3. Bifurcated states

Here we demonstrate that a small change in a transport coefficient can lead to a bifurcation between a benign, saturated state (the long-lived mode, LLM) and an explosive instability for the n = 1 kink-ballooning mode. The bifurcation is summarized in Fig. 3 where we follow the nonlinear evolution of the mode starting with the same initial conditions and linear perturbation, but using slightly different transport coefficients. With S = 106, thermal conductivity $\kappa_\perp = 4 \times 10^{-6}$ and viscosity $\mu = 1 \times 10^{-5}$, the mode goes through an exponential growth phase but saturates at a small amplitude (curve (1) in Fig. 3(a)).
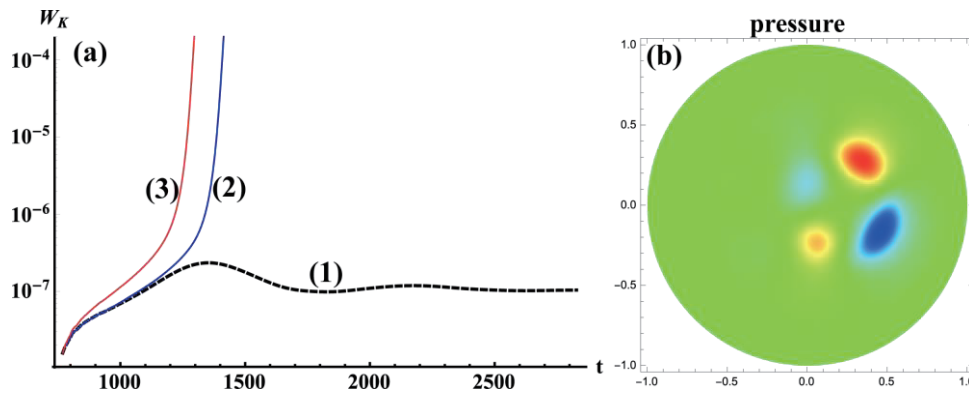
Fig.3 (a) Time histories of the total kinetic energy in the n ≥ 1 modes during the nonlinear evolution of the n = 1 kink-ballooning mode. (b) Saturated pressure field for the long-lived mode (curve (1) in (a)). In order to bring out the details, the axisymmetric component (n = 0) has been subtracted

In a slightly less dissipative system with $\kappa_\perp = 3.5 \times 10^{-6}$ but $\mu = 1 \times 10^{-5}$ still, the mode initially follows a similar path and goes through an exponential-growth phase (curve (2) in (a)). However, instead of saturating, it gradually enters a super-exponential regime where the growth rate itself increases rapidly, eventually becoming explosive. A similar effect is seen with reduced viscosity: with $\mu = 6 \times 10^{-6}$, $\kappa_\perp = 4 \times 10^{-6}$ the mode again transitions into the explosive regime (curve (3)).

4. Summary and discussion

In this work we demonstrate that the nonlinear evolution of a pressure-driven n = 1 kink-ballooning mode can exhibit a bifurcation between a benign final state with little confinement degradation–a long-lived mode (LLM), and an explosive instability that results in a fast disruption with very short precursors. The bifurcation depends sensitively on assumed transport levels and the initial perturbation amplitude. Large diffusive transport or too small a perturbation leads to a saturated n = 1 LLM. Equivalently, there is a transport-dependent critical perturbation amplitude, $v_{cr} = v_{cr}(\eta, \mu, \kappa_\perp, ...)$, such that $v > v_{cr}$ leads to explosive behavior. The long-lived mode itself is metastable and can be pushed into the explosive regime, again with a finite perturbation above a threshold. Thus it is possible that a LLM can abruptly terminate with a fast disruption.

Acknowledgements

References

[1] R.S. Granetz, E.M. Hollmann, D.G. Whyte, et al., Nucl. Fusion, 47:1087, 2007.

[2] E. M. Hollmann, P. B. Aleynikov, T. Fulop, et al., Phys. Plasmas, 22:021802, 2015.

[3] P.C. de Vries, M.F. Johnson, B. Alper, et al., Nucl. Fusion, 51:053018, 2011.

[4] E. D. Fredrickson, K. McGuire, Z. Chang, et al., Phys. Plasmas, 2:4216, 1995.

[5] E. D. Fredrickson, K. M. McGuire, Z. Y. Chang, et al., Phys. Plasmas, 3:2620, 1996.

[6] M. S. Chu, J. M. Greene, L. L. Lao, et al., Phys. Rev. Lett., 77:2710, 1996.

[7] R. Jayakumar, T. C. Luce, T. S. Taylor, et al., Phys. Plasmas, 9:5043, 2002.

[8] J. I. Paley, P. Andrew, S. C. Cowley, et al., J. Nucl. Mater., 337-339:702, 2005.

[9] A. Y. Aydemir. Phys. Fluids B, 4:3469, 1992.

[10] Steven C. Cowley and Mehmet Artun, Phys. Reports, 283:185, 1997.

[11] H. R. Wilson and S. C. Cowley, Phys. Rev. Lett., 92:175006, 2004.

[12] J. I. Paley, P. Andrew, S. C. Cowley, W. Fundamenski, J. Nucl. Mater., 337-339:702, 2005.

Turbulence study with microwave imaging reflectometer in KSTAR plasmas

W.Lee[1], S.H.Ko[1], M.J.Choi[1], J.Leem[2], G.S.Yun[2], H.K.Park[1,3], W.X.Wang[4], R.V.Budny[4], K.W.Kim[5], N.C.Luhmann,Jr.[6], and the KSTAR team

[1]National Fusion Research Institute, Daejeon 34133, South Korea

[2]Pohang University of Science and Technology, Pohang, Gyeongbuk 37673, South Korea

[3]Ulsan National Institute of Science and Technology, Ulsan 44919, South Korea

[4]Princeton Plasma Physics Laboratory, Princeton, New Jersey 08543, USA

[5]Kyungpook National University, Daegu 41566, South Korea

[6]University of California at Davis, Davis, California 95616, USA

Abstract

Characteristics of electron density fluctuations in low-density L-mode plasmas heated tangential neutral beam injection has been analyzed. The frequencies of the fluctuations from cross-coherence spectra are quasi-coherent: the peak frequencies range from ~150 kHz to ~400 kHz and the bandwidths are from ~150 kHz to 250 kHz. The poloidal wavenumbers estimated from the peak frequencies and poloidal rotation velocities of the fluctuations are ~2−4 cm^{-1}, which have been found to be qualitatively comparable to those of the fastest growing modes (with maximum linear growth rates) predicted from linear GYRO simulations. On the other hand, the measured wavenumbers are roughly a factor of three larger than those of the transport-dominant modes (with maximum mixing length estimates), which seem to be related to the fluctuations at lower peak frequencies (~80 kHz to ~150 kHz) observed in some of the cross-coherence spectra. A nonlinear GTS simulation has shown that the lower frequency mode can be driven nonlinearly.

1. Introduction

In recent study for the L-mode discharges heated by tangential neutral beam injection (NBI) in KSTAR [1], ion-gyroscale fluctuations in the electron density were measured and characterized using a microwave imaging reflectometer (MIR) [2, 3]. Spatial scale in poloidal direction ($\ell_\theta/\rho_i = 5-10$) and temporal scale ($\tau_c = 2-6$ μs) of the measured fluctuations were found to be linearly dependent on the local equilibrium parameters relevant to ion-gyroscale turbulence, where ℓ_θ is the poloidal correlation length, ρ_i is the ion gyroradius, and τ_c is the correlation time. For one of the NBI-heated L-mode discharges, the poloidal wavenumbers of dominant modes (or most unstable modes) at two radii in a core region, estimated from the peak frequencies and poloidal rotation velocities of the fluctuations in laboratory frame, were consistent with those predicted from linear and nonlinear gyrokinetic simulations [4]. Here, the linear stability calculation with the GYRO code [5] was carried out without consideration of external flow and its shear, while the nonlinear simulation with the GTS code [6, 7] included equilibrium E × B flow and its shear. Note that the poloidal wavenumbers obtained from the two (linear and nonlinear) simulations were similar, and this similarity may be due to a weak E × B flow shear.

The comparison study of the poloidal wavenumbers of the dominant modes between the measurement and linear gyrokinetic simulation for more NBI-heated L-mode discharges has been extended to examine universality of the result in reference [4], and discussed the reason why these two results can be comparable to each other in the core region of these plasmas. Here, we have used two different definitions for the dominant mode from the linear simulation: the 'fastest growing mode' with maximum linear growth rate and the 'transport-dominant mode' with maximum mixing length estimate. For the latter, a number of simulation studies already demonstrated that the linear modes with maximum mixing length estimates resemble the transport-dominant modes obtained from nonlinear simulations [8, 9, 10]. Thus, the transport-dominant mode can be considered as the dominant mode predicted by nonlinear simulation.

2. Poloidal wavenumbers of dominant modes in a core region

The poloidal wavenumbers (k_θ) of dominant modes can be deduced from two experimentally measured parameters: peak frequency (f_{peak}) and poloidal rotation velocity (v_θ) of the broadband fluctuations in the laboratory frame, both of which were obtained from 1D measurements in the poloidal direction. This is based on a simple relationship, $2\pi f_{peak} \approx k_\theta v_\theta$, indicating that the f_{peak} of fluctuations (turbulence or coherent mode) primarily depends on k_θ and v_θ.

Typically, coherent (bandwidth $\Delta f \sim$ a few kHz) modes or quasi-coherent modes ($\Delta f \sim$ tens of kHz, up to ~150 kHz) modes [11] can be identified from their power spectra whereas the broadband ($\Delta f \sim$ hundreds of kHz) fluctuations of small-amplitude sometimes are not clear in the spectra. For such broadband fluctuations, the peak frequency can be obtained from cross-coherence spectra. Note that the cross-coherence is a measure of similarity between two signals (from different positions in space) as a function of frequency. Cross-coherences of the signals from multiple poloidal channels with respect to a reference channel can have their local peaks around a single frequency, which has been chosen as the peak frequency. Figure 1 demonstrates examples of two frequency analysis methods, Fourier analysis and cross-coherence analysis. For the fluctuations at two radii in the discharge #9008, broadband fluctuations with a local peak (at ~280 kHz for the fluctuations at R ~ 2.05 m and ~170 kHz for those at R ~ 2.10 m) are clearly identified in the coherence spectra of multichannel signals but not in the spectrum of a single channel signal. Note that another broadband fluctuations can be seen around a lower frequency of ~90 kHz in the coherence spectra for the fluctuations at R ~ 2.05 m.
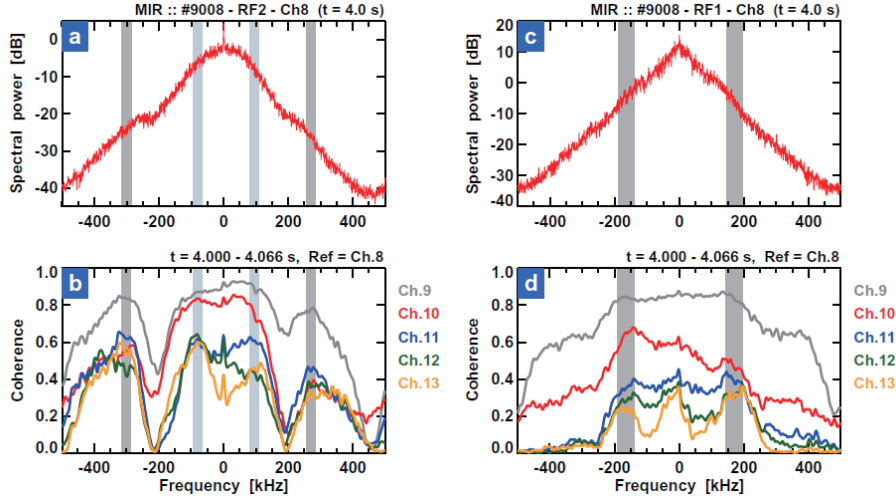
Fig.1 Frequency analysis results for the fluctuations at (a, b) R ~ 2.05 m and (c, d) R ~ 2.10 m in the discharge #9008. (a, c) spectrum of the MIR inphase/quadrature (IQ) signals from a center channel #8 at t = 4.0 s and (b, d) spectra of cross-coherences of the IQ signals from the poloidal channels 9 to 13 with respect to channel 8.

The time-delayed cross-correlations of the multichannel signals can provide the v_θ of fluctuations. The physical meaning of the obtained v_θ of fluctuations is well described in references [1, 12, 13]. For the fluctuations at two radii (~2.05 m and ~2.10 m) in the discharge #9008, the v_θ are ~4.9 km/s and ~4.4 km/s, respectively in ion diamagnetic drift direction (clockwise in the poloidal cross section) [1]. Therefore, the k_θ derived from the f_{peak} and v_θ are ~3.5 cm^{-1} and ~2.4 cm^{-1}, respectively.

3. Comparison with the results of linear gyrokinetic simulation

The k_θ of the dominant modes estimated from the 1D MIR measurement are compared with those predicted from linear gyrokinetic simulation conducted using GYRO. In the linear GYRO simulation, we have included the parallel flow velocity ($U_\parallel$) and its shear ($\gamma_\parallel$), which is known to enhance the turbulence level [14, 15]. Figure 2 illustrates the simulation results with and without $U_\parallel$ and $\gamma_\parallel$. The linear growth rate (γ) and real angular frequency in the plasma frame (ω_0) are plotted as a function of the normalized poloidal wavenumber ($k_\theta\rho_s$), where ρ_s is the ion gyroradius at electron temperature. Note that the modes with positive (or negative) ω_0 propagate in the electron (or ion) diamagnetic drift direction. The destabilization effect of the parallel flow shear on both γ and ω_0 is small. The linear modes are most unstable at $k_\theta\rho_s \approx$ 0.3−0.5 except for the discharge #9008 at R ~ 2.10 m showing a flat growth rate from $k_\theta\rho_s$ ~ 0.5 (this value is chose as the dominant mode wavenumber).
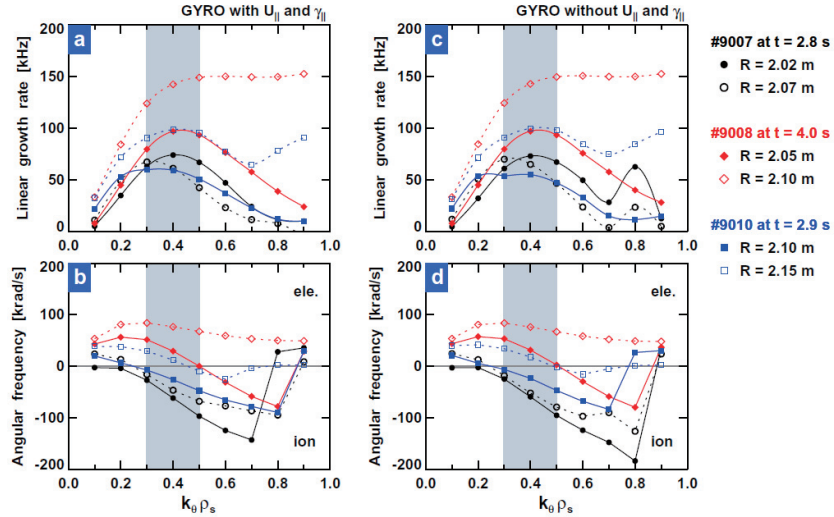
Fig. 2 Linear GYRO simulation results for the NBI-heated L-mode discharges at two radii (a, b) with and (c, d) without $U_\parallel$ and $\gamma_\parallel$: (a, c) the linear growth rate γ and (b, d) real angular frequency ω_0 as functions of the normalized poloidal wavenumber $k_\theta\rho_s$. The shaded region indicates the normalized wavenumber range in which the growth rates are the maximum. The linear modes with positive (or negative) ω_0 propagate in the electron (or ion) diamagnetic drift direction.

In this study, we have chosen the fastest growing mode as the dominant mode from linear simulation based on the result in reference [4]. However, former simulation studies showed that (1) linear modes in the transport-dominant wavenumber range persist in the nonlinear saturated phase [8] and (2) the wavenumbers associated with the maximum heat flux obtained from nonlinear simulation sometimes resemble those corresponding to the maximum of the mixing length estimate ($\gamma/k_\perp^2$) from linear simulations [9, 10]. Thus, the transport-dominant mode (with maximum $\gamma/k_\perp^2$) is considered as the dominant mode predicted from nonlinear simulations. The measured k_θ of the dominant modes by MIR are compared with those from GYRO simulation in figure 3. The k_θ from the measurements are qualitatively comparable to those of the fastest growing modes, whereas they are roughly a factor of three larger than those of the transport-dominant modes.
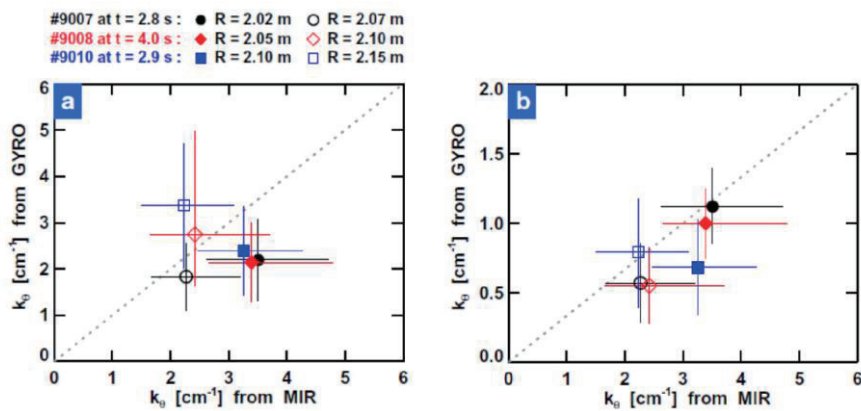
Fig. 3 Comparison of the poloidal wavenumbers of the dominant modes between the measurement and linear simulation for the NBI-heated L-mode discharges at two radii. The dominant mode from the linear simulation is defined as (a) the fastest growing mode and (b) transport-dominant mode.

130

In figure 1(b), one can find another broadband fluctuations with local peak around a lower frequency of ~90 kHz in the cross-coherence spectra, which is about one third of the higher frequency of ~280 kHz. It implies that the wavenumber of the lower frequency mode is about third of that of the higher frequency mode. Thus, we cautiously suggest that the higher frequency (or higher k_θ) mode is associated with the fastest growing mode (primary mode), whereas the lower frequency (or lower k_θ) mode with the transport-dominant mode (secondary mode nonlinearly driven by the primary mode).

4. Summary

We have characterized the electron density fluctuations measured by the multichannel MIR in the core region of the NBI-heated L-mode plasmas in KSTAR. The fluctuations are quasi-coherent from cross-coherence spectra, i.e., the bandwidth (~150 kHz to ~250 kHz) are comparable to the local peak frequencies (~150 kHz to ~400 kHz). The poloidal wavenumbers of the dominant modes responsible for the fluctuations have been deduced from the peak frequencies and poloidal rotation velocities of the fluctuations in the laboratory frame. And they have been compared to the wavenumbers of two types of the dominant modes predicted from linear GYRO simulation. The measured poloidal wavenumbers of ~2−4 cm^{-1} are found to be qualitatively comparable to the wavenumbers of the fastest growing modes (with maximum linear growth rates). On the other hand, the measured wavenumbers are roughly a factor of three larger than the wavenumbers of the transport-dominant modes (with maximum mixing length estimates), which seem to be related to the fluctuations at lower peak frequencies (~80 kHz to ~150 kHz) observed in some of the cross-coherence spectra.

References

[1] W.Lee, J.Leem, G.S.Yun, et al., Phys. Plasmas **23** (2016) 052510.

[2] W.Lee, J.Leem, G.S.Yun, et al., J. Instrum. **8** (2013) C10018.

[3] W.Lee, J.Leem, J.A.Lee, et al., Nucl. Fusion **54** (2014) 023012.

[4] W.Lee, J.Leem, G.S.Yun, et al., Rev. Sci. Instrum. **87** (2016) 11E134.

[5] J.Candy J. and R.E.Waltz, J. Comput. Phys. **186** (2003) 545.

[6] W.X.Wang, Z.Lin, W.M.Tang, et al., Phys. Plasmas **13** (2006) 092505.

[7] W.X.Wang, P.H.Diamond, T.S.Hahm, et al., Phys. Plasmas **17** (2010) 072511.

[8] T.Dannert and F.Jenko, Phys. Plasmas **12** (2005) 072309.

[9] F.Jenko, T.Dannert and C.Angioni, Plasma Phys. Control. Fusion **47** (2005) B195.

[10] J.Citrin, C.Bourdelle, P.Cottier. et al., Phys. Plasmas **19** (2012) 062305.

[11] H.Arnichand, R.Sabot, S.Hacquin, et al., Nucl. Fusion **55** (2015) 093021.

[12] Y.-c.Ghim, A.R.Field, D.Dunai, et al., Plasma Phys. Control. Fusion **54** (2012) 095012.

[13] J.E.Lee, G.S.Yun, W.Lee, et al., Sci. Report **7** (2017) 45075.

[14] R.E.Waltz, G.D.Kerbel and J.Milovich, Phys. Plasmas **1** (1994) 2229.

[15] C.M.Roach, I.G.Abel, R.J.Akers, et al., Plasma Phys. Control. Fusion **51** (2009) 124020.

Increase of turbulent fluctuations and bifurcation of perpendicular flow on the ELM-crash suppression under n=1 RMP

J.Lee[1], Y.M.Jeon[1], Y.In[1], G.Y.Park[1], M.J.Choi[1], G.S.Yun[2], M.Kim[3], W.Lee[1], J.H.Lee[1], W.H.Ko[1], H.K.Park[1,3] and KSTAR team

[1]National Fusion Research Institute, Daejeon 34133, Republic of Korea

[2]Pohang University of Science and Technology, Pohang 37673, Republic of Korea

[3]Ulsan National Institute of Science and Technology, Ulsan 44919, Republic of Korea

Abstract

The evidence of perpendicular flow ($v_\perp$) bifurcation at the onset of ELM-crash suppression has been measured using electron cyclotron emission imaging (ECEI) system for the first time in KSTAR. The ECEI has shown that (1) resonant magnetic perturbation (RMP) enhances small scale turbulent fluctuations in the edge toward the ELM-crash suppression phase, (2) the induced turbulence regulates growth of the ELM filament via nonlinear interaction between them. Cross spectra and correlation analysis among the ECEI channels revealed that the ELM crashes get suppressed along with a rapid reduction of $v_\perp$ close to zero (small but finite value) together with decrease of its shear.

1. Introduction

The high-confinement (H-mode) is characterized by the formation of transport barrier at the edge, which develops a steep pressure gradient called pedestal [1]. The H-mode is considered a milestone for achieving higher density and temperature for ignition conditions. However, due to the steep pressure gradient and associated high current density at the edge, the H-mode is accompanied with burst of magnetohydrodynamic instabilities referred to as the edge-localized modes (ELMs) [2]. The growth of ELMs leads to periodic collapse of the pedestal through an explosive bursting, and thereby damages the plasma facing components and divertor as well as reduction in plasma energy confinement by ~10-20 %.

One method to control ELMs is to perturb the edge of magnetic fields, which enhances particle transport and keeps the edge pressure gradient below the threshold of ELM crash. This method, called resonant magnetic perturbation (RMP), has been applied in several tokamaks.

2. Increase of turbulent fluctuations in ELM-crash suppression

Correlation analyses among ECEI channels were performed to understand the underlying physics of ELM-crash suppression. Figure 1 shows the cross-phase and coherence measurement of 5 (radial) $\times$ 3 (poloidal) ECEI channels, which are roughly covering 10×5 cm^2 near the plasma separatrix. The broadband and low frequency coherent modes ($f < 70\,kHz$) exist along the poloidal direction in narrow radial zone during the ELM-crash suppression [3]. It means that the RMP cannot suppress the onset of ELM filament but instead provide the damping against the ELM crashes, and the ELM-crash suppression is

characterized by the coexistence of ELM filament and turbulent eddies at the edge.
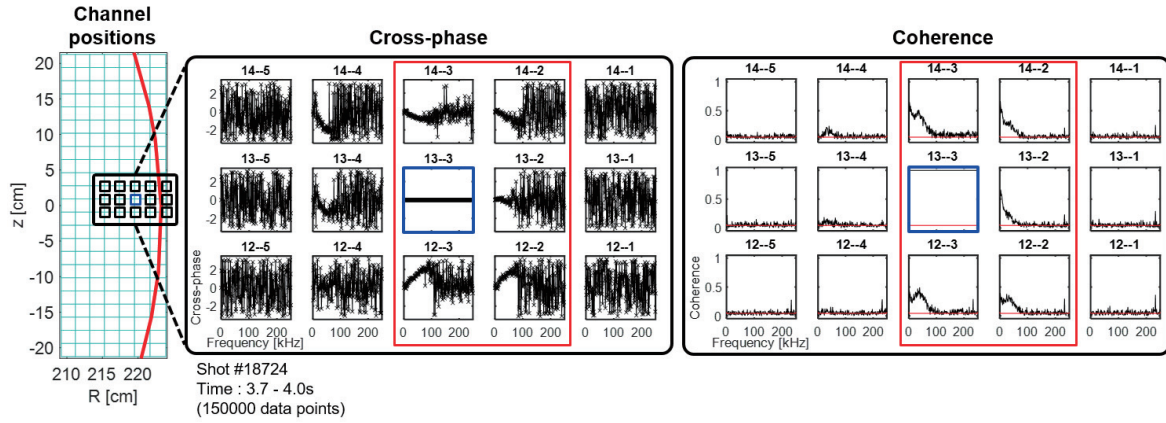
Fig. 1 The cross-phase and coherence measurement using ECEI channels. The red line is the separatrix position and the blue box indicates the reference channel for analysis. The red horizontal line in the coherence plot is the statistical error limit.

3. Bifurcation of perpendicular flow at the onset of ELM-crash suppression

The velocity of modes in the ECEI view (dubbed as pattern velocity v_{pt}) can be decomposed into poloidal (v_{pol}) and toroidal (v_{tor}) velocity components as

$$v_{pt} = v_{pol} - v_{tor} \times \tan \alpha_* + v_{ph}/\cos \alpha_*,$$

Where α_* is pitch angle near the midplane and v_{ph} is the phase velocity of mode. In terms of mode pitch, above equation can be rewritten as

$$v_{pt} = v_\perp / \cos \alpha_*$$

With the perpendicular velocity $v_\perp$ because $v_\perp = v_{pol} \cos \alpha_* - v_{tor} \sin \alpha_* + v_{ph}$. Therefore the pattern velocity of mode in the ECEI view can be interpreted into the perpendicular velocity in general sinece the α_* is quite small ($\cos \alpha_* \approx 1$).

Figure 2 is the time history of the perpendicular flow velocity near the pedestal $v_{\perp,ped}$ and $v_{\perp,ped}$ shear at the transition into and out of ELM-crash suppression. The $v_{\perp,ped}$ estimated by the rotation of turbulent eddies has a value of ~ 10 km/s along the electron diamagnetic direction during the ELM-crash mitigated phase. The rapid $v_{\perp,ped}$ could prevent the penetration of resonant field into plasma, leading to the effective screening of RMPs [4]. The RMP screening disturbs the response of ELM and makes difficult to suppress the ELM crashes. As the RMP field strength exceeds the threshold, the plasma transits to the ELM-crash suppressed state and rapid bifurcation of $v_{\perp,ped}$ is observed at the edge. The bifurcated $v_{\perp,ped}$ in the ELM-crash suppressed phase is typically small on the order of ~1 km/s and its shear also decreases. The decrease of $v_{\perp,ped}$ shear could lead to the increase of turbulent fluctuations at the edge in the ELM-crash suppressed phase.

Time history of v⊥ in the transition of ELM-crash suppression under n=1 RMP
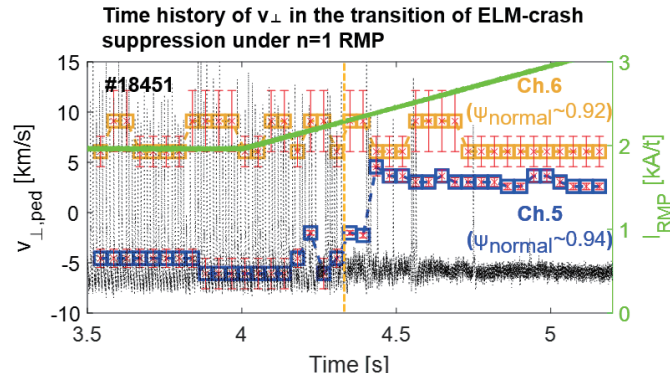
Fig. 2 Time history of $v_{\perp,ped}$ and $v_{\perp,ped}$ shear under slowly varying RMP field strength (n=1, +90 phasing) with respect to the ELM phase transition.

In related experiments, the hysteresis in the resonant field strength was clearly observed at the transition into and out of the ELM-crash suppression. The RMP coil magnitude was slowly increased and decreased in single discharge to compare the field strength at the transition into and out of the ELM-crash suppression (Fig. 3). The RMP field strength differed when entering and exiting the ELM-crash suppression; the RMP coil magnitude to enter the ELM-crash suppression was ~30% (~0.5kA/t) higher than the ramping down phase (the ELM-crash mitigated phase). These observations suggest that the plasma state of the ELM-crash suppression is completely different from that of the ELM-crash mitigation.

Time history of v⊥ in transition into and out of ELM-crash suppression under n=1 RMP
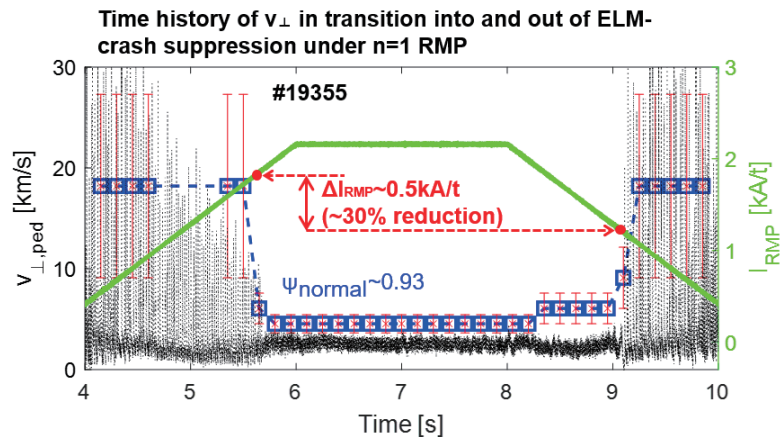
Fig. 3 Time trace of $v_{\perp,ped}$ in transition into and out of ELM-crash suppression with RMP coil current I_{RMP}.

4. Summary

The onset of ELM-crash suppression under low-n RMP is characterized by the reduction of $v_{\perp,ped}$ and $v_{\perp,ped}$ shear as well as increase of turbulent fluctuations. The bifurcation of $v_{\perp,ped}$ and $v_{\perp,ped}$ shear was slightly ahead of the transition into and out of ELM-crash suppression, and thus the change of $v_{\perp,ped}$ is a prerequisite for the ELM phase transition. The hysteresis of the RMP field strength suggests that the plasma state of the ELM-crash suppression is completely different from the previous state.

Acknowledgements

References

[1] F.Wagner, G.Becker, K.Behringer, et al., Phys. Rev. Lett. **49** (1982) 1408.

[2] J.W.Conner, Plasma Phys. Controlled Fusion **40** (1998) 531.

[3] G.S.Yun, W.Lee, M.J.Choi, et al., Rev. Sci. Instrum. **81** (2010) 10D930.

[4] J.Lee, G.S. Yun, M.J Choi, et al., Phys. Rev. Lett. **117** (2016) 075001.

[5] M.Becoulet, F.Orain, P.Maget, et al., Nucl. Fusion **52** (2012) 054003.

Control of edge localized modes by pedestal deposited impurity in the HL-2A tokamak

Y.P. Zhang [1], D. Mazon [2], X.L. Zou [2], W.L. Zhong [1], J.M. Gao [1], K. Zhang [1],

P. Sun [1], C.F. Dong [1], Z.Y. Cui [1], Yi Liu [1], Z.B. Shi [1], D.L. Yu [1], J. Cheng [1],

M. Jiang [1], J.Q. Xu [1], M. Isobe [3,4], G.L. Xiao [1], W. Chen [1], S.D. Song [1],

X.Y. Bai [1], P.F. Zhang [1], G.L. Yuan [1], X.Q. Ji [1], Y.G. Li [1], Y. Zhou [1], L. Delpech [2],

A. Ekedahl [2], G. Giruzzi [2], T. Hoang [2], Y. Peysson [2], X.M. Song [1], X.Y. Song [1],

X. Li [1], X.T. Ding [1], J.Q. Dong [1], Q.W. Yang [1], M. Xu [1], X.R. Duan [1], Y. Liu [1]

and the HL-2A team [1]

[1] Southwestern Institute of Physics, PO Box 432, Chengdu 610041, China

[2] CEA, IRFM, F-13108 Saint-Paul-lez-Durance, France

[3] National institute for Fusion Science, National Institutes of Natural Sciences, 322-6 Oroshi-cho,

Toki 509-5259, Japan

[4] SOKENDAI (The Graduate University for Advanced Studies), 322-6 Oroshi-cho, Toki 509-5292, Japan

Abstract

Effect of the pedestal deposited impurity on the edge-localized mode (ELM) behaviour has been observed and intensively investigated in the HL-2A tokamak. Impurities have been externally seeded by a newly developed laser blow-off (LBO) system. Both mitigation and suppression of ELMs have been realized by LBO-seeded impurity. Measurements have shown that the LBO-seeded impurity particles are mainly deposited in the pedestal region. During the ELM mitigation phase, the pedestal density fluctuation is significantly increased, indicating that the ELM mitigation may be achieved by the enhancement of the pedestal transport. The transition from ELM mitigation to ELM suppression was triggered when the number of the LBO-seeded impurity exceeds a threshold value. During the ELM suppression phase, a harmonic coherent mode (HCM) is excited by the LBO-seeded impurity, and the pedestal density fluctuation is significantly decreased, the electron density is continuously increased, implying that HCM may reduce the pedestal turbulence, suppress ELMs, increase the pedestal pressure, thus extending the Peeling–Ballooning instability limit. It has been found that the occurance of the ELM mitigation and ELM suppression closely depends on the LBO laser spot diameter.

1. Introduction

The high confinement (H-mode) operational scenario is the most promising regime for achieving self-ignited devices using the tokamak plasma confinement concept [1–3]. The H-mode is characterized by a steep plasma pressure gradient at the plasma edge, i.e. edge pedestal or edge transport barrier (ETB), which leads to strong self-driven plasma currents, resulting in an edge MHD instability referred to as edge-localized mode (ELM) [4]. A large quantity of particles and energy are lost from the plasma during large amplitude (type-I) ELMs. The ELM event occurs in very short timescales (~100 µs) [5]. Therefore,

ELM bursts can constitute a serious threat to plasma facing component (PFC) lifetime by erosion and melting from the strong heat load. Furthermore, the impurity source due to the impact of ELM burst on the PFC can pollute the plasma and deteriorate the plasma performance. For a large fusion device with burning plasma like the international tokamak experimental reactor (ITER), this situation will become worse. Previous studies have predicted that~20 MJ of plasma stored energy will be released during an uncontrolled type-I ELM burst [6]. It could exceed several times the tolerable material limits of PFCs. Calculations show that the released energy per ELM burst must be less than 1 MJ in order to avoid unacceptable damage to the ITER PFCs. Understanding the physics of ELMs and controlling ELMs are therefore crucial and urgent issues for present-day tokamak experiments. In particular, a high confinement with controlled ELMs of the plasma operation is essential to achieve a high fusion power gain, an essential element of the ITER project.

ELM control has been extensively studied theoretically and experimentally in magnetic fusion devices [7–11]. In order to ensure an appropriate lifetime of PFCs in ITER, it is anticipated that at full plasma current robust ELM control technique will be required, either suppressing the ELMs completely or, at least, reducing the divertor heat flux per ELM. Therefore, there are two primary forms related to the ELM control. The first is ELM mitigation which increases the ELM frequency f_{ELM} relative to the intrinsic one whilst at the same time reduces the divertor peak heat flux. Since the relation $f_{ELM} \times \Delta W_{ELM} \sim$ constant (here ΔW_{ELM} is the energy loss per ELM), holds for intrinsic ELMs on many tokamaks, increasing the f ELM should decrease the ΔW_{ELM} as we desire. The latter type of ELM control is ELM suppression, which completely avoids the occurrence of large amplitude ELM bursts and simultaneously increases pedestal transport to flush the impurities from the plasma core region by alternative edge instabilities (quasi-coherent modes) rather than the ELMs. Numerous efforts have been dedicated to explore the effective techniques for ELM control and many techniques have been developed. Existing methods for ELM control include resonant magnetic perturbations (RMPs) [10–20], supersonic molecular beam injection (SMBI) [8, 21–24], small pellet pacing [3, 25–30], fast vertical jogs of the plasma columns [31, 32], and lower hybrid current drive (LHCD) [33–35]. ELM control has been achieved with RMPs in JET [14, 17], DIII-D [6, 10], ASDEX Upgrade [11], MAST [13, 16, 28], and KSTAR [12, 18], with pellet pacing in DIII-D [3] and ASDEX Upgrade [7, 25–30], with SMBI in HL-2A [8, 22–24], EAST [21] and KSTAR [22], with plasma jogs in TCV [31] and ASDEX Upgrade [32], and with LHCD in EAST [33–35] and HL-2A [36].

In this paper, we describe a novel experimental demonstration of ELM control by laser blow-off (LBO) system, and elucidate the physics of the results. Experimental results in several devices suggested that LBO is an effective and well established technique to study impurity transport investigation [37–40]. In addition to the impurity transport, the effect of LBO injected impurities on the ELM dynamics has been studied in the HL-2A tokamak. Both the mitigation and suppression of the ELMs have been successfully achieved by means of LBO.

The remainder of this paper is organized as follows. Section 2 describes the experimental condition including the experimental setup and the primary experimental systems used in this work. Section 3 presents the experimental results of ELM mitigation by spontaneous impurity seeding. Section 4 presents the study on ELM control by LBO impurity in the H-mode plasmas. Finally, the paper is summarized in section 5.
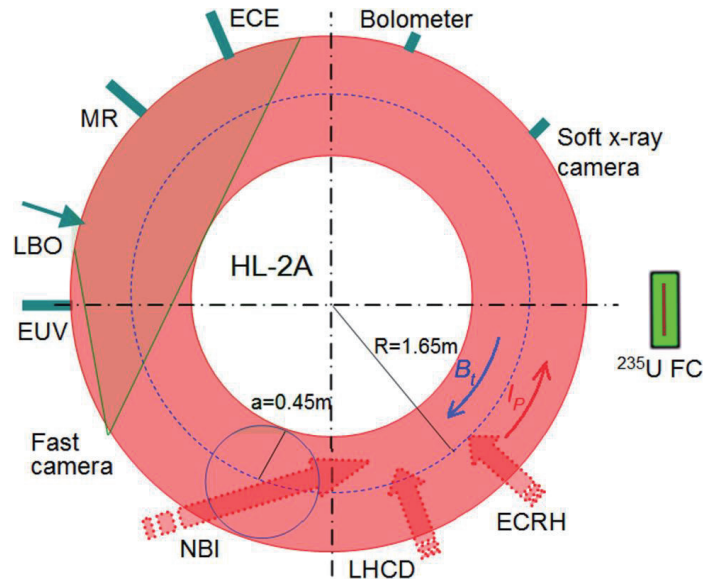
Fig.1 Arrangement of the HL-2A device together with the installation positions of the main systems used in this experiment. The laser blow-off (LBO) impurity injection system is installed on the equatorial-plane port and the impurities are vertically injected.

2. Experimental conditions

The HL-2A device is a medium-size tokamak with closed divertor chambers [41]. Its major and minor radii are R = 1.65m and a = 0.4 m, respectively. The achieved operation parameters are as follows: the plasma current I_p is 450 kA, the toroidal magnetic field at the magnetic axis is 2.7 T, the central line-averaged electron density n e is 5.5×10^{19} m^{-3}, the electron and ion temperatures are 5 keV and 2.8 keV, respectively. The magnetic field B_t is directed to be clockwise (top view), whereas the plasma current I_p is oriented to be counter-clockwise in the standard operation. Figure 1 depicts the arrangement of the HL-2A device together with the installation positions of the main systems used in this work. In this study, the discharge of HL-2A is maintained in the closed divertor configuration with bottom single null. The single null configuration is formed at the beginning of the discharge and sustained until the end of the discharge. The main parameters of the ELM control experiment are shown in table 1.

Three auxiliary heating and current drive systems have been developed for HL-2A as follows: (1) electron cyclotron resonance heating (ECRH), consisting of six gyrotrons with the working frequency of 68 GHz, operates in the ordinary mode for delivering 3 MW (6 × 0.5 MW) power with 1 s pulse length; (2) neutral beam injection (NBI), including four positive-ion sources; the beam injection energy is typically 40 keV and a total beam power of up to 2.0 MW (4 × 0.5 MW) is delivered for 2 s, and the neutral beam is tangentially co-injected into plasma; (3) lower hybrid current drive (LHCD), consisting of a passive-active multi-junction (PAM) launcher with the working frequency of 3.7 GHz; the peak parallel refractive index n $_{//0}$ is 2.75 and the available power is 1.0 MW for 1 s. The total output power of the auxiliary heating and current drive systems in HL-2A is about 6.0 MW.

A laser blow-off (LBO) impurity injection system has been built for HL-2A [38, 40]. This system is installed on the equatorial-plane port and the impurities are vertically injected into plasma, as shown in figure 1. A YAG laser with a pulse length of 10 ns and the wavelength of 1064 nm is employed for the LBO system. Its energy can reach up to 2 J. The target metal material is deposited onto a 42 mm × 42 mm × 2 mm quartz substrate with the thickness of several microns. The target plate is placed inside a vacuum tube located at the mid-plane diagnostic port of HL-2A, of which the position is approximately 710 mm away from the plasma boundary. The diameter of the LBO laser spot can be changed in the range of 2–6 mm. The LBO system has particular advantages for impurity injection: (1) well-controlled injected particle quantity; (2) localized deposition of the injected particles; (3) precise control of injection time. Several experiments exploited LBO to study impurity transport, as described for example in [40, 42]. ELM control, resulting from impurity particle penetration into the pedestal region by LBO, has been realized for the first time in HL-2A. In this experiment, three kinds of metal impurities (Al, Fe, W) were injected into the ELMy H-mode plasma. Impurity related information is obtained from the detection of emission of injected impurity particles located in different spatial regions. Line emission is measured by an extreme ultraviolet (EUV) spectrometer [43] and D_α detection arrays. Soft x-ray emission is detected by soft x-ray cameras with 25 µm Beryllium(Be) filters. Plasma global radiation is measured by bolometric arrays. In addition, a new high-speed visible light camera system has been developed recently. The camera frame rate using full pixel (1280 × 800) can be up to 7500 fps. Therefore, the camera system can provide some information about the LBO injected impurities with high spatiotemporal resolution.

Three fuelling tools can be used to control the density profile: gas puffing (GP) from the low-/high-field side (LFS/HFS), SMBI from the LFS and HFS, and pellet injection (PI) from the LFS mid-plane. SMBI is an efficient fuelling method which is considered to be an improvement over conventional GP [44]. The electron density profile is measured with an eight-chord HCN laser interferometer ($\lambda = 337$ µm)[45] in the central region of the plasma ($\rho < 0.6$) and the edge density profile is measured with frequency modulated continuous microwave reflectometers (MR) [46]. The electron temperature is measured by an electron cyclotron emission (ECE) radiometer with 16 channels [47]. The ion temperature is measured by a charge exchange recombination spectroscopy (CXRS) with 32 channels [48]. The detection of the D–D fusion neutron emission rate is performed by a ^{235}U fission chamber (FC) with uranium oxide of 3 g [49]. The FC is positioned about 1.5 m away from the diagnostic port at the equatorial plane of the outboard side of the HL-2A tokamak, as shown in figure 1. Currently, the FC system is operated in pulse counting mode, and the sampling time is set at 1 ms.

Table 1. Main parameters in the ELM control experiment in HL-2A.

Plasma current, I_p	150–200 kA
Central line averaged electron density, n_e	$(1–3) \times 10^{19}$ m^{-3}
Central electron temperature, T_e	1–2 keV
Toroidal magnetic field, B_t	1.3 T
Plasma edge safety factor, q_{95}	4.0–6.0
Effective ionic charge, Z_{eff}	2.0–3.0
LBO injection impurity	Al, Fe, W
NBI power and pulse width	0.8–1.2 MW, 500 ms
ECRH power and pulse width	1.0–1.5 MW, 400 ms

3. ELM mitigation by spontaneous impurity injection

The first ELMy H-mode plasma in HL-2A was realized with ECRH and NBI in 2009 [50]. At present, H-mode plasma experiments are one of the most important research topics in the HL-2A tokamak and have achieved rich research results [22–24, 51–54]. During the HL-2A experimental campaign in 2015, it was observed that ELMs were significantly mitigated by the spontaneous impurity injection during an ELMy H-mode discharge. Figure 2 illustrates the time evolution of the main parameters of this discharge with ELM mitigation by spontaneous impurity injection. The spikes observed in the divertor D_α signal in figure 2(g) represent ELMs. The plasma current and the toroidal magnetic field in this discharge are 160 kA and 1.32 T, respectively. Auxiliary heating with 0.9MW NBI and 1.2 MW ECRH is employed. The ELM mitigation occurs following the total plasma radiation power suddenly increases at t = 678 ms as shown in figure 2(c) relative to the previous amplitude. During the interval of 678–732 ms, the frequency of the divertor D_α signal (figure 2(g)) representing ELMs strongly increases while their amplitude decreases sharply, suggesting that the ELMs are effectively mitigated during this phase. The shaded area denotes the time interval in which ELMs are mitigated. It maintains during several energy confinement times (~16 ms). The neutron yield (figure 2(e)), and the plasma inner stored energy (figure 2(h)) are almost constant during the ELM mitigation phase. Moreover, the H98y2 factor [55] is about 1.65 during this phase, as shown in figure 2(f). These imply that the plasma during the mitigation phase is still in the high confinement state.

With the sudden increase in the radiation power, the plasma loop voltage (figure 2(b)) begins to increase significantly, while the central electron temperature (figure 2(d)) measured by ECE radiometer gradually decreases. All these experimental evidences show that there are some impurities entering into the plasma at t = 678 ms. Measurements of a EUV system also demonstrates this point. Figure 3 shows that the FeXVI impurity distribution measured by the EUV before, during and after ELM mitigation. The EUV system in HL-2A is a spectrometer with spectrum measurement. It works in the wavelength range of 3–50 nm and it is equipped with a gold-coated varied-line-spacing holographic grating with curvature of 5606 mm and a back illuminated charge-coupled device with size of 6.6×26.6 mm^2 (255×1024 pixels). The time resolution of the EUV spectrometer is 200 ms. The ELM mitigation lasted 54 ms. Therefore, we can obtain three impurity profiles before, during and after the ELM mitigation. From figure 3, it is clearly

observed that the level of the FeXVI impurity radiation during the ELM mitigation phase is much higher than that before and after the ELM mitigation phase. In addition, the distributions before and after the mitigation phase are identical, though after the mitigation the temperature remains lower and the density increase. Thus, it is reasonable to infer that there are Fe impurity particles enter the plasma during the ELM mitigation phase. The distributions presented in figure 3 are line-integrated data. The increased signal in the plasma core during the mitigation phase can be associated to the enhanced signal in an external region. Therefore, the impurity deposition position can not be determined by the distributions of line-integrated radiation obtained by EUV. Note that the sight light of the EUV in the range of -20 cm $< z < -15$ cm was blocked by the cooling water pipe of the HL-2A device, unfortunately. The impurity profile is therefore interrupted in this position range. Moreover, no impurities were actively injected into the plasma by SMBI, PI and LBO at t = 678 ms. The material of the partial PFCs of HL-2A is stainless steel. Therefore, the Fe impurity entering into the plasma at t = 678 ms should be spontaneous. That is, the ELMs are mitigated by spontaneous impurity injection.

It is very important to know the impurity particle source deposition in order to better interpret the results of the ELM mitigation by impurity. To facilitate the understanding of the impurity ELM mitigation, the bolometer array was employed to obtain the information of the spontaneous impurity injection during ELM mitigation. The 3D profile of the plasma radiation density is calculated from measurements of the bolometer array with Abel inversion. A local impurity particle source can be determined by the maximum of the plasma radiation power density. Figure 4 shows the time evolution of the radial profile of plasma radiation power density measured with the bolometer array for ELM mitigation shot 27011. In figure 4, it can be observed that there is a sharp variation in the radiation power density and the maximum amplitude is located at r $\sim$ -32 cm, here the negative sign represents the low field side of the plasma. Thus, the spontaneous impurity is deposited mainly around r $\sim$ -32 cm. The pedestal top is located at -32 cm, as determined by data from the reflectometry. This indicates that the injected spontaneous impurity particles penetrate the edge plasma and are mainly deposited in the pedestal region, as shown in figure 4.

In order to study the effect of the impurities on transport in the pedestal, the latter was characterized by an O-mode reflectometer. Figures 5(a) and (b) show the time evolution of the density fluctuation power spectra at pedestal top and foot, respectively. The turbulence intensity is obtained by integrating the power spectrum of fluctuations in the 50–500 kHz frequency. The evolution of the turbulence intensity at pedestal top and foot is plotted in figures 5(c) and (d), respectively. Figure 5(e) is the plasma radiation power density measured with a bolometer array. It is clearly shown that the density fluctuation increases significantly with the entry of impurities, showing that ELM mitigation is strongly correlated to the enhanced transport induced by turbulence in the pedestal. Thus the ELM mitigation may be achieved by the transport enhancement triggered by the impurity deposition in the pedestal.
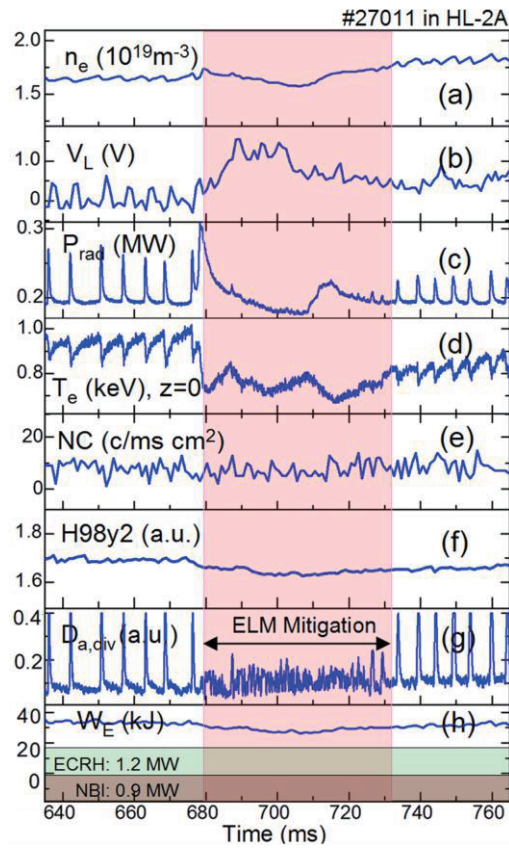
Fig. 2 Time evolution of the main parameters of an ELMy H-mode discharge with ELM mitigation by spontaneous impurity injection. (a) Central line-averaged electron density. (b) Plasma surface loop voltage. (c) Total plasma radiation power. (d) Central electron temperature. (e) Neutron flux monitor. (f) H98y2 factor. (g) Divertor D_α signal. (h) Plasma inner stored energy, ECRH and NBI monitors. The shaded area represents the time interval in which ELMs are mitigated.
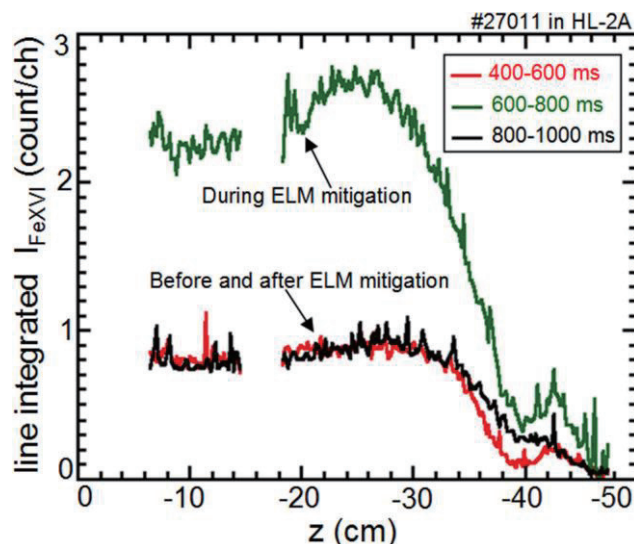
Fig. 3 Distribution of line-integrated FeXVI radiation measured by EUV before, during and after ELM mitigation. The sight light of the EUV in the range of -20 cm $< z < -15$ cm was blocked by the cooling water pipe of the HL-2A device. The radiation profile was therefore interrupted in this position range.
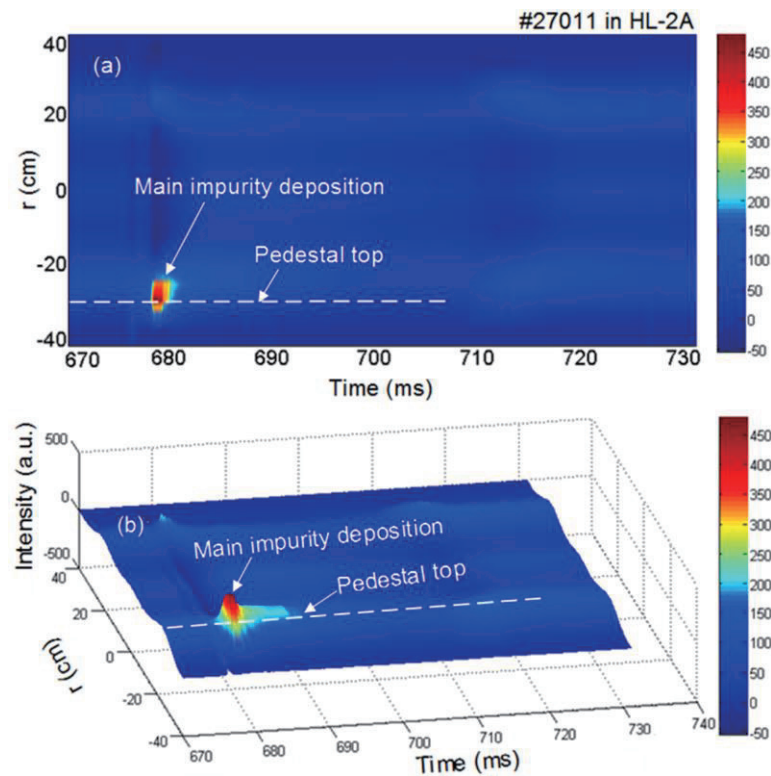
Fig. 4 Time evolution of the radial profile of plasma radiation power density calculated with data from the bolometer array for ELM mitigation shot 27011. (a) and (b) are the contour map and the 3D profile of the plasma radiation power density, respectively. The impurity deposition and the pedestal top are indicated by arrows and dashed lines, respectively. The pedestal top is determined by measurements of the reflectometry.

4. ELM control by LBO-seeded impurity

In the 2016 HL-2A experimental campaign, ELM control by actively injected impurity with LBO was performed and studied in order to verify the above-mentioned scenarios. In this experiment, three kinds of metal impurities (aluminum (Al), iron (Fe), tungsten (W)) with different atomic numbers were separately injected into the ELMy H-mode plasma. Both mitigation and suppression of ELMs have been successfully achieved by the LBO-seeded impurity. In the following the results of this experiment will be described in detail.

4.1. ELM mitigation by LBO-seeded impurity

The quantity of impurities injected by LBO can be flexibly adjusted by varying the diameter of the laser beam. ELM mitigation is achieved by injecting Fe and Al impurities. A typical ELM mitigation discharge by LBO-seeded Fe impurity is shown in figure 6. The plasma current and the toroidal magnetic field are 160 kA and 1.32 T, respectively. The ELMy H-mode is realized with 0.5 MW LHCD and 0.9 MW NBI. During the ELMy H-mode phase, the LBO system is triggered at 900 ms to start injecting Fe impurity into the plasma. At 903 ms, the soft x-ray emission intensity (figure 6(b)) and the plasma radiation power (figure 6(e)) increase significantly, and there is a slight increase in the electron density (figure6(a)). These

observations indicate that the LBO-seeded impurity has entered in the plasma at this time.

Figure 6(c) is the divertor D_α signal, it can be observed that there is a clear difference in the ELM frequency and ELM amplitude before and after LBO. The ELM frequency increases while the ELM amplitude decreases, implying that ELMs are effectively mitigated. The shaded area in figure 6 represents the time interval in which ELMs are mitigated, i.e. the duration of the LBO-seeded impurity influence. The impurity influence should not be constant during the whole mitigation phase. The seeded impurity profile can be calculated with data from bolometer array. As shown in figure 6, the influence time of LBO-seeded impurity, which corresponds to the ELM mitigation phase, is much longer than the impurity concentration life time. Figures 6(d) and (f) represent the H98y2 factor and the plasma inner stored energy, respectively. From these figures, it can be observed that both the H98y2 factor and the plasma inner stored energy are almost unchanged by LBO-seeded impurity during the LBO influence phase. These indicate that the plasma confinement is not degraded and still in the high confinement state. Thus, the ELM mitigation by LBO-seeded impurity can be successfully achieved. The ELM mitigation terminates at t = 927 ms when ELM bursts restored to the state before the injection of the LBO-seeded impurity.

Figure 7 displays the density profiles measured by the microwave reflectometry during the L-mode (520 ms), ELMy H-mode (898 ms) and ELM mitigation (912 ms) phases. From this figure, a clear density pedestal structure can be identified during both ELMy H-mode and ELM mitigation phases. The top and foot of the pedestal structure are located approximately at r = 30.2 cm and r = 33.3 cm, respectively. Therefore, the width (Δ ped) of the pedestal is about 3.1 cm. In addition, the height (n ped) of the pedestal is 1.5×10^{19} m^{-3}. The density pedestal structure during the ELM mitigation phase is exactly the same than that during the ELM phase. This means that the pedestal structure is still intact as before the ELM mitigation. Observations of the process of the LBO-seeded impurity injection for ELM mitigation by a fast visible camera. The sequence of the images is presented for the time points (t_1, t_2, …, t_6) marked by an arrow in figure 9. The images are coupled with the magnetic configuration reconstruction obtained by the EFIT code. The frame rate and the pixel of the camera are set by 10 kfps and 512×512, respectively. The exposure time is 20 µs. The LBO-seeded impurity is noted by arrows. Thus, the plasma during ELM mitigation is still in the high confinement state, which is consistent with the results of the H98y2 factor and the plasma inner stored energy. Figure 8 shows the profiles of the ion temperature before and after the ELM mitigation phase. It can be clearly seen that the impact of the LBO-seeded impurity radiation on the temperature profiles. The ion temperature at the edge decreases immediately, while the temperature in the core changes slightly. Then the temperature in the core drops as much as that at the edge.

Information on the location of the LBO-seeded impurity can be obtained by a bolometer array and a fast visible camera. The plasma radiation power density profile has been measured with the bolometer array. Figure 9(d) displays time evolution of the plasma radiation power density radial profile for shot 29305. From this figure, it can be seen that the clear image of the LBO-seeded impurity in plasma appears at about 903 ms and lasts for about 7 ms. The LBO-seeded impurity particles penetrate the edge plasma and are mainly deposited in the pedestal region, as shown in figure 9(d). A more intuitive process of LBO-seeded impurity injection for ELM mitigation can be observed by a fast visible camera, as shown in figure 10. The frame rate and the pixel of the camera are set by 10 kfps and 512×512, respectively. Therefore, the camera

system can provide some information about the LBO-seeded impurities with high spatio-temporal resolution. The sequence of the images in figure 10 is presented for the time points (t_1, t_2, …, t_6) marked by an arrow in figure 9. The LBO system is triggered at 900 ms. Image t_2 is the first frame picture with impurity appearing, which indicates that the total time of LBO response time and the impurity propagation time from the substrate to the plasma is about 2.8 ms. Image t_5 is the last frame picture with impurity appearing. Thus, the injection of the LBO-seeded impurity into the plasma lasts about 7 ms. The images are coupled with the magnetic configuration reconstruction obtained by the EFIT code. EFIT reconstructions can provide important information on the evolution of the plasma configuration. From figure 10, it can be clearly observed that the LBO-seeded impurity is deposited mainly at the plasma edge. The measurement of the visible camera is consistent with the results of the bolometer array.

Figures 9(b) and (c) show the time evolution of the density fluctuation power spectra in the pedestal top and foot, respectively. During ELM mitigation, the density fluctuations are enhanced obviously. This phenomenon is the same as that during spontaneous impurity ELM mitigation. The edge particle flux during LBO-seeded impurity ELM mitigation discharge is measured by Langmuir probe, as shown in figure 11. Figure 11(a) is the divertor D_α signal and the ELM mitigation phase is noted by the double arrows. The time windows are marked with red (I) and blue (II) shadow areas and the corre sponding durations are 880–890 ms during the ELMy phase and 905–915 ms during the ELM mitigation phase, respectively. Figure 11(b) is the fluctuation driven edge particle flux power spectra during ELMy H-mode phase (red) and ELM mitigation phase (blue). From figure 11, it can be clearly seen that the two edge particle flux power spectra during the two phases are obviously different. Compared with the edge particle flux power spectrum during ELMy H-mode phase, the power spectrum with low frequency (f < 7 kHz) decreases, while that with higher frequency (f > 7 kHz) increases. This strongly indicates that the formation of large-scale (low-frequency) turbulence or transport events are prevented by the LBO-seeded impurity, while more small-scale (high-frequency) turbulence or transport events are excited. This exper imental result is consistent with the idea raised by [56, 57].
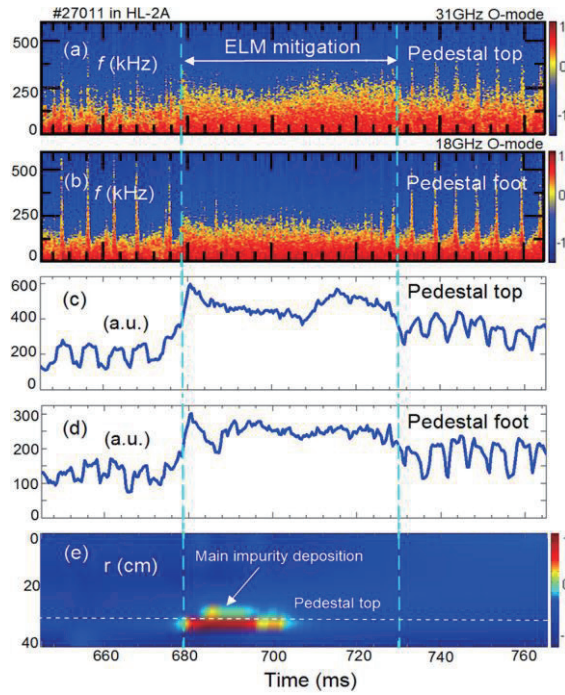
Fig.5 The density fluctuation power spectra in pedestal top (a) and pedestal foot (b). (c) and (d) are the turbulence intensity in pedestal top and foot, respectively. (e) is the plasma radiation power density measured with the bolometer array. The two dashed lines point the ELM mitigation interval.
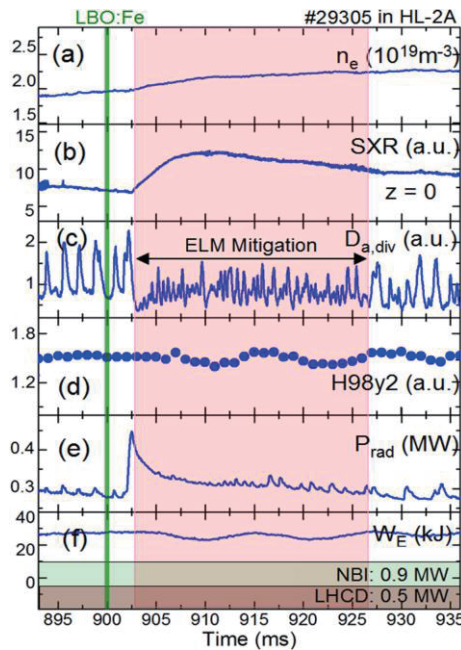
Fig.6 Time evolution of the main parameters of a typical ELMy H-mode discharge with ELM mitigation by LBO-seeded Fe impurity. (a) Central line-averaged electron density. (b) Central line-integrated soft x-ray radiation intensity. (c) Divertor D_α signal. (d) H98y2 factor. (e) Total plasma radiation power. (f) Plasma inner stored energy, LHCD and NBI monitors. The shaded area represents the time interval in which ELMs are mitigated.
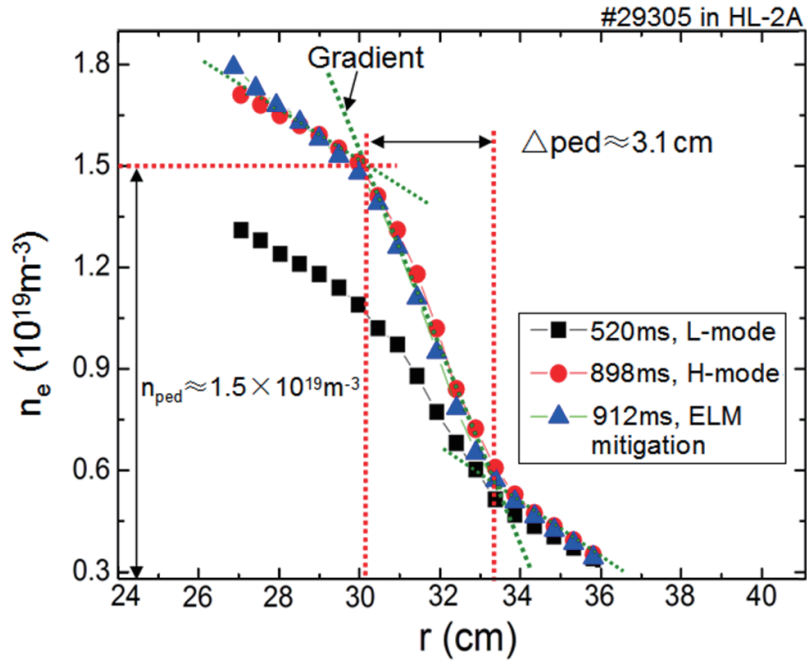
Fig.7 Density profiles measured by microwave reflectometry for the L-mode, H-mode and ELM mitigation phases. The density pedestal structure during ELM mitigation is exactly the same as that during ELM phase. The width (Δ ped) and height (n ped) of the pedestal are about 3.1 cm and 1.5×10^{19} m^{-3}, respectively.
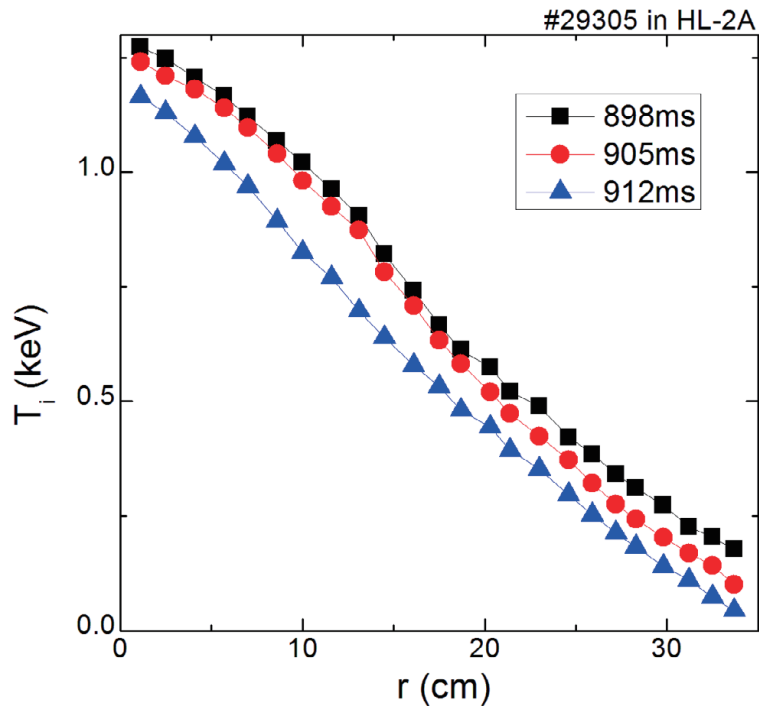
Fig.8   Ion temperature profiles before and after the ELM mitigation phase.
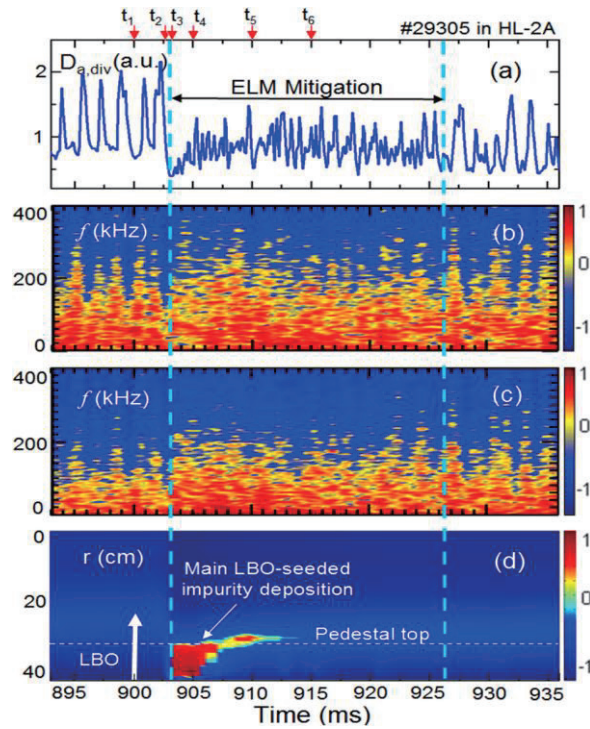
Fig.9 Experimental results of ELM mitigation using LBO-seeded Fe impurity. (a) is the divertor D_α signal, and the time interval of ELM mitigation is indicated by the double vertical dashed lines. (b) and (c) are the density fluctuation power spectra in the pedestal top and pedestal foot, respectively. (d) is the plasma radiation power density measured with the bolometer array. The impurity deposition and the pedestal top are noted by arrows and horizontal dashed lines, respectively.
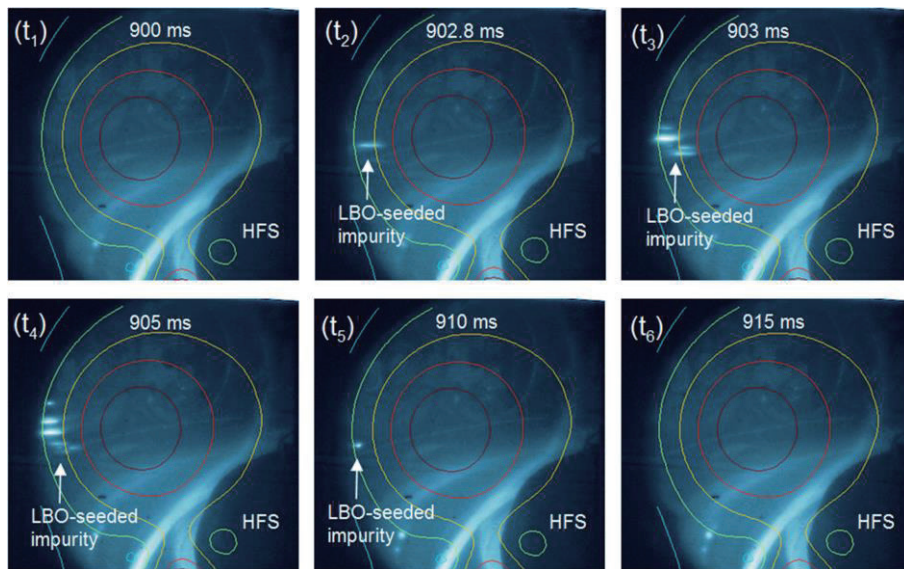
Fig.10 Observations of the process of the LBO-seeded impurity injection for ELM mitigation by a fast visible camera. The sequence of the images is presented for the time points (t_1, t_2, …, t_6) marked by an arrow in figure 9. The images are coupled with the magnetic configuration reconstruction obtained by the EFIT code. The frame rate and the pixel of the camera are set by 10 kfps and 512 × 512, respectively. The exposure time is 20 μs. The LBO-seeded impurity is noted by arrows.
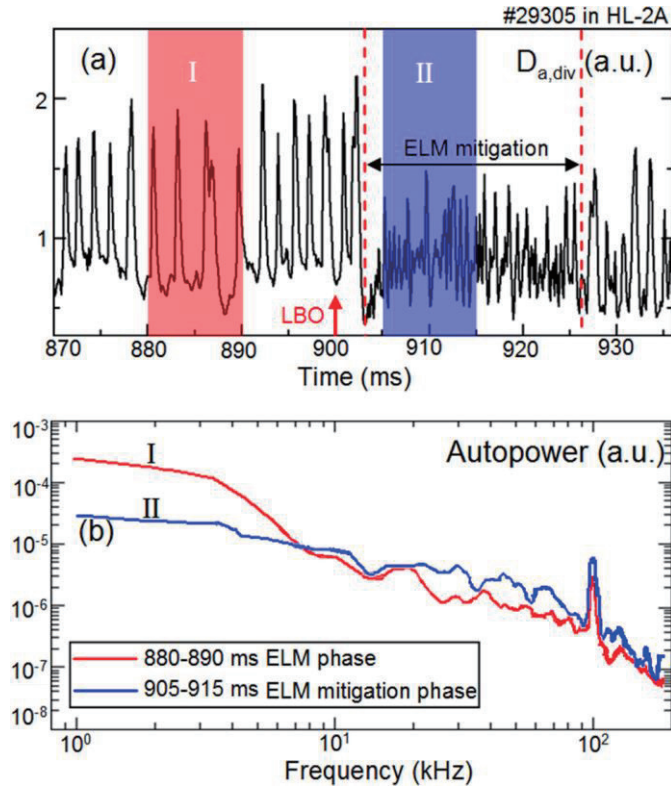
Fig.11   (a) Time evolution of the divertor D_α signal. (b) Edge particle flux power spectra during ELMy H-mode phase (red) and LBO-seeded impurity driven ELM mitigation phase (blue). The time windows in chart (a) are marked with red (I) and blue (II) shadow areas and the corresponding durations are 880–890 ms during the ELMy phase and 910–920 ms during the ELM mitigation phase, respectively.

4.2. ELM suppression and HCM excitation by LBO-seeded impurity

ELM suppression has been achieved by injecting LBO-seeded W impurity with higher atomic number. W is a promising divertor material for future magnetic fusion devices like ITER because its unique advantages, such as high melting point, low sputtering yield, and low tritium absorption. Thus, intense research activities have been conducted during the last few years on W impurity [58–63]. Figure 12 illustrates a typical ELM mitigation by LBO-seeded W impurity. The plasma current and the toroidal magnetic field are 160 kA and 1.32 T, respectively. The ELMy H-mode is realized at 830 ms with 0.5 MW LHCD and 0.9 MW NBI. At 900 ms, the LBO system is triggered to start injecting W impurity into the plasma. The ELM mitigation occurs after the LBO-seeded impurity enters the plasma at ~903 ms, when the divertor D_α signal frequency increases while the divertor D_α signal frequency amplitude decreases, as shown in figure 12(b). Phase I in figure 12 corresponds to the time interval from the triggering of LBO system to the beginning of the ELM mitigation. Phase II corresponds to the ELM mitigation phase. Phase II lasts a very short time (~2 ms).

At ~905 ms, a transition from ELM mitigation to ELM suppression occurs after a further decrease in the divertor D_α signal, when the bursts of the divertor D_α signal completely disappear and the divertor D_α signal is kept at a very low level. All these observations indicate that the ELMs are suppressed thoroughly

during this phase. The ELM suppression phase is marked as III, as shown in figure 12. The H98y2 factor, the neutron flux monitoring and the plasma inner stored energy are plotted in figures 12(c), (d) and (f), respectively. It should be noted that the latter three signals are almost constant throughout the transition process. These indicate that the plasma still remains in a high confinement state during ELM suppression.

To study the transition process from ELM mitigation to ELM suppression, the information about the density fluctuation and the LBO-seeded impurity before and after this event is obtained, as shown in figure 13 by the dotted lines. Figure 13(a) is the divertor D_α signal and the ELM suppression phase is noted by the double arrows. Figure 13(b) and (c) show, respectively, the time evolution of the density fluctuation power spectra in the pedestal top and foot, which are measured by the reflectometry. Figure 13(d) is the plasma radiation power density measured with a bolometer array. From these figures, a physical picture of the process can be inferred as the following. (1) Phase I: the LBO system is triggered at 900 ms during ELMy H-mode phase. (2) Phase II: the LBO-seeded W impurity enters the ELMy H-mode plasma at~903 ms, and then the density fluctuations are enhanced and ELMs are effectively mitigated. The turbulence behavior during this phase is the same as that during LBO-seeded Fe impurity ELM mitigation. The duration of this phase is very short. (3) Phase III: during this phase, ELMs are completely suppressed, and more surprisingly, the pedestal turbulence measured by the Doppler reflectometry is also nearly suppressed as shown in figures 13(b) and (c). From figure 13(d), it can be observed that the power density of plasma radiation becomes stronger gradually, implying that more and more impurities entering the plasma. This indicates that the ELM mitigation-suppression transition strongly correlates with the increasing of LBO-seeded impurities entering the plasma. It suggests that the ELM mitigation-suppression transition maybe triggered when the amount of the LBO-seeded impurities entering the plasma exceeds a certain threshold value. This point will be discussed more in detail in the section 4.3.

Figures 13(b) and (c) show the time evolution of the density fluctuation power spectra in the pedestal top and foot, respectively. The pedestal density fluctuations are enhanced during ELM mitigation phase, as previously described. During ELM suppression phase, the pedestal density fluctuations are nearly suppressed. However, the analysis of the magnetic signal has shown that a harmonic coherent mode (HCM) is excited during this ELM suppression phase as shown in figure 14, where figure 14(a) presents the divertor D_α signal, figure 14(b) is the magnetic probe signal measured by Mirnov coil, figure 14(c) presents the time-frequency spectrum of the magnetic fluctuations, and the two dashed lines delimit the ELM suppression interval. The frequency range of HCM is from 10 to 100 kHz. During this phase, as the pedestal turbulence is nearly suppressed, the base line of the divertor D_α signal is significantly reduced, and the plasma density continuously increases as shown in figure 14. This HCM is very similar to that observed in EAST, where a harmonic coherent mode is spontaneously excited during an ELM suppression phase [64]. The fundamental frequency of the EAST HCM is about 12−15 kHz, and during its presence, ELMs are disappeared, the pedestal turbulence is totally suppressed, the base line of the divertor D_α signal is significantly decreased, and the plasma density is continuously increased. Furthermore, it has been found that strong interaction exists between different harmonics of HCM and background turbulence, and energy transfer can be transferred from the background turbulence to HCM. This could explain the reduction of the pedestal turbulence and the enhancement of the particle confinement with HCM. Similarities exist between

HCM and the edge harmonic oscillation (EHO) observed during the Quiescent H-mode plasmas in the DIII-D tokamak [65], for example, the spatial location, the fundamental frequency, and the multiple harmonic features. However, the impact of EHO on the plasma is quite different to that of HCM. EHO modulates the pedestal turbulence, regulates the particle transport, suppresses ELMs, and maintains the plasma for a steady state [50, 66–68], while HCM suppresses the pedestal turbulence, reduces the particle transport, and raises the plasma density. These suggest that HCM could extend the Peelin–Ballooning instability limit for ELM triggering, as predicted by theory[69]. As shown by the present experiments, HCM can not only be spontaneously excited in H-mode plasmas [64], but also externally excited with impurity seeding. In the future our effort will focus on the investigation of the excitation mechanism of HCM.

4.3. Comparison of LBO-seeded impurities for ELM control

In the previous section, effects of heavy metallic impurities as Fe and W on ELMs have been reported. As shown in figure 15, the ELM mitigation has been also observed with lighter metallic impurity Al. The mitigation phase lasts about 14 ms, in which the total radiation power and the soft-x ray signal remain at a high level, and the H98y2 factor is almost unchanged. This is the same phenomenology observed during the impurity Fe ELM mitigation.

Now it is important to know the dependence of the ELM mitigation or suppression on the impurity parameter as the diameter of the LBO laser spot diameter D for different metallic impurities. Figures 16(a)–(c) plot the amplitude of ELMs as a function of the LBO laser spot diameter D for Fe, Al and W, respectively. The target thickness used in this experiment is 5 μm. The black square markers correspond to the case where the impurity injection has no effect on ELMs, the red circle markers correspond to the ELM mitigation case by impurity imjection, and the blue triangle markers correspond to the ELM suppression case by impurity injection. For Fe, the ELM mitigation occurs when D is in the range of (3.65 mm, 3.83 mm), and the ELM suppression occurs when D is larger than 3.83 mm; for Al, the ELM mitigation occurs when D is in the range of (4.62 mm, 4.98 mm), and the ELM suppression occurs when D is larger than 4.98 mm; for W, due to lack of data, only ELM suppression has been observed for D larger than 3.54 mm, D should be less than the latter for the observation of the ELM mitigation. It should be noted that higher the atomic charge Z of the impurity, less is the value of D for the ELM mitigation and suppression. This seems to indicate that the occurance of the ELM mitigation and suppression depend on the quantity of electron injected with seeded impurity, or Z_{eff} of the impurity. Therefore, ELMs can be controlled by regulating the quantity and type of injected impurities.
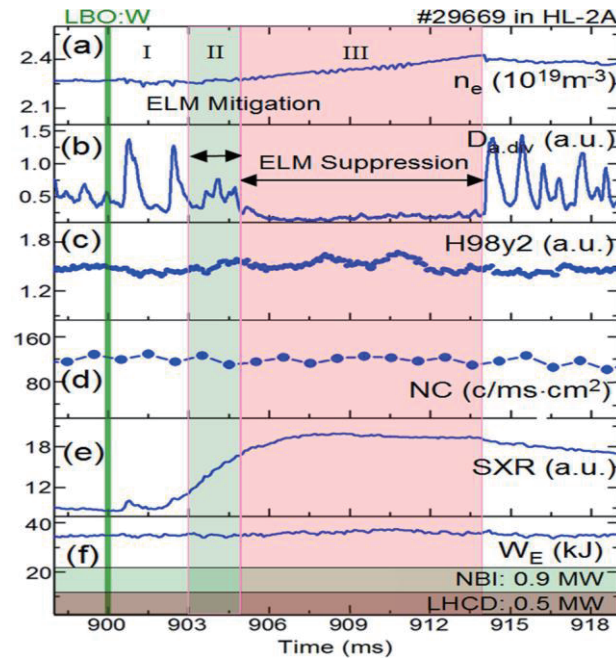
Fig.12 Time evolution of the main parameters of a typical ELMy H-mode discharge with ELM suppression by LBO-seeded W impurity. (a) Central line-averaged electron density, (b) divertor D_α signal, (c) H98y2 factor. (d) Neutron flux monitor. (e) Central line-integrated soft x-ray radiation intensity. (f) Plasma inner stored energy, LHCD and NBI monitors. The first (II) and second (III) shadow areas represent the time intervals in which ELMs are mitigated and suppressed, respectively.
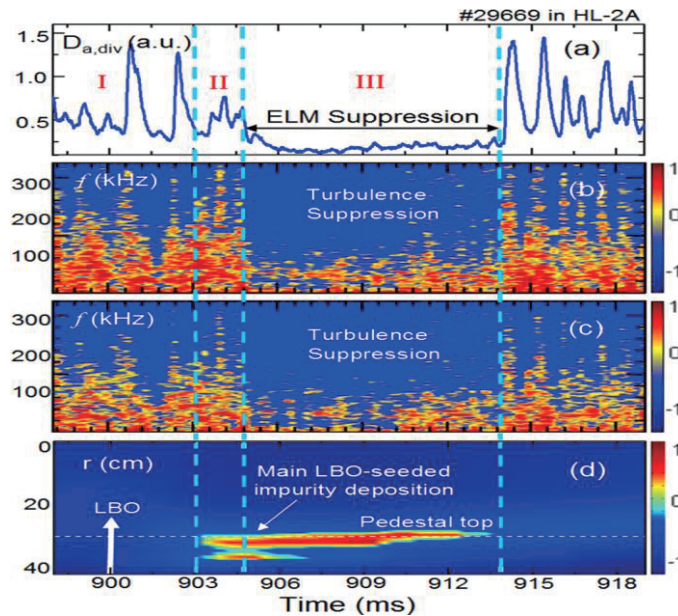
Fig.13 Experimental results of ELM suppression using LBO-seeded impurity. (a) is the divertor D_α signal. (b) and (c) are the density fluctuation power spectra in pedestal top and pedestal foot, respectively. (d) is the plasma radiation power density measured with the bolometer array. The impurity deposition and the pedestal top are indicated by arrows and horizontal dashed lines, respectively.
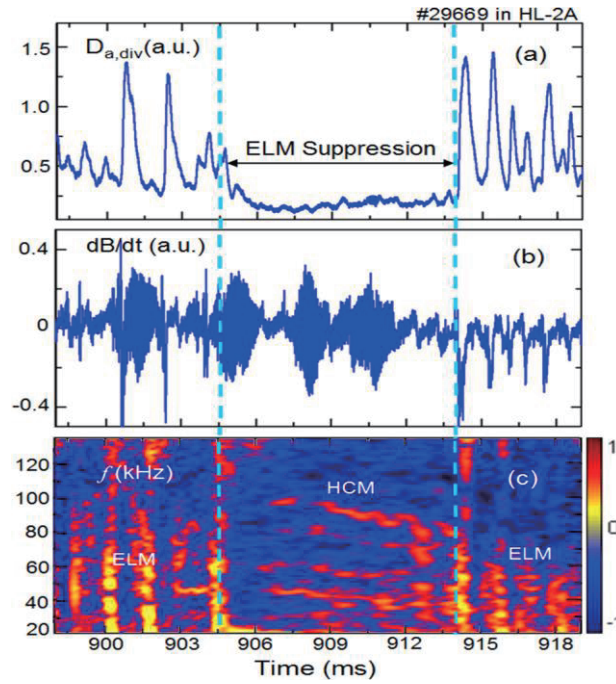
Fig.14 Observation of the harmonic coherent mode (HCM) during the ELM suppression phase. (a) Divertor D_α signal. (b) Magnetic probe signal measured by the Mirnov coil. (c) Time-frequency spectrum of the magnetic fluctuation signal. The two dashed lines delimit the ELM mitigation interval.
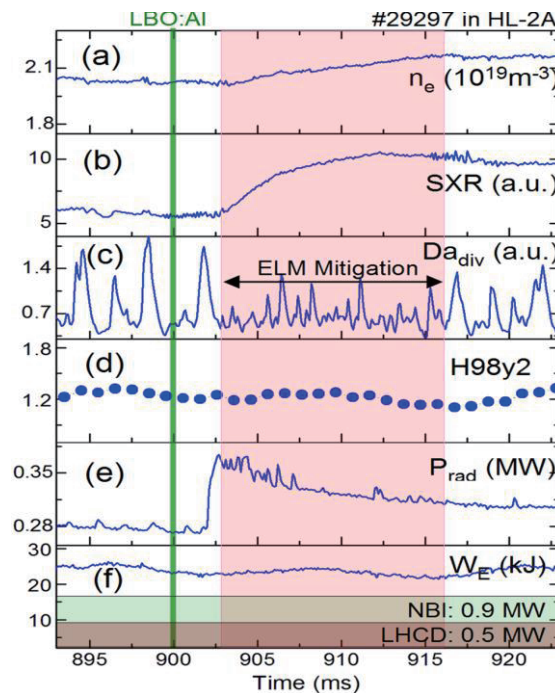
Fig. 15 Time evolution of the main parameters of a typical ELMy H-mode discharge with ELM mitigation by LBO-seeded Al impurity. (a) Central line-averaged electron density. (b) Central line-integrated soft x-ray radiation intensity. (c) Divertor D_α signal. (d) H98y2 factor. (e) Total plasma radiation power. (f) Plasma inner stored energy, LHCD and NBI monitors. The shaded area represents the time interval in which ELMs are mitigated.
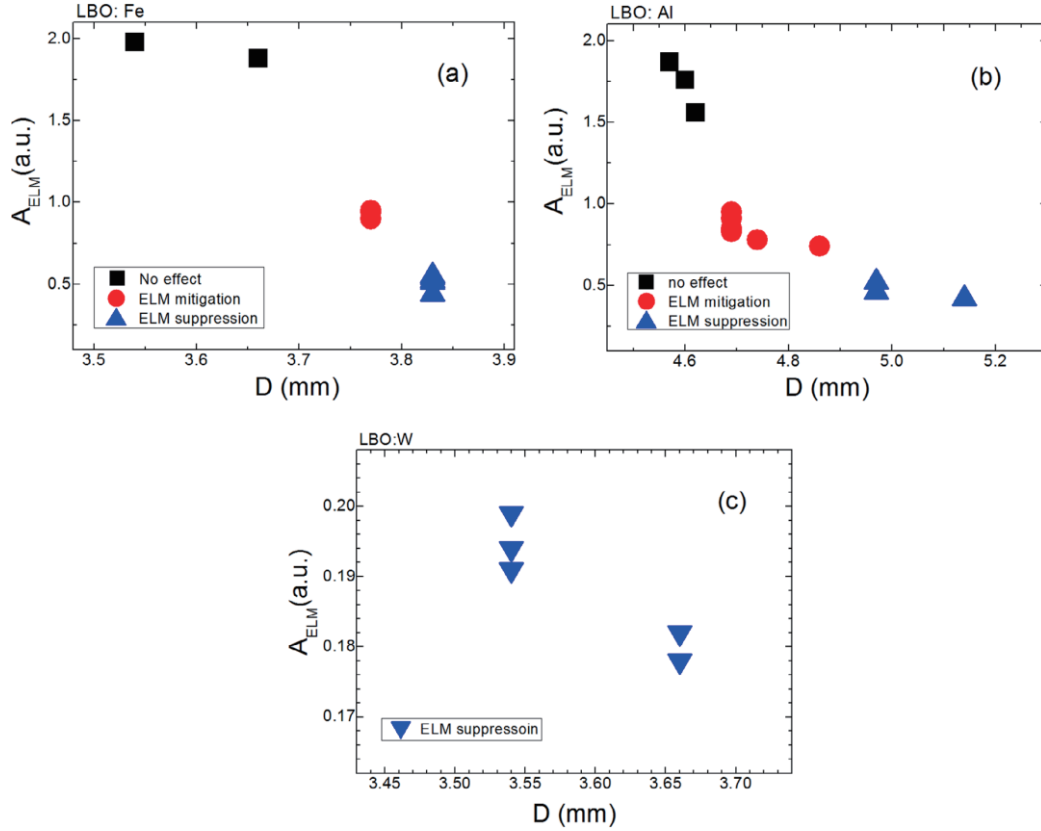
Fig.16 ELM amplitude A_{ELM} as a function of the LBO laser spot diameter D in the LBO ELM control discharges with different impurities. (a) Fe, (b) Al, (c) W. The thickness of the impurity targets used in this experiment is 5 μm. Note that, for W, only ELM suppression has been obtained due to the lack of data.

5. Conclusions

In 2015 HL-2A experimental campaign, it was accidentally observed that the ELMs were mitigated by the spontaneous impurity during an ELMy H-mode discharge. In order to verify Figure 16. ELM amplitude A_{ELM} as a function of the LBO laser spot diameter D in the LBO ELM control discharges with different impurities. (a) Fe, (b) Al, (c) W. The thickness of the impurity targets used in this experiment is 5 μm. Note that, for W, only ELM suppression has been obtained due to the lack of data. Active ELM control experiments were performed and studied using the LBO system in the 2016 HL-2A experimental campaign. Three kinds of metal impurities (Al, Fe, W) were separately injected into the ELMy H-mode plasma. ELM mitigation is reproduced by LBO-seeded Al and Fe impurity. The deposition location of the LBO-seeded impurity is observed with a bolometer array and a fast visible camera. During ELM mitigation phase, the impurity particles are mainly deposited in the pedestal region and the density fluctuation in the pedestal is significantly increased. ELM mitigation may be achieved by the pedestal transport enhancement after impurity deposition in the pedestal.

ELM suppression was also obtained in this experiment with LBO-seeded Al, Fe and W impurities. The transition process from ELM mitigation to ELM suppression has been clearly observed. The transition is triggered when the amount of the LBO-seeded impurity exceeds a certain threshold value. The pedestal

density fluctuation is significantly reduced during ELM suppression phase, and a harmonic coherent mode is excited, implying that ELM suppression is associated with the onset of HCM triggered by LBO seeded impurity, and suggesting that HCM could extend the Peeling-Ballooning instability limit, as predicted by the theory. This regime in ELM suppression plasma is different to the recent ELM-free H-mode in HL-2A [51]. The dependence of the ELM mitigation and suppression on the LBO laser spot diameter has been demonstrated, indicating the quantity of electrons injected with impurity is likely the key parameter for controlling ELMs.

References

[1] Wagner F. et al 1982 Phys. Rev. Lett. 49 1408

[2] Doyle E.J. et al 2007 Progress in the ITER physics basis: chapter 2: plasma confinement and transport Nucl. Fusion47 S18

[3] Baylor L.R. et al 2013 Phys. Rev. Lett. 110 245001

[4] Zohm H. 1996 Plasma Phys. Control. Fusion 38 105

[5] Loarte A. et al 2003 Plasma Phys. Control. Fusion 45 1549

[6] Evans T.E. et al 2006 Nat. Phys. 2 419

[7] Lang P.T. et al 2013 Nucl. Fusion 53 043004

[8] Xiao W.W. et al 2012 Nucl. Fusion 52 114027

[9] Liu Y. et al 2016 Plasma Phys. Control. Fusion 58 114005

[10] Evans T.E. et al 2004 Phys. Rev. Lett. 92 235003

[11] Suttrop W. et al 2011 Phys. Rev. Lett. 106 225004

[12] Jeon Y.M. et al 2012 Phys. Rev. Lett. 109 035004

[13] Valovič M. et al 2013 Plasma Phys. Control. Fusion55 025009

[14] Liang Y. et al 2013 Nucl. Fusion 53 073036

[15] Paz-Soldan C. et al 2015 Phys. Rev. Lett. 114 105001

[16] Kirk A. et al 2013 Nucl. Fusion 53 043007

[17] Chapman I.T. et al 2016 Plasma Phys. Control. Fusion58 014017

[18] Kim J. et al 2017 Nucl. Fusion 57 022001

[19] Toi K. et al 2014 Nucl. Fusion 54 033001

[20] Sun Y. et al 2017 Nucl. Fusion 57 036007

[21] Zou X.L. et al 2012 Proc. 24th Int. Conf. on Fusion Energy 2012 (San Diego, CA, 2012) [PD/P8-08] (www-naweb.iaea.org/napc/physics/FEC/FEC2012/index.htm)

[22] Xiao W.W. et al 2014 Nucl. Fusion 54 023003

[23] Ma Q. et al 2016 Nucl. Fusion 56 126008

[24] Rhee T. et al 2012 Phys. Plasmas 19 022505

[25] Lang P.T. et al 2003 Nucl. Fusion 43 1110

[26] Lang P.T. et al 2004 Nucl. Fusion 44 665

[27] Lang P.T. et al 2012 Nucl. Fusion 52 023017

[28] Lang P.T. et al 2015 Plasma Phys. Control Fusion 57 045011

[29] Valovič M. et al 2015 Nucl. Fusion 55 013011

[30] Valovič M. et al 2016 Nucl. Fusion 56 066009

[31] Degeling A.W. et al 2003 Plasma Phys. Control. Fusion45 1637

[32] Lang P.T. et al 2004 Plasma Phys. Control. Fusion 46 L31

[33] Li J. et al 2013 Nat. Phys. 9 817

[34] Liang Y. et al 2013 Phys. Rev. Lett. 110 235002

[35] Chen R. et al 2015 Nucl. Fusion 55 033012

[36] Xiao G.L. et al 2017 Phys. Plasmas 24 122507

[37] Giannella R. et al 1994 Nucl. Fusion 34 1185

[38] Cui Z.Y. et al 2006 Chin. Phys. Lett. 23 2143

[39] Guirlet R. et al 2009 Nucl. Fusion 49 055007

[40] Cui Z.Y. et al 2013 Nucl. Fusion 53 093001

[41] Xu M. et al 2015 Nucl. Fusion 55 104022

[42] Rice J.E. et al 1984 Nucl. Fusion 24 1205

[43] Cui Z.Y. et al 2014 Rev. Sci. Instrum. 85 11E426

[44] Yao L. et al 2004 Nucl. Fusion 44 420

[45] Zhou Y. et al 2007 Rev. Sci. Instrum. 78 113503

[46] Zhong W.L. et al 2014 Rev. Sci. Instrum. 85 013507

[47] Ding X.T. et al 2006 Rev. Sci. Instrum. 77 10F528

[48] Yu D.L. et al 2014 Rev. Sci. Instrum. 85 11E402

[49] Zhang Y.P. et al 2012 Phys. Plasmas 19 112504

[50] Duan X.R. et al 2010 Nucl. Fusion 50 095011

[51] Zhong W.L. et al 2013 Nucl. Fusion 53 083030

[52] Zhong W.L. et al 2016 Plasma Phys. Control. Fusion 58 065001

[53] Zhong W.L. et al 2017 Plasma Phys. Control. Fusion59 014030

[54] Maingi R. et al 2010 Phys. Rev. Lett. 105 135004

[55] ITER Physics Basis Expert Groups on Confinement, Transport and Confinement Modeling and Database and ITER Physics Basis Editors 1999 Nucl. Fusion 39 2175

[56] Gruzinov I. et al 2002 Phys. Rev. Lett. 89 255001

[57] Gruzinov I. et al 2003 Phys. Plasmas 10 569

[58] Zurro B. et al 2014 Plasma Phys. Control. Fusion 56 124007

[59] Murakami I. et al 2015 Nucl. Fusion 55 093016

[60] Dux R. et al 2011 Nucl. Fusion 51 053002

[61] Angioni C. et al 2014 Nucl. Fusion 54 083028

[62] Casson F.J. et al 2015 Plasma Phys. Control. Fusion 57 014031

[63] Beurskens M.N.A. et al 2013 Plasma Phys. Control. Fusion 55 124043

[64] Zhou C. et al 2017 Nucl. Fusion submitted

[65] Greenfield C.M. et al 2001 Phys. Rev. Lett. 86 4544

[66] Suttrop W. et al 2003 Plasma Phys. Control. Fusion 45 1399

[67] Suttrop W. et al 2005 Nucl. Fusion 45 721

[68] Oyama N. et al 2005 Nucl. Fusion 45 871

[69] Xi P.W., Xu X.Q. and Diamond P.H. 2014 Phys. Rev. Let

Fusion neutron production with deuterium neutral beam injection and enhancement of fast-ion physics study in LHD

M. Isobe[1,2], K. Ogawa[1,2], T. Nishitani[1], N. Pu[2], H. Kawase[2], and LHD Experiment Group[1]

[1]National Institute for Fusion Science, National Institutes of Natural Sciences, Toki 509-5292, Japan
[2]SOKENDAI (The Graduate University for Advanced Studies), Toki 509-5292, Japan

Abstract

The deuterium operation of the Large Helical Device (LHD) heliotron started in March 7, 2017, after long-term preparation and commissioning works necessary to execute the deuterium experiment. A comprehensive set of neutron diagnostics was implemented to accelerate energetic-particle physics research in the LHD. The calibrated ex-vessel neutron flux monitor indicated that the total neutron emission rate in the first deuterium campaign reached 3.3×10^{15} n/s in inward shifted magnetic field configuration where confinement of helically trapped energetic ions is predicted to be better. Performance of the vertical neutron camera was verified by changing the plasma position and/or magnetic field strength. Triton burnup study was also conducted.

1. Introduction

In high-temperature deuterium plasmas heated by deuterium neutral beam (NB) injection, fusion neutrons are generated due to d-d fusion reaction. Fusion neutron has been one of the attractive objects for diagnosing beam-ion behaviors in addition to fusion gain assessment because generated neutrons in deuterium NB-heated deuterium plasmas are dominated by neutrons resulting from beam-plasma reactions. Deceleration of beam ions following NB turn-off was checked for the first time by measuring total neutron emission rate S_n in the Princeton Large Torus [1]. Subsequently, a beam blip injection method was developed to enhance accuracy of analysis on slowing-down property on beam ions in tokamaks [2-4]. After that, a rapid drop of S_n due to fishbone mode destabilized by perpendicularly-injected beam ions was found in the Poloidal Divertor Experiment [5]. Based on these backgrounds, diagnostics based upon nuclear technology have been steadily enhanced, in particular, in large tokamaks such as the Joint European Torus (JET) [6-8]. In the near future, neutron and gamma-ray diagnostics will play the leading role in assessing fusion output and/or energetic-ion confinement property in the International Thermonuclear Experiment Reactor [9-11].

Turning one's eyes to helical/stellarator devices, fusion neutron measurement was performed in Wendelstein 7-A for the first time in helical/stellarator devices. Then, the decay time of S_n following NB turn-off was analyzed to check whether beam ions were decelerated classically without loss or not [12]. Subsequently, total neutron emission rate and/or yield measurements were conducted in the Heliotron-E [13, 14], the Advanced Toroidal Facility [15], the Compact Helical System [16, 17], and the Wendelstein 7-AS

[18, 19]. Because those devices were small- and/or medium-sized and their heating systems were not as intense, S_n were very low, by about $10^9 \sim 10^{10}$ n/s. In such a case, the usage of neutron diagnostic was limited and was not very effective in studying confinement property of energetic ions. The helical plasma research entered a new stage on March 7, 2017. The deuterium operation began in the Large Helical Device (LHD), which is the world's largest-class helical device in order to explore a higher-confinement plasma regime. One of the primary purposes of the LHD deuterium project is to demonstrate that confinement capability of energetic ions is relevant to the future burning plasma in helical systems. Note that energetic-ion physics studies such as ripple transport of beam ions [20-22], effect of toroidicity-induced Alfvén eigenmodes [23-25], energetic-particle continuum modes [26], resistive interchange modes [27] on beam ion loss, and effects of resonant magnetic perturbation field on beam ion loss [28] have been intensively conducted by using various energetic-particle diagnostics such as scintillator-based escaping energetic-ion diagnostic and charge-exchanged neutral particle analyzers [29] in the hydrogen operation phase in the LHD. Because these diagnostics do not provide directly information of energetic ions at core domain, we have concentrated on phenomenological and qualitative arguments regarding energetic ion's behavior. Since fusion neutron signals are newly available, the deuterium plasma experiment can provide an important opportunity to enhance energetic-particle physics study in the LHD. The LHD is capable of producing fusion neutrons over 1×10^{16} n/s, which is much higher than that observed in the small and medium class helical/stellarator devices. To extend energetic-particle physics study in the LHD, a comprehensive set of neutron diagnostics was prepared before the start of deuterium operation consisting of the neutron flux monitor (NFM), the neutron activation system, the vertical neutron camera (VNC), the neutron fluctuation diagnostic, and scintillating-fiber detectors for triton burnup. In this paper, hardware on neutron diagnostics prepared for the LHD deuterium operation is described.

2. Status of neutron diagnostics in LHD

To extend energetic-particle physics studies in the LHD, a comprehensive neutron diagnostic system was developed. The neutron diagnostics prepared for the first deuterium campaign of the LHD are listed in Table 1. The NFM is essential in the LHD operation in addition to physics purposes since annual neutron budget permitted by the Nuclear Regulation Authority of Japan is set to be 2.1×10^{19}. Therefore, the LHD cannot be operated without the NFM. Conceptual design of the LHD neutron diagnostics was performed before the initial operation of LHD [30]. Component technology test and/or development was initiated in around 2000 and a more concrete system was proposed subsequently [31]. As for the system development, we initiated development of a wide dynamic range NFM based on leading-edge digital technologies at the outset [32]. The NFM on LHD consists of three sets of two detectors as schematically depicted in Fig. 1(a). Each set has an ^{235}U fission chamber (FC), and a ^{10}B counter or a ^{3}He counter. The FC line can provide very wide dynamic range and fast-time response capabilities. It was designed so as to realize neutron pulse counting rate up to 5×10^9 cps. The FC line is responsible for middle- to high-neutron yield shots when NBs are injected. Other neutron counters can work for low-neutron yield shot such as electron cyclotron resonance heating (ECRH) shot without NB injection. Prior to the deuterium operation of the LHD, in situ calibration of the NFM was carried out from November 7 to 18, 2016, by using intense a ^{252}Cf spontaneous

fission neutron source with radioactivity of about 800 MBq [33, 34] following the method standardized in Ref. 35. The FC line can cover S_n over 10^{17} n/s. Because the maximum S_n in the LHD is expected to be $(1\sim2)\times10^{16}$ n/s, the NFM developed for the LHD can cover the entire region of the expected S_n.

In the LHD, high-performance VNC of eleven channels was installed to measure neutron emission profile. The overview of the LHD-VNC is schematically drawn in Fig. 1(b). This is the first neutron camera in helical/stellarator devices in the world. The stilbene scintillation detector was chosen as a fast-neutron detector in terms of brightness and good neutron (n)-gamma (γ)-ray discrimination capability through various detector tests at accelerator-type fusion neutron facilities. The LHD-VNC system is characterized by MHz range operation capability with automated n-γ-ray discrimination function based on a leading-edge field-programmable gate array technology [36] and negligibly small cross talk fraction [37, 38]. The neutron collimator is made of made of heavy concrete and is embedded in a hole in the concrete floor (2.0 m thick) of the torus hall. Radially aligned eleven stainless steel pipes (1.5 m long × 3 cm ϕ) are embedded in a heavy concrete as a path for birth neutrons. Detailed information of the LHD-VNC hardware will be available in Refs. 37 and 38.
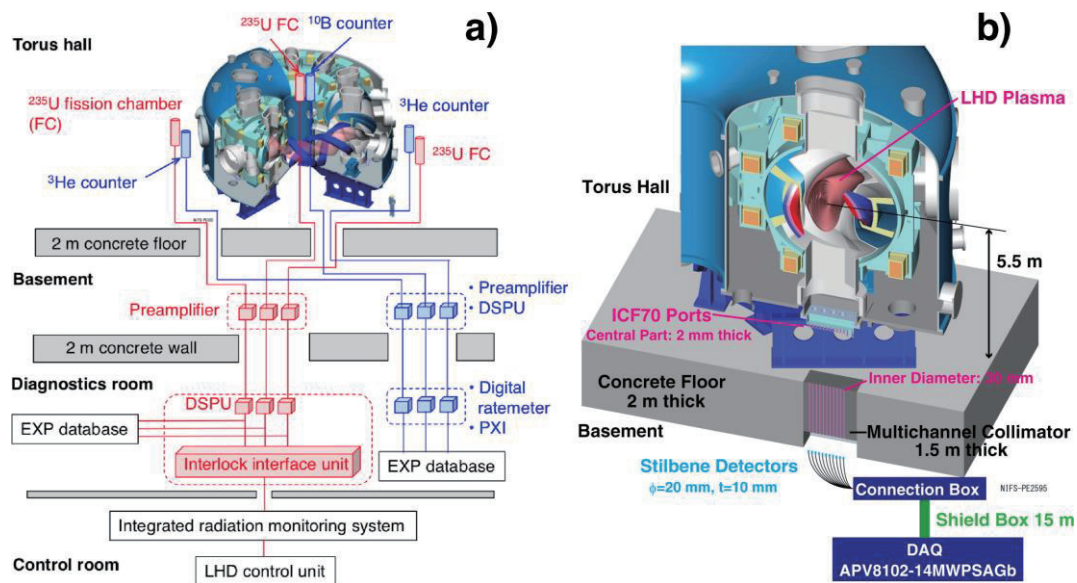
Fig 1. Arrangement of neutron flux monitor and vertical neutron camera

Triton burnup study is one of the primary physics subjects in the LHD deuterium project to demonstrate that confinement capability of energetic ion, in particular, MeV ion, is relevant to a fusion reactor plasma. The triton burnup ratio, which is defined as the ratio of secondary d-t neutron yield to primary d-d neutron yield, YDT/YDD has been examined in several tokamaks. In this work, initial study on triton behavior was performed by measuring 14 MeV neutrons generated by secondary d-t reaction in a deuterium plasma with a neutron activation technique [39] and scintillating-fiber (Sci.-Fi.) detector [40-42]. In addition to these, neutron fluctuation detector (NFD) with a fast-neutron sensor consisting of ZnS:Ag phosphor embedded in a hydrogenous polymer matrix is installed to measure fast-neutron fluctuation with

high time resolution [43]. The LHD deuterium operation has begun with a comprehensive set of neutron diagnostics listed in Table 1.

Table 1. A list of neutron diagnostics for the LHD deuterium operation

Diagnostics	Measurement target	Role	Status
(1) NFM	Total neutron emission rate	Neutron yield management Fusion output Global fast-ion confinement	Working
(2) NAS	Total neutron yield Secondary D-T neutron yield	Neutron yield management Triton burnup	Working
(3)VNC	Neutron emission profile	Beam ion profile Beam ion transport by EPM/AE	Working
(4)Sci-Fi detector	Secondary D-T neutron emission rate	Triton burnup	Working
(5)Fast-neutron scintillation detector	Neutron fluctuation	Beam ion transport by EPM/AE	Working
(6) γ-ray scintillation detector	Prompt γ-ray flux	Knock on ion tail Confinement of MeV ion D-3He reaction rate	Working

References

[1] Strachan J.D *et al* 1981 Nucl. Fusion **21** 67.

[2] Heidbrink W.W. Kim Jinchoon, and Groebner R.J. 1988 Nucl. Fusion **28** 1897.

[3] Heidbrink W.W. *et al* 1990 Phys. Fluids B **3** 3167.

[4] Tobita K., Tani K., Nishitani T., Nagashima K., and Kusama Y. 1994 Nucl. Fusion **34** 1097.

[5] McGuire K. *et al* 1983 Phys. Rev. Lett. **50** 891.

[6] Sadler G.J., Conroy S.W., Jarvis O.N., Adams J.M., and Hone M.A. 1990 Fusion Technol. **18** 556.

[7] Heibrink W.W. and Sadler G.J. 1994 Nucl. Fusion **34** 535.

[8] Jarvis O.N. 1994 Plasma Phys. Control. Fusion **36** 209.

[9] Kiptily V.G., Cecil F.E., and Medley S.S. 2006 Plasma Phys. Control. Fusion **48** R59.

[10] Krasilnikov A.V *et al* 2005 Nuclear Fusion **45** 1503.

[11] Sasao M., Nishitani T., Krasilnikov A., Popovichev S., Kiptily V.G., and Källne J. 2008 Fus. Sci. Technol. **53** 604.

[12] Weller A., and Maa☐berg 1985 Report No**. IPP 2/278**, Max-Planck-Institut für Plasmaphysik.

[13] Besshou S., Motojima O., Sato M., Sano F., Obiki T., Iiyoshi A., and Uo K. 1985 Nucl. Instrum. Meth. **A237** 590.

[14] Iki E. *et al* 1997 Fus. Eng. Des. **34-35** 603.

[15] Wade M.R., Thomas C.E., Colchin R.J., Rome J.A., England A.C., Fowler R.H. 1995 Nucl. Fusion **35** 1029.

[16] Isobe M., Sasao M., Osakabe M., Fujita J., Okamura S., Kumazawa R., Minami T., Matsuoka K., and Takahashi C. 1997 Rev. Sci. Instrum. **68** 532.

[17] Isobe M., Sasao M., Okamura S., Osakabe M., Kubo S., Minami T., Matsuoka K., Takahashi C., and CHS Group 1998 J. Plasma Fusion Res. SERIES **1** 366.

[18] Wolle B., Weller A., Schill S., Gadelmeier F., Baloui T., and Beikert G. 1999 Rev. Sci. Instrum. **70** 1197.

[19] Rust N., Reimbold S., Hübner K., Gadelmeier F., Penningsfeld F.P., and Weller A. 2000 27th EPS Conference on Contr. Fusion and Plasma Phys. Budapest, 12-16 June 2000 ECA Vol. **24B** 1621.

[20] Saida T. *et al* 2004 Nucl. Fusion 44 488.

[21] Osakabe M. *et al* 2010 Fus. Sci. Technol. **58** 131.

[22] Ogawa K. *et al* 2012 Plasma Fus. Res. **7** 2402014.

[23] Ogawa K. *et al* 2012 Nucl. Fusion **52** 094013.

[24] Ogawa K. *et al* 2012 Plasma Sci. Technol. **14** 269.

[25] Ogawa K. *et al* 2013 Nucl. Fusion **53** 053012.

[26] Isobe M, Ogawa K., Toi K., Osakabe M., Nagaoka K., Shimizu A., Spong D.A., Okamura S., CHS, and LHD Experiment Group 2010 Contrib. Plasma Phys. **50** 540.

[27] Ogawa K., Isobe M., Toi K., Watanabe F., Spong D.A., Shimizu A., Osakabe M., Ohdachi S., Sakakibara S., and LHD Experiment Group 2010 Nucl. Fusion **50** 084005.

[28] Ogawa K., Isobe M., Toi K., Shimizu A., Osakabe M., and LHD Experiment Group 2014 Plasma Fus. Res. **9** 3402097.

[29] Isobe M. *et al* 2010 Fus. Sci. Technol. **58** 426.

[30] Sasao M., Isobe M., Osakabe M., Taniike A., Iguchi T., Takada E., Iida T., and Wada M. 1997 Fus. Eng. Des. **34-35** 595.

[31] Isobe M. *et al* 2010 Rev. Sci. Instrum. **81** 10D310.

[32] Isobe M. *et al* 2014 Rev. Sci. Instrum. **85** 11E114.

[33] Isobe M. *et al* submitted to IEEE Transactions on Plasma Science.

[34] Nishitani T. *et al* accepted for publication in Fus. Eng. Des.

[35] Strachan J.D. *et al* 1990 Rev. Sci. Instrum. **61** 3501.

[36] Ogawa K., Isobe M., Takada E., Uchida Y., Ochiai K., Tomita H., Uritani A., Kobuchi T., and Takeiri Y. 2014 Rev. Sci. Instrum. **85** 11E110.

[37] Kawase H., Ogawa K., Nishitani T., Pu N., and Isobe M. submitted to IEEE Transactions on Plasma

Science.

[38] Kawase H., Ogawa K., Nishitani T., Pu N., Murakami S., and Isobe M. submitted to Plasma Fusion Research.

[39] Pu N., Nishitani T., Isobe M., Ogawa K., Kawase H., Tanaka T., Li S.Y., Yoshihashi Y., and Uritani A. 2017 Rev. Sci. Instrum. **88** 113302.

[40] Wurden G.A., Chrien R.E., Barnes Cris W., Sailor W.C., Roquemore A.L., Lavelle M.J., O'Gara P.M., and Jordan R.J. 1995 Rev. Sci. Instrum. **66** 901.

[41] Sailor W.C., Barnes Cris W., Chrien R.E., and Wurden G.A. 1995 Rev. Sci. Instrum. **66** 898.

[42] Nishitani T., Hoek M., Harano H., Isobe M., Tobita K., Kusama Y., Wurden G.A., and Chrien R.E. 1996 Plasma Phys. Control. Fusion **38** 355.

[43] Ogawa K., Isobe M., Kawase H., Nishitani T., Pu. N., and LHD Experiment Group submitted to Plasma and Fusion Research.

Simulation with MEGA code of energetic particle driven instabilities

Y. Todo[1,2]

[1]National Institute for Fusion Science, National Institutes of Natural Sciences, Toki 509-5292, Gifu, Japan

[2]Graduate University for Advanced Studies, Toki 509-5292, Gifu, Japan

Abstract

MEGA is a hybrid simulation code for energetic particles interacting with an magnetohydrodynamic (MHD) fluid. The distribution formation process in the collisional slowing-down time scale of energetic ions for various beam deposition power (P_{NBI}) and slowing-down time (τ_s) was investigated with MEGA code. The multi-phase simulation technique, which is a combination of classical simulation and hybrid simulation, is applied for the long time simulation. The physical parameters other than P_{NBI} and τ_s are similar to those of a Tokamak Fusion Test Reactor (TFTR) experiment (Wong et al 1991 Phys. Rev. Lett. 66 1874) where toroidal Alfvén eigenmode (TAE) bursts take place recurrently. With increasing volume-averaged classical energetic ion pressure, which is well proportional to $P_{NBI}\tau_s$, the energetic ion confinement degrades monotonically due to the transport by the TAEs. The volume-averaged energetic ion pressure depends only on the volume-averaged classical energetic ion pressure, not independently on P_{NBI} or τ_s. The energetic ion pressure profile resiliency, where the increase in energetic ion pressure profile is saturated, is found for the cases with the highest $P_{NBI}\tau_s$ where the TAE bursts take place.

1. Introduction

Hybrid simulations of energetic particles and MHD are useful tools to analyze both the Alfvén eigenmodes (AEs) and the energetic-particle transport. In most of the hybrid simulations, the initial energetic particle distribution is assumed, and the evolution of AEs and energetic particles is simulated as an initial value problem for a short time of the growth and saturation of the AEs, which is typically ∼1 ms. However, we should notice that the energetic particle distributions in the experiments are formed in a longer time scale of the collisional slowing down time for energetic particles interacting with the AEs. Then, comprehensive simulations that include the energetic particle source (birth of alphas, NBI, ICRF), collisions of energetic particles with the bulk plasma particles, energetic-particle losses, and the interactions between energetic particles and AEs are needed for the understanding of the energetic particle distribution in the experiments and the prediction of future experiments. The author and his collaborators have tried to develop such comprehensive simulations of energetic particles and AEs with the energetic ion source, collisions, and losses [1-10]. We performed the first numerical demonstration of TAE bursts with parameters similar to a TFTR experiment [11] and reproduced many of the experimental characteristics [4]. However, the saturation amplitude of the magnetic field fluctuation normalized by the toroidal field was $\delta B/B \sim 2\times10^{-2}$, which is higher by one order of magnitude than the value $\delta B/B \sim 10^{-3}$ inferred from the experimental plasma displacement measurements. In the simulation of [4], the only nonlinearity retained

was the nonlinearity in the energetic-particle orbits, while the nonlinear MHD effects were neglected. The nonlinear MHD effects on the evolution of a TAE was carefully investigated, and it was found that the energy transfer from the TAE to the nonlinearly generated zonal modes with toroidal mode number n=0 and higher harmonics reduces the saturation level of the TAE [12, 13]. A hybrid simulation with both the MHD nonlinearity and the energetic ion source, collisions, and losses was constructed using the δf particle simulation method for energetic particles to reduce the numerical noise [6]. The TAE bursts were reproduced with the δf simulation, but the energetic ion velocity distribution was purely parallel to the magnetic field and the pitch-angle scattering was neglected because of the limitation of the δf simulation model developed in [6]. The multi-phase simulation, which is a combination of classical simulation and hybrid simulation for energetic particles interacting with an MHD fluid, was developed in order to investigate the energetic ion distribution formation process with beam injection, collisions, losses, and transport due to the AEs with the MHD nonlinearity [8, 9]. We use the MEGA code [1] for both the classical and hybrid simulations. We run alternately the classical simulation without MHD perturbations and the hybrid simulation with MHD perturbations. The multi-phase simulation is a comprehensive simulation, which deals with both the AEs and the energetic ion transport as self-consistently and realistically as possible, yet attainable on a tractable timescale. It was demonstrated with the multi-phase simulation of DIII-D discharge#142111 that the energetic ion spatial profile is significantly flattened due to the interaction with the multiple AEs and that the energetic ion pressure profile is in agreement with that of the experiment with the root-mean-square of the deviations same as the error bar [9]. The predicted temperature fluctuation profiles of n = 3, 4, and 5 modes were quantitatively compared with ECE measurements, and it was found that the fluctuation profiles as well as phase profiles are in very good agreement with the measurements. Additionally, the saturated amplitudes are within a factor of 2 of those measured. The nonlinear MHD effects that prevent the AE amplitude from increasing to a large amplitude observed in a reduced simulation [4] are included in the hybrid simulation. The energetic ion profile stiffness that was observed in the DIII-D experiments was also investigated with the multi-phase simulation, and it was demonstrated that the resonance overlap of multiple eigenmodes accounts for the profile stiffness with the sudden increase in energetic ion transport with increasing beam power [10]. In this work, we apply the multi-phase simulation to tokamak plasmas for various beam deposition power (P_{NBI}) and slowing-down time (τ_s) with the other parameters similar to the TFTR experiment [14]. For the same beam deposition power (P_{NBI}=10 MW) and the slowing-down time (τ_s=100 ms) as those used in [4, 6], we see that the TAE bursts take place with time intervals 2 ms, which is close to that in the experiment, and the maximum amplitude $v_r/v_A \sim 3 \times 10^{-3}$. For the lowest beam deposition power (P_{NBI}=5 MW) and the shortest slowing-down time (τ_s=20 ms), the amplitude of the dominant TAE is kept at a steady level $v_r/v_A \sim 4 \times 10^{-4}$.

2. Simulation Results

We examine the volume-averaged energetic ion pressure and the energetic ion profile for various P_{NBI} and τ_s. We see the monotonic degradation of the energetic ion confinement and the profile resiliency, where the energetic ion pressure profiles are saturated with increasing volume-averaged classical energetic ion pressure which is well proportional to $P_{NBI}\tau_s$. Volume-averaged energetic ion beta value in the simulation

results is plotted versus volume-averaged classical energetic ion beta $<\beta_h>$ in Fig. 1(a). The line in the figure represents $<\beta_h> = <\beta_{h\ classical}>$. We see that the reduction of $<\beta_h>$ from $<\beta_{h\ classical}>$ increases monotonically for higher $<\beta_{h\ classical}>$ which indicates the monotonic degradation of energetic ion confinement with increasing $<\beta_{h\ classical}>$. We see a reduction of energetic ion beta by 20% for $<\beta_{h\ classical}>$ = 0.3%. It is interesting to note that the data points look located on one curve, while the data points represent the results for various beam deposition power P_{NBI} and slowing-down time τ_s. This indicates that the most important parameter that determines the energetic ion confinement is $<\beta_{h\ classical}>$ rather than the independent parameters, P_{NBI} or τ_s. Volume-averaged classical energetic ion beta $<\beta_{h\ classical}>$ is well proportional to the product of the two parameters $P_{NBI}\tau_s$. The ratio of the neutron rate to the classical neutron rate is also plotted Fig. 1(b). We see the monotonic degradation in the neutron rate with increasing $<\beta_{h\ classical}>$. The neutron rate is about 35% of the classical neutron rate for $<\beta_{h\ classical}> \sim 0.015$ with P_{NBI}=10MWand τ_s=100 ms. This is close to the results of [4] where the stored energetic ion energy is 40% of the classical simulation result.

The energetic ion β profiles are compared in Fig. 2 for case D (P_{NBI}=5 MW, τ_s=100 ms), case H (P_{NBI}=10 MW, τ_s=60 ms), and case I (P_{NBI}=10 MW, τ_s=100 ms) with the highest $<\beta_{h\ classical}>$. We see the energetic ion beta profiles are very similar r, and are saturated with the increase of $<\beta_{h\ classical}>$ by factor of 2 from case D to case I. This saturation of the energetic ion pressure profile with increasing beam power is called profile resiliency, and the energetic ion profile is regarded as 'stiff' when the energetic ion transport suddenly increases for the beam power or the energetic ion profile gradient above critical values. In our simulations based on a DIII-D equilibrium, it was demonstrated that the profile stiffness is brought about by resonance overlap of multiple AEs. The profile resiliency was not observed in the simulations presented in [10]. It was discussed that the profile resiliency would take place if the phase space was fully covered by the resonance overlap from the plasma center to the edge. We would like to point out that the recurrent AE bursts occur with a constant time interval for case I. This type of AE bursts was not observed in the simulations presented in [10]. The phase space may be fully covered by the resonance overlap when the AE bursts take place as was demonstrated with the simulations of AE bursts in [4].
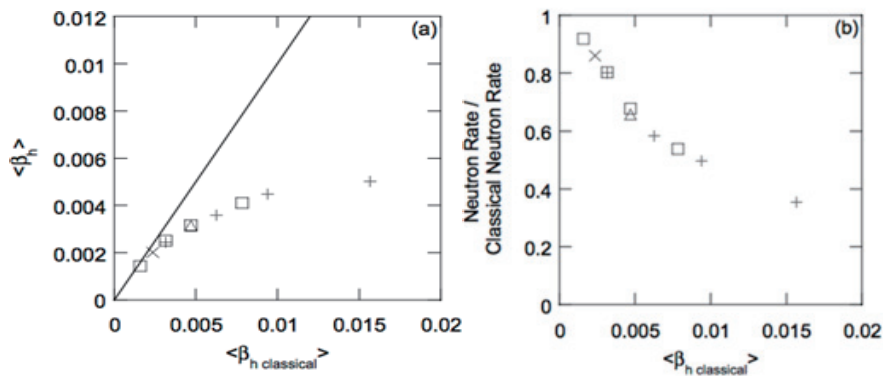
Fig. 1 (a)Volume-averaged energetic ion beta $<\beta_h>$ and (b) ratio of the neutron rate to the classical neutron rate versus volume averaged classical energetic ion beta $<\beta_{h\ classical}>$. The line in panel (a) represents $<\beta_h>=<\beta_{h\ classical}>$ [14].

Fig. 2 Energetic ion beta profiles for case D (P_{NBI}=5 MW, τ_s=100 ms), case H (P_{NBI}=10 MW, τ_s=60 ms), and case I (P_{NBI}=10 MW, τ_s=100 ms) [14].

References

[1] Todo Y and Sato T 1998 Phys. Plasmas **5** 1321

[2] Todo Y and Sato T 1999 J. Plasma Fusion Res. **2** 263

[3] Todo Y, Watanabe T-H, Park H-B and Sato T 2001 Nucl. Fusion **41** 1153

[4] Todo Y, Berk HL and Breizman BN 2003 Phys. Plasmas **10** 2888

[5] Todo Y *et al* 2010 Fusion Sci. Technol. **58** 277

[6] Todo Y, Berk HL and Breizman BN 2012 Nucl. Fusion **52** 033003

[7] Bierwage A, Todo Y, Aiba N and Shinohara K 2014 Nucl. Fusion **54** 104001

[8] Todo Y, Van Zeeland MA, Bierwage A and Heidbrink W 2014 Nucl. Fusion **54** 104012

[9] Todo Y, Van Zeeland MA, Bierwage A, Heidbrink W and Austin M 2015 Nucl. Fusion **55** 073020

[10] Todo Y, Van Zeeland MA and Heidbrink W 2016 Nucl. Fusion **56** 112008

[11] Wong KL *et al* 1991 Phys. Rev. Lett. **66** 1874

[12] Todo Y, Berk HL and Breizman BN 2010 Nucl. Fusion **50** 084016

[13] Todo Y, Berk HL and Breizman BN 2012 Nucl. Fusion **52** 094018

[14] Todo Y 2016, New J. Phys. **18** 115005

Characteristic Properties and Effects of Energetic-Ion-Driven Geodesic Acoustic Modes in Reversed Magnetic Shear Plasmas of LHD

K. Toi , K. Ogawa, T. Ido, A. Shimizu, S. Morita, M. Osakabe and LHD Experiment Group

National Institute for Fusion Science, Toki 509-5292, Gifu, Japan

Abstract

In a helical device, LHD, a reversed magnetic shear (RS-) configuration was generated by counter neutral beam injection current drive where the beam driven current reduces extermnal rotational transform. In the RS-configuration, the rotational transform profile has a local minimum away from the magnetic axis, and energetic ion driven geodesic acoustic modes (EGAMs) and reversed magnetic shear Alfven eigenmodes (RSAEs) are concurrently excited.   In this configuration plasma, spontaneous increase in bulk ion temperature up to 1.8 times is observed at the plasma center.   The EGAM frequency has no response to the ion temperature increase and is by 25 - 40 % lower than the GAM frequency derived from gyrokinetic theory.   However, the EGAM frequency increases clearly during on-axis electron cyclotron heating, following the dependence of a square-root of electron temperature.   No clear suppression of microturbulence is observed during the ion temperature-rise.   It is interpreted that the ion tempearure rise is caused by ion heating due to ion Landau damping of EGAM.   That is, the effective heating power density is comparable to the ion heating power density estimated from the EGAM damping.

1. Introduction

Reversed magnetic shear (RS-) configuration of a tokamak plasma is a promising candidate scenario for steady-state operation in ITER, because high plasma confinement developing internal transport barrier (ITB) and high bootstrap current fraction can be easily achieved.   In a helical device LHD, generation of a RS- configuration was attempted for realizing improved confinement with ITB.   The configuration was obtained by neutral beam current drive (NBCD) in the conter direction to reduce extermnal rotational transform.   Thus obtained rotational transform profile has a local minimum away from the magnetic axis. In the RS-palsma energetic ion driven geodesic acoustic modes (EGAMs) and reversed magnetic shear Alfven eigenmodes (RSAEs) are concurrently excited[1].   In this presentation,   characteristics of EGAM and impacts on bulk plasma are discussed.

2. Characteristic properties of EGAM in the RS-plasma of LHD

Magnetic fluctuations of EGAM has an axisymmetric structure, i.e., toroidal mode number n=0, and has a standing wave structure in poloidal direction having m=2 or a character dominated by propagating m=1 sturucture.   Potential fluctuations of EGAM are measured by a heavy ion beam probe technique in a few RS-plasmas.   Magentic fluctuations of EGAM behave similarly to the potential fluctuations.   In Fig.1, the radial profiles of the root-mean-square of EGAM potential fluctuations ϕ_{G_rms} are shown for jusr

before (t=5.65 s) and in the initial pahse of spontaneous ion-temperature-rise (t=6.00 s), of which phenomenon is discussed in the next section.   They localize near the plasma center and can be fitted with the Gaussian shape: $\phi_{G\_rms}(\rho)=\phi_{G\_rms}(0)exp[-(k_ra)^2\rho^2]$.   Here, k_r is the radial wave number and $\phi_{G\_rms}(0)$ is the value at the plasma center.   From Fig.1, $k_r = 6.4 \sim 7.5$ m^{-1} and $\phi_{G\_rms}(0)$=1.2 kV are derived.
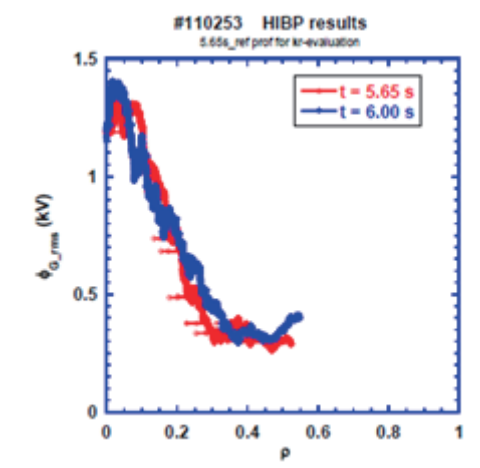
Fig.1 Radial profiles of the root-mean squre of EGAM potential fluctuations at two time slices just before and in the initial phase of spontaneous ion-temperature-rise.

3. Spontaneous increase in bulk ion temperature and ECH of the RS-plasma

An interesting finding in the RS-plasma of LHD is that spontaneous increase of bulk ion temperature at the plasma center often takes place during a certain characteristic phase of the plasma shot.   The local minimum value of the rotational transform ι_{min} can be accurately obtained from the time evolution of the RSAE frequency.   That is, the ι_{min} value is derived at the time that the temporal sweeping of the RSAE frequency takes the minimum.   When ι_{min} passes 1/3, the bulk ion temperature starts to increase linearly for about 0.4 s, as shown with a shaded period in Fig.2.   In this shot, the time that ι_{min} passes 1/3 is t=5.85 s.   The T_{io}-rise ceases suddenly.   When the line averaged density becomes appreciably higher more than ~ 0.8x10^{19} m^{-3}, T_{io} reaches to ~ 1 keV and decays gradually as shown with a broken line in Fig.2.   When high power ECH of 2.5 MW is applied from t=6.8 s to 7.3 s, central electron temperature increases more than 4 keV, so that T_{io} derived from the Doppler broadening of ArXVII line emission no longer indicates the value at the plasma center.   So far, the reason for the sudden onset and stop of the T_{io}-increase is not clarified, and is under investigation.
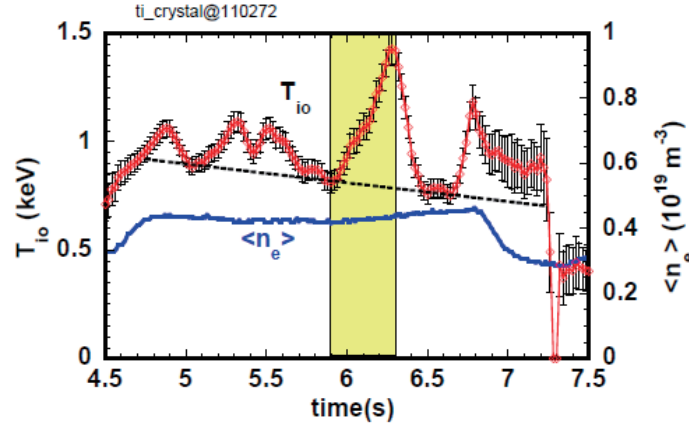
Fig.2 Time evolution of bulk ion temperature at the plasma center T_{io} and line averaged electron density $<n_e>$ in an RS-plasma exhibiting the spontaneous T_{io}-rise.   The dotted line indicates the ion temperature expected by collisional process.

4.   Comparison of observed EGAM frequency with several model estimations

According to gyrokinetic theory, the frequency of GAM depends on ion temperature T_i as well as electron temperature T_e as $f_{GAM} = \frac{1}{2\pi R}\sqrt{\frac{2T_e}{C_z m_i}}\sqrt{1+\frac{7}{4}\frac{T_i}{T_e}}\sqrt{1+\frac{\iota^2}{2}}$, where R, C_z and ι are respectively the plasma major radius, plasma mass ratio to the proton mass m_i and the rotational tramsform [2].   We estimate the GAM frequency by the equation using the plasma parameters measured at the plasma center, because the EGAM localizes near the plasma center as shown in Fig.1.   For the period where T_{io} increases linearly in time from 0.75 keV to 1.4 keV and T_{eo}=1.3 keV stays constant in time, f_{GAM}=24.2 kHz for T_{io}=0.75 keV and f_{GAM}=29.0 kHz for T_{io}=1.4 keV are inferred with C_z=1.5 including neon doping. However, the observed EGAM frequency is 18.0 kHz at T_{io}=0.75 keV and is 17.1 kHz at T_{io}=1.4 keV. These frequencies are respectively ~75 % and ~60% of the GAM frequencies by gyrokinetic theory.   The EGAM frequency is noticeably lower than the GAM frequency as first pointed out theoretically [3].   An interesting new finding is that the frequency has no or very weak dependence on ion temperature.   If the expression of EGAM frequency removing ion temperature dependence $f_{EGAM} = \frac{1}{2\pi R}\sqrt{\frac{2T_e}{C_z m_i}}\sqrt{1+\frac{\iota^2}{2}} \cong$

$\frac{1}{2\pi R}\sqrt{\frac{2T_e}{C_z m_i}}$ is adopted, the frequency is predicted as 17.1 kHz and agrees with the observed values very well. Moreover, from the time evolution of the EGAM frequency during ECH in shot shown in Fig.2, the frequency reaches ~31 kHz.   This value is consistent with the frequency estimated by the expression of f_{EGAM}.

5. Correlation between spontaneous ion-temperature-rise and EGAM fluctuation power

In the previous section, the tempearture dependences of the EGAM frequency are clarified from two distict time evolutions of the spontaneous ion-temperature-rise (T_{io}-rise) and electron cyclotron heating in

the RS-plasmas produced by counter NBCD in LHD. We investigate possible mechanisms of spontaneous T_{io}-rise as shown in Fig.2. The T_{io}-rise is observed in low density regime of $<n_e> \lesssim 0.6$ x 10^{19} m^{-3} and high plasma current of $|I_p| \gtrsim 100$ kA. When $<n_e>$ is increased above $<n_e> \gtrsim 0.8$ x 10^{19} m^{-3}, T_{io} reaches ~ 1keV in the initial phase of the RS-plasma and then gradually decreases without the particular T_{io}-rise. It should be noted that density fluctuations of microturbulence are not suppressed during the spontaneous T_{io}-rise, so that it should not be caused by transport reduction in ion channel. The other possible candidate mechanism is an increase of ion heating power which might be related to ion Landau damping of EGAM. Before actual estimation of the ion heating power, we investigate correlation between temporal behaviors of EGAM fluctuation power and T_{io}. The EGAM fluctuation power is evaluated as time average of the auto correlation power $< b_\theta * b_\theta >_{EGAM}$ using magnetic fluctauations generated by EGAM. Figure 3 shows time evolution of T_{io} and $< b_\theta * b_\theta >_{EGAM}$ in a relatively high density RS-plasma having high NBCD current up to 150 kA. As seen from Fig.3, the EGAM fluctuation power rapidly increases with increase in counter NB driven current. In this shot, T_{io} first increases to ~ 1 keV and then decreases monotonically with increase in plasma current up to ~150 kA. In this shot, ι_{min} passes the rational value 1/3 at the time indicated by a broken vertical line. On the other hand, as shown in Fig.2, T_{io} spontaneously increases when ι_{min} decreases below 1/3 in low density RS-plasma. Time evolution of EGAM fluctuation power $< b_\theta * b_\theta >_{EGAM}$ is shown in Fig.4 togeter with T_{io} and the time derivative dT_{io}/dt. During the T_{io}-rise phase shown by a shaded zone (5.9 s < t < 6.3 s) the EGAM fluctuation power does not increase as that in high density shot shown in Fig.3, and even decrease slightly and then gradually increases. The T_{io}-rise suddenly ceases with sudden jump-up of the EGAM fluctuation power. In the period from t =6.6 s to 6.8 s, T_{io} again inreases, accompanying a clear drop of the EGAM fluctuation power. The fluctuation power is enhanced by ECH from t=6.8s. These behaviors of the EGAM fluctuation power correlate well with the T_{io}-increase. This observation suggests that EGAM damping would contribute to the T_{io}-rise. The ion heating power density by EGAM damped by ion Landua damping is estimated as, $P_{G-i}=2\gamma_G W_G$ [4], where γ_G is the damping rate of EGAM which can be estimated by GAM damping rate derived from gyrokitetic theory [2]. The quantity W_G is the EGAM fluctuation energy generated by ExB flow and is expressed as $W_G=\frac{1}{2} m_i n_i \frac{(k_r \phi_{G-rms})^2}{B^2}$. It should be noted that the ion-temperature-rise occurs in the plasma core region of $r/a \lesssim 0.5$. From the observed dT_{io}/dt shown in Fig.4 (right), the effective ion heating power density evaluated with dW_i/dt (W_i: ion stored energy) is ~1.5-3.0 kW/m^3. On the other hand, the ion heating power density estimated with $P_{G-i}=2\gamma_G W_G$ is 0.52-4.3 kW/m^3. Here, γ_G = 2.5-15x10^3 s^{-1} and W_G=0.10-0.14 J/m^3 are estimated with the experimentally obtained data k$_r$=7 m^{-1}, ϕ_{G-rms}=1.2 kV, n_i=0.4x10^{19} m^{-3}, T_{io}=0.8-1.1 keV, T_{eo}=1.3 keV and B=1.375 T. The ion heating power density by EGAM is comparable to the observed effective ion heating power density. In addition, Figure 4(left) indicates that the EGAM frequencies do not respond to ion-tempearature-rise but clearly depends on electron temperature increase by ECH.
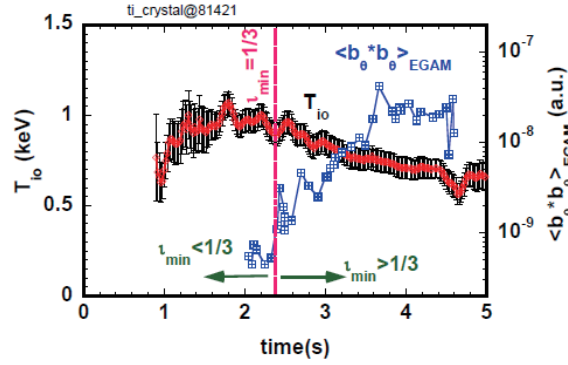
Fig.3 Time evolution of T_{io} and the EGAM magnetic fluctuation power $<b_\theta*b_\theta>_{EGAM}$. The vertical line indicates the time that the local minimum of the rotational transform ι_{min} decreases below 1/3. At the time the line averaged electron density is relatively high, $<n_e>$ =0.8x10^{19} m^{-3}. Toroidal plasma current driven by counter NBIs reaches 150 kA at t=4.5 s in the counter direction.
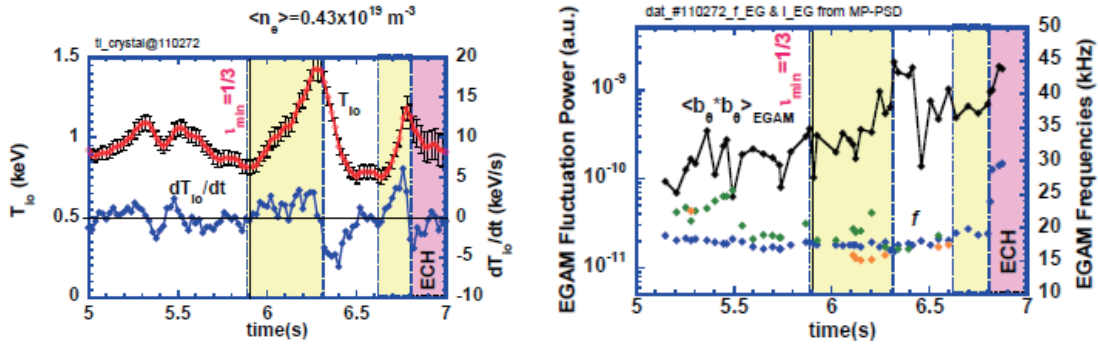
Fig.4 (left) Time evolutions of EGAM fluctuation power and the frequencies of several EGAM spectral peaks, (right) Time evolutions of T_{io} and the time derivative dT_{io}/dt.

6. Summary

In reversed magnetic shear plasmas of LHD produced by counter neutral beam current drive, energetic ion driven GAMs (EGAMs) are excited quasistationary without bursting character and rapid frequency chirping. They exhibit bursting character with rapid frequency chirping during intense ECH. In th RS plasmas, the temperature dependences of the excited EGAM frequency are clarified using two temperature increasing phases, i.e., spontaneous ion-temperature-rise keeping constant electron temperature and strong electron heating by ECH. The EGAM frequency is by 25 % to 40 % lower than the GAM frequency predicted from gyrokinetic theory, and has a clear dependence of the square-root of electron temperature but no or very weak ion temperature dependence. During spontaneous ion temperature rise, no clear suppression of microturbulence density fluctuations is observed. This increase of bulk ion temperature is explained by bulk ion heating by ion Landau damping of EGAM, because the ion heating power density estimated using experimentally measured EGAM potential fluctuations is comparable to the observed effective ion heating power density.

References

[1] K. Toi et al., Phys. Rev. Lett. **105** (2010) 145003

[2] H. Sugama and T.H. Watanabe, Phys. Plasmas **13** (2006) 012501

[3] G.Y. Fu, 2008 *Phys. Rev. Lett.* **101** (2008) 185002

[4] M. Sasaki, K. Itoh and S-I. Itoh, Plasma Phys. Control. Fusion **53** (2011) 085017

Enhancement of radial transport of energetic ion by helically-trapped energetic-ion-driven resistive interchange mode in LHD

K. Ogawa[1, 2], M. Isobe[1, 2], H. Kawase[2], T. Nishitani[1], R. Seki[1, 2], M. Osakabe[1,2], and LHD Experiment Group[1]

[1]National Institute for Fusion Science, National Institutes of Natural Sciences, Toki-city, Gifu, Japan

[2]SOKENDAI, Toki-city, Gifu, Japan

Abstract

Deuterium experiment was initiated to achieve higher-temperature and higher-density plasmas in March 2017 in the Large Helical Device (LHD). The central ion temperature notably increases compared with that in hydrogen experiments. However, energetic particle modes called the helically-trapped energetic-ion-driven resistive interchange modes (EIC) are often excited by intensive perpendicular neutral beam injections on high ion-temperature discharges. The mode leads to significant decrease of the ion temperature or to limiting the sustainment of the high ion-temperature state. To understand the effect of EIC on the energetic ion confinement, the radial transport of energetic ions is studied by means of the vertical neutron camera newly installed on LHD. Decreases of line-integrated neutron emission profile in core channels are obtained.

1. Introduction

Sustainment of high-temperature and high-density plasmas is required for realizing the nuclear fusion reactor. However, energetic particle transport induced by magnetohydrodynamic (MHD) modes triggered by energetic particles may lead to prevention of achieving high-performance plasmas and/or sustaining long-duration of high-performance discharges. In currently performed neutral-beam-heated deuterium plasma discharges, neutrons are mainly created by beam-plasma reactions. This means that neutron diagnostics can be used for studying energetic ion physics. In Large Helical Device (LHD), deuterium experiment was initiated to achieve higher-temperature and higher-density plasmas in March 2017 [1]. The central ion temperature becomes around 10 keV using neutral beam injections. However, the resistive interchange modes destabilized by energetic particles called the helically-trapped energetic-ion-driven resistive interchange mode (EIC) [2] are often excited by intensive perpendicular neutral beam injections. Accordingly, sustainment of the high ion-temperature state was limited. Hence, to understand the effect of the EIC on the beam ion confinement, beam ion transport and/or beam ion loss are studied by means of the comprehensive neutron diagnostics newly installed on the LHD such as a neutron flux monitor (NFM) and vertical neutron camera (VNC). This paper shows the observation of radial transport of beam ions due to the EIC.

2. Experimental Setups

The LHD is the world's largest heliotron device with a major radius/minor radius of 3.9 m/~0.6 m. The maximum toroidal magnetic field strength is around 3 T. The LHD is equipped with three tangentially-injected beams (NNB) having acceleration voltage of around 180 keV and two perpendicularly-injected beams (PNB) having acceleration voltage of 40 to 80 keV. The total injection power of NNB is around 15 MW, whereas that of PNB is around 18 MW. The typical pitch angle of beam ions injected by NNB is around 30 degrees, whereas that of PNB is 90 degrees. Therefore, beam ions injected by NNB mainly have passing orbits and those injected by PNB mainly have helically-trapped orbits. The total neutron emission rate (S_n) is measured by the absolutely calibrated NFM. The primary detector for measuring S_n is installed on the central axis of the LHD. The details of NFM are discussed in Ref. 3. Line integrated neutron emission profiles are measured by using the VNC newly installed on the basement level of the torus hall (Fig.1) [4]. The VNC capable of operation over MHz counting rate consists of an eleven-channel collimator made from a heavy concrete, stilbene fast-neutron scintillation detectors coupled with a photomultiplier having a high-gain stability, and the data acquisition system (DAQ) equipped with the leading edge fast analogue to digital converter and field programmable gate array (FPGA). The waveform acquired with 1 GHz sampling rate and shaping parameters of each pulse can be obtained simultaneously. Therefore, online and offline neutron-gamma discrimination are possible.
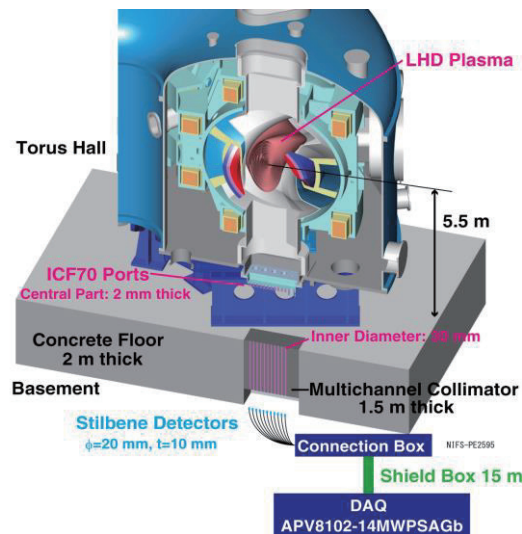
Fig. 1 Schematic drawing of vertical neutron camera installed on LHD.

3. Experimental Results

Figure 2 shows the typical time evolution of high ion-temperature discharges in LHD. Here, Rax_vac, Bt, PNB, Prad, Te0, Ti0, and b☐ represent the magnetic axis position, the toroidal magnetic field strength, injection powers of NBs, the radiation power measured by the resistive bolometer, the central electron temperature measured by the Thomson scattering diagnostics, the central ion temperature measured by the charge exchange recombination spectroscopy diagnostics, and the magnetic fluctuation amplitude measured

by the Mirnov coil installed on the vacuum vessel where the frequency range of the magnetic fluctuation is from 1 kHz to 200 kHz so as to cover the EIC frequency. Here, the range of ne_av and Te0 is 0.5~2.0×10^{19} m^{-3} and 1~4 keV, respectively. Note that the line-integrated density rapidly increases due to the carbon pellet injection at t of 4. 52 s in order to obtain sufficient intensity of the carbon line emission to measure the ion temperature. In this experiment, NNBs inject hydrogen beams and PNBs inject deuterium beams. Strong bursting EICs are clearly seen by the intensive PNB injection in b□. EIC bursts associate with concurrent decreases of S_n, increases of Prad, and decreases of Ti0. This suggests that beam ions are lost due to EIC bursts from the plasma and hit the plasma facing components. Here, decreases of Ti0 is the result of degradation of beam ion confinement by EIC burst. It is worth noting that almost 50 % of S_n is dropped within 10 ms. Line-integrated neutron emission profiles are measured by the VNC in this discharge. Here, the time resolution of neutron counts (C_n) is set to be 10 ms. Here, the maximum pulse counting rate is around 4×10^4 cps because the neutron-gamma ratio is 1 to 3 in the central channel, i.e., R of 3.72 m. Figure 3 shows time evolutions of PNB, b and C_n in eight channels. Here, R of 3.72 m, 3.90 m, and 4.17 m correspond to near Rax, normalized minor radius of 0.5, and normalized minor radius of 1.0, respectively. The decay of C_n on R of less than 3.81 m becomes noticeably shorter due to the EIC burst. Neutron counts decay gradually without EIC burst from t of 5.16 s; the decay time of C_n on R of 3.72 m is around 90 ms. On the other hand, with EIC burst, neutron counts decay rapidly, and the decay times becomes less than 20 ms. Here, ne_avg and Te0 are almost constant in the time period as shown in Fig.3. In the core channel (normalized minor radius less than 0.5) the C_n drops up to 50 %, whereas that in the edge channel stays almost the same.
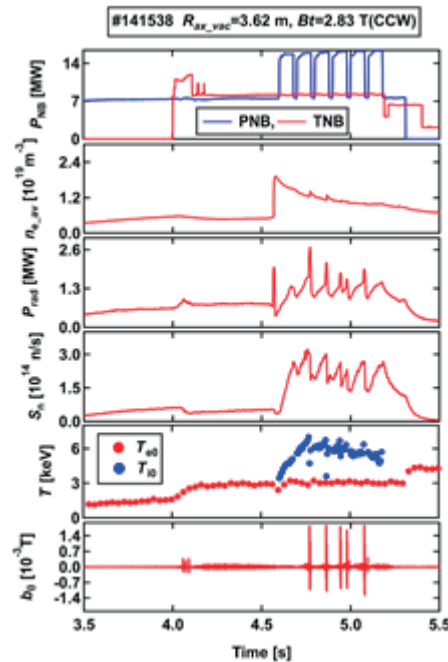
Fig.2 Typical time evolution of plasma discharges in R_{ax_vac}/Bt of 3.62 m/2.83 T.
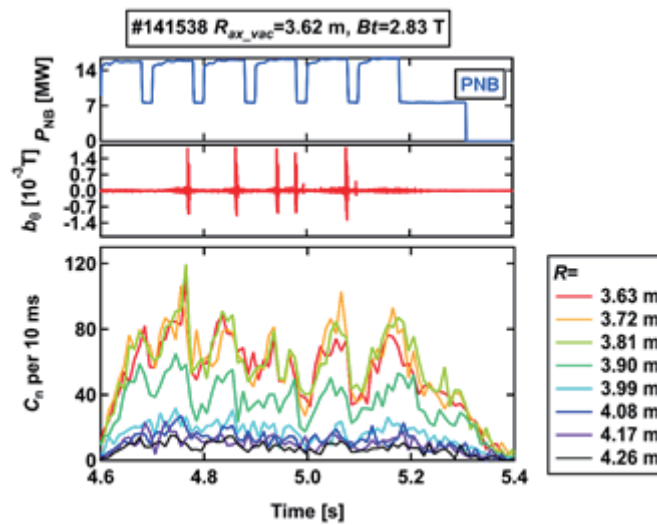
Fig.3 Time evolutions of the injection power of PNB, magnetic fluctuation amplitude, and neutron counting rates.

4. Summary

Energetic particle mode named EICs destabilized by intensive PNB injections is often excited on high ion-temperature discharges in LHD. Intermittent decreases of S_n up to 50 % associated with EIC are observed using the NFM. The line-integrated neutron emission profile measured by VNC remarkably changes due to EIC bursts. Sufficient drops of C_n are caused in the core channels (normalized minor radius less than 0.5), whereas there is almost no change of C_n in the edge channels.

Acknowledgments

References

[1] Osakabe M. et al 2017 Fusion Sci. Technol. **72** 199.

[2] Du X. D. et al 2015 Nucl. Fusion **56** 016002.

[3] Isobe M. et al 2014 Rev. Sci. Instrum **85** 11E114.

[4] Ogawa K. et al 2014 Rev. Sci. Instrum **85** 11E110.

Summary abstract of presentation at 11th APFA & 26th ITC entitled fusion research and international collaboration in Asian region

S.Morita[1,2] and A3 team

[1]National Institute for Fusion Science, Toki 509-5292, Gifu, Japan

[2]Graduate University for Advanced Studies, Toki 509-5292, Gifu, Japan

Abstract

Results of A3 Foresight Program among China, Japan and Korea are briefly summarized in terms of personal exchange, paper publication, conference presentation, A3 seminar, PhD student education and future prospect.   Existing and constructing devices in Asian region are also introduced in brief except for the three countries.

1. Introduction

Results of A3 program collaboration carried out during past five years (August 2012 - July 2017) are reported as plenary talk in the 11th Asia Plasma and Fusion Association Conference (11th APFA) and the 26th International Toki Conference (ITC-26) [1].   The presentation titled by "Fusion research and international collaboration in Asian region" also includes fusion activities in Asian countries.   A summary abstract of the plenary talk is presented in the final A3 seminar at Chongqing in China.

2. Recent activities on magnetic fusion research in Asian region

Existing magnetic fusion devices in China, Japan and Korea have been already introduced many times in past A3 seminars.   Then, other devices are introduced in the seminar toward further extension of the international collaboration in Asian region.
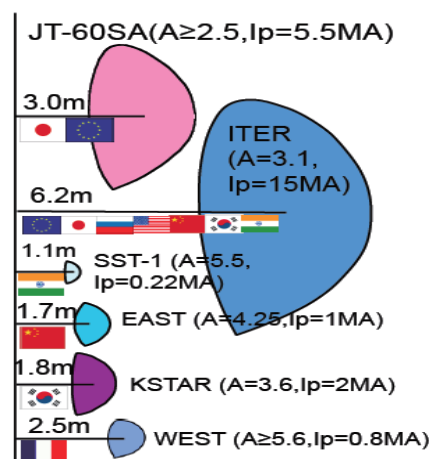
Fig.1 World superconducting tokamaks

2-1. JT-60SA (Japan)

JT-60SA (JAERI Tokamak-60 Super Advanced: I_p=5.5MA, B_T=2.25T, R/a=2.97/1.18m, κ = 1.93, δ = 0.5, q_{95}=3, V_p=133m^3) [2] shown in Fig. 1, which is characterized by high β_N operation and can be a flexible test stand for ITER, is a supporting device for ITER based on joint international research and development project between Japan and Europe.   It is expected a contribution to early realization of fusion energy by addressing key physics and engineering issues for ITER and DEMO.   Main subjects of JT-60SA are supplement of ITER toward DEMO by operating long pulse discharges (~100s) with high-performance plasmas and fostering of young researchers for playing a leading role in ITER and DEMO in addition to experiments for supporting ITER.   Goal of JT-60SA is a simultaneous achievement of key performances required for DEMO.   The first plasma is now scheduled on September, 2020.

2-2. SST-1 (India)

The first plasma of SST-1 (Steady state superconducting tokamak: I_p=220kA, B_T=3T, R/a=1.1/0.2m) [3] is obtained on June, 2013 at Institute for Plasma Research (IPR) at Gandhinagar.   At present, ohmic discharges with electron cyclotron heating (P_{ECH}=250kW) are achieved at I_p=60kA, B_T=1.5T with pulse duration of 0.4s.   Increase in B_T will be attempted in upcoming experiments.   There are some difficulties in cooling down the PF coils.   Simultaneous cool-down of PF and TF coils are not possible in current hydraulic scenarios.   Therefore, alternative experiments on low loop voltage operation with LHCD are planned in SST-1 in addition to an appropriate impurity control during discharges.

2-3. IR-T1 (Iran)

IR-T1 tokamak (I_p=60kA, B_T=0.9T, R/a=0.45/0.125m) [4] is being operated at Plasma Physics Research Center of Azad University in Tehran.   Typical plasma parameter ranges in ohmic discharges with limiter configuration are $50<T_e<200$eV, $1\leq n_e\leq 3\times10^{13}$cm^{-3}, $12<\tau_d<24$ms and $0.5\leq\tau_E\leq3$ms.   Studies are mainly done on MHD analysis, current disruption and mode locking.

2-4. GLAST (Pakistan)

GLAST tokamak (Glass Spherical Tokamak: I_p=50kA, B_T=0.4T, R/a=0.15/0.09m) [5] is being operated at NTFP in Islamabad.   The vacuum vessel is made of Pyrex glass as indicated in the device name.   Ohmic discharges are produced in GLAST with typical plasma parameters of T_e~400eV and τ_p~10ms.

2-5 KTM (Kazakhstan)

KTM tokamak (Kazakhstan Tokamak for Material Testing: I_p=750kA, B_T=1T, R/a=0.86/0.43m) [6,7] is being operated at NNC in Kurchatov.   Studies using ohmic discharges are mainly done under collaboration with Russia.

3. Summary of A3 foresight program
3-1. Personal exchange

Personal exchange (days/persons) in the A3 foresight program during past five years is listed in Table 1. In Japan the personal exchange is summarized at each Japanese fiscal year, i.e. April to March, while in China it is summarized at each calendar year, i.e. January to December. It should be then noted that the list includes certain uncertainty. It indicates that the personal exchange is steadily carried out among three countries including participations to the A3 seminar. Since in practice bilateral international collaboration programs, e.g. joint working group and post-CUP collaborations between Japan and China, Japan-Korea international collaboration, are running among three countries, the list does not indicate the whole personal exchange. In addition to the general personal exchange several young researchers have been fostered by staying during a long period in another country based on the A3 program.

Table 1 Personal exchanges among China, Japan and Korea

Year	C⇒J	J⇒C	C⇒K	K⇒C	J⇒K	K⇒J
2012	105/15	146/14	10/4	18/4	17/6	143/14
2013	236/28	76/10	65/15	42/16	60/13	56/7
2014	148/24	111/20	118/15	15/3	12/2	109/15
2015	476/55	139/24	231/26	22/4	92/15	93/16
2016	423/49	283/41	195/30	80/21	79/15	0/0
2017	301/36	69/6	94/12	74/10	0/0	78/15

3-2. Publications and conference presentations

Many papers have been published in scientific journals with peer reviews based on the collaboration of A3 program. The papers published with acknowledgement to the A3 foresight program, "This work was partly supported by the JSPS-NRF-NSFC A3 Foresight Program in the field of Plasma Physics", are listed in Table 2. Totally 210 papers are published in scientific journals with peer reviews and 310 papers are published in reports without reviews. In addition, 170 outputs from the A3 program are presented in the international conferences. In particular, 9 outputs are presented as an invited talk in the international conferences.

Table 2 Paper publications and conference presentations

Year	With referee	Without referee	International conference
2012/Aug-2013/Mar	6	17	-
2013/Apr-2014/Mar	42	73	16 (3 invited talks)
2014/Apr-2015/Mar	54	7	76 (1 invited talk)
2015/Apr-2016/Mar	45	17	33 (1 invited talk)
2016/Apr-2017/Mar	47	126	42 (3 invited talk)
2017/Apr-2017/Jul	16	81	5 (1 invited talk)

3-3. A3 seminars and proceeding publications

During past five years totally twelve A3 seminars are held in three countries including a coordinator meeting (1st A3 seminar) for triggering the A3 foresight program.   A3 seminars on Atomic and molecular processes in plasmas are also held for discussions of tungsten atomic structures and spectra which are necessary for tungsten diagnostics based on tungsten spectroscopy.   All the seminar proceedings are published in NIFS-PROC series except for 4th A3 seminar.

1st A3 seminar (coordinator meeting, 2012/8/22-23, Korea)

2nd A3 seminar (2013/1/22-25, Japan): NIFS-PROC-92 June 24, 2013

3rd A3 seminar (2013/5/20-23, China): NIFS-PROC-95 December 5, 2013

4th A3 seminar (2013/11/3-4, Korea): no proceedings

5th A3 seminar (2014/6/23-26, Japan): NIFS-PROC-97 October 30, 2014

6th A3 seminar (2015/1/6-9, China): NIFS-PROC-98 December 25, 2015

7th A3 seminar (2015/5/19-22, Korea): NIFS-PROC-100 July 25, 2016

8th A3 seminar (2015/12/1-4, Japan): NIFS-PROC-101 September 9, 2016

9th A3 seminar (2016/5/17-20, China): NIFS-PROC-102 January 23, 2017

10th A3 seminar (2016/11/22-25, Korea): proceedings are published in NIFS-PROC series

11th A3 seminar (2017/7/11-14, Japan): proceedings are published in NIFS-PROC series

12th A3 seminar (2017/12/12-15, China): proceedings are published in NIFS-PROC series

A3 A&M seminar (2012/7/30-8/4, Lanzhou): NIFS-PROC-91 February 1, 2013

A3 A&M seminar (2014/7/28-8/1, Lanzhou): NIFS-PROC-99 February 1, 2016

A3 A&M seminar (2016/7/26-28, Chengdu): NIFS-PROC-103 March 17, 2017

4. PhD student education and future prospect

4-1. PhD student education

Graduated students who received PhD in foreign countries of Asian region are investigated for future development of fusion research.   At present education of international PhD students in the field of fusion research is too much localized in Japan as follows;

- NIFS (Sokendai: 2006-2017): 34 (China: 23, India: 6, Pakistan: 1, Bangladesh: 1, Indonesia: 1,
                                                           Thailand:1, Taiwan: 1)

- QUEST (Kyushu Univ.: 2004-2017): 12 (China: 6, India: 4, Pakistan: 1, Bangladesh: 1)

- Heliotron (Kyoto Univ.: 2013-2017): 3 (China: 2, Korea: 1)

- Laser fusion (Osaka UNiv.: 1996-2017): 4 (China: 3, Korea: 1)

- ASIPP (USTC: 2013-2017): 3 (India: 1, Pakistan: 2)

It strongly suggests that personal exchanges of PhD students among Asian countries need to be further improved to enhance the fusion research activities.

4-2 future prospect

In Asian region several new devices are now constructing or designing for fusion research, e.g.

JT-60SA in QST for supporting ITER, HL-2M in SWIP for studying burning plasma and divertor physics, CFQS (Chinese First Quasi-axisymmetric Stellarator) in SWTJU for testing reduced neoclassical transport and good particle orbit and H-1 Heliac in USC which is transferred from ANU in Australia.   In addition, fusion study is also considered at Chiang Mai Univ. in Thailand using a small toroidal device.   Start of helical plasma research in China makes the international collaboration closer and easier because there is no essential difference between tokamak and stellarator.   Enhanced activities on fusion research at many countries in Asian region strongly request further development of international collaboration.

Acknowledgements

References

[1] 11th APFA and ITC-26, PL3, Ceratopia Toki, Gifu, Japan, 5-8 December 2017.

[2] H.Shirai, P.Barabaschi, Y.Kamada and JT-60SA team, Nucl. Fusion 57 (2017) 102002..

[3] S.Pradhan et al., Nuclear Fusion 55 (2015) 104009..

[4] R.Alipour, M.Ghoranneviss and A.Salar Elahl, AIP Advances 7 (2017) 115303.

[5] R.Khan, M.Nazir, A.Ali, S.Hussain and G.M.Vorobyev, Fus. Eng. Design 126 (2018) 10.

[6] ITER Newsline, 26 June 2017.

[7] B.Chektybayev, G.Shapovalov and A.Kolodeshnikov, Rev. Sci. Instrum. 86 (2015) 053505.

Experimental study of runaway electrons mitigation using supersonic molecular beam on HL-2A

Y.B. Dong[1], Y.P. Zhang[1], C.Y. Chen[1], H. Zhuang[2], Z. Chen[3], L. Zeng[2], X.Q. Ji[1], Yuan Xu[1], Y. Liu[1], Y. Xu[1] and HL-2A team

[1]Southwestern Institute of Physics, PO Box 432, Chengdu 610041, China

[2] Institute of Plasma Physics, Chinese Academy of Science, Hefei 23031, China

[3]State Key Laboratory of Advanced Electromagnetic Engineering and Technology, College of Electrical and Electronic Engineering, Huazhong University of Science and Technology, Wuhan 430074, China

1. Introduction

Disruption is one of major threats in future reactor-size tokamaks. Due to a sudden loss of confinement, the plasma produces excessive heat loads onto plasma facing components, inducing strong electromagnetic forces and currents in the structures, and hence, resulting in multi-MeV runaway electrons [1, 2]. The potential damage due to large runaway currents generated by the disruption is a key issue for the next generation tokamak. Therefore, disruption mitigation is essential for future fusion devices, such as ITER [3]. MGI is one of the candidates foreseen to be used as a standard mitigation tool in future tokamaks. It aims at reducing the deleterious effects of the disruption. So far, MGI experiments have been carried out on several tokamaks, including TEXTOR [4], DIII-D [5], ASDEX Upgrade [6], Alcator C-Mod [7] and JET [8, 9]. Encouraging results have been obtained. Another new method to mitigate plasma disruption is the SMBI, which has been developed on the HL-2A [10]. However, the optimization of injection scenarios (e.g., gas species and amount) is still an open question.
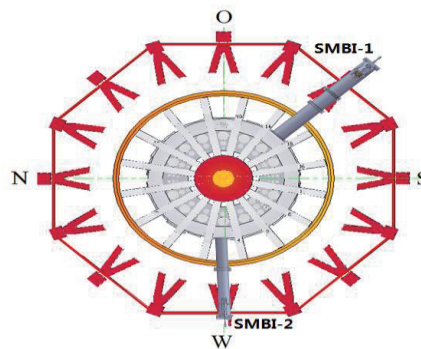
Fig. 1 Location of two SMBI systems and relevant diagnostics on HL-2A.

2. Disruption mitigation system

The improved SMBI system at HL-2A, which has similar mechanical structure with the old ones[10], meets a lot of demanding functional requirements, such as a larger orifice(0.5mm of diameter), a quite shorter opening time (0.2ms), and its maximum throughput is up to 1.0×10^{21} (10ms, 50bar). The SMBI clusters are produced at liquid nitrogen during a supersonic adiabatic expansion of moderate backing pressure gases into vacuum through a Laval nozzle. The SMBI was triggered by a negative voltage spike in the loop voltage signal prior to the thermal quench (TQ). Location of the SMBI systems used for experiments is shown on figure 1.

3. Experimental results

Recently, disruption mitigation experiments with SMBI have been carried out in the HL-2A tokamak to study various injection scenarios and gas jet penetration. In the experiments on HL-2A, SMBI has been used to mitigate the disruption by injecting Ar and Ne gases during the current quench. Plasma parameters of the two tokamaks are shown as follow: R=1.65m, a=0.40m, I_P=110-180kA, B_T=1.3T, n_e=1.0-1.8$\times 10^{19}$m^{-3}. Injected particles of a gas are about $N_{Ar} \sim 10^{20}$ and $N_{Ne} \sim 10^{21}$.

The runaway current during intentional disruptions caused by argon injection with MGI was successfully mitigated by SMBI with a number of injected about 1.0×10^{21} atoms, as shown in figure 2. Light gases, such as helium, are selected in this experiment for its high efficiency in increasing the density. Runaway current, synchrotron emission and the number of neutron events are reduced by an order of magnitude.
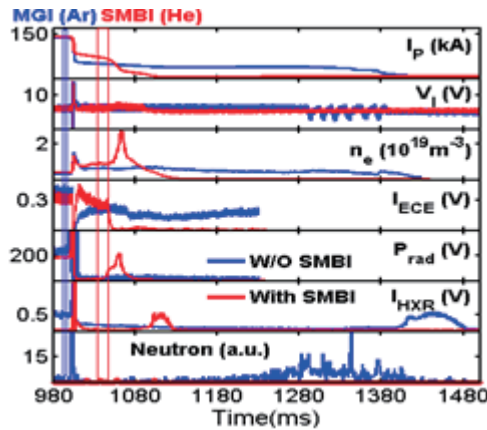
Fig. 2 The disruption was triggered by MGI with Ar gas, and then the runaway current was mitigated by using SMBI to inject He gas.

Furthermore, comparison of different gases has been performed. In figure 3, both the argon and helium have been injected by SMBI to mitigate the runaway current caused by argon injection with MGI. The SMBI gas puff into disruptive plasma efficiently prevented the runaway electron generation in HL-2A. Analysis of the experimental data has shown that these disruptions have been characterized by relatively high electron temperature and a very fast increase of plasma density, thus decreasing the runaway

production rate.
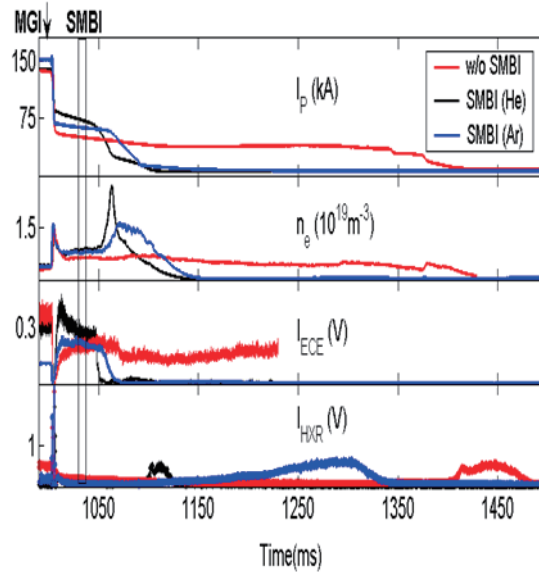
Fig.3 Comparison of runaway current mitigation for Ar injection versus helium injection

These experiments suggest that SMBI might be viable for runaway mitigation in future tokamaks even though core penetration of jet neutrals is not achieved. An understanding of this paradox is obtained by modeling, which shows that the initial cooling of the plasma periphery triggers a very rapid growth of low-order tearing mode, resulting in a stochastic region over much of the plasma. This allows rapid transport across the entire plasma, and could explain the effectiveness of SMBI mitigation in HL-2A in spite of the shallow penetration of the neutral gas jet.

The supersonic beam injection of impurities after thermal quench triggers the onset of large MHD activities before the runaway formation. Depending on the amount of energy stored in the core and the amount of gas injected, the plasma stability can be sustained during a few of those internal disruptions until it eventually ends up in a major disruption. There is strong connection between the frequency evolution of the n=1 oscillation and the beginning of the formation of runaway plateau. Figure 4 shows time traces of showing plasma current, magnetic fluctuation and spectrum of MHD activities in shot 23053 in HL-2A.

MHD activities increases simultaneously with the runaway plateau formation. Analysis of Mirnov coils measurements shows that this mode frequency lies between 2 and 8 kHz (shot to shot variation), and has an n = 1 structure. The increase of the mode frequency is accompanied by an increase of oscillation amplitudes. Determination of the poloidal number is more difficult by Mirnov coils measurements because of some signals are saturated. The tomography analysis of soft X-ray signals is used to analyze the poloidal mode structure of the MHD activity. The soft X-ray tomography confirms the speculation that the plasma is dominant by m=2 mode (figure 5).

To further clarify the mechanism of the MHD mode, the analysis of cross correlation and electron

temperature perturbation has been done. The correlation analysis between magnetic probe and ECE signals. Near the location at r=16cm, ECE data is not available. Figure 6 reveals that there is a phase reversal near q=2 surface, which demonstrates a typical tearing mode behavior.
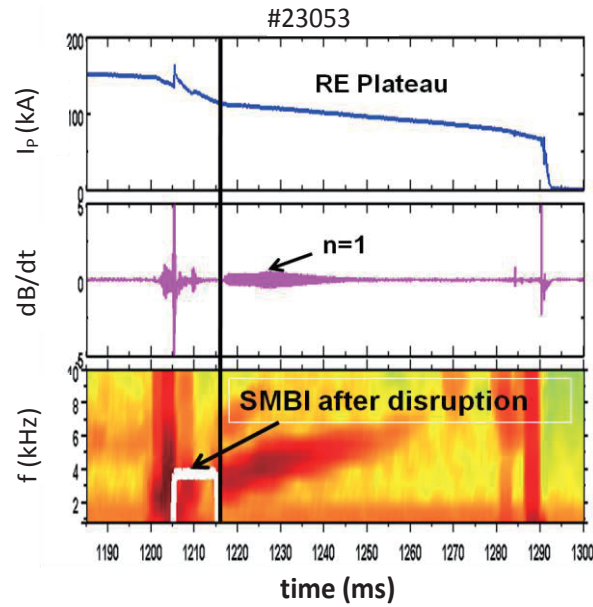
Fig. 4 Time traces showing plasma current, MHD activity and spectrum of MHD activity in shot 23053 in HL-2A.
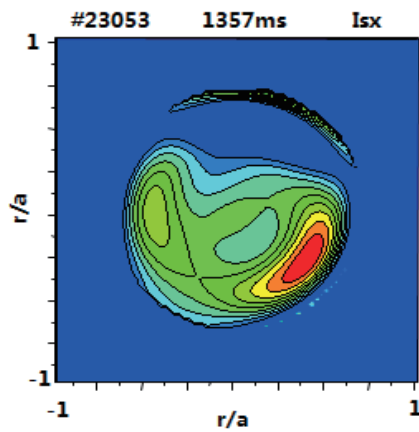
Fig.5 Contour plots of the tomographically reconstructed soft X-ray emission show the internal plasma motion.
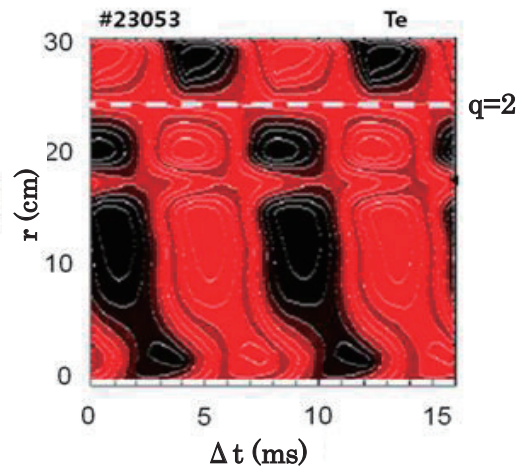
Fig.6 The analysis result of correlation and electron temperature perturbation.

4. Discussion

In the present SMBI mitigation experiments at HL-2A, the RE plateau is achieved even at $B_T = 1.3T$, much lower than the B_T threshold observed in other tokamaks. In order to check this experimental result, disruptions are deliberately triggered by injection of large amounts of Argon using the MGI valve on J-TEXT tokamak. The RE plateau has also been achieved during major disruption after Ar injected by MGI during pre-thermal quench phase. By comparing different inject amount, we found that runaway electrons were suppressed by a larger number of Ar atoms. Through scanning B_T and $\overline{n}_e$, both B_T and $\overline{n}_e$ threshold are observed in J-TEXT. The threshold of B_T is 1.2T, similar to that found in HL-2A. The RE plateau is easier to obtain at the lower electron densities, as expected.

Magnetic fluctuation is observed at the beginning of the current quench, which can cause strong RE losses and even prevent RE generation. A survey of discharges gives the relations between the level of the magnetic fluctuation and plasma parameters (toroidal field, plasma density, plasma current, heating power, etc.). Magnetic fluctuation is mainly contributed from the background plasma and the level is strongly dependent on the toroidal magnetic field and plasma electron density.

Acknowledgement

References

[1] Plyusnin V.V., et al., 2006 Nucl. Fusion 46 277.

[2] Yoshino R., et al., 1999 Nucl. Fusion 39 151.

[3]Hender T.C. et al 2007. Nucl. Fusion 47 128–200

[4]Bozhenkov S.A. et al 2008. Plasma Phys. Control. Fusion 50 105007

[5]Hollmannn E.M. et al 2005 .Nucl. Fusion 45 1046

[6]Pautasso G. et al 2009. Plasma Phys. Control. Fusion 51 124056

[7]Whyte D.G. et al 2007. J. Nucl. Mater. 363–365 1160–7

[8]Gill R.D., et al 2000. Nuclear Fusion, Vol. 40, No. 2, 163

[9] Lehnen M. et al 2009. 36th EPS Conf. (Sofia, Bulgaria)

[10]LianghuaYao, et al 2007. Nucl.Fusion 47 1399

Plasma response to the RMP application in LHD and Tokamaks

S. Ohdachi[1,2], T.Bando[1,2], K. Y. Watanabe[1] , and LHD Experiment group[1]

[1]National Institute for Fusion Science, Toki 509-5292, Gifu, Japan

[2]SOKENDAI (Graduate University for Advanced Studies), Toki 509-5292, Gifu, Japan

'

Abstract

Plasma response to the externally applied magnetic field is fairly complicated issue. The physics of the shielding and penetration has not been fully understood at the present moment. Two new observations, which may improve the understanding of the RMP physics, found in the deuterium campaign of LHD is reported. (1) The threshold value of the RMP coil current when the external field penetrates the plasma is significantly reduced in the deuterium campaign. (2) The amplitude of the energetic particle driven interchange mode (EIC) increases with deuteron NBI injection. EIC is suppressed by the RMP when the field does penetrate the plasma.

1. Introduction

In order to sustain the high-performance plasma having an edge transport barrier, instabilities related to the steep pressure gradient in the edge region is a critical issue. For example, the heat flux released by the excitation of the edge localized mode (ELM) is hazardous for the divertor of the next-generation Tokamak devices, such as the ITER. It is thus urgent to find a way to control the edge MHD activities. Though the resonant magnetic perturbation (RMP) is the most promising candidate to control the ELMs, the detailed mechanism how the RMP affects the MHD activities, has not been fully understood. Therefore, three projects toward the understanding of the RMP effects were conducted in the category IIb of the A3 collaboration. (1) Equilibrium determination when the RMP is applied: (2) Visualization of the MHD activities: (3) Control of the MHD activities using RMP: In this report, the change of the penetration condition of the RMP (1) and the effect of the RMP on the energetic particle driven MHD mode are presented (2).

2. Threshold of the RMP field to penetrate the plasma

Externally applied RMP field is shield by the LHD plasma. When the external magnetic field is increased and exceeds the threshold value, the external field penetrates the plasma. At the penetration timing change of the plasma response field and the formation of the magnetic island is observed. The threshold value of the RMP current is investigated in the deuterium campaign of the LHD started from March 2017. The model how the external field penetrate the plasma has not been fully established. It was pointed out that the threshold value is related to the poloidal flow velocity. Another possible model is related with the stability of the MHD instabilities. In the hydrogen experiments, it was not possible to determine which model can explain the experimental observation better. The dependence of threshold of

the RMP (m/n = 1/1) penetration are compared. The penetration threshold in D plasmas is quite smaller than that in the H plasmas in the wide range of the plateau collisionality regime. Ideal one-fluid MHD equations does not explicitly contain the information of the mass of the ions. It is thus noted that most of the MHD instabilities can be described by the one fluid model. Therefore, it is quite likely the characteristics of the MHD instabilities has not been changed with the change of the ion species. As is expected, no significant change in the MHD instabilities are observed in D plasma experiment. However, since the collisionality and the neo-classical viscous force are different with different ion species, the flow velocity profile might be changed in the deuterium experiments. Therefore, since the penetration threshold is quite different in D plasma, the physics related with flow velocity seems to be more important elements to affects the shield / penetration issues.

3. Effects of the RMP on the energetic particle driven MHD instabilities.

Confinement of the energetic particles (EP) is essential for the realization of the magnetically confined fusion reactor. Energetic particles are not well confined when the EP driven MHD modes, such as the EP driven resistive interchange mode (EIC) observed in the Large Helical Device (LHD), are excited. Understanding of the mechanism how the EP drives the MHD instability is quite important for developing the scheme to control EP driven mode. LHD is a Heliotron type device where the rotational transform is created by the two helical coils (L=2/M=10). As a consequence, helically twisting region where the magnetic field strength is weak (blue region in Fig, 1(A)) appears. EPs having perpendicular velocity components are trapped in this region and making precession motion helically. The rotation frequency of this precession motion is slow enough to interact with the pressure driven MHD modes with toroidal/poloidal mode number m/n = 1/1 [1]. It is similar to the classical fishbone mode where the trapped EP destabilized the marginally stable MHD mode (interchange mode in the EIC and kink modes in the fishbones). In the deuterium experiments of LHD, the heating power of the perpendicular injected NBI is enhanced.
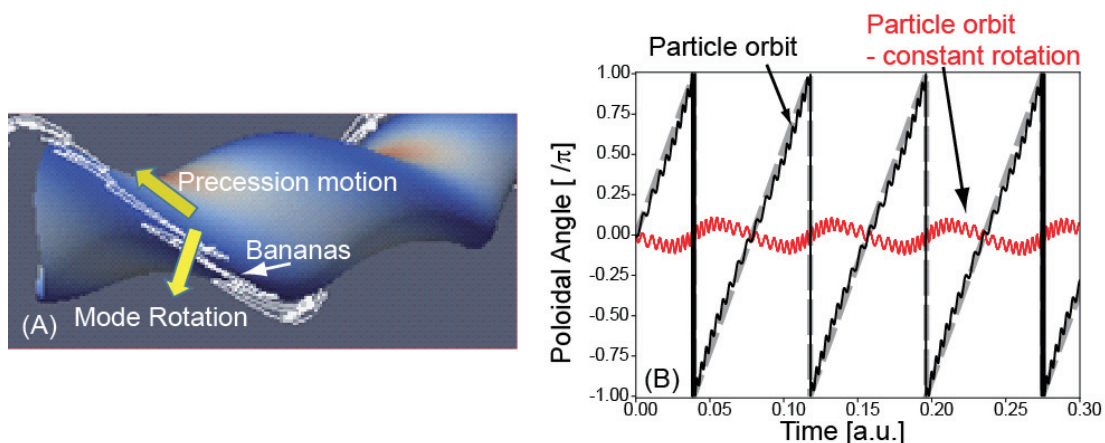
Fig.1 (A) Schematic view of the motion of the helically trapped particles. (B) Poloidal angle of the trapped EP as a function of time (black solid line) is shown. Red line shows the particle motion when the constant rotaiting motion (shown by dashed grey line) is removed.

It is found that the amplitude of the MHD bursts of the EIC is thereby enhanced and the effects on the EP confinement and the bulk plasma transport, e.g. achievable ion temperature, is also enhanced [2]. Schemes to control the EIC modes are thus required. In order to develop effective control schemes, a deeper understanding of the excitation mechanism is required. Excitation mechanism of the EIC is found to be closely related to the orbit of the EPs. The orbit of the helically trapped particle consists of the precession motion and the small-scaled banana-like motion. Though the rotation frequency of the precession motion is almost constant, there is an acceleration section at the inward side and a slowing down section at the outward side. This variation of the velocity, shown in Fig. 1(B), is the reason why the helically trapped EP can be coupled with the MHD instabilities having the mode number of $m/n = 1/1$. If the energy transfer from the EP to the mode is estimated by evaluating the correlation of the fluctuating component of the precession motion and the MHD mode as $< \tilde{v}(t) \cdot \tilde{E}(t) >$, a resonance is found when the MHD mode rotates poloidally -1.2 times of the poloidal component of the heliccally trapped EP motion. Here, $\tilde{v}(t)$ is the fluctuating component of the precession velocity and the $\tilde{E}(t)$ is the perpendicular electric field induced by the the MHD instabilities. This resonance disucssed here is consistent with the following observations found in the hydrogen [1] / deuterium experimental campaing. 1) MHD mode rotates in the electron diamagnetic drift direction while the EP moves in the ion diamagnetic drift direction.
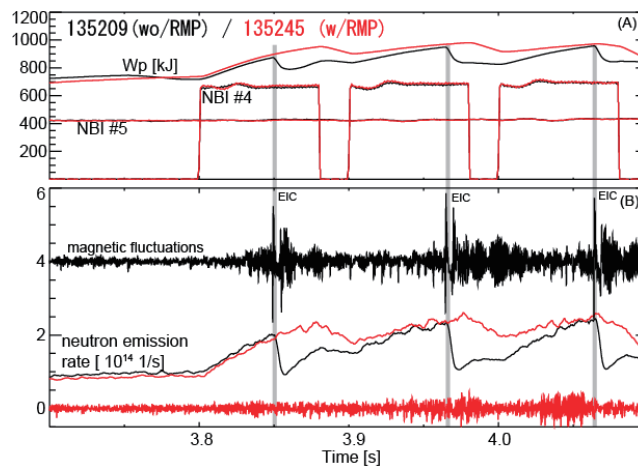
Fig. 2   (A) Stored energy and timing of the injection of the pependicularly NBIs are shown. (B) Neutron emission rate and the magnetic fluctuations with and without RMP are shown.

2) The mode frequency is almost the same with the precession frequence of the initial velocity of the NB-injected EP; the mode frequency depends clearly on the the accaralation voltage of perpendicularly injected NBI [2]. In addition to the velocity variation effects, the EIC is sensitive to orbit deviation from the magnetic surface. When the plasma is heated by the ECH and the radial width of the resistive mode is reduced by increasing the electron temperature and/or the global magnetic shear where the interaction of the EP with MHD mode becomes smaller, the EIC mode was found to be suppressed [3]. Furthermore, it may be related with the observation that the EICs are excited with the larger energetic particle pressure of the D beam than that of the H beam. It is possible this effect is caused by the higher-energy D beam make wider banana-motion where the interaction is smaller. As another contolling scheme, RMP applications is

also performed, as shown in the Fig. 2. Bursts of the magnetic fluctuations due to the EIC excitation dissappears when the RMP field is applied. EIC bursts disappear when the external field does penetrate the plasma as shown in Fig. 3 (B); The phase of the plasma response field close to zero indicates the penetration of the RMP. This method works only in the high relatively high-density discharges where the EIC mode is more stable.   This suppression might be caused by the change of the orbit of the energetic particle and/or the suppression of the resistive interchange mode by the magnetic island formation. The achieved ion temperature and the neutron emission rate, shown in Fig. 3(A) is not affected significantly by the RMP application. RMP application is, therefore, found to be a effective method to control the EIC.
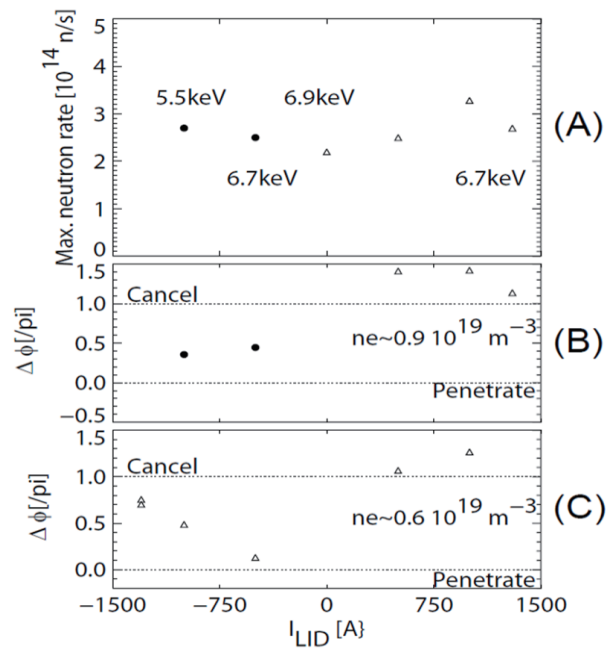
Fig. 3 Achieve ion temperature (A) and the phase of the plasma response field with respect to the applied phase of the RMP. (B) shows the higher density case and (C) shows relatively lower density case. Closed symbols shows the disappearance of the EIC mode.

References

[1] X. D. Du., et al., Phys. Rev. Lett. **114** (2015) 155003, Nucl. Fusion **56** (2016) 016002

[2] T. Bando, S. Ohdachi, et. al., submitted to Nucl. Fusion

[3] X. D. Du., et al., Phys. Rev. Lett. **118** (2017), 125001

Neutron and gamma-ray effects on charge-coupled device during deuterium discharges in Large Helical Device

<u>Y. Liu[1]</u>, S. Morita[1, 2], T. Oishi[1, 2], M. Goto[1, 2] and X.L. Huang[2]

[1]Department of Fusion Science, Graduate University for Advanced Studies, Toki 509-5292, Gifu, Japan

[2]National Institute for Fusion Science, Toki 509-5292, Gifu, Japan

Abstract

Charge-coupled device (CCD) is widely used as the detector of vacuum spectrometer for impurity transport study in fusion devices. Recently, deuterium plasma experiments have been started in Large Helical Device (LHD). A lot of neutrons are produced with energies of 2.45MeV and 14.1MeV in D-D and D-T reactions, respectively. Meanwhile, gamma rays are emitted from plasma facing components and laboratory structural materials in a wide energy range through neutron capture. These neutrons and gamma rays resultantly have a serious effect on plasma diagnostic systems. Therefore, it is important to examine an effect of neutrons and gamma rays on the CCD. Several CCDs of vacuum spectrometers installed on LHD at different locations are used to examine the neutron and gamma ray effects. An additional CCD placed in a special shielding box, which is made of polyethylene with boron and lead, is also used for detailed analysis.

I. Introduction

Charge coupled device (CCD) is widely used as the detector of spectrometer in fusion device [1-4]. In fusion devices, deuterium is usually used for fueling. However, a lot of neutrons with energy of 2.45 MeV are produced during D-D operation. Tritons generated by D-D fusion reaction have a subsequent reaction with bulk deuterons, i.e. D-T reaction, and yield higher-energy neutrons of 14.1 MeV. It is well known such neutrons causes serious problems on the CCD including signal noise. On the other hand, gamma rays emitted from plasma facing components and laboratory structural materials, which are caused by neutrons capture, also produce huge background signal noise. These background noises lower the CCD capability of measuring a high-quality spectrum, e.g. degradation of signal-to-noise ratio (SNR) and deterioration of CCD itself.

In Large Helical Device (LHD), which is one of the largest superconducting fusion devices, deuterium plasma experiments have started on March 2017 under operational regulations of annual neutron yield limited to 2.1×10^{19} in the first year and maximum neutron production rate of limited to 1.9×10^{16} n/s [5]. The D-D experiment has been therefore carried out at the neutron production rate of $1\text{-}10\times10^{15}$ n/s. Many CCDs are equipped on vacuum spectrometers working in vacuum ultraviolet (VUV) and extreme ultraviolet (EUV) ranges. Although these CCDs are located in different toroidal positions and different distances from LHD plasma center, strong background noises caused by neutrons and gamma rays have been observed in all the CCDs during D-D experiments. Effects of neutrons and gamma rays on the CCD

are then examined.   An additional CCD placed in a special shielding box, which is made of polyethylene with boron and lead and located at 10 m away from the LHD plasma center, is used to quantitatively examine the origin of the CCD noise by changing the shielding material.

2. Experimental set-up

A space-resolved EUV spectrometer called EUV_Long2 [6] is installed for impurity profile measurement at wavelength range of 50-500 Å.   A back-illuminated CCD is used as the detector by setting the short axis along the wavelength dispersion direction.   The long axis is set perpendicular to the wavelength dispersion direction for the vertical profile measurement.   The CCD routinely works at sub-image mode with five-pixel binning in the long axis and two-pixel binning in the short axis, and the resultant CCD output signal has an image size of 204 × 127 channels.   The temporal resolution of EUV_Long2 is 100 ms.   The vertical observation range in the profile measurement is ~0.5 m corresponding to half of the vertical plasma diameter at the horizontally elongated plasma cross section. Two grazing-incidence EUV spectrometers called EUV_Short [7] and EUV_Long [8] are used to observe impurity line emissions in the wavelength range of 10-130 Å and 50-500 Å, respectively.   The wavelength spectrum is sequentially obtained at each 5 ms interval with full-binning mode in CCD (Andor model DV420).   Both spectrometers are installed on #10-O port at a distance of ~9 m away from the plasma center and the tungsten pellet is also injected at the same port.   Three 20 cm normal incidence VUV spectrometers named "VUV102R", "VUV106R", and "VUV109L" have been installed in LHD routinely monitoring of impurity spectra at a distance of ~9 m from LHD plasma center [9].   Each spectrometer covers a wavelength range of 300-1050 Å (VUV109L), 1000-1850 Å (VUV106R), and 1550-2400 Å (VUV102R), respectively, in a single discharge.   Temporal evolutions of the VUV spectrum are obtained with a time resolution of 5ms in full-binning mode of CCD (Andor model DV420).   A Johann-type x-ray crystal spectrometer (XCS) [10] has been installed at a distance of ~7 m from LHD plasma center for core ion temperature measurement.   Back-illuminated CCD of Andor model DV420 is also used for measuring Doppler broadening of He-like resonance line of ArXVII, TiXXI, CrXXIII, or FeXXV in full-binning mode.
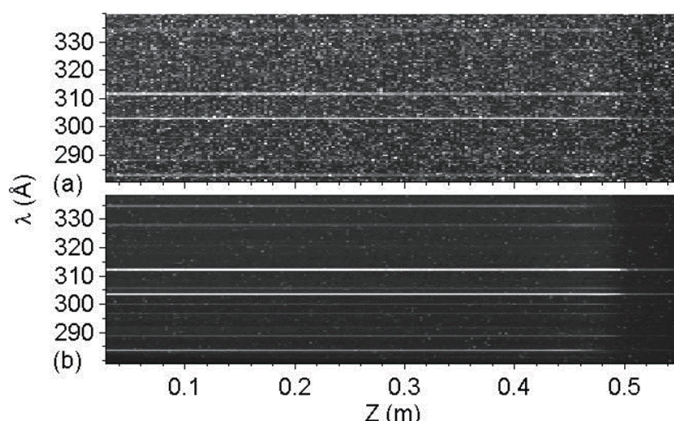
Fig.1 CCD images taken from EUV_Long2 in (a) deuterium and (b) hydrogen discharges, respectively.

3. Experimental Results

a. Neutron and gamma-ray effects on CCDs of VUV and EUV spectrometers

The CCD images are measured with EUV_Long2 in deuterium and hydrogen discharges as shown in Fig. 1(a) and (b), respectively.   The neutron rate in the deuterium discharge is 1.2×10^{15} n/s.   In these two discharges, EUV_Long2 is fixed to observe upper-half LHD plasma.   The horizontal axis of CCD image, Z(m), represents the vertical direction of LHD plasmas.   The vertical axis, λ, represents the wavelength.   Two strong emission lines existing in both images are HeII at 303.78 Å and CIV at 312.42 Å. Many noises are observed with large counts in Fig. 1(a) which are dominantly caused by neutrons and gamma rays.   The noises observed in Fig. 1(b) are considerably weak, which are caused by energetic neutral particles in hydrogen discharge.   The vertical profiles of HeII obtained from Fig. 1 are shown in Fig. 2 for a single CCD channel at wavelength interval of $303.56 Å \leq \lambda \leq 304.03$ Å.   The HeII profile from the hydrogen discharge denoted with solid line shows a small noise, while the HeII profile from the deuterium discharge denoted with dotted line includes many noises.   Meanwhile, EUV spectra are measured with EUV_Long at wavelength range of 130-340 Å.   When the EUV spectrum is plotted with a single frame at t = 4.5 s as shown in Fig .3 with solid line, a lot of noises caused by neutron and gamma rays are appeared in the spectrum.   When the spectrum is accumulated during 4.3-4.7 s as shown in Fig. 3 with dotted line, the noises can be averaged and the presence of impurity lines seems to be visible.

The CCDs are usually operated in the sub-image and full-binning modes.   Totally six CCDs measuring the wavelength spectrum in the full-binning mode are located at different distances from the LHD plasma center.   Neutron and gamma ray effects on these 6 CCDs are analyzed over several frames. The results are plotted in Fig. 4 for 102RVUV (solid circles), 106RVUV (solid squares), 109LVUV (solid triangles), EUV_Long (open circles), EUV_Short (open squares) and XCS (open triangles).   The abscissa indicates noise counts in certain channel at a single CCD frame.   The noise counts are basically proportional to the incident γ-ray or neutron energy, if they lose their all energies within a single channel of CCD.   Although this is a drastic assumption, the resultant figure may indicate certain interesting result. The vertical axis means the total numbers of CCD channel having the same noise counts, which are analyzed using several frames.   Then, Fig. 4 indicates pulse height analysis for γ-ray and neutron energies coming on the CCD.   We can understand from the figure that the noise counts of XCS CCD is the largest because the CCD distance from LHD plasma center is the shortest.   It may also indicate the incident energy of γ-ray or neutron on the CCD is bigger compared to other CCD.
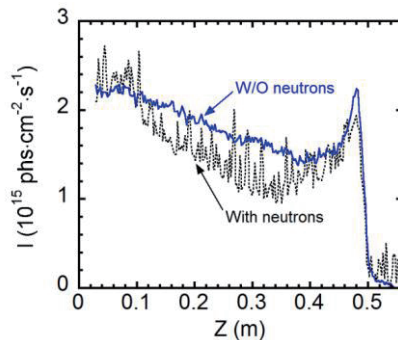
Fig. 2. Vertical profiles measured by EUV_Long2 in hydrogen (solid) and deuterium (dotted)
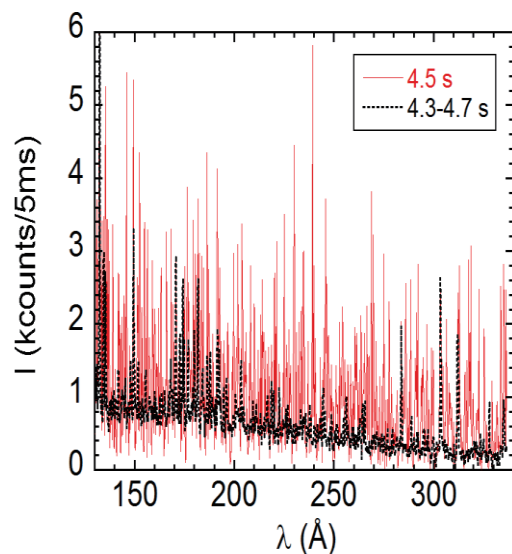
Fig. 3. Raw EUV spectrum from a single CCD frame measured at t = 4.5 s (solid line) and EUV spectrum averaged with 80 CCD frames during 4.3-4.7 s (dotted line).
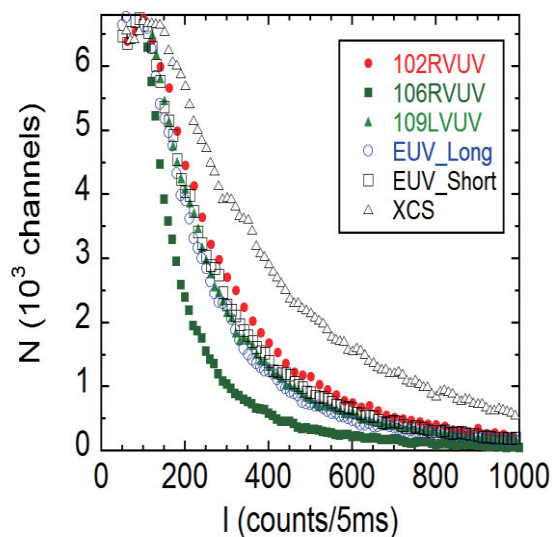
Fig. 4. Total number of CCD channels against noise counts at single CCD channel for 102RVUV (solid circles), 106RVUV (solid squares), 109LVUV (solid triangles), EUV_Long (open circles), EUV_Short (open squares) and XCS (open triangles).

b. Noise test on shielding CCD

Additional CCD (DV420) is placed in a special shielding box at a distance of ~10 m from LHD plasma center.   Effects of γ-ray and neutrons on the CCD are tested in four different ways, as shown in Fig. 5.   In Fig. 5(a), the CCD is exposed to neutrons and gamma rays without any shielding.   Next, the CCD is placed in the shielding box with 1.5cm thick lead and 10cm thick polyethylene as shown in Fig. 5(b) and 5(c), respectively.   In Fig. 5(d), the CCD is shielded by both the lead and polyethylene plates.   The polyethylene plate contains 10% boron which is effective for neutron absorption.   The CCD image is then

examined under different four conditions.   The result is plotted in Fig.6 in the same way as Fig.4, while the vertical axis is normalized by neutron rate, n_0.   It is found the shielding effect of lead is clearly better than that of polyethylene.   The mass attenuation coefficients of lead and polyethylene, μ, for γ-rays [11] are plotted against the energy in Fig. 7(a).   The attenuation ratio, I / I_0, is calculated from μ, density of shielding materials, ρ, and thickness, t, in the following equation;

$$I / I_0 = e^{-\mu \rho t}, \qquad\qquad\qquad\qquad\qquad [1]$$

where I_0 and I are the γ-ray flux before and after passing through the shielding material.   The result is plotted in Fig. 7(b).   Since most of gamma rays have energies larger than 1 MeV, an averaged attenuation ratio of γ-rays in lead is obtained to be 0.4634 assuming the γ-ray energy range of 1-5 MeV and the normal incidence of γ-rays.   Here, noise ratio is defined as Z / Z_0.   The values of Z and Z_0 are noise counts measured with and without shielding, respectively.   Both values are normalized by the neutron rate.   As a result, the values of Z / Z_0 are experimentally determined to be 57.49% for lead, 80.71% for polyethylene and 28.66% for both lead and polyethylene.
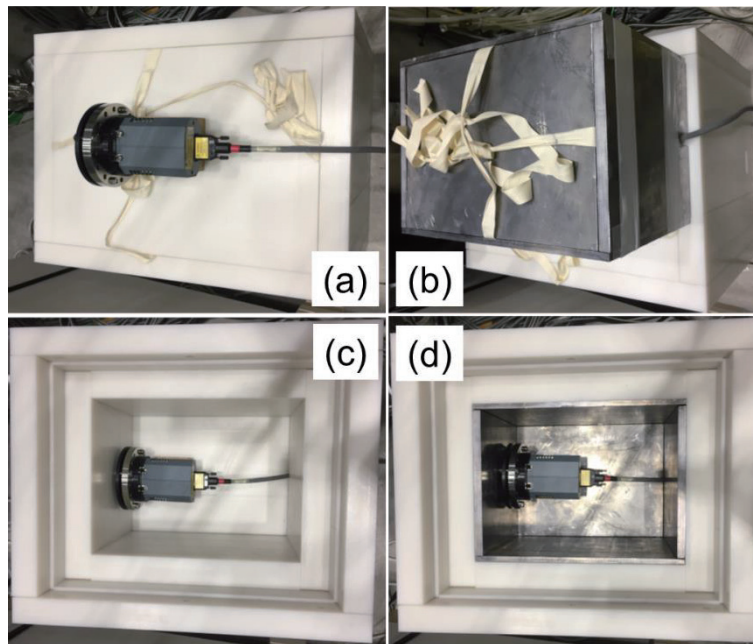
Fig. 5 (a) CCD without shielding, (b) CCD with lead, (c) CCD with polyethylene included 10% B and (d) CCD with polyethylene and lead.

Lead is quite ineffective for reducing the neutron energy due to the big mass.   So, lead can only attenuate the γ-rays.   In the case of polyethylene with 10% boron, on the other hand, the reaction process with neutrons is quite complicated.   Low-energy neutrons after reacting with boron and hydrogen in the polyethylene can emit γ-rays with energies of 0.48 MeV and 2.2 MeV, respectively.   Meanwhile, low-energy γ-rays can be attenuated by polyethylene.   Therefore, the effect of γ-rays on CCD can be quantitatively calculated from the data of lead, assuming the noise counts per gamma ray, $\eta(\gamma)$ and neutron, $\eta(n)$.   Here, total CCD noise counts, Z_0, is expressed by

$$Z_0 = I_0(\gamma) \times \eta(\gamma) + I_0(n) \times \eta(n), \tag{2}$$

where $I_0(\gamma)$ and $I_0(n)$ are fluxes of γ-rays and neutrons, respectively.   When the CCD is shielded by lead, the equation is simply modified by

$$Z = I(\gamma) \times \eta(\gamma) + I(n) \times \eta(n), \tag{3}$$

where $I(\gamma)$ and $I(n)$ are fluxes of γ-rays and neutrons when CCD is shielded by lead.   The attenuation of γ-rays is already obtained from Fig. 7(b) as

$$I(\gamma) = 0.4634 \times I_0(\gamma). \tag{4}$$

If the neutrons have no collision in the lead, we obtain a relation of

$$I(n) = I_0(n). \tag{5}$$

The noise ratio is already obtained from the experiment as

$$Z = Z_0 \times 0.5749. \tag{6}$$

From eqs. (2)-(6), thus, the ratio of noise counts caused by gamma ray to the total noise counts, $I_0(\gamma) \times \eta(\gamma) / Z_0$, can be obtained to be 79.22%. The ratio for neutrons, $I_0(n) \times \eta(n) / Z_0$, is 20.78%.
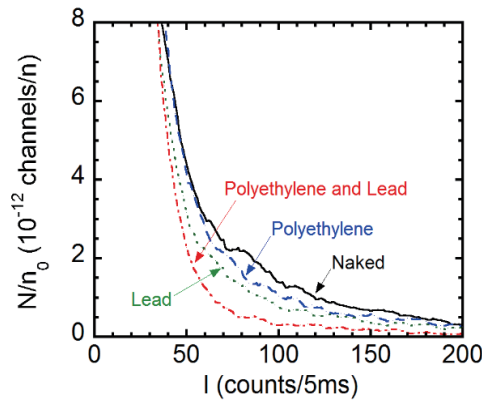
Fig. 6 Total number of CCD channels against noise counts at single CCD channel for CCD without shielding and with polyethylene (dashed), lead (dotted) and polyethylene and lead (dash-dotted).
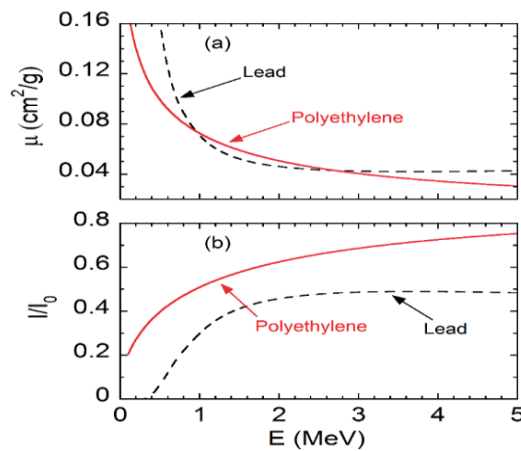
Fig. 7 (a) X-ray mass attenuation coefficients and (b) attenuation ratio of 1.5 cm thick lead and 10 cm thick polyethylene with 10% boron.

4. Summary

Deuterium plasma experiments are carried out in LHD with high fluxes of background neutrons and γ-rays. Although a lot of signal noises are observed in the CCD image, the effect on the profile measurement is relatively small if the impurity line is strong. The noise effect is more serious in the wavelength spectrum measurement appearing so many spike noises. Even in the case, however, the impurity spectra are visible if several CCD frames are integrated and the spike noise is averaged along the CCD channel. The effect of neutron and γ-ray is the largest for XCS CCD because the distance from LHD plasma center is shortest. The noise effect is also quantitatively examined using a special CCD placed in a shielding box made of 1.5 cm thick lead and 10 cm thick polyethylene with 10% boron. As a result, the γ-ray contribution to the total CCD noise can be determined to be 79.22%, and it is found that the neutron contribution is relatively small, i.e. 20.78%.

Acknowledgements

References

[1] R. Reimer, A. Dinklage, R. Fischer et al., Rev. Sci. Instrum. 84, 113503 (2013).

[2] K.H. Burrell, D.H. Kaplan, P. Gohil et al., Rev. Sci. Instrum. 72, 1 (2001).

[3] L. Zhang, S. Morita, Z. Xu et al., Rev. Sci. Instrum. 86, 123509 (2015)

[4] W.H. Ko, H. Lee, D. Seo et al., Rev. Sci. Instrum. 81, 10D740 (2010).

[5] M. Osakabe, Y. Takeiri, T. Morisaki et al., Fusion Sci. Technol. 72, 199-210 (2017).

[6] C. Dong, S. Morita, M. Goto, and H. Zhou, Rev. Sci. Instrum. 81, 033107 (2010).

[7] M. B. Chowdhuri, S. Morita and M. Goto, Appl. Opt. 47, 135-146 (2008).

[8] M. B. Chowdhuri, S. Morita and M. Goto, Rev. Sci. Instrum. 78, 023501 (2007).

[9] T. Oishi, S. Morita, X. Huang et al., Plasma Fusion Res. 10, 3402031 (2015).

[10] S. Morita and M. Goto, Rev. Sci. Instrum. 74, 2375 (2003).

[11] J.H. Hubbell and S.M. Seltzer, National Inst. of Standards and Technology-PL, Gaithersburg, MD (United States). Ionizing Radiation Div., 1995.

Application of fast ADC system in Thomson scattering diagnostic

I. Yamada[1], H. Funaba[1], R. Yasuhara[1], J. Lee[2], Y. Huang[3], C. Liu[3], and Y. Wang[3]

[1]National Institute for Fusion Science, Toki 509-5292, Gifu, Japan

[2]National Fusion Research Institute, Daejeon 34133, South Korea

[3]Southwestern Institute of Physics, Chengdu 610041, China

Abstract

In laser Thomson scattering diagnostic systems, charge integrating analog-to-digital converters have been widely used to obtain raw data of the Thomson scattering signals. Recently, fast gigasampling digitizers are available at a reasonable price. In the LHD, KSTAR and HL-2A Thomson scattering systems, such fast gigasampling digitizers have been introduced to improve the data quality and reliability. We have started to test the digitizers and obtained the initial results on LHD, KSATR and HL-2A.

1. Introduction

The LHD Thomson scattering system has routinely measured electron temperature (T_e) and electron density (n_e) profiles of LHD plasmas at 144 spatial points along the LHD major radius. [1][2] In the LHD Thomson scattering system, charge integrating analog-to-digital converters (ADCs) have been used for 20 years to measure integrated values of Thomson scattering signal intensities. When both the Thomson scattering signal intensity and signal-to-noise ratio are high, good results on T_e and n_e have been obtained with the charge integrating ADCs. However, since the Thomson scattering cross section is very small, Thomson scattering signal intensities are usually also weak. Then, careful signal acquisition and processing are required, especially in worse experimental conditions. Fast gigasampling ADCs are attractive to obtain more reliable Thomson scattering data.

2. Gigasampling analog-to-digital converter

Figure 1 shows the principle of the Thomson scattering signal measurement using a charge integrating ADC. The ADC measures the integrated value of the signal during the ADC gate level is low (open). In the LHD Thomson scattering system case, the full width at half maximum of Thomson scattering signal and the gate width are ~40 nsec and ~100 nsec, respectively

First, the Thomson scattering signal + background level, S1, is measured during the proceeding Gate 1. After 25 microsec, only background signal, S2, is measured. True Thomson scattering is estimated from TS = S1 − S2. If the experimental condition is good, the true Thomson scattering signal is accurately obtained. However, the background level may be changed and undesired noises may appear in actual experiments. In addition, signal saturation may occur as shown in Fig. 2. It is difficult to directly know such phenomena when charge integrating ADCs are used. In contrast, they are correctly and easily observed, and accurate estimation of the Thomson scattering signal intensity is possible when fast ADCs are used.

Fast gigasampler digitizers, whose bandwidth is higher than ~100 MHz and sampling rate is faster than ~1GS/s, were very expensive. The price per input channel is ten times higher than that of a charge integrating ADC. However low cost and compact fast ADC modules are now commercially available at reasonable price from some electronics instruments companies. Roughly speaking, the price per input channel of the fast ADC is ~500 USD, and that of the traditional charge integrating ADC is ~400 USD.
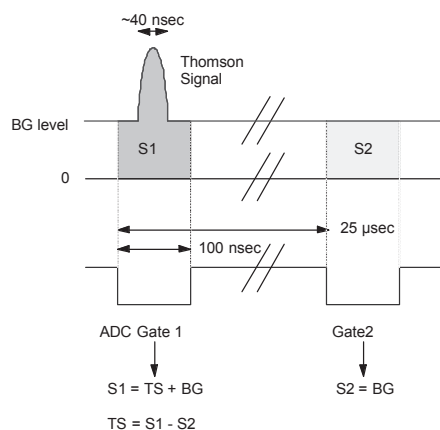
Fig.1 Principle of the measurements with the charge integrating ADC.
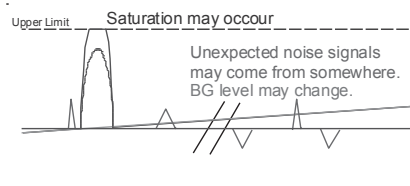
Fig.2 A few unexpected phenomena may occur in actual experiments, resulting in experimental errors.

3. Initial results on LHD

We have developed a first ADC system based on the CAEN V1742B in LHD, and tested it since 2016. The bandwidth and sampling rate of the fast ADC are 500 MHz and up to 5 GS/s, respectively. When the ADC works at the sampling rate of 5 GS/s, total measurement time length is 200 nsec. The specification is considered to be enough for our Thomson scattering measurements. Figure 3 shows an example of the pulse shapes of Thomson scattering signals obtained in the 2017 LHD experiment campaign by using the CAEN V1742B. The LHD polychromators have five spectral channels, Ch.1-CH.5, to detect Thomson scattering signals. The spectral Ch.1 is the closest to the incident laser wavelength, and the Ch.5 is the lowest wavelength channel. Clear Thomson scattering signals were obtained with the fast ADC system, as shown in Fig.3. From the measured signals, we can estimate the background level more accurately than the charge integrating ADCs. It is confirmed that no significant noise signal appeared in this case. Figure 4 shows an example of a temporal history of T_e at the plasma center measured by a polychromator and fast

ADC system. In the plasma discharge, the plasma was generated at t = 3.0 sec and the discharge ended at t = 7.8 sec. The estimated T_es are in good agreements with the results by charge integrating ADCs, as expected.
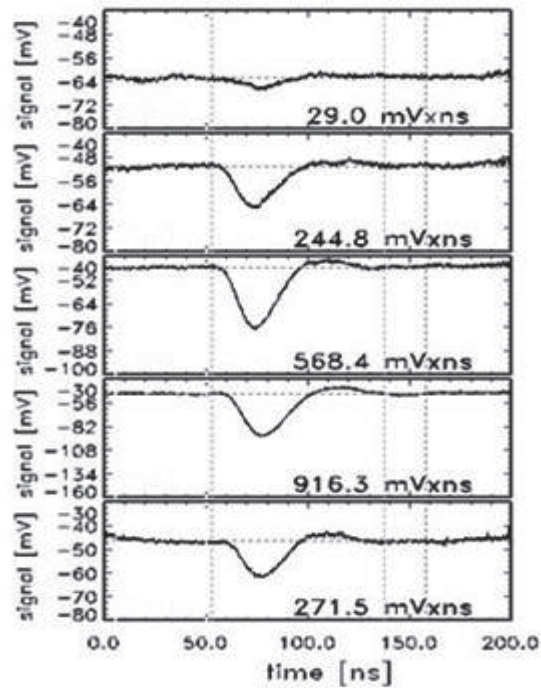
Fig.3. Example of Thomson scattering signals measured by a LHD polychromator.
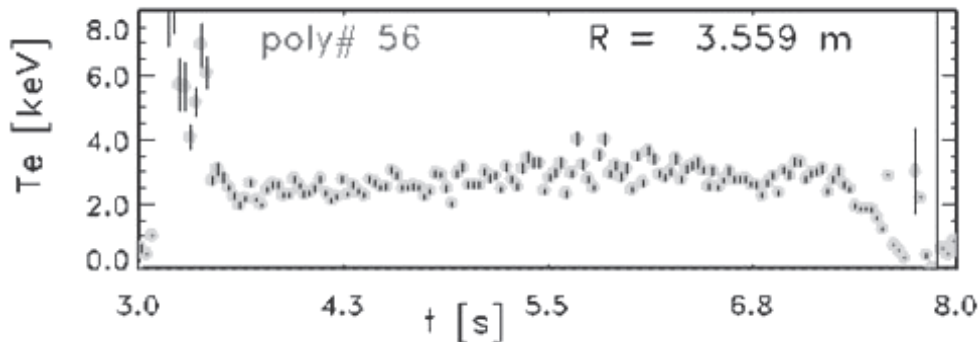
Fig. 4 Example of obtained T_e at the plasma center.

4. Initial results on KSTAR

The KSTAR Thomson scattering team has already installed the fast ADC system, based on the CAEN V1742B, for all 27 KSTAR polychromators, and operated the system in the 2017 KSTAR experiment campaign. [3][4] Figure 5 a) shows an example of Thomson scattering signals from a KSTAR polychromator that has four wavelength channels. We have verified that the fast gigasampling digitizer system also work well in the KSATR Thomson scattering system. As shown in Fig. 5 b), two unexpected

structures seen at t ~ 80 nsec and 113 nsec. We consider that they are stray light components generated inside the KSATR vacuum vessel.When the signal is measured by a charge integrating digitizer, the undesired noise components may cause large experimental error because the charge integrating digitizer cannot distinguish the true Thomson scattering signal and noise components. By using the fast digitizer, we can estimate true Thomson scattering signal intensity more accurately even in such cases. T_es obtained from the new fast digitizer system and previous charge integrating digitizer system show good agreements when both the signal intensities and the signal-to-noise ratio are relatively high.

5. Recent progress on HL-2A

The HL-2A Thomson scattering team has already used another type of fast digitizer to measure Thomson scattering signals and obtained good results. [5][6] Recently they have newly introduced the same model of fast digitizers as LHD and KSATR for the HL-2A/2M Thomson scattering system. They will be operated from the 2018 HL-2A experiment campaign.

6. Summary

We have a plan to replace the charge integrating ADC system with the fast gigasampler ADC system to measure more accurate and reliable Thomson scattering signals. We have installed two fast ADCs and operated them in the 2017 LHD Campaign. In addition, similar fast digitizer system has been also introduced in the KSATR Thomson scattering system. The fast digitizer systems works well as expected in both the LHD and KSATR Thomson scattering system. The same model digitizer will be also operated on HL-2A in 2018. By using the fast ADC systems, data accuracy and reliability will be improved.
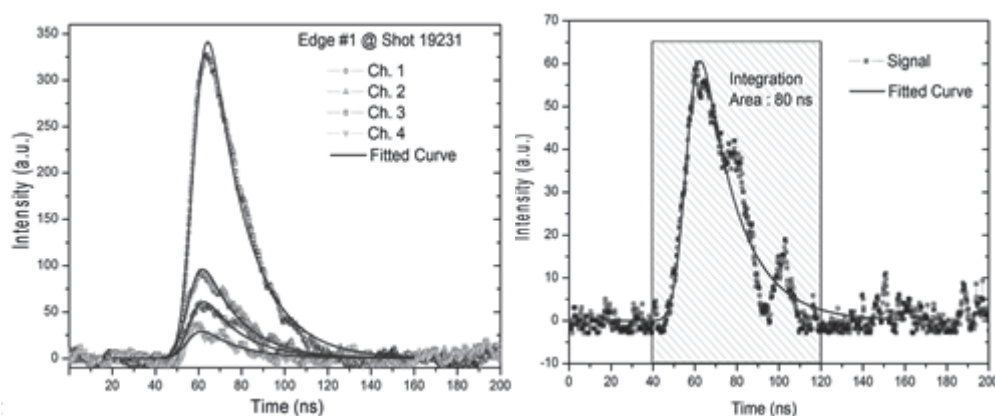
Fig.5 a) Example of Thomson scattering signals measured with the fast digitizer on KSATR (Left). In this case, a few background structures are seen (right). By using a fast digitizer, true Thomson scattering signal is obtained.

References

[1] I. Yamada *et al.*, Fusion Sci. Tech., **58**, 345 (2010).

[2] I. Yamada *et al.*, Rev. Sci. Instrum., **87**, 11E531 (2016).

[3] J. H. Lee *et al.*, Rev. Sci. Instrum., **80**, 10D528 (2010).

[4] J. H. Lee *et al.*, JINST., **12**, C12035 (2017)

[5] C. Liu *et al.*, JINST, **10**, C12062 (2015).

[6] Z. Fen et al., JINST, **12**, C11012 (2017).

Theory and simulation for turbulent transport and confinement

Yasuaki KISHIMOTO and Kenji Imadera

Kyoto University

1. Primary results resulting from the participation to A3 Program

Through the participation of the present A3 program, we have significantly developed the activity for theory and simulation of turbulent transport and confinement in magnetically confined fusion plasmas primarily based on the gyro-kinetic model in global toroidal geometry covering from core to edge incorporating with local dispersion analyses. Specifically, we have focused on the elucidation of L-mode transport regulated by non-local and non-diffusive processes exhibiting resilience and stiffness in profile formation and self-similarity in profile relaxation coupled with intermittent bursts, which are the basis in understanding fusion plasmas with toroidal geometry [1,2]. Here, global effects are found to play important roles in leading such constraints as a flux driven non-thermodynamics equilibrium system with heat source and sink. Namely, the system is not isolated but opened to outside, which allows to establish rich structure formation as a dissipative system not only in real space but also in phase space.

This feature is illustrated schematically in Fig.1, where different types of fluctuations with different scales from micro-electron scale (ρ_e: electron gyro-radius) to macro-device scale (a: plasma minor radius or L: typical scale length of plasma density and temperature) through meso-scales $\left(\rho_i L\right)^{1/2}$ and $\left(\rho_e L\right)^{1/2}$ ascribed to toroidal coupling force are excited primarily due to free energy sources associated with thermo-dynamic force such as the spatial gradient of pressure, current, flow [3-4]. These free energies include not only those from linear drive but also nonlinear one referred to as zonal modes, e.g. zonal flow, field and pressure. These fluctuations are allowed to diffuse and/or propagate in radial direction referred to as turbulence spreading and/or diffusion [5].

Those different types of dynamics with different spatio-temporal scales are coupled with each other under the global constraint regulated by heat input and output and are self-organized leading to quasi-stationary structures [1-2].

In order to realize simulations including all key ingredient shown in Fig.1, we have developed a code, GKNET [1-3, 6-8], the gyro-kinetic based numerical experiment of tokamak, which is the full-f flux-driven global toroidal code based on the gyro-kinetic model with heat/momentum source and sink. Capability in using both adiabatic electrons and kinetic electrons is now available, so that trapped electron mode (TEM) can be treated [9]. Recently, an electromagnetic version of the GKNET based on the δf model has been implemented in linear regime, so that the finite-β effect on the ITG mode and also kinetic ballooning mode (KBM) can be studied [10]. The GKNET is going to be incorporated with the electromagnetic gyro-fluid model which includes the effect of non-adiabatic electrons.

Using the framework of A3, we have joint works with theory and simulation group at SWIP (Prof. J.Q Li) for the study of turbulent transport in global toroidal geometry using GKNET. The fluid models in simulating the TEM has been progressing. We had also intensive discussions with Prof. D. L. Yu, the experimental group of HL-2A at SWIP, especially for ion internal transport barrier (ITB) in HL-2A, which studied the characteristics of formation and distraction of ITB's during ECH application [11]. Based on the experiment, we have started a collaboration to investigated related ITB dynamics using GKNET which can simulate TEM influenced by the effect of ECH [9]. In Kyoto University, we had successfully reproduced ITB formations trigger by co-injection of neutral beam in the plasmas with weak and/or reversed magnetic field configuration for the first time using GKNET [6]. Based on the result, we have stared the collaboration with SWIP group in trying to identify such ITB formation in the HL-2A experiment. We had also intensive collaboration with DULT (Z.X. Wang) using GKNET. Specifically, under the A3 program, we have studied two subjects based on the nonlinear simulation, one is studies for the formation and sustainment of self-organized global profile and $E \times B$ staircase in tokamak plasmas [12], and the other is statistical studies for turbulent transport in flux-driven tokamak plasmas [13]. Those issues are primary concerns in understanding L-mode plasma.

Using the framework of A3, we have colloborated with theory/simulation group at NFRI (Dr. H. Jhang, Dr. J. Kim, Dr. J. M. Kwon) as for the methodology in modeling and simulating turbulent transport in global toroidal system. In the group, studies for turbulent transport and MHD including their interaction have been significantly progressed and many interesting results have been emerging. Specifically, a particle-in cell (PIC) based δf code, gKPSP, has been developed, which is the global full torus configuration available for arbitrary cross-section with electrostatic modeling while including kinetic electron, has been implemented [14]. Recently, the details of linear and nonlinear TEM dynamics and associated turbulent transport including the shaping effect of cross section have been studied extensively [15]. It is worthwhile to perform benchmarking between GKNET and gKPSP for TEM dynamics, which was discussed during the visit as a future work. In the following, we describe main results which have been done under A3 program.
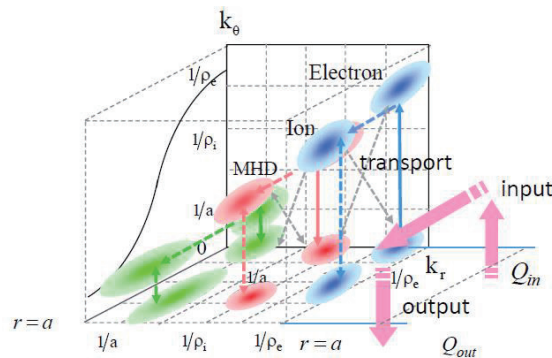
Fig.1 distribution of various scale fluctuations in (k_r, k_θ) plain and radial direction in toroidal plasma and the global effect, e.g. radial spreading, in flux driven system (by Kishimoto et al.)

2. Formation of global profile and E×B staircase in tokamak plasmas [12]

We have investigated the mechanism for the formation of a meso-scale quasi-regular long-lived $E \times B$ shear flow pattern coupled with pressure corrugations, referred to as the "$E \times B$ staircase", based on GKNET simulations. The structures are found to be initiated during the saturation phase of the ITG mode with a radially extended structure with nearly up-down symmetry and is established as it evolves into a quasi-steady turbulence, leading to a self-organized global temperature profile and to meso-scale isomorphic profiles of the radial mean electric field and the temperature. The latter quasi-regular $E \times B$ shear flow pattern is primarily attributed to an even-parity zonal flow produced by the extended ITG mode where the flow direction at the central part and that at both edges is opposite. It is also found that the zonal flow pattern exhibits an in-phase relation with the mean $E \times B$ flow variation induced by the temperature relaxation, i.e. the zonal pressure, so that the $E \times B$ flow is reinforced. This process is repeated quasi-periodically, sustaining self-organized structures and resulting in intermittent bursts of turbulent transport.

3. Statistical studies for turbulent transport in flux-driven tokamak plasmas [13]

We have investigated flux-driven ITG driven turbulence and associated transport regulated by non-local and non-diffusive processes are investigated using statistical methods based on GKNET simulations. To elucidate the transport, we introduced a size probability distribution function (PDF) for heat flux eddies in real space, $P(S)$ with S the eddy size. The size PDF is found to be fitted by three piecewise power laws with exponent α as $P \propto S^{-\alpha}$ in a quiescent phase providing a base heat flux, while, in a bursting phase, exhibits non-power law irregular humps corresponding to the quasi-coherent structure reaching to $S \sim 1000$. Such a coherent structure is ascribed to the spontaneous alignment of small scale eddies discussed in Sec.2. Resultantly, a large amount of free energy is extracted from the system through the event, by which a self-organized profile is established. Thus, the transport is found to be regulated by the mixture of a quasi-deterministic and a probabilistic process, which leads to stiffness and resilience in the profile formation and self-similarity in the relaxation.

4. ITB formation in gyrokinetic flux-driven ITG turbulence [6]

We have investigated ITB formation by toroidal momentum injection in gyrokinetic flux-driven ITG turbulence. It is found that momentum source can change the mean radial electric field Er through the radial force balance, leading to ITB formation in which the ion thermal diffusivity decreases to the neoclassical transport level. Only co-current toroidal rotation in outer region can benefit the ITB formation in weak magnetic shear plasma, showing a qualitative agreement with the observations in experiments. The underlying mechanism is identified to originate from a positive feedback loop between mean Er shear and resultant momentum flux. Such a mechanism can also benefit the ITB formation around minimum safety surface q_{min} in reversed magnetic shear plasma.

5. Global linear micro-instability analysis referring to HL-2A plasma with ITB [8]

We study linear micro-instabilities using parameters referring to HL-2A plasma with ion ITB by means of the global toroidal gyrokinetic code GKNET including kinetic electron dynamics. It is found that

a new type of drift mode, which real frequency is low and changes the sign from electron diamagnetic direction to that of ion continuously as poloidal wavenumber increases, dominates plasmas with peaked density together with steep ion and electron temperature profiles. The instability is found to be sensitive to the perpendicular electron temperature, similar to standard trapped electron modes, which is consistent with the observation of ion-ITB collapse after ECRH in the HL-2A experiment.

Acknowledgements

References

[1] K. Imadera et al., 25th Fusion Energy Conference, TH/P5-8 (2014).

[2] Y. Kishimoto et al., 26th Fusion Energy Conference, TH/P3-2 (2016).

[3] Y. Kishimoto et al., Phys. of Plasmas, **3**, 1289 (1996).

[4] Y. Kishimoto et al., Plasma Phys. Controlled Fusion, **41**, A663 (1999).

[5] J. Q. Li and Y. Kishimoto, Phys. Plasmas, **11**, 1493 (2004).

[6] K. Imadera et al., 26th Fusion Energy Conference, TH/P3-3 (2016).

[7] K. Obrejan, K. Imadera et al., Plasma and Fusion Res., 403042 (2015)

[8] K. Obrejan, K. Imadera et al., Comput. Phys. Comm. **216**, 8 (2017).

[9] Z. H. Qin, K. Imadera et al., submitted to Plasma Fusion Res.

[10] A. Ishizawa, K. Imadera et al., PLASMA-2018 (2018).

[11] D. L. Yu et al., Nucl. Fusion **56**, 056033 (2016).

[12] W. Wang, Y. Kishimoto et al., submitted to Nucl. Fusion.

[13] W. Wang, Y. Kishimoto et al., submitted to Nucl. Fusion.

[14] J. M. Kwon et al., Nucl. Fusion **52**, 013004 (2012).

[15] L. Qi, J. M. Kwon, et al., 26th Fusion Energy Conference, TH/P3-4 (2016).

Reviews on MCF research in USTC supported by A3 Program

Jian Liu[1]

[1]Department of Modern Physics and School of Nuclear Science and Technology,

University of Science and Technology of China, Hefei, Anhui 230026, China

Abstract

In this proceeding, we summarize the main works done under the support of A3 program by the group of USTC [1-28]. We have focused on four aspects, including the geometric algorithms, the physics of runaway electrons, the technology of machine learning, and the constructions of software for plasma simulations. Different kinds of geometric algorithms, such as volume-preserving algorithms, symplectic-preserving algorithms, Lorentz covariant symplectic algorithms, and symplectic Particle-in-Cell algorithms are constructed and applied in studying plasma physics. A new phenomenon called collisionless pitch-angle scattering is found for energetic runaway electrons. Meanwhile, we studied the technology of machine learning which is used to clean the raw data from tokamak experiments. We also started a software project, the GAPS project, to improve the study and applications of geometric algorithms.

1. Geometric algorithms

Secular dynamics of relativistic charged particles has theoretical significance and a wide range of applications. However, conventional algorithms are not applicable to this problem due to the coherent accumulation of numerical errors. To overcome this difficulty, we develop a volume-preserving algorithm (VPA) with long-term accuracy and conservativeness via a systematic splitting method. Applied to the simulation of runaway electrons with a time-span over 10 magnitudes, the VPA generates accurate results and enables the discovery of new physics for secular runaway dynamics.

We construct high order symmetric volume-preserving methods for the relativistic dynamics of a charged particle by the splitting technique with processing. By expanding the phase space to include the time t, we give a more general construction of volume-preserving methods that can be applied to systems with time-dependent electromagnetic fields. The newly derived methods provide numerical solutions with good accuracy and conservative properties over long time of simulation. Furthermore, because of the use of an accuracy-enhancing processing technique, the explicit methods obtain high-order accuracy and are more efficient than the methods derived from standard compositions. The results are verified by the numerical experiments. Linear stability analysis of the methods shows that the high order processed method allows larger time step size in numerical integrations.

We study the Lorentz force equation of charged particle dynamics by considering its K-symplectic structure. As the Hamiltonian of the system can be decomposed as four parts, we are able to construct the numerical methods that preserve the K-symplectic structure based on Hamiltonian splitting technique. The newly derived numerical methods are explicit, and are shown in numerical experiments to be stable over

long-term simulation. The error convergency as well as the long term energy conservation of the numerical solutions is also analyzed by means of the Darboux transformation.

We studied the Lorentz covariance of algorithms. Under Lorentz transformation, both the form and performance of a Lorentz covariant algorithm are invariant. To acquire the advantages of symplectic algorithms and Lorentz covariance, a general procedure for constructing Lorentz covariant canonical symplectic algorithms (LCCSAs) is provided, based on which an explicit LCCSA for dynamics of relativistic charged particles is built. LCCSA possesses Lorentz invariance as well as long-term numerical accuracy and stability, due to the preservation of a discrete symplectic structure and the Lorentz symmetry of the system. For situations with time-dependent electromagnetic fields, which are difficult to handle in traditional construction procedures of symplectic algorithms, LCCSA provides a perfect explicit canonical symplectic solution by implementing the discretization in 4-spacetime. We also show that LCCSA has built-in energy-based adaptive time steps, which can optimize the computation performance when the Lorentz factor varies.

Particle-in-cell (PIC) simulation is the most important numerical tool in plasma physics. However, its long-term accuracy has not been established. To overcome this difficulty, we developed a canonical symplectic PIC method for the Vlasov–Maxwell system by discretizing its canonical Poisson bracket. A fast local algorithm to solve the symplectic implicit time advance is discovered without root searching or global matrix inversion, enabling applications of the proposed method to very large-scale plasma simulations with many, e.g. 109, degrees of freedom. The long-term accuracy and fidelity of the algorithm enables us to numerically confirm Mouhot and Villani's theory and conjecture on nonlinear Landau damping over several orders of magnitude using the PIC method, and to calculate the nonlinear evolution of the reflectivity during the mode conversion process from extraordinary waves to Bernstein waves.

Explicit high-order non-canonical symplectic particle-in-cell algorithms for classical particle-field systems governed by the Vlasov-Maxwell equations are developed. The algorithms conserve a discrete non-canonical symplectic structure derived from the Lagrangian of the particle-field system, which is naturally discrete in particles. The electromagnetic field is spatially discretized using the method of discrete exterior calculus with high-order interpolating differential forms for a cubic grid. The resulting time-domain Lagrangian assumes a non-canonical symplectic structure. It is also gauge invariant and conserves charge. The system is then solved using a structure-preserving splitting method discovered by He et al. [preprint arXiv:150506076 (2015)], which produces five exactly soluble sub-systems, and high-order structure-preserving algorithms follow by combinations. The explicit, high-order, and conservative nature of the algorithms is especially suitable for longterm simulations of particle-field systems with extremely large number of degrees of freedom on massively parallel supercomputers. The algorithms have been tested and verified by the two physics problems, i.e., the nonlinear Landau damping and the electron Bernstein wave.

2. Runaway electron physics

We discover that the tokamak field geometry generates a toroidicity induced broadening of the pitch-angle distribution of runaway electrons. This collisionless pitch-angle scattering is much stronger than the collisional scattering and invalidates the gyro-center model for runaway electrons. As a result, the

energy limit of runaway electrons is found to be larger than the prediction of the gyro-center model and to depend heavily on the background magnetic field.

The secular full-orbit simulations of runaway electrons with synchrotron radiation in tokamak fields are carried out using a relativistic volume-preserving algorithm. Detailed phase-space behaviors of runaway electrons are investigated in different dynamical timescales spanning 11 orders. In the small timescale, i.e., the characteristic timescale imposed by Lorentz force, the severely deformed helical trajectory of energetic runaway electron is witnessed. A qualitative analysis of the neoclassical scattering, a kind of collisionless pitch-angle scattering phenomena, is provided when considering the coupling between the rotation of momentum vector and the background magnetic field. In large timescale up to 1 s, it is found that the initial condition of runaway electrons in phase space globally influences the pitch-angle scattering, the momentum evolution, and the loss-gain ratio of runaway energy evidently. However, the initial value has little impact on the synchrotron energy limit. It is also discovered that the parameters of tokamak device, such as the toroidal magnetic field, the loop voltage, the safety factor profile, and the major radius, can modify the synchrotron energy limit and the strength of neoclassical scattering. The maximum runaway energy is also proved to be lower than the synchrotron limit when the magnetic field ripple is considered.

3. Machine learning

Traditional data cleaning identifies dirty data by classifying original data sequences, which is a class-imbalanced problem since the proportion of incorrect data is much less than the proportion of correct ones for most diagnostic systems in Magnetic Confinement Fusion (MCF) devices. When using machine learning algorithms to classify diagnostic data based on class-imbalanced training set, most classifiers are biased towards the major class and show very poor classification rates on the minor class. By transforming the direct classification problem about original data sequences into a classification problem about the physical similarity between data sequences, the class-balanced effect of Time-Domain Global Similarity (TDGS) method on training set structure is investigated. Meanwhile, the impact of improved training set structure on data cleaning performance of TDGS method is demonstrated with an application example in EAST POlarimetry-INTerferometry (POINT) system.

To guarantee the availability and reliability of data source in Magnetic Confinement Fusion (MCF) devices, incorrect diagnostic data, which cannot reflect real physical properties of measured objects, should be sorted out before further analysis and study. Traditional data sorting cannot meet the growing demand of MCF research because of the low-efficiency, time-delay, and lack of objective criteria. A Time-Domain Global Similarity (TDGS) method based on machine learning technologies is proposed for the automatic data cleaning of MCF devices. Traditional data sorting aims to the classification of original diagnostic data sequences, which are different in both length and evolution properties under various discharge parameters. Hence the classification criteria are affected by many discharge parameters and vary shot by shot. The focus of TDGS method is turned to the physical similarity between data sequences from different channels, which are more essential and independent of discharge parameters. The complexity arisen from real discharge parameters during data cleaning is avoided in the TDGS method by transforming the general data sorting problem into a binary classification problem about the physical similarity between data sequences.

As a demonstration of its application to multi-channel measurement systems, the TDGS method is applied to the EAST POlarimetry-INTerferometry (POINT) system. The optimized performance of the method has reached 0.9871±0.0015.

4. The GAPS project

Nonlinear and multi-scale dynamical processes are ubiquitous in different fields of scientific and engineering researches. Especially in plasma physics, where long-range collective phenomena dominate, advanced numerical schemes and powerful computing software are required for solving complex physical and technical problems. The GeoAlgorithmic Plasma Simulator (GAPS) project is initiated in order to solve various difficult yet key problems in plasma-related domains by applying advanced geometric algorithms and modern large-scale simulation techniques. The Accurate Particle Tracer (APT) code is one product of the GAPS project and aims to facilitate the systematic large-scale applications of advanced algorithms for particle dynamical simulations.

The Accurate Particle Tracer (APT) code is designed for systematic large-scale applications of geometric algorithms for particle dynamical simulations. Based on a large variety of advanced geometric algorithms, APT possesses long-term numerical accuracy and stability, which are critical for solving multi-scale and nonlinear problems. To provide a flexible and convenient I/O interface, the libraries of Lua and Hdf5 are used. Following a three-step procedure, users can efficiently extend the libraries of electromagnetic configurations, external non-electromagnetic forces, particle pushers, and initialization approaches by use of the extendible module. APT has been used in simulations of key physical problems, such as runaway electrons in tokamaks and energetic particles in Van Allen belt. As an important realization, the APT-SW version has been successfully distributed on the world's fastest computer, the Sunway TaihuLight supercomputer, by supporting master–slave architecture of Sunway many-core processors. Based on large-scale simulations of a runaway beam under parameters of the ITER tokamak, it is revealed that the magnetic ripple field can disperse the pitch-angle distribution significantly and improve the confinement of energetic runaway beam on the same time.

5. Conclusion

In summary, thanks to the A3 project, we have made fruitful results in different aspects of plasma physics. These results will be pushed forward in the future, and keep benefiting the development of usage of fusion energy.

References

[1].Xiao, J., et al., Local energy conservation law for a spatially-discretized Hamiltonian Vlasov-Maxwell system. Physics of Plasmas, 2017. 24(6): p. 062112.

[2].Wang, Y., et al., The accurate particle tracer code. Computer Physics Communications, 2017. 220(Supplement C): p. 212-229.

[3].Liu, J., T. Lan, and H. Qin, Improvement of training set structure in fusion data cleaning using Time-Domain Global Similarity method. Journal of Instrumentation, 2017. 12(10): p. C10004.

[4].Zhang, R., et al., Explicit symplectic algorithms based on generating functions for charged particle dynamics. Physical Review E, 2016. 94(1): p. 013205.

[5].Zhang, R., et al., On the structure of the two-stream instability–complex G-Hamiltonian structure and Krein collisions between positive- and negative-action modes. Physics of Plasmas, 2016. 23(7): p. 072111.

[6].Zhang, R., et al., Application of Lie Algebra in Constructing Volume-Preserving Algorithms for Charged Particles Dynamics. Communications in Computational Physics, 2016. 19(5): p. 1397-1408.

[7].Xiao, J., et al., Explicit high-order noncanonical symplectic algorithms for ideal two-fluid systems. Physics of Plasmas, 2016. 23(11): p. 112107.

[8].Wang, Y., H. Qin, and J. Liu, Multi-scale full-orbit analysis on phase-space behavior of runaway electrons in tokamak fields with synchrotron radiation. Physics of Plasmas, 2016. 23(6): p. 062505.

[9].Wang, Y., J. Liu, and H. Qin, Lorentz covariant canonical symplectic algorithms for dynamics of charged particles. Physics of Plasmas, 2016. 23(12): p. 122513.

[10].Liu, J., Y. Wang, and H. Qin, Collisionless pitch-angle scattering of runaway electrons. Nuclear Fusion, 2016. 56(6): p. 064002.

[11].Lan, T., et al., Design of geometric phase measurement in EAST Tokamak. Physics of Plasmas, 2016. 23(7): p. 072109.

[12].He, Y., et al., Explicit K-symplectic algorithms for charged particle dynamics. Physics Letters A, 2016.

[13].He, Y., et al., High order volume-preserving algorithms for relativistic charged particles in general electromagnetic fields. Physics of Plasmas, 2016. 23(9): p. 092109.

[14].He, Y., et al., Hamiltonian particle-in-cell methods for Vlasov-Maxwell equations. Physics of Plasmas (1994-present), 2016. 23(9): p. 092108.

[15].He, Y., et al., Higher order volume-preserving schemes for charged particle dynamics. Journal of Computational Physics, 2016. 305: p. 172-184.

[16].Zhang, R., et al., Volume-preserving algorithm for secular relativistic dynamics of charged particles. Physics of Plasmas (1994-present), 2015. 22(4): p. 044501.

[17].Xiao, J., et al., Explicit high-order non-canonical symplectic particle-in-cell algorithms for Vlasov-Maxwell systems. Physics of Plasmas (1994-present), 2015. 22(11): p. 112504.

[18].Xiao, J., et al., Variational symplectic particle-in-cell simulation of nonlinear mode conversion from extraordinary waves to Bernstein waves. Physics of Plasmas (1994-present), 2015. 22(9): p. 092305.

[19].Qin, H., et al., Canonical symplectic particle-in-cell method for long-term large-scale simulations of the Vlasov–Maxwell equations. Nuclear Fusion, 2015. 56(1): p. 014001.

[20].Qin, H., et al., Comment on "Hamiltonian splitting for the Vlasov–Maxwell equations". Journal of Computational Physics, 2015. 297: p. 721-723.

[21].He, Y., et al., Volume-preserving algorithms for charged particle dynamics. Journal of Computational Physics, 2015. 281: p. 135-147.

[22].He, Y., et al., Hamiltonian time integrators for Vlasov-Maxwell equations. Physics of Plasmas (1994-present), 2015. 22(12): p. 124503.

[23].Zhang, R., et al., Canonicalization and symplectic simulation of the gyrocenter dynamics in

time-independent magnetic fields. Physics of Plasmas (1994-present), 2014. 21(3): p. 032504.

[24].Liu, J., Z. Yu, and H. Qin, A Nonlinear PIC Algorithm for High Frequency Waves in Magnetized Plasmas Based on Gyrocenter Gauge Kinetic Theory. Communications in Computational Physics, 2014. 15(04): p. 1167-1183.

[25].Liu, J., et al., What is the fate of runaway positrons in tokamaks? Physics of Plasmas (1994-present), 2014. 21(6): p. 064503.

[26].Xiao, J., et al., A variational multi-symplectic particle-in-cell algorithm with smoothing functions for the Vlasov-Maxwell system. Physics of Plasmas (1994-present), 2013. 20(10): p. 102517.

[27].Chen, Q., et al., Canonical symplectic structure and structure-preserving geometric algorithms for Schrödinger-Maxwell systems. Journal of Computational Physics, 2017.

[28].Chen, Q., H. Qin, and J. Liu, Photons, phonons, and plasmons with orbital angular momentum in plasmas. Scientific Reports, 2017. 7: p. 41731.

The Accurate Particle Tracer Code

Yulei Wang[1], Jian Liu[1], Hong Qin[1], ZhiYu[2], Yicun Yao[1]

[1]Department of Modern Physics and School of Nuclear Science and Technology,

University of Science and Technology of China, Hefei, Anhui 230026, China

[2]Theory and Simulation Division, Institute of Plasma Physics,

Chinese Academy of Sciences, Hefei, Anhui 230031, China

In this proceeding, we give a short introduction about our recent work on runaway electrons [Computer Phys. Communications 220 (2017)]. The Accurate Particle Tracer (APT) code is designed for systematic large-scale applications of geometric algorithms for particle dynamical simulations. Based on a large variety of advanced geometric algorithms, APT possesses long-term numerical accuracy and stability, which are critical for solving multi-scale and nonlinear problems. To provide a flexible and convenient I/O interface, the libraries of Lua and Hdf5 are used. Following a three-step procedure, users can efficiently extend the libraries of electromagnetic configurations, external non-electromagnetic forces, particle pushers, and initialization approaches by use of the extendible module. APT has been used in simulations of key physical problems, such as runaway electrons in tokamaks and energetic particles in Van Allen belt. As an important realization, the APT-SW version has been successfully distributed on the world's fastest computer, the Sunway TaihuLight supercomputer, by supporting master–slave architecture of Sunway many-core processors. Based on large-scale simulations of a runaway beam under parameters of the ITER tokamak, it is revealed that the magnetic ripple field can disperse the pitch-angle distribution significantly and improve the confinement of energetic runaway beam on the same time.

Nonlinear and multi-scale dynamical processes are ubiquitous in different fields of scientific and engineering researches. Especially in plasma physics, where long-range collective phenomena dominate, advanced numerical schemes and powerful computing software are required for solving complex physical and technical problems. The GeoAlgorithmic Plasma Simulator (GAPS) project is initiated in order to solve various difficult yet key problems in plasma-related domains by applying advanced geometric algorithms and modern large-scale simulation techniques. The Accurate Particle Tracer (APT) code is one product of the GAPS project and aims to facilitate the systematic large-scale applications of advanced algorithms for particle dynamical simulations.

Particle dynamical simulations play important roles in numerical studies of plasmas. Various codes have been developed and used widely for solving problems including the particle acceleration in magnetic reconnection [1,2], fast particle dynamics in Tokamaks [3,4], wave–particle interactions in earth magnetosphere [5], and particle transportation in plasma turbulences [6,7]. The particle dynamical simulation is also a main method of solving differential stochastic equations, when stochastic processes of plasmas are considered, such as the simulation of runaway dynamics during disruptions of tokamak operations [8]. Although fruitful results have been achieved, the accumulation of numerical errors makes

traditional codes unreliable after longterm simulations which are unavoidable for addressing multi-scale and nonlinear problems. Real physical information may also be distorted due to the breakdown of original physical structures in computation schemes. To guarantee long-term numerical accuracy and stability, a series of advanced geometric algorithms has been systematically developed recently [9–34], which bound the global numerical errors by preserving geometric structures. On the other hand, the further development and application of geometric algorithms need interdisciplinary cooperation. An efficient platform for researchers in different fields is needed to integrate the latest trans-disciplinary achievements.

Different from the particle dynamical codes equipped with traditional algorithms and focusing only on some specific physical application scenarios [1–3,6,7], the APT code is based on geometric algorithms with secular stability, and its algorithm and physical libraries can also be extended conveniently to accomplish tasks in various research fields. Therefore, APT not only can be used to address multi-scale and nonlinear problems, but also serves as a universal platform for researchers from different fields, such as plasma physics, accelerator physics, space science, fusion energy research, computational mathematics, software engineering, and high-performance computation.

The underlying model of APT is the first principle particle dynamical equations (see Fig. 1). In simulations of plasma systems, the distribution of plasmas is sampled statistically in the phase space. Using appropriate geometric algorithms, APT traces each sample point accurately by solving full-orbit Lorentz force equations that are the characteristic line equations of the Vlasov equation. If considering the random collisional terms, the Langevin approach is used, which transfers the collisional terms to random forces [35]. The external electromagnetic fields are set up through analytical functions, or discrete field configuration data obtained from experiments or simulations. There already exist many built-in electromagnetic field configurations for typical physical problems in APT. Self-consistent calculation of APT is implemented through dynamical field models, namely, field functions with variable parameters evolving together with the phase-space states of all particles.

The APT code is implemented in standard C language and can be distributed directly on Unix-like operation system. For non-Unixlike systems, users can build APT via Unix-like compatibility layers, such as Cygwin and MSYS. The APT code consists of seven main modules, including the I/O module, the initialization module, the particle pusher module, the parallelization module, the field configuration module, the external force-field module, and the extendible module. The I/O module calls the libraries from Lua and Hdf5 projects. The input configuration files consist of several Lua scripts which make it convenient and flexible for users to set the parameters of physical problems. The output data is stored in the Hdf5 format, which enables users to access data in a file-system-like way and simplifies data analysis. The initialization module provides a number of methods for statistical sampling. The particle pusher module contains various advanced geometric algorithms, including volume-preserving and symplectic integrators with different orders and stability domains. Traditional algorithms such as Runge–Kutta method with different orders are also available. It is thus convenient to choose appropriate algorithms for solving realistic problems and studying numerical methods under complex physical setup. To boost large-scale applications of geometric algorithms, the parallelization module of the stable APT distribution supports the MPI parallelization. Another version of APT supporting CUDA is also developed. As an important parallel version, the branch

version APT-SW has been built recently for the world's fastest supercomputer, the Sunway TaihuLight supercomputer [36], which provides more than ten million computation cores and has the peak performance of 125PFlops [37]. To fully utilize the computation ability of the Sunway TaihuLight, APT-SW is designed to support the Sunway many-core parallelization. Supported by the powerful computation capacity, APT-SW can be used to simulate processes with large amounts of sampling particles, complex field configurations, and multi-timescales spanning more than 10 orders. The field configuration module and the external force-field module contain respectively various electromagnetic configurations and other external non-electromagnetic force fields, such as radiation force, collisional force, bremsstrahlung force, and gravitation field. Written by the bash-script, the extendible module provides a convenient way to extend the source code. Following the interfaces of APT and a three-step extending procedure, one can easily add new configuration parameters, field configurations, external forces, algorithms, and initialization functions into APT. These new packages form a new version of APT, and can also be used by other researchers.

APT has been used in the study of geometric numerical methods and the simulations of some multi-scale physical processes [38,39]. The multi-scale dynamics of runaway electrons in tokamaks is studied by secular simulations over 1012 time steps. Using the relativistic volume-preserving algorithm in APT, the refined structures of runaway transit orbits are revealed. The APT code shows long-term numerical accuracy and enables the discovery of novel mechanisms such as neoclassical collisionless pitch-angle scattering and new runaway energy limit rule [38,39]. Meanwhile, the evolution of energetic particle distribution in Van Allen belt is simulated by tracing massive sampling particles. The symplectic Euler pusher for relativistic dynamics is employed. The evolution of energetic particles in the terrestrial magnetic field is recovered precisely.

New physical results have been obtained based on the large-scale simulations of APT-SW. The long-term evolution of the runaway electron beam under the realistic parameters of ITER tokamak is simulated on the TaihuLight supercomputer. This simulation involves approximately 107 samplings, 1011 iteration steps, and more than 1021 floating-point operations, which is currently the largest particle simulation. Both the neoclassical collisionless pitch-angle scattering [38] and the magnetic ripple stochastic effect are considered [39,40]. Without magnetic ripple field, after long-term evolution, the pitch-angle distribution tends to be concentrated in a small interval and has non-zero average value, which is consistent with the results in Ref. [39]. However, if the magnetic ripple is considered, the pitch-angle distribution can be significantly dispersed. Meanwhile, the poloidal profile of runaway beam is proven to be squeezed towards tokamak core by the magnetic ripple field, which serves as an evidence to the improved confinement of runaway electrons.
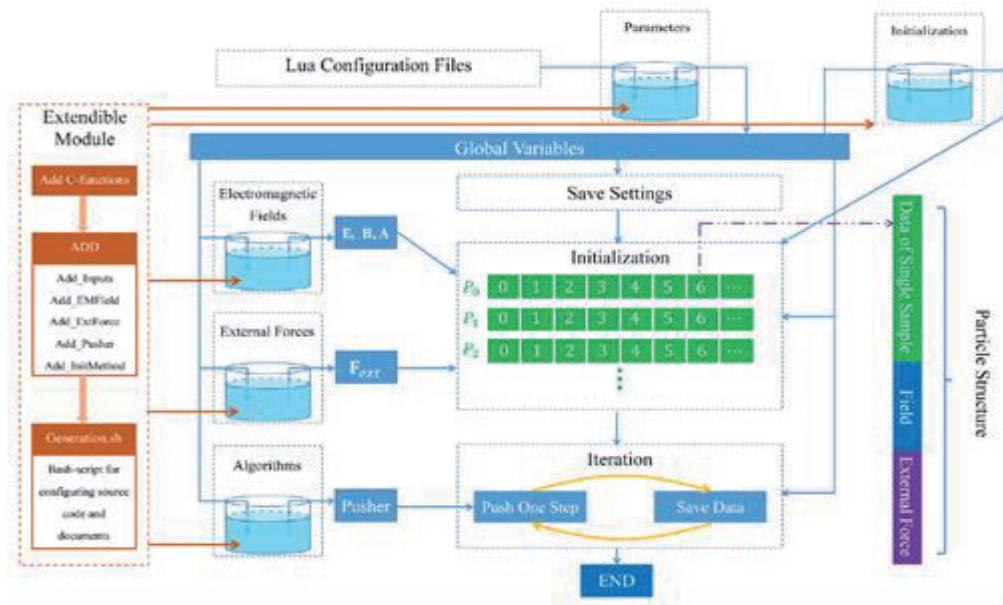
Fig. 1 Diagram of the APT architecture. The blue arrows denote the flow of procedure, while the brown parts represent the extendible module. In the Initialization box, sampling particles assigned to different processors are marked by $P_0, P_1, \cdots$.

References

[1] A. Perona, D. Borgogno, L.-G. Eriksson, Comput. Phys. Comm. 185 (1) (2014) 86.

[2] B. Hamilton, L. Fletcher, K. McClements, A. Thyagaraja, Astrophys. J. 625 (1) (2005) 496.

[3] D. Pfefferlé, W. Cooper, J. Graves, C. Misev, Comput. Phys. Comm. 185 (12) (2014) 3127.

[4] R. White, M. Chance, Phys. Fluids 27 (10) (1984) 2455.

[5] Z. Su, H. Zhu, F. Xiao, H. Zheng, M. Zhang, Y.-M. Liu, C. Shen, Y. Wang, S. Wang, Phys. Plasmas 21 (5) (2014) 052310.

[6] S. Dalena, P. Chuychai, R. Mace, A. Greco, G. Qin, W. Matthaeus, Comput. Phys. Comm. 183 (9) (2012) 1974.

[7] R.C. Tautz, Comput. Phys. Comm. 181 (1) (2010) 71.

[8] L.-G. Eriksson, P. Helander, Comput. Phys. Comm. 154 (3) (2003) 175.

[9] R.I. McLachlan, G.R.W. Quispel, J. Phys. A: Math. Gen. 39 (19) (2006) 5251.

[10] J. Candy, W. Rozmus, J. Comput. Phys. 92 (1) (1991) 230.

[11] H. Qin, X. Guan, Phys. Rev. Lett. 100 (3) (2008) 035006.

[12] H. Qin, J. Liu, J. Xiao, R. Zhang, Y. He, Y. Wang, Y. Sun, J.W. Burby, L. Ellison, Y. Zhou, Nucl. Fusion 56 (1) (2015) 014001.

[13] H. Qin, S. Zhang, J. Xiao, J. Liu, Y. Sun, W.M. Tang, Phys. Plasmas 20 (8) (2013) 084503.

[14] X. Guan, H. Qin, N.J. Fisch, Phys. Plasmas 17 (9) (2010) 092502.

[15] R. Zhang, J. Liu, H. Qin, Y. Wang, Y. He, Y. Sun, Phys. Plasmas 22 (4) (2015) 044501.

[16] J. Xiao, J. Liu, H. Qin, Z. Yu, Phys. Plasmas 20 (10) (2013) 102517.

[17] Y. He, H. Qin, Y. Sun, J. Xiao, R. Zhang, J. Liu, Phys. Plasmas 22 (12) (2015) 124503.

[18] R. Zhang, J. Liu, Y. Tang, H. Qin, J. Xiao, B. Zhu, Phys. Plasmas 21 (3) (2014) 032504.

[19] Y. He, Y. Sun, J. Liu, H. Qin, J. Comput. Phys. 305 (2016) 172.

[20] Y. He, Y. Sun, J. Liu, H. Qin, J. Comput. Phys. 281 (2015) 135.

[21] P. Channell, C. Scovel, Nonlinearity 3 (2) (1990) 231.

[22] P.J. Channell, Comput. Sci. Discovery 7 (1) (2014) 015001.

[23] Y. He, Z. Zhou, Y. Sun, J. Liu, H. Qin, Phys. Lett. A (2016).

[24] J. Squire, H. Qin, W.M. Tang, Phys. Plasmas 19 (8) (2012) 084501.

[25] M. Kraus, O. Maj, Physica D 310 (2015) 37.

[26] M. Kraus, Variational integrators in plasma physics, 2013. ArXiv preprint arXiv 1307 5665.

[27] C.L. Ellison, J. Finn, H. Qin, W.M. Tang, Plasma Phys. Control. Fusion 57 (5) (2015) 054007.

[28] J. Li, H. Qin, Z. Pu, L. Xie, S. Fu, Phys. Plasmas 18 (5) (2011) 052902.

[29] R.I. McLachlan, P. Atela, Nonlinearity 5 (2) (1992) 541.

[30] B. Shadwick, A. Stamm, E. Evstatiev, Phys. Plasmas 21 (5) (2014) 055708.

[31] R. Zhang, H. Qin, Y. Tang, J. Liu, Y. He, J. Xiao, Phys. Rev. E 94 (1) (2016) 013205.

[32] R. Zhang, Y. Wang, Y. He, J. Xiao, J. Liu, H. Qin, Y. Tang, Explicit symplectic algorithms based on generating functions for relativistic charged particle dynamics in time-dependent electromagnetic field, 2016. ArXiv preprint arXiv 1610 05390.

[33] B. Zhu, R. Zhang, Y. Tang, X. Tu, Y. Zhao, J. Comput. Phys. 322 (2016) 387.

[34] J. Xiao, J. Liu, H. Qin, Z. Yu, N. Xiang, Phys. Plasmas 22 (9) (2015) 092305.

[35] M. Cadjan, M. Ivanov, J. Plasma Phys. 61 (01) (1999) 89.

[36] Top500 Website, https://www.top500.org/lists/2016/06/.

[37] H. Fu, J. Liao, J. Yang, L. Wang, Z. Song, X. Huang, C. Yang, W. Xue, F. Liu, F.E.A. Qiao, Sci. China Inf. Sci. 59 (7) (2016) 072001.

[38] J. Liu, Y. Wang, H. Qin, Nucl. Fusion 56 (6) (2016) 064002.

[39] Y. Wang, H. Qin, J. Liu, Phys. Plasmas 23 (6) (2016).

[40] J. Rax, N. Fisch, L. Laurent, Plasma Phys. Control. Fusion 35 (SB) (1993) B129.

Preference-based performance measures for Time-Domain Global Similarity method

Ting. Lan[1], Jian. Liu[1], Hong. Qin[1,2]

[1]School of Nuclear Science and Technology, USTC, Hefei, Anhui 230026, China
[2]Plasma Physics Laboratory, Princeton University, Princeton, NJ 08543, USA

Abstract

For Time-Domain Global Similarity (TDGS) method, which transforms the data cleaning problem into a binary classification problem about the physical similarity between channels, directly adopting common performance measures could only guarantee the performance for physical similarity. Nevertheless, practical data cleaning tasks have preferences for the correctness of original data sequences. To obtain the general expressions of performance measures based on the preferences of tasks, the mapping relations between performance of TDGS method about physical similarity and correctness of data sequences are investigated by probability theory in this paper. Performance measures for TDGS method in several common data cleaning tasks are set. Cases when these preference-based performance measures could be simplified are introduced.

1. Introduction

To guarantee the availability and reliability of data source, a general-purposed Time-Domain Global Similarity (TDGS) method based on machine learning techniques has been developed, which sorts out the incorrect fusion data by classifying the physical similarity between channels [1]. In the model selection and evaluation process of TDGS method, different performance measures lead to models of various generalization abilities [2, 3]. Choices of performance measures depend on the required generalization ability of models, or say preferences of tasks. Setting preference-based performance measures helps to perform corresponding tasks better. For TDGS method, directly adopting common performance measures, such as precision, recall, F-factor, confusion matrix, and Receiver Operating Characteristics (ROC) graphs, could only guarantee the performance for physical similarity between data sequences [4-6]. Nevertheless, practical data cleaning tasks have requirements for the correctness of original data sequences. For example, some data cleaning tasks require high recall rate of incorrect data, and some tasks require high precision of correct data. To improve the performance of TDGS method in data cleaning tasks, new performance measures based on the preferences of corresponding tasks should be set.

Each sample of TDGS method is the combination of two data sequences from different channels of MUlti-channel Measurement (MUM) systems. By tagging the sample completely constituted by correct data as physical similarity, and tagging the sample containing at least one incorrect data sequence as physical dissimilarity, the data cleaning problem turns into a binary classification problem about physical similarity between data sequences. When defining the prediction performance of TDGS method, True Positive (TP) refers that predicting results and actual sample tags are both dissimilar. True Negative (TN) refers that predicting results and actual sample tags are both similar. However, when defining the required prediction performance for data cleaning tasks, TP and TN refer to the incorrect and correct sequences which are correctly predicted. To set performance measures according to the preferences of tasks, the mapping relations between performance of TDGS method about physical similarity and correctness of data sequences should be explicit first. However, these mapping relations are complex and influenced by many

factors, such as the data structure of samples, performance of models, the rule for judging the correctness of data based on given physical similarity, and the judging order. To obtain the general expression of preference-based performance measures for TDGS, the mapping relations between performance of TDGS method about physical similarity and correctness of data sequences are investigated by probability theory in this paper. Based on these mapping relations, we set preference-based performance measures for several common data cleaning tasks. By adopting these new performance measures in the model selection and evaluation process, models generated by TDGS method could best meet the preferences of tasks in probability.

The mapping relations between performance of TDGS method about physical similarity and correctness of data sequences are decided by the rules for judging the correctness of data based on given physical similarity (see Fig. 1). Here we adopt an absolute algorithm, i.e., by scanning through all samples tagged with similarity first, tag the sequences contained in the similar samples as correct data, and tag the other data as incorrect data. Based on this judging rule, the mapping relations between performance about physical similarity and correctness of data sequences can be analyzed by probability theory. In view that every prediction about physical similarity is independent of each other, the probability of judging the correctness of data is the product of the probabilities of all predictions employed in the judging process [7]. For example, according to the adopted judging rule, a correct data sequence S_0 would be predicted as incorrect if all samples containing S_0 are predicted as dissimilarity. Therefore, the probability of judging a correct data sequence as incorrect can be decided according to the number of similar samples containing S_0, the probability of predicting similar samples as dissimilarity, the number of dissimilar samples containing S_0, and the probability of predicting dissimilar samples as dissimilarity. Based on the mapping relations between performances of TDGS method about physical similarity and the correctness of data, performance measures for several common data cleaning tasks are set in this paper. Meanwhile, the correlative relations between these preference-based performance measures and performance parameters about physical similarity are analyzed. When preference-based performance measures are strong positive correlative with certain parameter, these performance measures could be simplified.

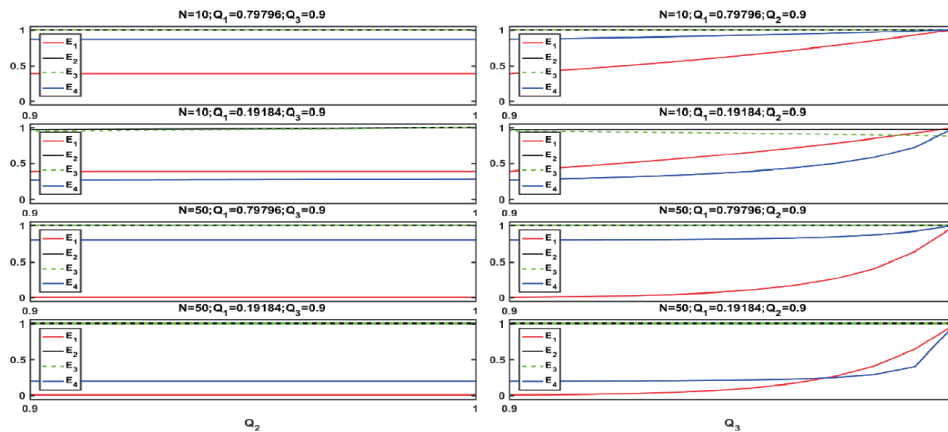Fig.1 The change relations between performance parameters about physical similarity and preference-based performance measures are plotted. Q_2 denotes recall rate of similar samples. Q_3 denotes recall rate of dissimilar samples. E_1 denotes recall of incorrect data. E_2 denotes precision of incorrect data. E_3 denotes recall of correct data. E_4 denotes precision of correct data. [8]

2. Summary

Data cleaning tasks could be performed better by setting preference-based performance measures. In this paper, we provide the mapping relations between performance of TDGS method about physical similarity and correctness of data sequences by probability theory. Based on these mapping relations, preference-based performance measures for several common data cleaning tasks are set for TDGS method. Meanwhile, the correlative relations between these new performance measures and performance parameters are analyzed.

By setting preference-based performance measures, the preferences of data cleaning tasks could be best meet by TDGS method in probability. When these new performance measures are strong positive correlative with certain parameter, preference-based performance measures could be simplified. Next step, we would further improve the performance of TDGS method by adopting different rules for judging the correctness of data based on given physical similarity. The rule adopted in this paper is an absolute judging rule. Next step, we could adopt a non-absolute judging rule. For example, the sequence which is dissimilar from 90% of the other sequences can be tagged as incorrect data. The degree parameter introduced by the judging rule changes the mapping relations between performance of TDGS method about physical similarity and correctness of data sequences. In some cases, proper setting of the degree parameter would improve the data cleaning performance of TDGS method.

References

[1] T. Lan, J. Liu, H. Qin, and L. Li Xu, ArXiv e-prints (2017), 1705.04947.

[2] N. Karayiannis and A. N. Venetsanopoulos, Artificial neural networks: learning algorithms, performance evaluation, and applications, vol. 209 (Springer Science & Business Media, 2013).

[3] R. Kohavi et al., in Ijcai (Stanford, CA, 1995), vol. 14, pp. 1137–1145.

[4] C. Goutte and E. Gaussier, in European Conference on Information Retrieval (Springer, 2005), pp. 345–359.

[5] D. M. Powers (2011).

[6] T. Fawcett, Pattern recognition letters 27, 861 (2006).

[7] R. Durrett, Probability: theory and examples (Cambridge university press, 2010).

[8] Lan T, Liu J, Qin H. Preference-based performance measures for Time-Domain Global Similarity method[J]. Journal of Instrumentation, 2017, 12(12): C12008.

Progress Towards High Regimes on HL-2A

Yi Liu[1], M. Xu[1], L.W. Yan[1], Y. Xu[1], X.M. Song[1], J.Q. Dong[1], X.T. Ding[1], L.Y. Chen[1], B. Lu[1], D.Q.Liu[1], J. Rao[1], W.M. Xuan[1,] Q.W. Yang[1], G.Y. Zheng[1], X.L. Zou[2], Y. Q. Liu[3], W.L. Zhong[1], K.J. Zhao[1], X.Q. Ji[1], W.C.Mao[1], Q.M.Wang[1], Q. Li[1], J.Y. Cao[1], Z.Cao[1], G.J. Lei[1], J.H. Zhang[1], X.D. Li[1], X.Y. Bai[1], J. Cheng[1], W. Chen[1], Z.Y.Cui[1], L. Delpech[2], P.H. Diamond[4], Y.B.Dong[1], A. Ekedahl[2], T. Hoang[2], Y. Huang[1], K. Ida[5], K. Itoh[5], S.-I. Itoh[6], M. Isobe[5], S. Inagaki[6], D. Mazon[2], S.Morita[5], Y. Peysson[2], Z.B. Shi[1], X.G. Wang[7], G.L. Xiao[1], D.L.Yu[1], L.M.Yu[1], Y.P. Zhang[1], C.H.Cui[1], B.B.Feng[1], M.Huang[1], B.Li[1], G.S.Li[1], H.J.Li[1], Qing Li[1], J.F.Peng[1], Y.Q.Wang[1], B.S.Yuan[1], X.R.Duan[1]Yong Liu[1] and HL-2A team

[1]Southwestern Institute of Physics, P.O. Box 432, Chengdu 610041, China
[2]CEA, IRFM, F-13108 Saint-Paul-lez-Durance, France
[3]CCFE, Culham Science Centre, Abingdon, Oxfordshire, OX14 3DB, UK
[4]CASS & Department of Physics, UCSD, La Jolla, CA 92093, USA
[5]National Institute for Fusion Science, 322-6 Oroshi-cho, Toki-shi 509-5292, Japan
[6]Research Institute for Applied mechanics, Kyushu University,Kasuga, Kasuga keon 6-1, 816-8580, Japan
[7]Harbin Institute of Technology, Harbin, Hei Long Jiang 150006, China

Abstract

Significant progress has been made recently in the following areas: the first High coupling efficiency of lower-hybrid current drive (LHCD) with the Passive-Active Multi-junction (PAM) antenna was successfully demonstrated in H-mode on the HL-2A tokamak; double critical impurity gradients of electromagnetic turbulence were observed in H-mode plasmas; A new pedestal mode, leading an inward particle flux, was observed prior to each ELM onset; Various ELM mitigation techniques have been investigated, including supersonic molecular beam injection (SMBI), impurity seeding, resonant magnetic perturbation (RMP) and lower-hybrid wave (LHW); The ion internal transport barrier was observed in the neutral beam injection (NBI) heated plasmas; Neoclassical tearing modes (NTMs) driven by the transient perturbation of local electron temperature during the non-local thermal transport events have been observed, and a new-type non-local transport triggered by the ion fishbone was found; Long-lasting runaway electron plateau was achieved after argon injection and the runaway current was successfully suppressed by SMBI; It was found that low-n Alfvenic ion temperature gradient (AITG) modes can be destabilized in ohmic plasmas even with weak magnetic shear and low pressure gradients; For the first time, the synchronization of geodesic acoustic mode (GAM) and magnetic fluctuations was observed in the edge plasmas, revealing the frequency entrainment and phase lock; Spatiotemporal features of zonal flows have been studied by using multi-channel correlation Doppler reflectometers.

1. Introduction

In recent years the HL-2A tokamak programme has been aimed to address the key physic issues relevant to ITER. In order to achieve the goal, many subsystems such as auxiliary heating and diagnostic systems, have been upgraded or developed. The newly developed 3.7 GHz lower-hybrid current drive (LHCD) system in HL-2A consists of a Passive-Active Multi-junction (PAM) launcher [1]. The first LHCD experiments with the PAM in H-mode [2] were carried out. The coupled LH power reached 900 kW in H-mode plasmas. One H-mode discharge is shown in Fig. 1. The LH power can be coupled at large

plasma-launcher gap (e.g. 11cm gap for 0.5MW coupled power), and assist in triggering and sustaining H-modes. Some advanced diagnostic systems have been developed and upgraded, including a multi-channel HCOOH laser interferometer and polarimeter [3,4] for density and Faraday rotation measurement, a 384-channel electron cyclotron emission imaging (ECEI) system for 2D electron temperature fluctuation measurement [5], a multi-channel correlation Doppler backscattering reflectometer (DBS) for poloidal rotation and turbulence measurement [6], a Doppler coherence imaging system for toroidal rotation measurement, a high-frequency magnetic probe array for detecting high mode-number (m/n=20/30) MHD instabilities, a wide-angle infrared (IR) periscopes diagnostic for observing plasma wall interaction in the main chamber, etc. A variety of fuelling techniques, such as massive gas injection (MGI), gas mixture supersonic molecular beam injection (SMBI), have been developed or improved. These upgrades greatly enhanced the capability for the study of advanced plasma physics on the machine.

This paper is arranged as the following. H-mode physics results are given in section 2; ELM mitigation and control by various methods are summarized in section 3; Core plasma transport studies are presented in section 4; Section 5 is a brief summary

2. H-mode physics

In HL-2A, recent experiments in the area of H-mode physics were focused on the study of pedestal dynamics and underlying instabilities. The impact of impurity on pedestal dynamics and instabilities has been investigated recently (see Fig. 2). It was found that a broadband electromagnetic turbulence could be excited by impurities in the H-mode plasmas, and double critical impurity gradients of the turbulence were observed. In pedestal region, a new pedestal quasi-coherent mode (QCM), which led an inward particle flux, was observed prior to each ELM onset. It contributes significant additional density and its gradient/pressure gradient increase and may trigger the ELM onset. The origin of the oscillating radial electric field in intermediate confinement phase (I-phase) and its roles in the transition has been studied.
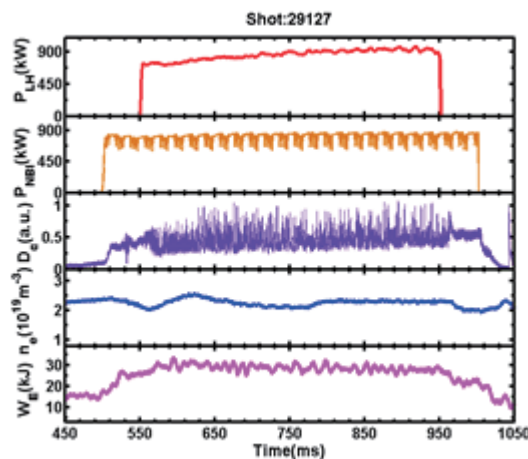
Fig.1 Time evolution of main parameters for the plasmas with coupled LHW power reaching 900 kW in H-mode.
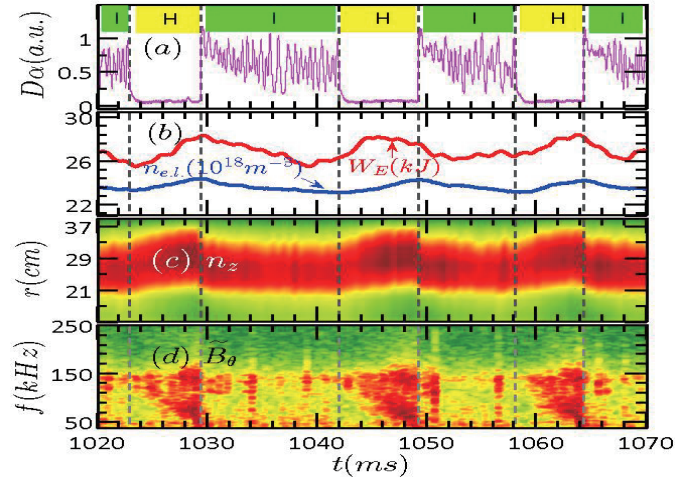
Fig.2 (a) Divertor D_α signal, (b) inner stored energy and line-averaged electron density, (c) effective impurity density, (d) spectrogram of magnetic fluctuations.

3. ELM Mitigation and Control

Various ELM mitigation or control techniques have been explored in HL-2A, including LHW, impurity seeding, RMP, SMBI and pellet injection. ELM mitigation experiments by using new LHW system with the PAM have been performed in HL-2A. The mitigation effect was synchronized with the increase of the pedestal turbulence measured by Doppler reflectometry. The ELM mitigation has been achieved by externally seeded impurities by means of laser blow-off (LBO) and SMBI systems. With SMBI technique, the experimental results indicated that the shallow deposition of SMBI is sufficient for ELM mitigation [10, 21]. ELM mitigation by applying n = 1 resonant magnetic perturbation was first obtained in recent HL-2A experiments. It was found that the ELM mitigation window is q_{95} = 3.65-3.85. The drop of core toroidal velocity measured by charge exchange recombination spectroscopy was always observed in ELM mitigation discharges correlated with density pump out.

Recently LHCD has been shown to be a new method for ELM mitigation. ELM mitigation experiments with LHCD have been performed in HL-2A as shown in Figure 3, the mitigation effect is synchronized with the increase of the pedestal turbulence measured by Doppler reflectometry, showing that the enhancement of the particle transport due to the pedestal turbulence could be the direct cause of the ELM mitigation.

Fig.3 Time trace of the line-averaged density (red solid line) and the plasma stored energy（blue dashed line）(a), the LHCD antenna gas puff signal (red dashed line) and the LHW monitoring (blue solid line) (b), the radiation measured by bolometer (c), the ELM frequency (d), and the intensity of the inter-ELM turbulence (e)

4. Core Plasma Transport

For the progress in core plasma transport, the iITBs were observed in the NBI heated plasmas. The results indicated the importance of flow 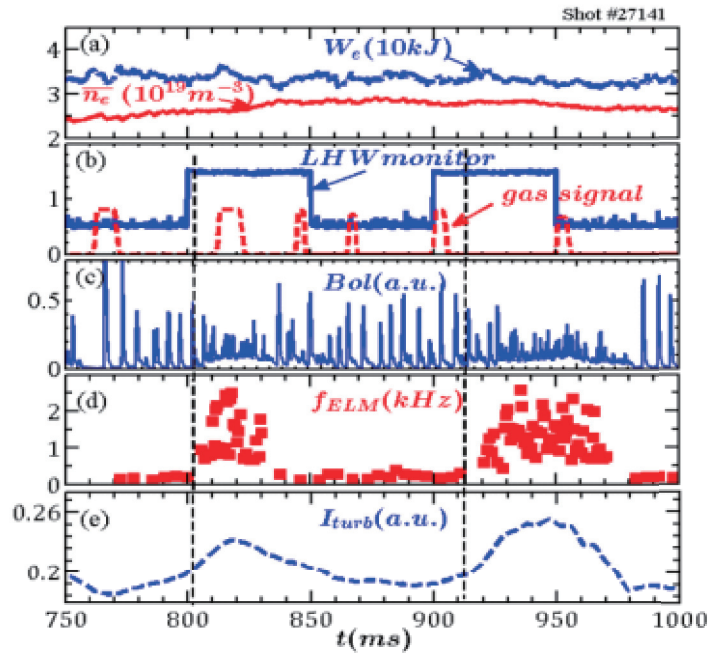shear on ITB sustainment. The effect of ECRH on the impurity transport has been investigated. The reduction of impurity concentration in the plasmas core was observed when the ECRH power deposited inside the sawtooth reversion surface [15]. The tungsten spectra have been investigated in extreme ultraviolet (EUV) wavelength range. Two isolated line emissions were found in the low temperature plasma phase. A quasi-coherent TEM in spectra of density fluctuations has been observed by multi-channel microwave reflectometers. The turbulence transition and the direct effect of the TEM on particle transport have been studied. For non-local heat transport, it was found that the critical values of β to induce the NTMs in nonlocal discharges were substantially lower than those without nonlocal transport. A new-type nonlocal transport triggered by the ion fishbone was observed. These findings revealed the dynamic interaction between turbulence and large-scale mode structures.

The ion internal transport barriers (iITBs) were observed in the NBI heated plasmas on the HL-2A tokamak. The position of the barrier foot, in the stationary state, coincides with the $q=1$ flux surface within its uncertainty of measurement. The ion temperature and toroidal rotation profiles are shown in figure 4. For these shots with ITB, long lasting modes (fishbone oscillations) were observed during the peaked ion temperature and velocity phases. Another interesting observation is that the $T_i(0.5)$ in the discharges without iITBs seems not lower than that with iITBs; and it is clear that the $T_i(0.5)$ declines when the maximum R/L_{Ti} is higher than 14. Further analysis indicates that the $R/L_{Ti}(0.2)$ increases with $R/L_{Ti}(0.5)$ for the discharges without iITB. When the $R/L_{Ti}(0.2)$ is higher than 14, the iITB is formed. The characters of ion thermal diffusivity indicate that there is a typical ITB in the region $\rho<0.4$ before ECRH phase. During

the ECRH phase without iITB, the χ_i is higher and can be up to ~8 m^2/s. The iITB are observed only in discharges of $T_i \geq T_e$, and are not otherwise, indicating that the temperature ratio plays a very important role in the iITB formation. The drift turbulence is analyzed with HD7 code and the results indicate that the ITG mode turbulence is dominant for the peaked ion temperature discharges.
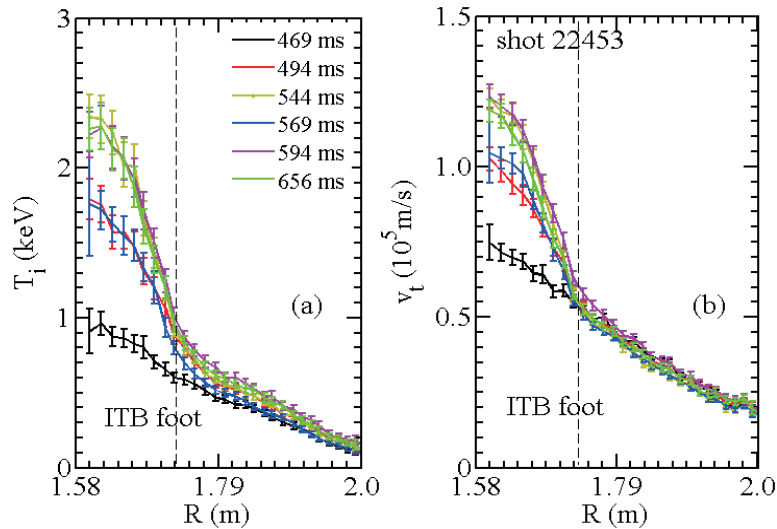
Fig.4 T_i (a) and v_t (b) profiles.

5. Summary

HL-2A tokamak has achieved significant progress in the studies of H-mode physics, ELM mitigation and control, core plasma transport, MHD and energetic particle physics, and edge turbulence.

Acknowledgment

References

[1]Bai X.Y.et al., Proc. 42nd EPS Conference on Plasma Physics, Lisbon (2015), P5.137.
[2] Li Y.G.et al,2016 JINST**11**C02002.
[3] Zhong W.L. et al., 2016 Phys. Rev. Lett.**117**, 045001.
[4] Chen W. et al.,2016 Nucl. Fusion **56** 044001.
[5] Zhong W.L. et al.,2016 Phys. Plasmas**23**, 060702 .
[6] Yang Z.C. et al 2016 Phys. Plasmas**23** 012515

Program of 12th A3 Seminar
(December 12 - 15, 2017, Chongqing, China)

December 11, 2017 (Monday) Registration: 15:00-22:00

December 12, 2017 (Tuesday)			
Session 1 (Opening) Chair: Prof. L.Q. HU	*08:30-08:40*	**Liqun HU** (ASIPP)	**Opening remarks**
		Baonian WAN (ASIPP)	**Welcome speech**
Session 2 (Progress of Devices) Chair: Prof. S. MORITA	*08:40-09:05*	**Jinping QIAN** (ASIPP)	Recent Progress of long pulse H-mode operation on EAST
	09:05-09:30	**Jong-Gu KWAK** (NFRI)	Status of KSTAR
	09:30-09:55	**Katsuyoshi TSUMORI** (NIFS)	Topics of NIFS NBI group in 2017
	09:55-10:20	**Yi LIU** (SWIP)	Progress Towards High Regimes on HL-2A
Break: *10:20-10:35*			
Session 3 (Summary for A3) Chair: Prof. J.G. KWAK	*10:35-11:00*	**Shigeru MORITA** (NIFS)	Summary abstract of presentation at 11th APFA & 26th ITC entitled fusion research and international collaboration in Asian region
	11:00-11:25	**Tianyang XIA** (ASIPP)	Summary of theory and simulation activities of ASIPP in A3 program
	11:25-11:50	**Jian LIU** (USTC)	Reviews on MCF research in USTC supported by A3 program
	11:50-12:15	**Jiansheng HU** (ASIPP)	Development of wall conditioning, fueling and ELM control in EAST with W divertor
Group Photo & Lunch: *12:15-14:00*			
Session 4 (Category I) Chair: Prof. J.S. HU	*14:00-14:25*	**Bingjia XIAO** (ASIPP)	The simulation of EAST vertical instability by TSC code
	14:25-14:50	**Hyun-Seok KIM** (NFRI)	Standardized plasma shape and its operation characteristics for KSTAR upgrade toward steady-state operation
	14:50-15:15	**Haiqing LIU** (ASIPP)	Improve core confinement with optimized q profile in long pulse H mode discharge on EAST
	15:15-15:40	**Zhengying CUI** (SWIP)	Progress in relation to VUV diagnostics in HL-2A
	15:40-16:05	**Mamoru SHOJI** (NIFS)	Simulation analysis of impurity transport induced by dust emission in the ergodic magnetic field line structures in the Large Helical Device
Break: *16:05-16:20*			

Session 5 (Category II) Chair: Prof. Kazuo TOI	16:20-16:45	**Tetsutaro OISHI** (NIFS)	Spectroscopic study of carbon impurity flow in the edge stochastic magnetic field layer of Large Helical Device
	16:45-17:10	**Rui DING** (ASIPP)	Recent progress on PWI studies on EAST
	17:10-17:35	**Yipo ZHANG** (SWIP)	Control of Edge Localized Modes by Pedestal Deposited Impurity in the HL-2A tokamak
	17:35-18:00	**Shuai GU** (ASIPP)	Recent progresses in RMP physic studies in EAST
Dinner: *18:00*			

December 13, 2017
(Wednesday)

Session 6 (Category I) Chair: Prof. W.C. LEE	08:30-08:55	**Jeehyun KIM** (NFRI)	Progress on new LHCD antenna development
	08:55-09:20	**Bojiang DING** (ASIPP)	Current profile control by LHCD in EAST
	09:20-09:45	**Daiji KATO** (NIFS)	Atomic data and spectra of tungsten highly charged ions studied by using CoBIT and LHD
	09:45-10:10	**Woochang LEE** (NFRI)	Turbulence study with microwave imaging reflectometer
Break: *10:10– 10:25*			
Session 7 (Category II) Chair: Prof. B.J. XIAO	10:25-10:50	**Naoko ASHIKAWA** (NIFS)	Recent analysis of key issues for fuel retention in fusion devices
	10:50-11:15	**Zhipeng CHEN** (HUST)	Investigation of density limit and MARFE by Polaris on J-TEXT tokamak
	11:15-11:40	**Seiki SAITO** (Kushiro College)	Molecular simulation for the investigation of helium bubble effects on plasma irradiation to tungsten material
	11:40-12:00	**Fuqiong WANG** (Donghua Univ.)	SOLPS modelling of edge plasma and impurity transport in EAST
	12:00-12:20	**Jeongwon LEE** (NFRI)	Efficient ECH-assisted plasma startup experiment using trapped particle configuration in KSTAR
Lunch: *12:30-14:00*			
Session 8 (Category III) Chair: Prof. A.Y. AYDEMIR	14:00-14:25	**Mitsutaka ISOBE** (NIFS)	Fusion neutron production with deuterium neutral beam injection and enhancement of fast-ion physics study in LHD
	14:25-14:50	**Yasushi TODO** (NIFS)	Simulations with MEGA code of energetic particle driven instabilities
	14:50-15:15	**Tieshuan FAN** (Peking Univ.)	Neutron diagnostics for EAST deuterium operation
	15:15-15:35	**Kunihiro OGAWA** (NIFS)	Enhancement of radial transport of energetic ion destabilized by helically trapped-energetic-ion driven resistive interchange mode in LHD
Break: *15:35–15:50*			
Session 9 (Category IV) Chair: Prof. M. ISOBE	15:50-16:15	**Kazuo TOI** (NIFS)	Characteristic Properties of Energetic-Ion-Driven Geodesic Acoustic Modes Observed in a Reversed Magnetic Shear Plasma of LHD
	16:15-16:40	**Yasuaki KISHIMOTO** (Kyoto Univ.)	Gyro-kinetic based numerical experiment of Tokamak : L-mode and the recipe to break it

	16:40-17:05	**Satoshi OHDACHI** (NIFS)	Plasma response to the RMP application in LHD and Tokamaks
	17:05-17:25	**Ting LAN** (USTC)	Preference-based performance measures for Time-Domain Global Similarity method
	17:25-17:45	**Yulei WANG** (USTC)	The accurate particle tracer code
Session 10 Chairs: Prof. L.Q. HU Prof. S. MORITA Prof. J.G. KWAK	17:45-18:00	**Meeting Discussion**	
		Dinner: *18:00*	

December 14, 2017
(Thursday)

Session 11 Joint Discussion (Category I) Chair: Prof. L.Q. Hu	*08:30-10:00* Plenary meeting on future collaboration at category I Plasma heating and current drive Active plasma control Integrated modelling MHD instability control Wall conditioning and effects
	Break: *10:00– 10:30*
Session 12 Joint Discussion (Category II) Chair: Prof. J.G. KWAK	*10:30-12:00* Plenary meeting on future collaboration at category II Plasma-wall interaction and edge plasma modelling Control of particle and power load Structure and evolution of pedestal Edge plasma diagnostics The interplay between core, SOL and pedestal
	Lunch: *12:00-14:00*
Session 13 Joint Discussion (Category III) Chair: Prof. S. MORITA	*14:00-15:30* Plenary meeting on future collaboration at category III Destabilisation of Alfvén waves and Energetic Particle Modes Interaction of fast ions with background MHD Runaways control and simulation Modification of the PFW by incident particles Identification of the fast particle modes
	Break: *15:30–16:00*
Session 14 Chairs: Prof. L.Q. HU Prof. S. MORITA Prof. J.G. KWAK	*16:00-18:00* **Summary of Joint Discussions**
	Dinner: *18:00*

December 15, 2017 (Friday)			
Session 15 (Category II) Chair: Prof. Y. LIU	*08:30-08:55*	**Ling ZHANG** (ASIPP)	Application of EUV spectroscopy diagonstics to tungsten behavior study on EAST
	08:55-09:20	**Soo Hyun SON** (NFRI)	Study of erosion/deposition pattern in KSTAR plasma discharges on mid-plane region
	09:20-09:45	**Cunfeng DONG** (SWIP)	Progress in impurity study based on EUV spectrometers in HL-2A
	09:45-10:05	**Jaehyun LEE** (NFRI)	Increased turbulent fluctuations and bifurcation of perpendicular flow on the ELM-crash suppression under n=1 RMP
	10:05-10:25	**Kai ZHANG** (SWIP)	The development of the multi-pulse laser blow-off system in the HL-2A tokamak and its preliminary application
Break: *10:25– 10:40*			
Session 16 (Category IV) Chair: Prof. Y. TODO	*10:40-11:05*	**Ahmet Yasar AYDEMIR** (NFRI)	An n=1 explosive instability and its role in disruptions
	11:05-11:30	**Yunbo DONG** (SWIP)	Dissipation of Runaway Current on HL-2A
	11:30-11:55	**Ichihiro YAMADA** (NIFS)	Application of fast ADC system in Thomson scattering diagnostic
	11:55-12:15	**Yang LIU** (NIFS)	Neutron and gamma-ray effects on charge-coupled device during D-D operation in Large Helical Device
Lunch: *12:30-14:00*			
Session 17 Chairs: Prof. L.Q. HU Prof. S. MORITA Prof. J.G. KWAK	*14:00-17:00*	**Discussions on A3 program** **Summary of A3 program in China** **Meeting closing**	
Dinner: *18:00*			

Participants of the 12th A3 Workshop in Chongqing

12 - 15 December, 2017, Chongqing, China

No	Nation	Affiliation	Name
1	Korea	NFRI	Jong-Gu KWAK
2	Korea	NFRI	Jeehyun KIM
3	Korea	NFRI	Hyun-Seok KIM
4	Korea	NFRI	Soo Hyun SON
5	Korea	NFRI	Ahmet Yasar AYDEMIR
6	Korea	NFRI	Woochang LEE
7	Korea	NFRI	Jeongwon LEE
8	Korea	NFRI	Jaehyun LEE
9	Japan	NIFS	Shigeru MORITA
10	Japan	NIFS	Daiji KATO
11	Japan	NIFS	Naoko ASHIKAWA
12	Japan	NIFS	Satoshi OHDACHI
13	Japan	NIFS	Mitsutaka ISOBE
14	Japan	NIFS	Yasushi TODO
15	Japan	NIFS	Kazuo TOI
16	Japan	NIFS	Tetsutaro OISHI
17	Japan	NIFS	Yang LIU
18	Japan	NIFS	Mamoru SHOJI
19	Japan	NIFS	Katsuyoshi TSUMORI
20	Japan	NIFS	Ichihiro YAMADA
21	Japan	NIFS	Kunihiro OGAWA
22	Japan	Kushiro College	Seiki SAITO
23	Japan	Kyoto Univ.	Yasuaki KISHIMOTO
24	China	ASIPP	Liqun HU
25	China	ASIPP	Baonian WAN
26	China	ASIPP	Xiaodong ZHANG
27	China	ASIPP	Bingjia XIAO
28	China	ASIPP	Junling CHEN

29	China	ASIPP	Xianzu GONG
30	China	ASIPP	Rui DING
31	China	ASIPP	Tianyang XIA
32	China	ASIPP	Haiqing LIU
33	China	ASIPP	Jinping QIAN
34	China	ASIPP	Bojiang DING
35	China	ASIPP	Biao SHEN
36	China	ASIPP	Jiansheng HU
37	China	ASIPP	Shuai GU
38	China	ASIPP	Ling ZHANG
39	China	HUST	Zhipeng CHEN
40	China	USTC	Ge ZHUANG
41	China	USTC	Jian LIU
42	China	USTC	Yulei WANG
43	China	USTC	Ting LAN
44	China	SWIP	Yi LIU
45	China	SWIP	Zhengying CUI
46	China	SWIP	Cunfeng DONG
47	China	SWIP	Kai ZHANG
48	China	SWIP	Yipo ZHANG
49	China	SWIP	Yunbo DONG
50	China	Peking Univ.	Tieshuan FAN
51	China	Donghua Univ.	Fuqiong WANG
52	China	ASIPP	Min XIAO
53	China	ASIPP	Yan CHAO
54	China	ASIPP	Yongkuan ZHANG
55	China	ASIPP	Shaohua DONG
56	China	ASIPP	Ruijie ZHOU
57	China	ASIPP	Sha WU